

CARDIFF
UNIVERSITY

PRIFYSGOL
CAERDYDD

pcatdes 

Materials for the Photocatalytic Treatment of Recalcitrant Organic Waste

Emir Bouleghlimat



Abstract

The photocatalytic degradation of cinnamic acid, by TiO_2 , has been studied extensively in aerobic and anaerobic conditions and in the presence of common salts often found in industrial waste waters. Analysis of the intermediates formed found that molecular oxygen is central to forming the important radicals for the main benzaldehyde mechanism by which cinnamic acid initially degrades, as well as a key component required for the mineralisation to carbon dioxide. In the absence of molecular oxygen an alternate, but slower, pathway becomes the prevalent. The hydroxyl driven mechanism is capable of decarboxylation of the initial carboxyl group but further oxidation does not occur at a reasonable rate.

By investigating the effect of salts in solution we found that sulfates and chlorides both interfere with degradation mechanisms and decrease the mineralisation efficiency of titania photocatalysis. Sulfates blocked important surface sites needed for substrate binding that inhibited the benzaldehyde pathway and slowed down the degradation pathway. Whilst chloride formed radical chlorine species ($\text{Cl}\cdot$) in the presence of TiO_2 that resulted in the increase of cinnamic acid removal and the emergence of new reaction pathways. $\text{Cl}\cdot$ competed with the superoxide radical anion ($\text{O}_2^{\cdot-}$) to attack across the double bond of cinnamic acid, decarboxylate and form several new acetophenone-derived intermediates. A widening of the intermediate map, through the formation of new intermediates, is coupled with a significant slowing of total mineralisation which presents real issues for photocatalytic waste water treatment where chloride ions are present. Additionally, the chlorine radical induced pathways produce intermediates of a greater toxicity; bringing the implication that partial oxidative degradation could result in waste water with an increased toxicity.

Anodic nanotubes were explored as an option for alternative materials to be used within photocatalytic reactors. Nanotubes anodised for 8 hours were found to be the most photoactive in the liquid phase, and in the surface degradation of contaminants, due to the wider pores that were structurally sound enough to not slope and reduce light penetration. The surface topography was identified as the key factor for promoting photocatalysis. It was also found that the materials had a cross-phase applicability, in that the most active liquid phase nanotubes were also the most efficient for surface degradation. The incorporation of tungsten into the anodisation process did not improve the photocatalytic activity. Photodeposition of palladium and gold resulted in a decrease in the degradative efficiency of the nanotube arrays.

Pd/TiO₂ and Au/TiO₂ powders were found to reduce the degradation rate of cinnamic acid in oxygenated conditions, although both metals improved the oxidation of surface deposits of carbon. In deoxygenated conditions, Pd/TiO₂ catalysts exhibited superior degradation of cinnamic acid in comparison to plain TiO₂ and gold doped catalysts. Enhancements in the mineralisation rates, to CO₂, were also found. The improvements were attributed to the presence of palladium improving charge separation and introducing new reaction sites capable of decarboxylating the alcohol and aldehyde functionalities, respectively. While the gold nanoparticles were poorly dispersed, they were found to increase the selectivity for phenylacetaldehyde, in deoxygenated conditions, by a factor of 5.

Acknowledgments

I would firstly like to thank my project supervisor, Professor Philip Davies, for giving me the opportunity to do a PhD in his group and providing me with all of his wisdom and support. This thesis wouldn't have happened without his attentive and rapid responses while proof reading and correcting each chapter. Not to mention the untold amounts of Casa XPS magic I have learned from him.

Secondly, I would like to thank the European Commission for funding my PhD and the PCATDES project as a whole.

To all my colleagues in the PCATDES project, I am grateful for the excellent research you have allowed me to be a part of, the interesting meetings we had and the friendships we formed.

Next, I would like to thank the many technical staff in Cardiff University's chemistry department for their aid in using the many apparatus, especially; Dr David Morgan for his help running and interpreting XPS, Dr Thomas Davies for running my samples on the FE-SEM and TEM, and Tom Williams for graciously allowing me to run so many samples on the GC-MS.

There are many friends around the department that have helped keep me sane throughout the years. There are too many to name but in particular I would like to thank Mark and Julia, because without our "short" lunches never would have been so much fun. And to all of the members of the surface science and catalysis group, from Rob through to Jonathan. Working around you has been a pleasure and I will never forget it.

Lastly, I would like to thank my family. To my parents, your never ending love and support has always helped and encouraged me to achieve as much as possible in life; and this thesis is no different. Everything you have done has helped me through these final months and it has meant the world to me. To my wife Sophie; I know I have been the bane of your life while writing this. I intend to continue to lovingly annoy you for the rest of our lives. You and Eli have no idea how much the moral support has meant to me, particularly in the final months when I was working until the early hours of the morning.

Contents

Chapter 1

Introduction and Literature Review

| | |
|---|----|
| 1.1 Project Background | 2 |
| 1.1.1 PCATDES | 2 |
| 1.1.2 Palm oil | 2 |
| 1.1.2 Palm Oil Composition | 3 |
| 1.1.3 Treatment methods | 4 |
| 1.2 Titania as a material | 6 |
| 1.3 Titania Photoactivated processes | 6 |
| 1.3.1 Charge trapping | 7 |
| 1.3.2 Charge recombination and charge lifetimes | 8 |
| 1.3.3 Anatase-Rutile Synergy | 9 |
| 1.3.4 Oxidative degradation | 11 |
| 1.3.4.1 Hole mediated mineralisation processes | 11 |
| 1.3.4.2 Electron Mediated Processes | 16 |
| 1.4 Use of Gold/Palladium | 20 |
| 1.4.1 The Schottky Barrier | 20 |
| 1.4.2 Au/TiO ₂ photo-reactivity | 22 |
| 1.4.2.1 Schottky Junction and Plasmonic Resonance | 22 |
| 1.4.2.2 Au/TiO ₂ Photo-Reactivity | 24 |
| 1.4.3 Pd/TiO ₂ Photoreactivity | 27 |
| 1.5 Aims of the Studies | 30 |
| 1.6 References | 31 |

Chapter 2

Experimental

| | |
|---|----|
| 2.1 Introduction | 42 |
| 2.2 Catalyst Preparation, Methods and Equipment..... | 42 |
| 2.2.1 Powdered Catalyst Preparation..... | 42 |
| 2.2.1.1 Preparation of Modified P25 (mP25)..... | 42 |
| 2.2.1.2 Pd/TiO ₂ Preparation..... | 42 |
| 2.2.1.3 Au/TiO ₂ Preparation..... | 43 |
| 2.2.2 TiO ₂ Nanotubes Preparation..... | 43 |
| 2.2.2.1 Anodisation equipment..... | 44 |
| 2.2.2.2 TiO ₂ Nanotubes..... | 45 |
| 2.2.2.3 WO ₃ /TiO ₂ Nanotubes..... | 45 |
| 2.2.2.4 Metal Loaded TiO ₂ Nanotubes..... | 45 |
| 2.2.3 Photocatalytic Reactor Experimental Set Up..... | 46 |
| 2.2.3.1 Reactor vessels..... | 46 |
| Liquid Phase Experimental Procedure..... | 46 |
| Surface Degradation Experimental Procedure..... | 48 |
| 2.2.3.2 Light Source..... | 48 |
| 2.2.4 UV/Visible Spectroscopy..... | 48 |
| 2.2.5 GC-MS..... | 50 |
| 2.2.6 Gas Chromatography..... | 51 |
| 2.2.7 CO ₂ Calibration..... | 52 |
| 2.3 Catalyst Characterisation..... | 52 |
| 2.3.1 X-Ray Photoelectron Spectroscopy, XPS..... | 53 |
| 2.3.2 Fourier Transformed Infrared Spectroscopy (FTIR)..... | 55 |
| 2.3.2.1 Attenuated Total Reflection..... | 56 |
| 2.3.2.2 Diffuse Reflectance Infrared Transform Spectroscopy (DRIFTS)..... | 57 |
| 2.3.3 X-Ray Diffraction..... | 58 |

| | |
|--|----|
| 2.3.5 UV Diffuse Reflectance Spectroscopy | 59 |
| 2.3.6 SEM - EDX..... | 59 |
| 2.3.7 Transmission electron microscopy | 61 |
| 2.4 Characterisation and Analytical Methodology..... | 63 |
| 2.5 References..... | 64 |

Chapter 3

The Effect of Salts on the Photocatalytic Degradation of Cinnamic Acid

| | |
|---|----|
| 3.1 Introduction | 68 |
| 3.1.1 Chemistry of Sulfate Radicals | 69 |
| 3.1.2 Chemistry of Chlorine radicals | 70 |
| 3.2 Results and Discussion | 72 |
| 3.2.1 The Degradation of Cinnamic Acid..... | 72 |
| 3.2.1.1 Photocatalytic Degradation of Cinnamic Acid and its Intermediates by Titania..... | 72 |
| 3.2.1.2 Degradation of Cinnamyl Alcohol..... | 74 |
| 3.2.1.3 CO ₂ capture experiments | 75 |
| 3.2.1.4 XPS Analysis of Fresh and Spent Catalysts | 76 |
| 3.2.1.5 Infrared studies of Fresh and Spent Catalysts..... | 80 |
| 3.2.1.6 X-Ray Diffraction Studies of Fresh and Spent Catalysts..... | 86 |
| 3.2.1.7 Proposed Model for the Photocatalytic Degradation of Cinnamic Acid | 86 |
| 3.2.2 The Effect of Sulfates on the Degradation of Cinnamic Acid | 89 |
| 3.2.2.1 Kinetic and Mechanistic Impact of Sulfate on Cinnamic Acid Degradation..... | 89 |
| 3.2.2.2 XPS studies of Spent Photocatalysts from Sulphated Reaction Media | 94 |
| 3.2.2.3 Infrared studies of Spent Photocatalysts from Sulphated Reaction Media..... | 95 |
| 3.2.2.4 XRD studies of Spent Photocatalysts from Sulphated Reaction Media | 98 |

| | |
|---|-----|
| 3.2.2.5 Discussion of the Impact of Sulfate on the Photocatalytic Degradation of Cinnamic Acid | 99 |
| 3.2.3 The Effect of Chlorides on the Degradation of Cinnamic Acid | 102 |
| 3.2.3.1 Kinetic Impact..... | 102 |
| 3.2.3.2 Mechanistic Impact of Chloride..... | 105 |
| 3.2.3.3 Photocatalytic Oxidation of Acetophenone, 2-Chloroacetophenone and 2'Chloroacetophenone | 107 |
| 3.2.3.4 XPS Studies of Spent Photocatalysts from Chlorinated Reaction Media..... | 110 |
| 3.2.3.5 XRD Studies of Spent Photocatalysts from Sulphated Reaction Media..... | 113 |
| 3.2.3.6 Infrared Studies of Spent Photocatalysts from Chlorinated Reaction Media | 114 |
| 3.2.3.7 Discussion of the Impact of Chloride | 117 |
| 3.3 Conclusions | 122 |
| 3.4 References | 123 |

Chapter 4

Metal Doped Titania Nanotubes for the Photocatalytic Degradation of Organic Contaminants

| | |
|--|-----|
| 4.1 Introduction | 127 |
| 4.1.1 The Development of Anodic Nanotubes..... | 128 |
| 4.1.1.1 First Generation Nanotubes | 128 |
| 4.1.1.2 Second Generation Nanotubes..... | 129 |
| 4.1.1.3 Third Generation Nanotubes..... | 130 |
| 4.1.2 Titania Nanotubes in Photocatalytic Processes..... | 131 |
| 4.2 Characterisation of Nanotube Photocatalysts | 132 |
| 4.2.1 Topographical Studies of Nanotube Arrays..... | 132 |
| 4.2.1.1 Titania Nanotubes | 132 |
| 4.2.1.2 Ti/W Mixed Oxide..... | 138 |

| | |
|---|------------|
| 4.2.1.3 Deposition of Gold and Palladium – Topography | 139 |
| 4.2.2 X-Ray Diffraction Studies | 141 |
| 4.2.3 UV Measurements of Nanotube Samples | 144 |
| 4.2.4 XPS Studies | 144 |
| 4.2.4.1 Titania Nanotube Arrays..... | 144 |
| 4.2.4.2 Ti/W Nanotube Arrays..... | 146 |
| 4.2.4.3 Gold and Palladium Decorated Nanotubes | 148 |
| 4.3 Photocatalytic Testing | 152 |
| 4.3.1 Reactivity of Plain Nanotube Arrays | 153 |
| 4.3.1.1 Liquid Phase Degradation of Cinnamic Acid | 154 |
| 4.3.1.2 Surface Degradation of Cinnamic Acid..... | 155 |
| 4.3.1.3 Surface Degradation of Stearic Acid | 156 |
| 4.3.2 Reactivity of Au/Pd Nanotube Arrays | 160 |
| 4.3.2.1 Liquid Phase Degradation of Cinnamic Acid | 160 |
| 4.3.2.2 Surface Degradation of Stearic Acid | 163 |
| 4.4 Conclusions..... | 167 |
| 4.5 References..... | 169 |

Chapter 5

Metal Loaded Nanoparticles for Photocatalytic Waste Water Treatment

| | |
|---|------------|
| 5.1 Introduction..... | 174 |
| 5.2 Photocatalyst Characterisation..... | 175 |
| 5.2.1 X-Ray Diffraction | 175 |
| 5.2.2 UV/Vis | 176 |
| 5.2.3 X-ray Photoelectron Spectroscopy Analysis | 177 |
| 5.2.4 DRIFTS-FTIR | 184 |

| | |
|--|-----|
| 5.2.5 Transmission Electron Microscopy Particle Size Study | 186 |
| 5.3 Results | 187 |
| 5.3.1 The Photoactivity of Palladium Catalysts | 187 |
| 5.3.1.1 Kinetic Impact | 187 |
| 5.3.1.2 Mechanistic Impact | 188 |
| 5.3.2 The Photoactivity of Gold Catalysts | 192 |
| 5.3.2.1 Kinetic Impact | 192 |
| 5.3.2.2 Mechanistic Impact | 193 |
| 5.3.3 Carbon Dioxide Capture Experiments | 193 |
| 5.4 Discussion | 195 |
| 5.4.1 Pd/TiO ₂ Catalysts | 195 |
| 5.4.2 Au/TiO ₂ Catalysts | 199 |
| 5.5 Conclusions | 203 |
| 5.6 References | 204 |

Chapter 6

Conclusions and Future Work

| | |
|---|-----|
| 6.1 The Effect of Salts on the Photocatalytic Degradation of Cinnamic Acid | 207 |
| 6.1.1 The Cinnamic Acid Photocatalysed Degradation Mechanism | 207 |
| 6.1.2 The Impact of Salts on the Degradation of Cinnamic Acid | 207 |
| 6.1.3 Future Considerations for Work | 208 |
| 6.2 Metal Doped Titania Nanotubes for the Photocatalytic Degradation of Organic Contaminants | 208 |
| 6.2.1 Titania Nanotubes and Their Photocatalytic Efficiency | 209 |
| 6.2.2 Ti/W Mixed Metal Oxide Nanotubes | 209 |
| 6.2.3 Gold and Palladium Doped Nanotubes | 210 |
| 6.2.4 Future Considerations for Work | 211 |

| | |
|---|-----|
| 6.3 Metal Loaded Nanoparticles for Waste Water Treatment | 211 |
| 6.3.1 Palladium Photocatalysts | 211 |
| 6.3.2 Gold Photocatalysis | 212 |
| 6.3.3 Future Considerations for Work | 212 |
| 6.4 References | 212 |
| | |
| Appendix 1 - Mass Spectra | 214 |
| Appendix 2 - Infrared Spectra | 223 |
| Appendix 3 - Xray Photoelectron Spectra | 227 |

Chapter 1 - Introduction and Literature Review

| | |
|---|----|
| 1.1 Project Background | 2 |
| 1.1.1 PCATDES | 2 |
| 1.1.2 Palm oil | 2 |
| 1.1.2 Palm Oil Composition | 3 |
| 1.1.3 Treatment methods | 4 |
| 1.2 Titania as a material | 6 |
| 1.3 Titania Photoactivated Processes | 6 |
| 1.3.1 Charge trapping | 7 |
| 1.3.2 Charge recombination and charge lifetimes | 8 |
| 1.3.3 Anatase-Rutile Synergy | 9 |
| 1.3.4 Oxidative degradation | 11 |
| 1.3.4.1 Hole mediated mineralisation processes | 11 |
| 1.3.4.2 Electron Mediated Processes | 16 |
| 1.4 Use of Gold/Palladium | 20 |
| 1.4.1 The Schottky Barrier | 20 |
| 1.4.2 Au/TiO ₂ photo-reactivity | 22 |
| 1.4.2.1 Schottky Junction and Plasmonic Resonance | 22 |
| 1.4.2.2 Au/TiO ₂ Photo-Reactivity | 24 |
| 1.4.3 Pd/TiO ₂ Photoreactivity | 27 |
| 1.5 Aims of the Studies | 30 |
| 1.6 References | 31 |

1.1 Project Background

1.1.1 PCATDES

A great deal of work is being performed, around the world, to tackle the issue of how to purify the large amounts of industrial effluent being produced in many industries. The PCATDES consortium is a collaborative effort, by 11 universities of 7 nationalities (Thailand, Malaysia, Vietnam, Spain, Germany, Turkey and the UK), that aims to harness the degradative power of semiconductor photocatalysis and incorporate novel photocatalysts into a light emitting diode based reactor. The key aims of the project were to: (1) address the relatively low photocatalytic activity rates of common commercial photocatalysts; (2) design novel photocatalytic materials suitable for incorporation into scaled up reactors; (3) take advantage of improvements in LED technology to create efficient, high intensity light sources to enhance the efficiencies and make the process commercially viable. [1]

1.1.2 Palm oil

Effective treatment of industrial waste water is a challenge faced by numerous

| Parameters | Value ^a | Regulatory discharge limits ^b |
|---|--------------------|--|
| Temperature (°C) | 80-90 | 45 |
| pH | 4.7 | 5.0-9.0 |
| Biochemical Oxygen Demand BOD ₃ ; 3days at 30 °C | 25,000 | 100(50) |
| Chemical Oxygen Demand | 50,000 | - |
| Total Solids (T.S) | 40,500 | - |
| Total Suspended Solids (T.S.S) | 18,000 | 400 |
| Total Volatile Solids (T.V.S) | 34,000 | - |
| Oil and Grease (O&G) | 4,000 | 50 |
| Ammonia-Nitrate (NH ₃ -N) | 35 | 150 |
| Total Kjeldahl nitrogen (TKN) | 750 | 200 |

*All values, except pH and temperature, are expressed in mgL-1; POME= Palm oil mill effluent

Figure 1.1.1:- Typical characteristics of raw palm oil mill effluent (POME) and the regulatory discharge limits for Malaysia [5]

countries around the world. For many countries the industrial growth far surpassed their capability, and in some cases their willingness, to find and apply methods to neutralise the dangers of the effluent. As of 2011, palm oil held the largest single share of the worlds vegetable oil market; taking up 28.2% of the 17 million tonnes of vegetable oil produced that year. [2] The major producers in the market in 2015, according to greenpalm.org, were; Indonesia (33.4MnT), Malaysia (19.9MnT), Thailand (1.8MnT), Colombia (1.2MnT) and Nigeria (0.8MnT). [3] In 2009 it was estimated that 6.5 kg of palm oil were consumed in the world per capita, with the production levels expected to continue to increase as demand in countries like China and India grow. [4] The crops popularity largely relies on the efficiency

per hectare of palm tree being ten times that of similar crops like rapeseed and sunflower oil, as well as its utilisation for biofuel production.

1.1.2 Palm Oil Composition

Palm oil mills are responsible for the treatment and digestion of palm fresh fruit branches (FFB) to kernels, palm oil and palm oil mill effluent. FFB are sterilised, stripped, digested and split into two separate processing streams. One stream produces kernels and hydrocyclone waste water, whilst the other produces crude palm oil and palm oil mill effluent (POME). Sterilisation, purification of the crude palm oil and hydrocyclone waste constitutes 36%, 60% and 4% of the total POME. [5] Large amounts of water are required for these processes where it is estimated to produce between 1 to 9 tonnes of POME for every tonne of crude palm oil produced. The actual characteristics of raw POME vary based on the season, raw material quality and the particular procedures implemented by the mill. However typical characteristics can be seen in **Figure 1.1.1**. The qualities of the waste often far exceed the allowed regulatory discharge limits and by law must be treated before being disposed of into water ways. The high BOD (biological oxygen demand) and COD (chemical oxygen demand) is especially problematic. BOD is the amount of oxygen required by biological organisms to breakdown organic matter present, whilst COD is the amount of oxygen that consumed during the decomposition of organic compounds and the oxidation of inorganic compounds. The disposal of raw POME into water ways would result in the depletion of dissolved oxygen and the subsequent destruction of animal and plant life in the ecosystem.



Figure 1.1.2:- A ponding system employed on oil mills in Thailand. (a) a resting pond, used to separate out oil and sludge (b) a covered pond (c) a close up of POME

Many compounds have been identified in POME. Generally, the organic composition of the effluent consists of lignin, tannin, and large chained polyacids like humic and fluvic acid. [6] Jamal *et al.* also found various phenolic compounds such as; 4-hydroxybenzoic acid, syringic acid, protocatechuic acid, *p*-coumaric acid. [7] Based on the structure of these compounds it was decided by the PCATDES consortium that cinnamic acid was an appropriate model compound that contained the key functionalities of the organic compounds present within POME, and effluent from the fishing industries.

1.1.3 Treatment methods

Several methods are employed to decompose the various constituents of the effluent. One of the main methods employed, in up to 85% of palm oil mills, is the “ponding” system. [5] Large POME ponds, an example of one in Thailand is shown in **Figure 1.1.2(a)**, are used to process slowly separates the oil and solid matter into a sludge before being pumped into an acidification pond. After acidification, the effluent is pumped into aerobic or anaerobic ponds for treatment. Both ponds utilise biological cells to degrade the effluent and reduce its BOD and COD. [8] Ponding, while low cost, takes up large amounts of space, is inefficient at degrading the effluent and release large amounts of CO₂, H₂S and CH₄. [9][10] Emitted gases can be captured from anaerobic digesters, with estimates show that one tonne of POME can

produce 28 m³ of methane. [11] If captured, this biogas can be used to generate electricity, where the greatest potential for energy production lies in on site gas capture and processing. [12] In Malaysia, however, 90 % of palm oil mills do not capture the emitted gases, leaving them to dissipate into and harm the environment. Testing has found that the various ponding processes can decrease the key characteristics to the required levels, COD can be reduced by 98.8% by anaerobic digestion, however these processes can take up to 90 days to complete. [13] Another drawback, from ponding, is the leeching of organic contaminants into the soil during the long ponding process. Whilst other methods exist and are being employed in the treatment of POME, none are efficient enough to hit the targets set by current restrictions, required to prevent environmental damage from occurring, in an economically viable timescale.

Considering that none of the current decomposition methods are effective or economical enough, other methods must be explored. Photocatalysis is a technique capable of the complete mineralisation of recalcitrant organic waste to H₂O and CO₂, presenting a suitable procedure to fully degrade the reduced COD POME to concentrations suitable for ejection into the environment. Of all the current photocatalytic materials available, titania is a cheap, versatile and non-toxic option that has demonstrated its ability to indiscriminately degrade almost any organic compounds.

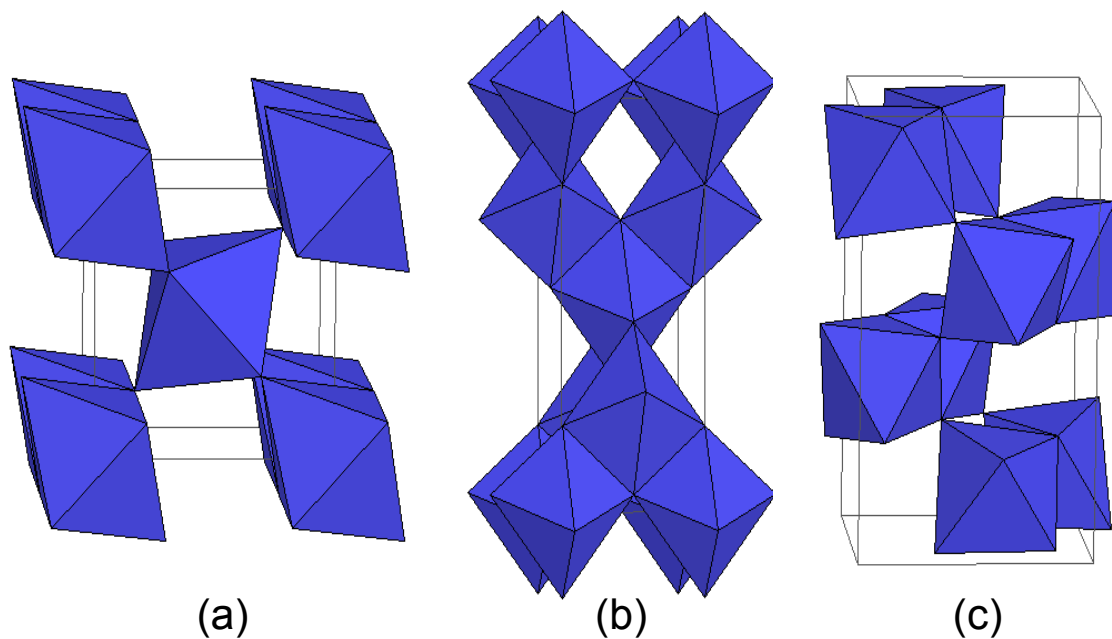


Figure 1.2.1:- Crystal structure of the three main titania polymorphs
(a) Rutile, (b) Anatase, (c) Brookite [19]

1.2 Titania as a material

Titania, titanium dioxide or TiO_2 , is an extremely versatile semiconductor oxide that has been applied in a wide array of technological uses. The three main crystallographic polymorphs are; anatase, rutile and brookite. Each polymorph is based on a distorted variation of a TiO_6^{2-} octahedral unit cell. Anatase and rutile have tetragonal crystal systems, whilst brookite has an orthorhombic system. [14] The most widely investigated polymorph of titania is rutile due to it being the most naturally abundant and thermodynamically more stable than anatase, calculations found it to be 1.2 – 2.8 kcal/mol more stable. [15] The crystal structure of rutile is shown in **Figure 1.2.1 (a)**. The octahedra are arranged in linear chains in the (001) direction, connected by the edges that give rutile the highest theoretical density of 4.26 g/cm^3 . [16] Anatase, although also tetragonal, differs to rutile because the octahedrons are connected by the vertices as shown in **Figure 1.2.1 (b)**. This gives anatase a lower density of 3.84 g/cm^3 . The first anatase single crystals were not successfully formed until 1993, when Levy *et al.* grew large crystals by chemical transport reactions which has since allowed the in depth investigation of homogeneous anatase surfaces. [17][18] In brookite, the least common phase, the unit cells are connected via both the vertices and the edges giving it the crystal structure in **Figure 1.2.1 (c)**. It is also the most difficult of the polymorphs to form artificially, receiving the least attention of the three, and tends to have properties that lie in the middle of the other two phases.

1.3 Titania Photoactivated processes

The photocatalytic properties, of titania, were famously exploited by Honda and Fujishima in 1972 when they found that using titania in an electrochemical cell sensitized the reaction to light stimuli and resulted in water splitting. [20] Following this discovery, Schrauzer and Guth showed in 1977 that titania powder could photo-split water, in the presence of N_2 , and produce NH_3 . [21] These initial discoveries paved the way for titania to become a leading material in photocatalytic water splitting and hydrogen production, [22][23][24][25][26][27] dye sensitized solar cells, [28] and the photocatalysed degradation of organic pollutants for water [29][30][31][32][33][34][35][36][37][38] and air purification. [39][40][41]



1.3.1 Charge trapping

Titania photocatalytic behaviour depends on the generation of electron/holes pairs that form on the femto-second timescale when photons hit the material with energy \leq bandgap, (**equation (1)**). Photogenerated charge carriers can either rapidly recombine soon after formation, <1 ps, [42] or transfer to the trapped state from which they recombine at a slower rate of 10 – 100 ns. **Equations 3** and **4** show the process of surface charge trapping of holes and electrons, respectively. Hole trapping occurs mostly on the surface and is generally believed to be localized to a bridging lattice oxygen ($O_s \cdot^-$) or possibly an adsorbed hydroxyl radical ($OH_s \cdot^-$). [43][44][45][46][47] Fundamentally, the hole is an O^{1-} species. First principle calculations indicate that many of the hole trapping states are contributed by adsorbed hydroxyl radical species that provide states just above the valence band, resulting in the common hole notation to be $Ti^{4+} \cdot -OH$. [48] Although deeply trapped holes do form, they are generally unreactive to recombination and reaction. [49] There is controversy over whether these bound hydroxyl radicals can dissociate from the surface to form free hydroxyl radicals. [50][51][52] It is believed that they possess too high a potential barrier to allow desorption, ruling out this process as the route to form free hydroxyl radicals, and instead other routes that will be discussed later are responsible for free hydroxyl radicals. However, Nosaka *et al.* have recently presented data disputing this theory. [53][54] Some data also suggests that hydroxyl radicals can form via h_{vb}^+ and e_{cb}^- mediated pathways. [55] Ab initio calculations, by Shapovalov *et al.*, suggested that a hole can delocalise across two surface oxygen atoms and transfer to adsorbed species. [56] These shallow trapped holes have a very high oxidation potential and are noted for being in thermal equilibrium with free hole species. [49] The role of water has found to be key in stabilising and trapping surface hole species. [57][58][59][60] Recent EPR data also showed evidence of surface and sub-surface trapped holes, and that the

shallow surface trapped hole species ($O^{\cdot-}$) require a complex environment including water to effectively stabilise them. [58]

The presence of hydroxyl radicals, on the titania surface, results in upwards band bending that pushes electrons from the surface into the bulk. Electrons then try to stabilise themselves by lowering their energy by migrating to lower energy states, that exist within the materials bandgap, and can result in the electron lifetime stretching into months. [61] Data suggests that electrons can be trapped both at surface sites, [47][62][63][64] in the anatase and rutile polymorphs, and at subsurface trapping sites. [52][56][57][65] Experimental and theoretical data indicates that Ti^{4+} sites are responsible for surface, and sub-surface, electron trapping. The manner in which the electron is trapped leads to the notation of Ti^{3+} -OH to describe the chemical state. Electron trapping has been measured to occur very rapidly (<500 fs), with the site lying around 0.8 eV below the conduction band. [66] Tamaki *et al.* found that photogenerated electrons reached the surface within 170 fs and subsequently underwent a trap hopping process between surface and shallow traps that took 500 fs. [67]

1.3.2 Charge recombination and charge lifetimes

When an electron and hole meet the pair recombines and releases energy via non-irradiative or irradiative pathways. The process is highly dependent on a number of factors including sample preparation, amount of charge transfer, the presence of scavengers, reaction temperature and irradiation light intensity. Being an indirect bandgap semiconductor, recombination cannot occur directly from the conduction band, as is evident from work by Leytner *et al.*, that found that 60% of trapped electron-hole pairs in an anatase crystal recombined with-in 25 ns resulting in the release of heat. [66] Other studies have found a particle size dependence on recombination rates, where decay times of 67 ps (2.1 nm), 405 ps (13.3 nm) and 66 ps (26.7 nm) were measured. [68] 90% of electron/hole pairs had recombined by 10 ns which presents a problematic implication for photocatalytic reactions, as these rates are faster than many if effective charge separation is not achieved. Recombination has been effectively retarded, allowing electron lifetimes of months, by use of ethanol as a hole scavenger in the absence of oxygen. [61] Clearly, electrons can have significant life times in the correct conditions. On the other hand, some groups have shown that encouraging the deep trapping of electrons can promote hole-driven oxidative photocatalysis. [67] The other routes for recombination are those in which the electrons relax in a radiative manner. [47] Photoluminescence spectroscopy indicated the two mechanisms for recombination in TiO_2 crystals that contributed to photoluminescence were:

1. relaxation of conduction band electrons into holes trapped in defects (h^+_{tr})
2. relaxation of conduction band and shallow trapped electrons into deep trapping states that span the Fermi energy. Deeply trapped electrons then recombine with valence band holes

While these studies provide a great deal of insight into how to avoid electron-hole recombination, they are not yet practically useful in conventional photocatalysis. Other well-established methods for charge separation, that will be discussed later in 1.3.3 and 1.4, are the mixing of titania polymorphs and the use of precious metals as electron traps.

1.3.3 Anatase-Rutile Synergy

Structural differences of the polymorphs are accompanied with important changes in optical properties. Anatase has long been realised to be the most active single phase of titania for photocatalytic purposes. [14][69][70][71][72] However, explanations for why this is the case must take into account several aspects. Anatase and rutile have differing band structures (Figure 1.3.1 (i)) resulting in anatase having an indirect band gap of 3.2 eV, whilst rutile has a direct bandgap of 3.0 eV. [18][70][73] The smaller bandgap of rutile allows for the absorption of a wider range of photons, it has long been believed that anatase exhibits an

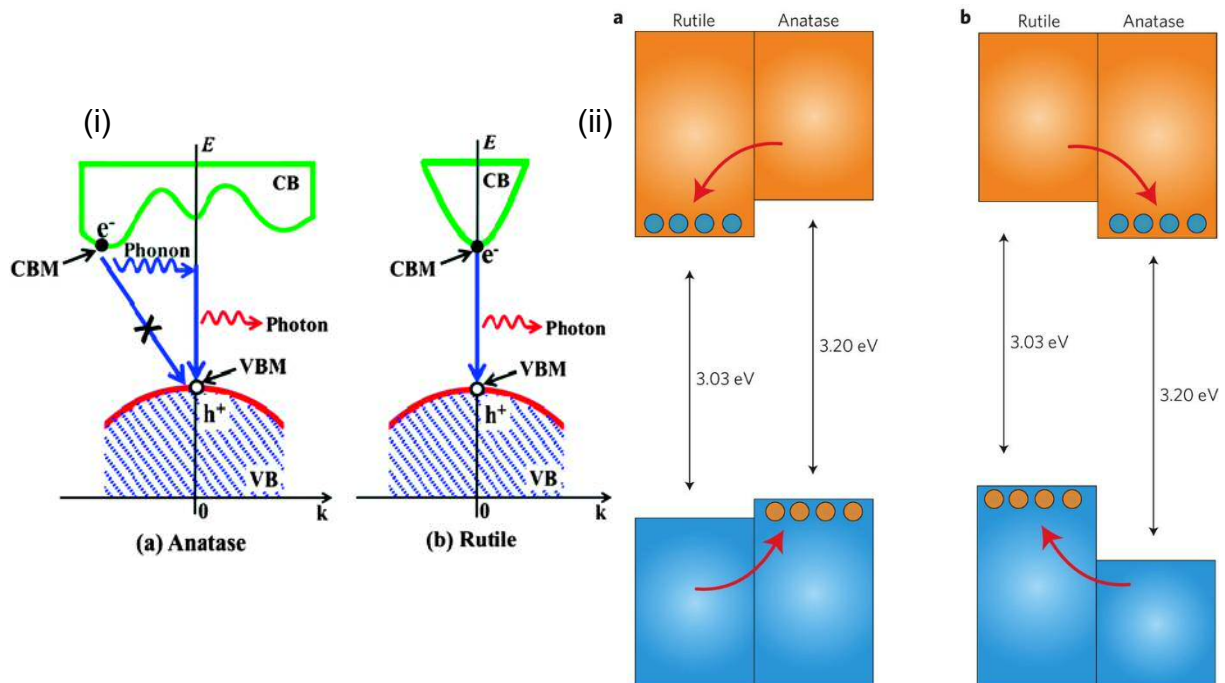


Figure 1.3.1:- (i) Direct charge recombination routes for the indirect bandgap polymorph anatase (a), and the direct bandgap polymorph rutile (b) [77] The blue line shows the route for recombination of the electron/hole pair. For anatase, direct recombination is forbidden. (ii) The two proposed models for bandgap alignment of a rutile/anatase interface. (a) is the generally agreed model, (b) is proposed by Scanlon *et al.* [76] The orange and blue blocks represent the valence and conduction bands, respectively. The orange and blue dots represent the h^+ and e^- , respectively.

energetically raised valence band that increases its redox potential in relation to adsorbed molecules that could facilitate improved transfer of more oxidising electrons. [69][74][75] However, more recent calculations have indicated that the valence band of anatase is 0.2 eV below rutile. [76] The indirect bandgap of anatase makes the direct recombination of electron/hole pairs impossible (**Figure 1.3.1 (i)(a)**), as the electrons must obey the transition selection rule of conserving momentum, resulting in an increase in electron/hole lifetime. [69][77][78] Studies have shown that when using anatase, electrons do not recombine from the conduction band, doing so instead from shallow electron traps. [79] Whereas for rutile, and brookite, the direct bandgap facilitates a more rapid recombination rate that decreases the lifetime and therefore the activity. After irradiation the electron/hole pairs, or excitons, must get to the surface to react with an adsorbed species. Rutile is only capable of generating holes near the surface by absorption of high energy photons which stop being detected at 3.59 eV, even though the photons were more energetic than the bandgap of rutile. Anatase, however, can very efficiently transport holes to its surface right up to photons with the same energy as the bandgap ($h\nu = E_g$). [70] The superior hole transportation means anatase can more effectively separate photo-generated charges, improving overall activity. Charge carrier efficiencies have been found to be affected by anisotropic factors, the ease of charges to diffuse in different crystallographic directions. [69][80][81] Recent data by Kim *et al.* also presented the theory that anatase is capable of producing free hydroxyl radicals by hole mediated processes, whilst rutile is restricted to surface based reactions which adds to the data explaining the superior reactivity of anatase crystals. [82][83].

While anatase is usually found to be the most photoactive phase in various photocatalytic processes, mixed phase catalysts like the commercial standard P25 exhibit reactivity that surpasses the individual phases. [72][84] Mixing the rutile and anatase phases, a 1:3 mix in the case of P25, produces a material with a decreased bandgap and improved activity due to the synergistic effects of having separate anatase and rutile particles in contact during reactions. There are two mechanisms currently proposed to explain charge transfer in an anatase-rutile mix that are shown in **Figure 1.3.1 (ii)**, Kavan *et al.* used electrochemical impedance analysis to show the conduction band of rutile is 0.2 eV below anatase, so upon irradiation the electrons transfer and accumulate in rutiles conduction band whilst the holes accumulate in anatases valence band (**Figure 1.3.1 (ii)(a)**). [18][85] However, more recent EPR experiments found the electrons flowed in the opposite direction, from rutile to anatase,

[86] and Scanlon *et al.* indicated that the anatase conduction may lie 0.2 eV below that of anatase, giving the situation shown in **Figure 1.3.1 (ii) (b)**. [76][87]

1.3.4 Oxidative degradation

Photocatalysed degradation of organic contaminants is driven by the oxidative and reductive mechanisms that result from semiconductor bandgap chemistry. Oxidative degradation, or advanced oxidation, has two key routes; oxidation by h^+ and other species formed by reaction with surface h^+ , and oxidative routes mediated by species formed from e^- cb. [31][43][44] **Figure 1.3.2** depicts the general mechanisms governing the photomineralisation of contaminants. Firstly we will discuss the mechanism to the right; the trapping of photogenerated holes on Ti-OH species, discussed previously as also being a bridging lattice oxygen, to form Ti \cdot -OH. After which we will discuss the mechanisms to the

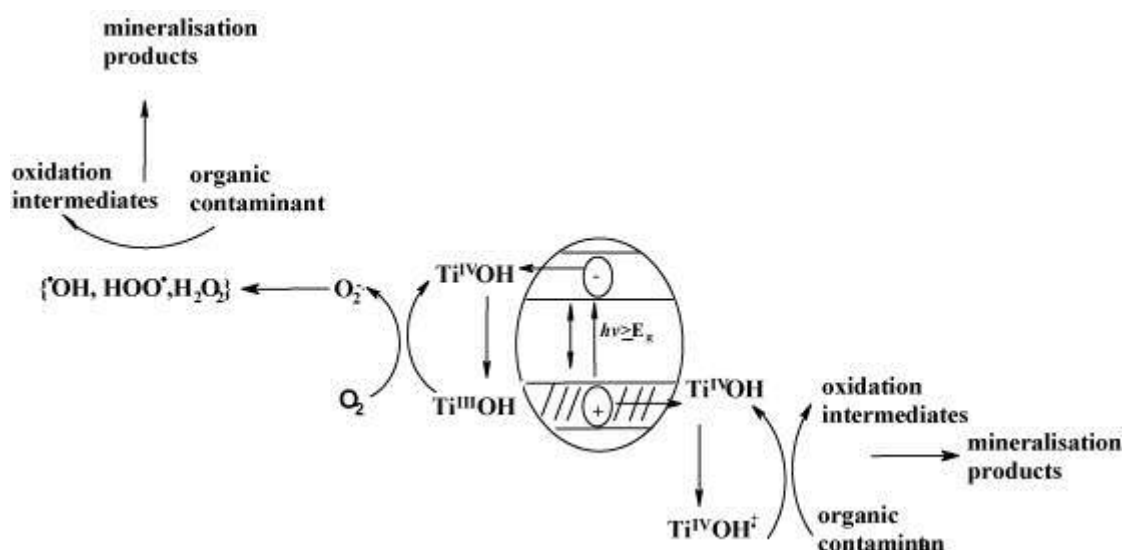


Figure 1.3.2:- A general mechanism showing how photogenerated charges become trapped or react to form oxidative species. The electron mediated pathway is seen on the left, and the hole mediated pathway is on the right. [31] left; the reduction of molecular oxygen, which forms various peroxide based species, which are known to be responsible for a wide array of oxidative chemistry.

1.3.4.1 Hole mediated mineralisation processes

The basis of hole mediated oxidation is the trapping of holes in shallow traps that act as electron acceptors on the surface of the photocatalyst. As discussed previously, the formation and stabilisation of surface trapped holes is dependent on an environment of strongly bound hydroxyl radicals and physisorbed water molecules. [58] The controversy surrounding the formation of free hydroxyl radicals, briefly discussed in 1.3.1, centres around whether surface formed hydroxyl radicals can readily dissociate into solution and where they

originate from. Some argue that the barrier to dissociation is too high resulting in this event being very unlikely, instead suggesting that the free radicals are a result of the electroreduction of oxygen. [50][52] Others argue that the electroreduction of oxygen is disfavoured and present evidence suggesting aqueous hydroxyl radicals can be formed on anatase surface sites. [53][54][88][89] Li *et al.* reported that hydroxylation of benzoic acid occurred when h^+_{vb} or e^-_{cb} were being scavenged independently. However, scavenging the holes species resulted in the hydroxyl moiety being derived from the labelled O_2 , whereas under electron scavenging conditions the hydroxyl came entirely from the H_2O . [55] Free hydroxyl radicals play an important role in degradative processes, but the controversy is currently unsolved. For the purpose of this review hydroxyl radicals will be considered a derivative of h^+ mediated processes.

Direct Hole Oxidation of Alcohols

A lot of evidence is available showing the ability of holes mediated pathways to oxidise organic pollutants. Surface trapped holes have long be characterised for having a great affinity for alcohols. [89][90] Kuznetsov *et al.* showed that using ethanol as a shallow hole trap effectively eliminated recombination to allow for the extension of a photoelectron's lifetime into months. [61] Whilst Tamaki *et al.* found alcohols could trap holes at rates of 100 ps and 1 ns for methanol and ethanol respectively. [91] Investigation of the alcohol degradation mechanism has shown both the surface holes and hydroxyl radicals are capable of degrading them, [89][92] Yu and Chuang *et al.* showed that ethanol degradation still occurred during high surface coverage conditions when water was blocked from reaching the surface, indicating degradation probably occurred through direct electron transfer to shallow trapped holes. **Equations (8)-(11)** illustrate the generally agreed upon mechanism based on the literature:

(8)

CH_3OH_{ads} (9)

Ti^{4+} Ti^{3+} (10)

(11)

Holes sitting in shallow traps, on the bridging oxygens, transfer to the methanol molecule (**Eq 9**) and form an alkoxy radical. The second step involves the transfer of an electron directly into the conduction band of the Ti^{4+} species in a process called current doubling, [93] that is evinced by the presence of molecular oxygen scavenging shallow trapped electrons.[94] Further oxidation to CO_2 via hole pathways is believed to be possible due to studies detecting CO_2 concentrations far above the concentration of hydroxyl radicals present. [89] Other aliphatic alcohols tend to show similar initial steps, to methanol, during photodegradation. During the gas phase photocatalytic oxidation of ethanol, Muggli *et al.* detected acetaldehyde, acetic acid, formaldehyde and formic acid. [95] Isotopic labelling showed the α -carbon was evolved first as CO_2 , indicating the sequential oxidation starting at the alcohol moiety. Whilst the mineralisation of isopropyl alcohol tends to oxidise either entirely through acetone, [96] or the immediate oxidation to CO_2 . [97]

Hydroxyl Radical Oxidation of Alcohols

Hydroxyl radicals and h^+ are sometimes thought of as similar species, especially when a bound hydroxyl radical is a common shallow hole trap. However, examination of the free radical's mechanistic behaviour sometimes shows different behaviour. [98][99] Photogenerated holes tend to behave as 1-electron acceptors, transferring electrons from bound species. Hydroxyl radicals on the other hand will almost always favour hydrogen abstraction over electron transfer. [100] A few rare cases when hydroxyl radicals do abstract an electron is in the reaction with oxalate, a molecule with no hydrogens, and the heteroatom rich, methylene blue. A major issue in examining the behaviour of surface trapped holes and free hydroxyl radicals, is that that it becomes increasingly difficult to distinguish the

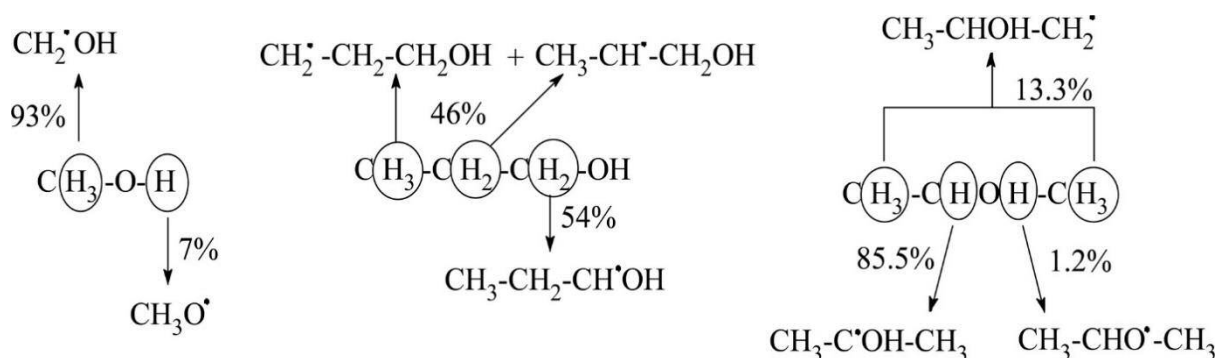


Figure 1.3.3:- The preference for where $\cdot\text{OH}$ deprotonates methanol, 1-propanol and 2-propanol [99] oxidative species; especially when the adduct does not contain a clear electrophilically added moiety. **Figure 1.3.3** shows the preference for hydrogen abstraction for several alcohols. [99] Hydroxyl radicals preferentially deprotonate methanol in the same position that h^+ abstracts

an electron from. The significance of this is minor, since methanol only has one position an electron can realistically be taken from, however the same preference is also seen for ethanol. Additionally isopropyl alcohol, under hydroxyl only and hydroxyl/hole conditions, preferentially forms acetone due to hydrogen/electron abstraction from the position α to the alcohol group. In all three cases, the intermediate gains a radical charge and loses a hydrogen, but the mechanism by which it is achieved differs. This compounds the clarification issue mentioned above; that discerning when a h^+ or a $\cdot OH$ is responsible is a difficult task, even in small chained organic species. An aromatic alcohol, like phenol, undergoes different mechanistic degradation altogether. [32][34] Intermediate mapping concludes that phenol, as well as toluene and benzene, [36][101] undergoes electrophilic addition to the aromatic ring that forms catechol and hydroquinone. It should also be noted that this hydroxyl radical electrophilic addition is susceptible to substituent effects. [102]

Carbonyl Oxidation

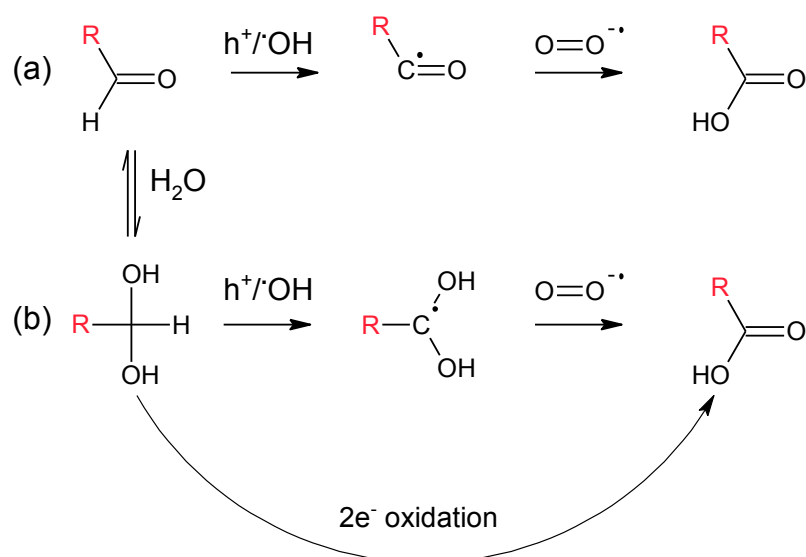


Figure 1.3.4: Mechanisms showing the photocatalytic oxidation of aldehydes. (a) shows the route for aldehydes where k_d lies close to the aldehyde form, (b) the route for aldehydes where k_d lies closer to the diol form

Aldehydes are oxidised through their corresponding carboxylic acid and has been found to rely on hole mediated pathways and addition of oxygen from another source. [103][104] Isotopic labelling experiments showed there were two mechanisms for the oxidation process, depending on the level of hydration of the aldehyde. Dehydrated aldehydes undergo hole mediated electron transfer and deprotonation, followed by insertion of a radical oxygen species (Figure 1.3.4 (a)). Whilst the hydrated aldehydes go through a two electron oxidation from the oxidised diol to form the corresponding carboxylic acid (Figure 1.3.4

(b)). For aliphatic aldehydes, the dissociation constant (k_d) lies closer to the diol form resulting in them generally following the mechanism (b); whilst aromatic aldehydes, like benzaldehyde, are not susceptible to hydration and so are more likely to oxidise via mechanism (a). The photo-oxidation of ketones is another process that has been found to involve photogenerated holes. [105] In the same manner as for alcohols and aldehydes, electron transfer from an α -carbon is the favoured first step followed by a deprotonation or hydrogen transfer. The formed carbon radical then reacts with oxygen. However, decomposition studies of acetone have shown other competing pathways involving trapped electron centres (Ti^{3+}) and direct nucleophilic attack by superoxide radicals. [106] All three pathways result in the formation of unstable organoperoxy radicals that are also observed for other ketones, including; 2-butanone, 4-heptanone, cyclopentanone and cyclohexanone. [105]

Hole Mediated Degradation of Saturated and Unsaturated Cyclic Compounds

A large portion of the literature concerning alkane and alkene hydrocarbons covers gas phase investigations, partially due to the poor solubility of alkanes in water. Gas phase decomposition of heptane, for example, produced near stoichiometric amounts of H_2O and CO_2 with observed intermediates being various aldehydes and ketones. [107] However, little information regarding the nature of the reactive species is provided, and it has already been noted that water greatly impacts the stability of shallow trapped holes so the studies would be difficult to compare. Cyclohexane, the most thoroughly examined non-aromatic, is oxidised to primarily to cyclohexanone, whilst the uncatalysed photo-oxidation forms cyclohexanol with 100% selectivity. [108] ^{18}O labelling indicated all oxygen added, in detected species, originated from the catalyst surface including the hydroxyl radicals responsible for the ring opening. [109] It was proposed that the hydroxyl radicals were drawn from the h^+ oxidation of adsorbed water. The saturated nature of cyclohexane prevents the susceptibility to electrophilic attack that is observed for aromatic ring compounds like benzene, [36][55][110][111] benzoic acid [55] and phenol. [32][34] The first stage of degradation, if no “anchor” is present, is the hydroxylation of the aromatic ring. Data collected by Bui *et al.* shows that anatase is significantly better suited to hydroxylate aromatic rings, where 70 – 90% of the incorporated oxygen came from the hole mediated oxidation of water, [37] evincing the conclusion by Kim *et al.*; that anatase can form free hydroxyl radicals and rutile is restricted to surface based processes. [54] Phenol degrades further through catechol, hydroquinone, benzaquinone and then to CO_2 . Rutile degraded phenol at a faster rate, than anatase, illustrating the importance of synergy between the two polymorphs. [36] An

additional pathway has also been mapped for benzene and naphthalene, showing oxidation preferentially occurs via a ring opening mechanism through a muconaldehyde intermediate. [83][110][111][112][113] This pathway is however only controlled by electron-derived species, like the super oxide ion, and so will be discussed in 1.3.4.2.

1.3.4.2 Electron Mediated Processes

Formation of the Superoxide (O_2^-) Radical Anion

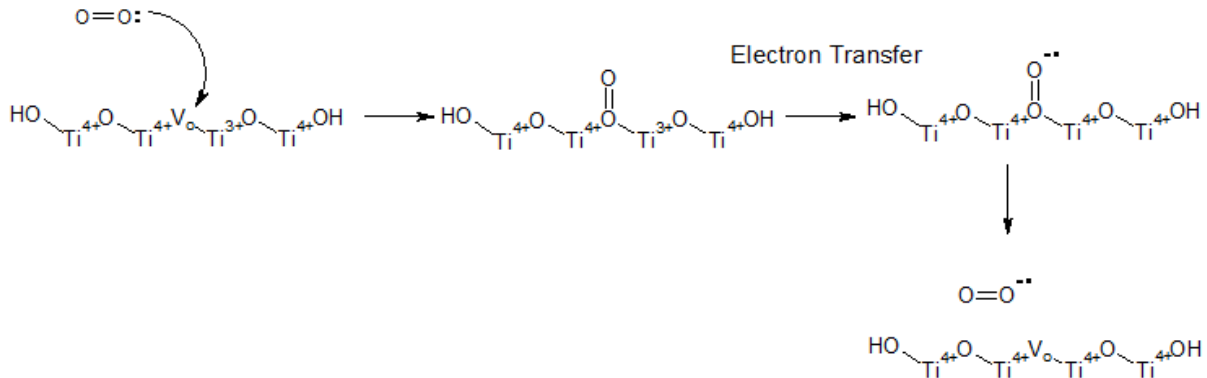


Figure 1.3.5:- Mechanistic route showing the formation of the superoxide radical anions by adsorption to an oxygen vacancy and electron transfer from a reduced Ti^{3+}

Hole-mediated processes are clearly very important to the degradation process. Additional to these pathways, however, is the impact of electron mediated processes. The conduction band electron (e^-_{cb}) is commonly delocalised around shallow traps in the titanium centres. [47][66][67] Direct reduction of an adsorbed molecules has been observed, although degradation is usually superseded by a rapid electron back-donation and an Antoniewicz-type desorption event. [114] Direct reduction is difficult to prove, as no real means exist to allow reliable marking of the surface states to know if direct electron transfer has occurred. Instead, the vast majority of literature on electron mediated pathways revolves around the reduction of molecular oxygen. Trapped electrons generate electrical fields that impact on the surrounding atoms through the Stark Effect, where deeply trapped electrons only affect the immediate titanate unit cell and surface trapped electrons produce changes across areas larger than the unit cell. [115] Szczepankiewicz *et al.* also noted that introducing O_2 molecules caused the



reduction of detected shallow trapped electrons and concluded that O_2 was scavenging electrons to become the superoxide radical anion ($O_2^{\bullet-}$), behaviour that has also been observed with EPR. [51][61] **Figure 1.3.5**, shows a general mechanism for the formation for the superoxide radical anion. Molecular oxygen occupies an oxygen vacancy and is photoreduced by a shallow trapped electron, represented here as a Ti^{3+} centre. $O_2^{\bullet-}$ is in equilibrium with its hydrogenated form, the hydroperoxyl radical (HO_2^{\bullet}), as seen in **Equation (13)**. $O_2^{\bullet-}$ and HO_2^{\bullet} will disproportionate to the hydroperoxyl anion which can abstract a proton to make hydrogen peroxide (**Equation 11 and 12**, respectively). At pH 7, the forward reaction of disproportionation is favoured, so $O_2^{\bullet-}$ is expected to behave as a strong brønstead base in any media. Such a strong basicity means $O_2^{\bullet-}$ is capable of deprotonating acids weaker than water.

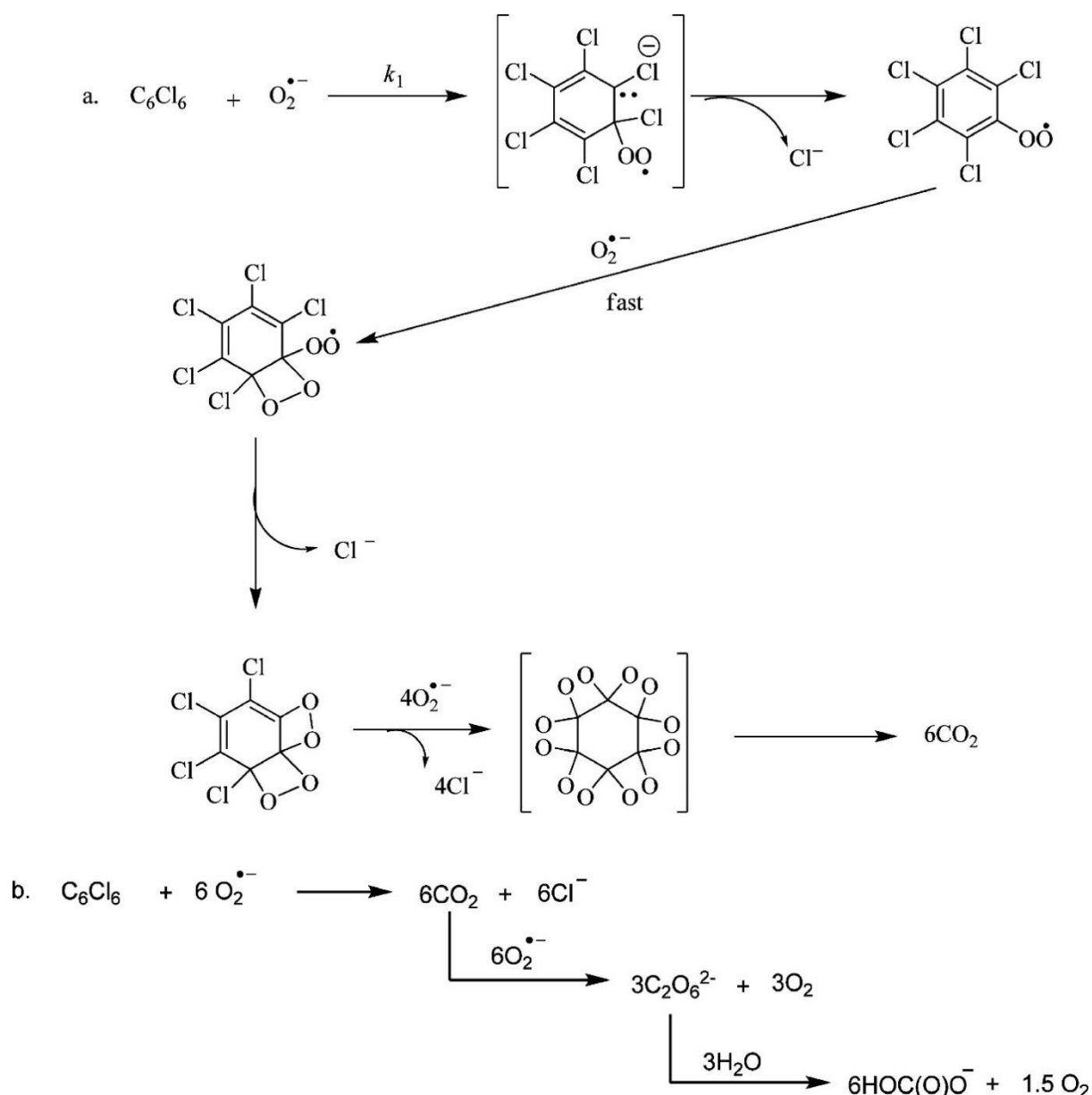


Figure 1.3.6:- A mechanism showing the superoxide radical anion driven degradation of hexachlorobenzene [123]

[116] Kinetic experiments found that $O_2^{\cdot-}$ could abstract a proton from various alcohols in acetonitrile, such as; isopropanol ($k = 0.01 \text{ M}^{-1} \text{ s}^{-1}$), ethanol ($k = 1.42 \times 10^2 \text{ M}^{-1} \text{ s}^{-1}$), methanol ($k = 1.1 \times 10^7 \text{ M}^{-1} \text{ s}^{-1}$) and water ($k = 1.0 \times 10^5 \text{ M}^{-1} \text{ s}^{-1}$). The capability of superoxide to abstract a hydrogen, as well as where the disproportionation equilibrium lies, means that at a neutral pH the hydroperoxyl radical (HO_2^{\cdot}) is likely to dominate. [117] HO_2^{\cdot} is however a more reactive oxidant, than $O_2^{\cdot-}$, and has been recorded abstracting allylic C-H bonds in hexadiene to form benzene and hydrogen peroxide. [118][119]

Nucleophilic Behaviour of $O_2^{\cdot-}$

The tendency of superoxide to show basic behaviour in the presence of H^+ or abstractable hydrogens suppresses some of its other potential roles in solution. In aprotic solvents superoxide has been reported as “remarkably nucleophilic”, easily attacking alkyl halides in dimethyl sulfoxide in an SN_2 reaction where a hydroperoxyl (ROO^{\cdot}) intermediate was detected using spin traps. [120][121][122] The susceptibility of halogenated hydrocarbons, in aprotic solvents, to superoxide nucleophilic attack led to the findings showing the transformation of: CCl_4 , $HCCl_3$, and $FCCl_3$ to a bicarbonate ion; $PhCCl_3$ to $PhC(O)OO^-$ and $PhCO_2^-$; and finally CF_3CCl_3 and $HOCH_2CCl_3$ to give their carboxylate anions. [122] Sugimoto *et al.* demonstrated that heavily halogenated aromatic compounds could be rapidly oxygenated by superoxide, dispelling the belief that halogenated aromatics were resistant to superoxide oxidation. [123] **Figure 1.3.6** shows the superoxide driven degradation of hexachlorobenzene. Attack by superoxide displaces a Cl^- ion to form a

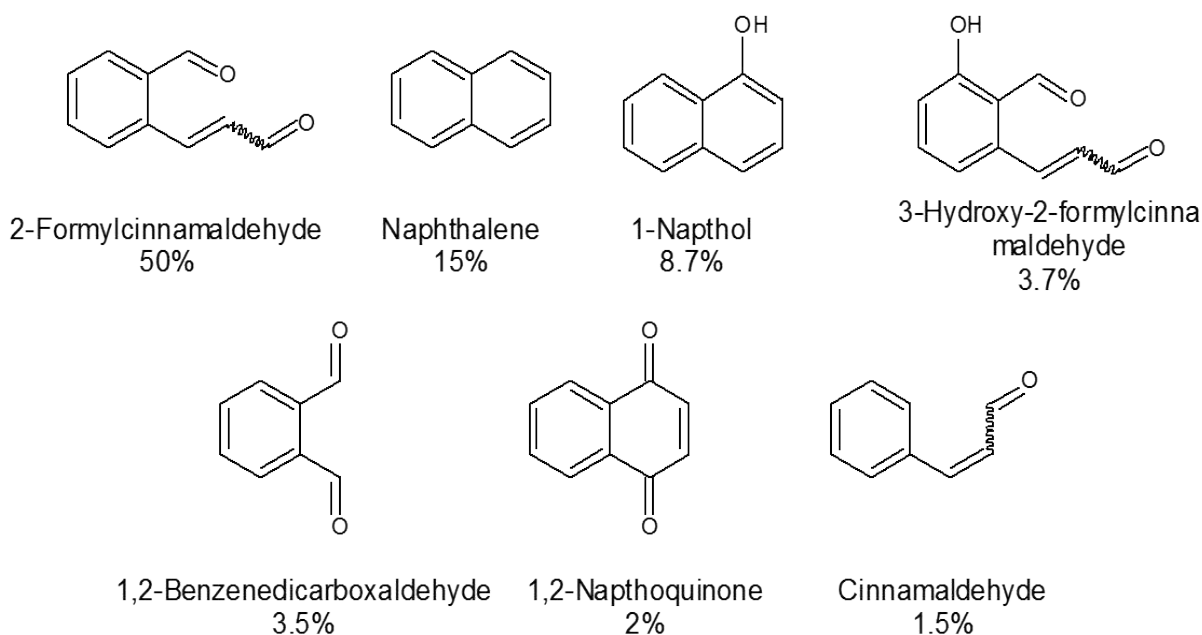


Figure 1.3.7:- The most abundant eluents detected after 120 minutes of reaction during the photocatalysed degradation of naphthalene [112]

pentachloro-monoperoxy-benzene species. This peroxy intermediate is rapidly oxygenated to be resolved with the evolution of six equivalents of carbon dioxide. The presence of chloride thus catalyses the reaction by providing facile leaving groups for the superoxide species to displace. However, in the presence of hydrogen sources, like protic solvents or acid protons, the nucleophilicity of superoxide becomes muted; illustrated by Ryding *et al.*, who showed the rate of gas phase S_N2 reactions with alkyl halides decreases as the number of water molecules in the cluster increased. [124] Although the nucleophilicity of O_2^- is muted in aqueous conditions, many studies indicate the vital role of superoxide in the ring opening of aromatics, [84][110][111][112][113] and, unexpectedly, the minor role in the hydroxylation mechanism of benzene. [37][125] Yang *et al.* illustrated that $\cdot OH$, alone, were a poor reactant in the ring opening of aromatic rings. [126] Intermediate mapping of naphthalene found various ring opened aldehyde, carboxyl and hydroxylated intermediates were commonly formed during the reaction (**Figure 1.3.7**). [112] The most abundant intermediate is 2-formylcinnamaldehyde at 50% after 120 minutes of reaction. It was proposed that superoxide cleaved the ring via a dioxetane transition species to form the muconaldehyde-type (di-aldehyde) intermediate, shown in **Figure 1.3.8 (i)**. [113] However, using ^{18}O -labelling in the TiO_2 led degradation of benzaldehyde, found that under no circumstances were two ^{18}O atoms incorporated into the product, and using $^{18}O_2$ resulted in the highest levels of ^{18}O in the reaction product. Due to oxygen exchange with the solvent, 3,5-di-*tert*-butylcatechol (DTBC) was used to block this process to ascertain more reliable information. [111] The presence of the ortho-dihydroxyl moieties ensures that “intradiol” products formed are dicarboxylic acids or anhydrides, eliminating the oxygen exchange mechanism with water. The studies showed that formation of muconic acid, from DTBC, did not occur and that the dioxetane mechanism was incorrect. The anhydride bridging oxygen for 5a and 5b came exclusively from molecular oxygen showing that the breaking of the C-C was solely induced by a molecular oxygen species. Extrapolating from this data one can assert that both hole and electron mediated pathways are required to ring open non or low halo aromatics. Additionally, one can hypothesise that further degradation products, like 1,2-benzenedicarboxaldehyde in **Figure 1.3.7**, are formed from a similar mechanism to the ring opening observed by Pan *et al.* A surface dependent aspect was also derived from their work. Levels of “extradiol” and “intradiol” formed were affected by the exposed phase presenting the idea that the oxygen insertion may occur on the surface. Other isotopic studies also indicated the inclusion of labelled molecular oxygen in hydroxylated aromatic rings, [55] and further study showed O_2 played a minor role in the formation of free hydroxyl radicals. [125]

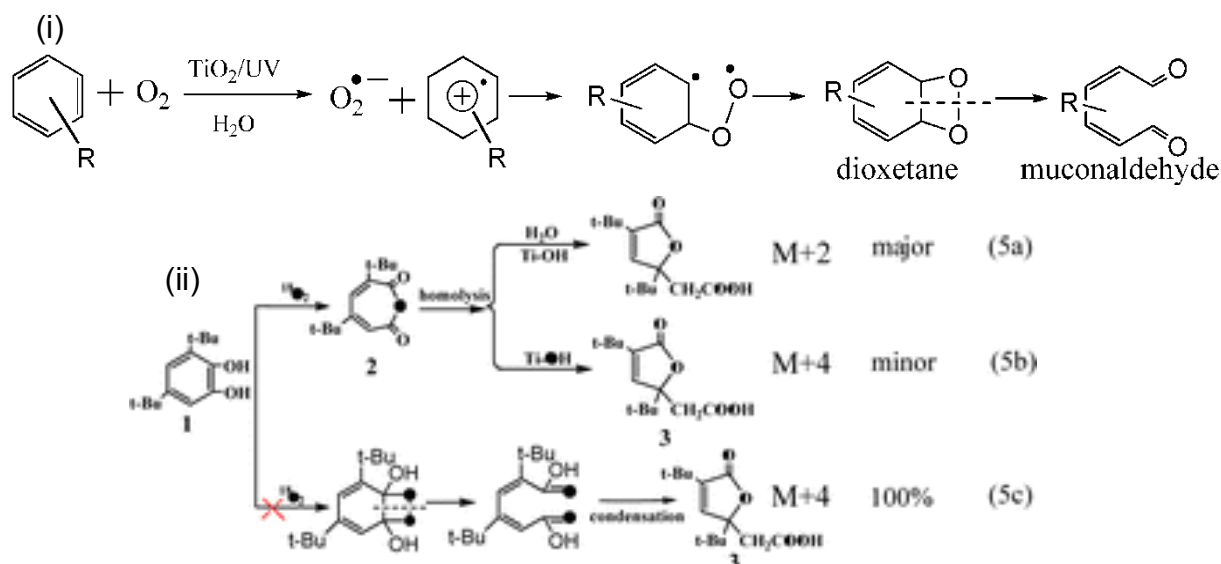


Figure 1.3.8:- (i) the mechanism for benzene ring opening via a dioxetane intermediate [113] (ii) the degradation routes for 3,5-di-tert-butylcatechol (DTBC). (5a) is the major intermediate and contains just one ^{18}O molecule, indicating the second oxygen must come from the unlabelled H_2O . (5b) is the minor intermediate that contains two ^{18}O (5c) is the intermediate that should form from the dioxetane pathway, but this pathway was not observed. [111]

1.4 Use of Gold/Palladium

Precious and non-precious metals have long been supported on various materials to change, control or improve (photo)catalytic properties. Gold, [26][127][128-133], silver, [134-137] palladium, [25-27][138-140] platinum, [26][141-144] copper, [26][145][146] amongst many other metals have been deposited or incorporated into TiO_2 to enhance its (photo)catalytic proficiency. The enhancements have been applied for many purposes, including; the extension of light absorption into the visible region, [147-149] hydrogen production from water splitting [25-27][128][150] selective photo-oxidation, [147][151] and photocatalysed degradation of organic pollutants. [127][129][137][138][149][152]

1.4.1 The Schottky Barrier

The Schottky barrier is the name given to the restrictive energetic barrier at a metal-semiconductor contact. **Figure 1.4.1** is a diagram illustrating the Schottky barrier for n and p-type semiconductors. Due to the differences in band structure between a metal and semiconductor, the Fermi level (E_F) of an appropriate metal sits within the semiconductor's bandgap (E_g). For an n-type semiconductor, if the difference in energy of the metal's Fermi level and the conduction band minimum is large enough (), then electrons can only cross the boundary from the semiconductor to the metal. The differing work functions of the metal and semiconductor, results in the movement of electrons into the metal until the Fermi

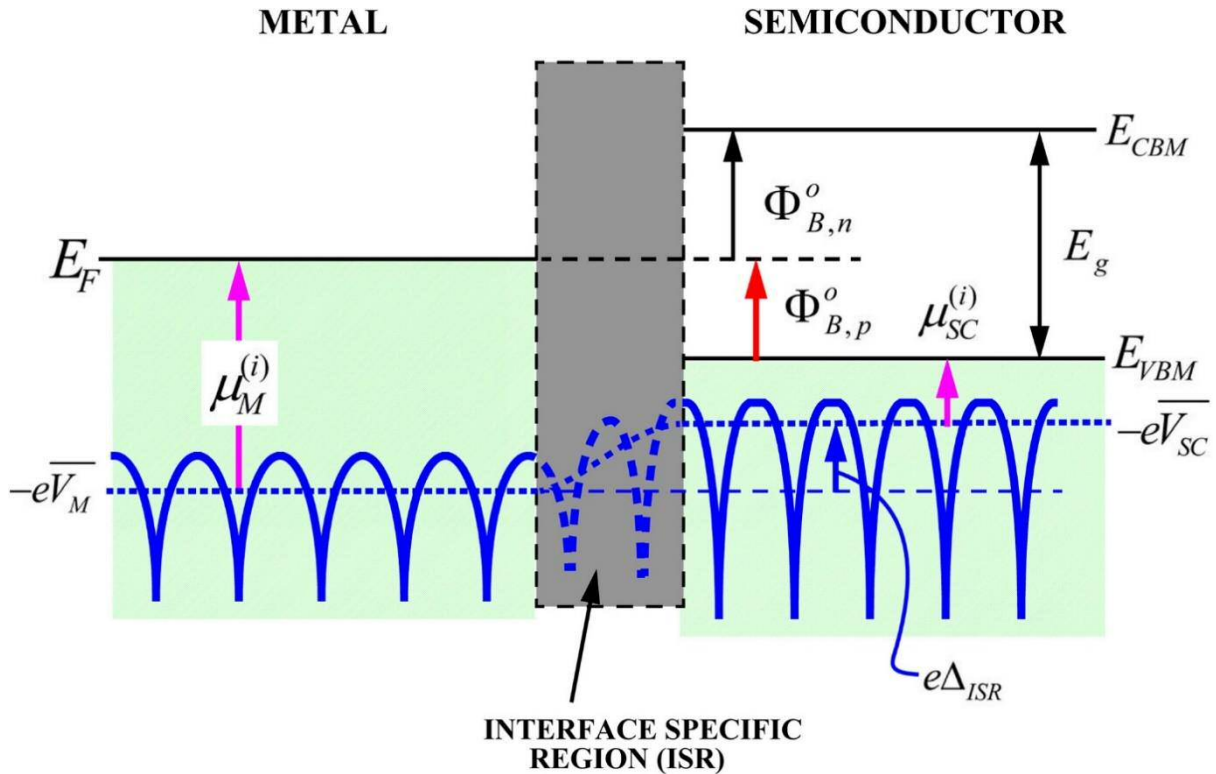


Figure 1.4.1:- A diagram illustrating the Schottky Barrier between a metal and a semiconductor [153]

E_{CBM} = Energy of conduction band minimum, E_{VBM} = Energy of Valence band maximum, E_F = Fermi level, E_g = Bandgap, $-eV_m$ = Average electrostatic potential for metal, $-eV_{sc}$ = Average electrostatic potential for semiconductor, $\Phi_{B,n}^o = \Delta E$ between E_F and E_{CBM} for n-type semiconductors

$\Phi_{B,p}^o = \Delta E$ between E_F and E_{VBM} for p-type semiconductors

energies are of an equal energy. This creates a Helmholtz double layer in the interfacial region that repels electrons travelling from the metal to the semiconductor. This results in the metal behaving as an “electron sink”, effectively improving the separation between the photo-generated electrons and the photo-holes. For p-type semiconductors, $\Phi_{B,p}^o$ represents the difference in energy between the metals Fermi level and the semiconductors valence band minimum (E_{VBM}). If $\Phi_{B,p}^o$ is large enough then the photo-generated holes will be trapped on the semiconductor while the electrons will be free to cross the boundary, again improving electron/hole separation. The height of barrier for Au/TiO₂, described by $\Phi_{B,p}^o$, has been experimentally observed to be dependent on particle size due to the effect on the apparent Fermi level. [133] However, it is currently believed that the double layer has a defined thickness in the nanometre range consequently restricts how small metal nanoparticles can be before they are no longer capable of exploiting the Schottky barrier. If the barrier is too small then charge carrier can easily cross it in both directions and is called an Ohmic contact.

[153][154] The conditions affecting the Schottky barrier have a large degree of variance and the barrier itself is often experimentally found to be inhomogeneous. [155][156]

1.4.2 *Au/TiO₂ photo-reactivity*

Although gold was long believed to be inert, discoveries in the 1980s by Hutchings [157] and Haruta [158][159] sparked an interest in the chemistry of gold nanoparticles. The number of publications has increased exponential since then, with Haruta *et al.*'s 1989 paper on CO oxidation receiving nearly 2500 citations. Gold nanoparticles, supported on TiO₂ and other materials, have been shown to be proficient in standard catalytic reactions such as: acetylene hydrochlorination; [157][162][163] CO oxidation; [164] selective oxidation of alcohols to aldehydes and acids; [165][166][167] olefin oxidation; [168] hydrogen peroxide production; [169] adding nucleophiles to alkynes; [170] and many other reactions. The thermally activated chemistry, that explains Au/TiO₂ heterogeneous catalysis, is a large and complex research area that cannot not appreciably be covered in this review, the reader is directed to reviews by Panyotov *et al.*, [94] Corma *et al.*[160] and Hutchings *et al.* [161] for greater detail on the subject.

1.4.2.1 *Schottky Junction and Plasmonic Resonance*

Interest in the use of gold in photocatalytic reactions stems from a number of factors. The, already discussed, Schottky junction at the metal-semiconductor boundary elicits improved photo-generated electron/hole separation by preventing electron movement back into the semiconductor and therefore making gold an electron sink. The nature of the barrier is dependent on the atomic structure at the metal-semiconductor interface (MS interface) which results in difficulty exactly characterising the Schottky barrier height. [153] Relative local barrier height (LBH) measurements, by Maeda *et al.*, found that small gold particles (a height of <0.4 nm) on a TiO₂ (110) surface had relative LBH values of -0.4 to 0eV, suggesting that particles of this size would donate electrons to the TiO₂ support. Whilst larger particles (>0.4 nm) had values between 0 and 0.8 eV. [171] This illustrates the particle size dependence discussed in **section 1.4.1**. [133] Gold nanoparticles are also capable of sensitizing TiO₂ to visible light radiation. It does so by the localised surface plasmonic resonance (LSPR) effect. Plasmonic resonance is the displacement of a metal nanoparticles electron cloud relative to the particle nuclei due to the incident light oscillation inducing a dipole in the material. The electrons move to correct the dipole but the constantly oscillating incident cause further perturbations the materials dipole. These oscillations, or plasmons, increase to match the wavelength of the incident light, up to the resonant frequency,

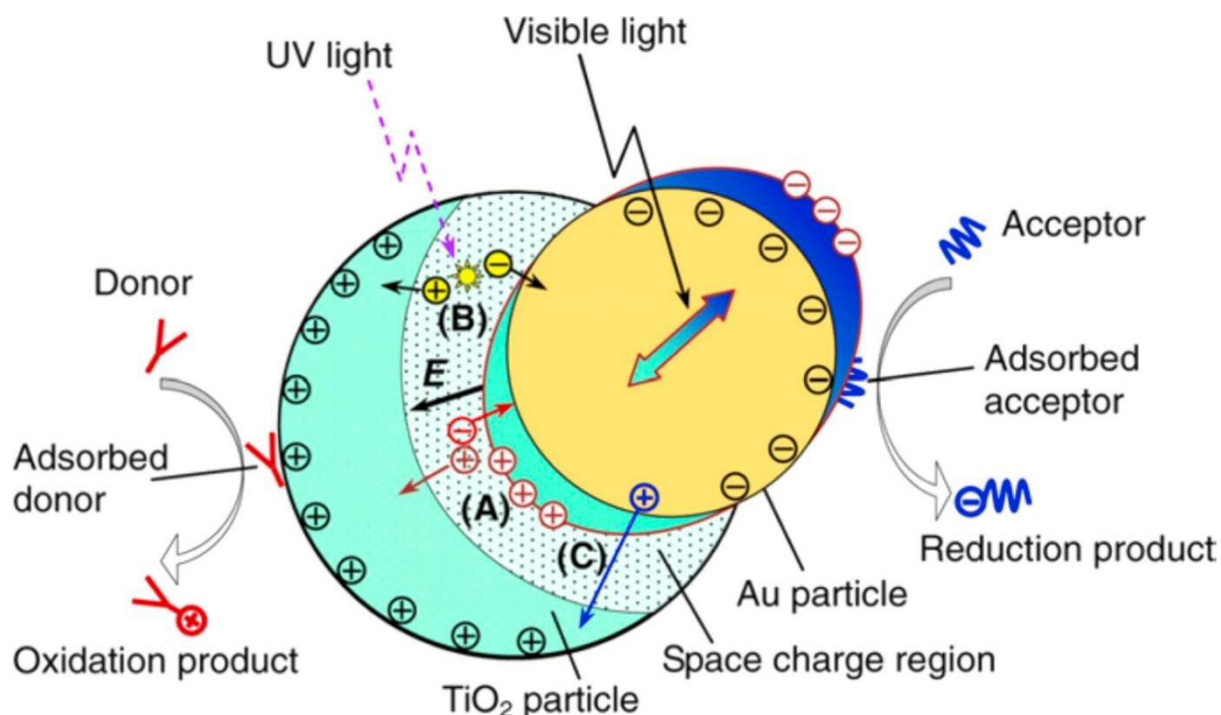


Figure 1.4.2:- A diagram showing the mechanism for localised plasmonic resonance on a Au/TiO₂ particle [154] modifying the absorption cross-section that results in a particle being capable of absorbing light of wavelengths up to 600nm. [65][147][154] **Figure 1.4.2** shows a schematic representation of the key processes in plasmonic photocatalysis. Energy absorbed at the gold particles, from the visible light photons, can be transferred to the titania support by an energy or charge carrier transfer; although the mechanistic details are still a point of contention. [172][94] Tatsuma *et al.* studied visible light illumination in gold and silver nanoparticles loaded on TiO₂ films and presented the hypothesis that plasmon resonance results in excited electrons that transfer to the conduction band of the TiO₂ support. [173][174] However, this theory was inconsistent as the surface plasmons, on the gold or silver nanoparticles, are charge density waves with no states equivalent to the valence band-conduction band structure of semiconductors. The excited electrons would therefore sit at the Fermi level and be unable to drive reactions. Later work determined that surface plasmon decay resulted in the production of electron hole pairs in the gold particles, the “hot” electrons of which rapidly quantum tunnel into the TiO₂. [175] Plasmonic electron transfer from gold to TiO₂ has been determined to occur as rapidly as 240 fs. [176] Additionally, plasmonic decay can result in direct photocatalytic mechanisms:

1. the re-radiation and absorption of similarly energetic photons by adsorbates, if intramolecular electronic transitions are allowed, and can be described by the Franck-Condon Principle; [177]
2. the rapid transfer of plasmon-generated electron to adsorbates that occurs as a distribution of energetic electrons due to Coulombic inelastic scattering within the material;
3. because of the elastic scattering, local lattice heating occurs which thermally excites adsorbed and adjacent molecules that can activate thermal catalytic pathways. [178][94]

Direct photocatalysis, from LSPR, is not the focus of this section of the literature review however. More pertinent is the indirect photocatalysis of Au/TiO₂ relating to LSPR stimulated pathways.

1.4.2.2 Au/TiO₂ Photo-Reactivity

The two key benefits of incorporating gold into titania photocatalysts are those associated with improved electron-hole separation from the introduction of the Schottky junction, and the harnessing of visible light through LSPR. Both benefits have been explored in the area of photocatalytic hydrogen production. [128][179] Rosseler *et al.* showed Au/TiO₂ was more proficient, than Pt/TiO₂, in sacrificial agent assisted water splitting to produce hydrogen. It was noted that the tendency of gold to exhibit charging led to the effective storage of electrons that enhanced electron/hole splitting and improved the reductive capabilities of the gold particles, whereas the ohmic contact found in platinum facilitates electron transfer to the solvent. Importantly, the author noted that efficiencies improved as particle size increased, the opposite trend observed in thermal catalysis. [180] Visible light hydrogen production is currently explained by two models: LSPR distributes energy to the titania particles, due to near field enhancements, where electron-hole separation occurs; [181] and the formation of “hot electrons” in the gold particles that transfer to the conduction band of titania. [182] The latter mechanism can be partially restricted due to the Schottky barrier height however.

The application of TiO₂ supported gold photocatalysts to photo-oxidation has resulted in mostly positive reports. Carneiro *et al.* reported that the oxidation of cyclohexane was hindered by the procedure responsible for depositing gold, rather than the gold itself. [183] As discussed in **section 1.3.4.1**, Almeida *et al.* showed that cyclohexane is oxidised by

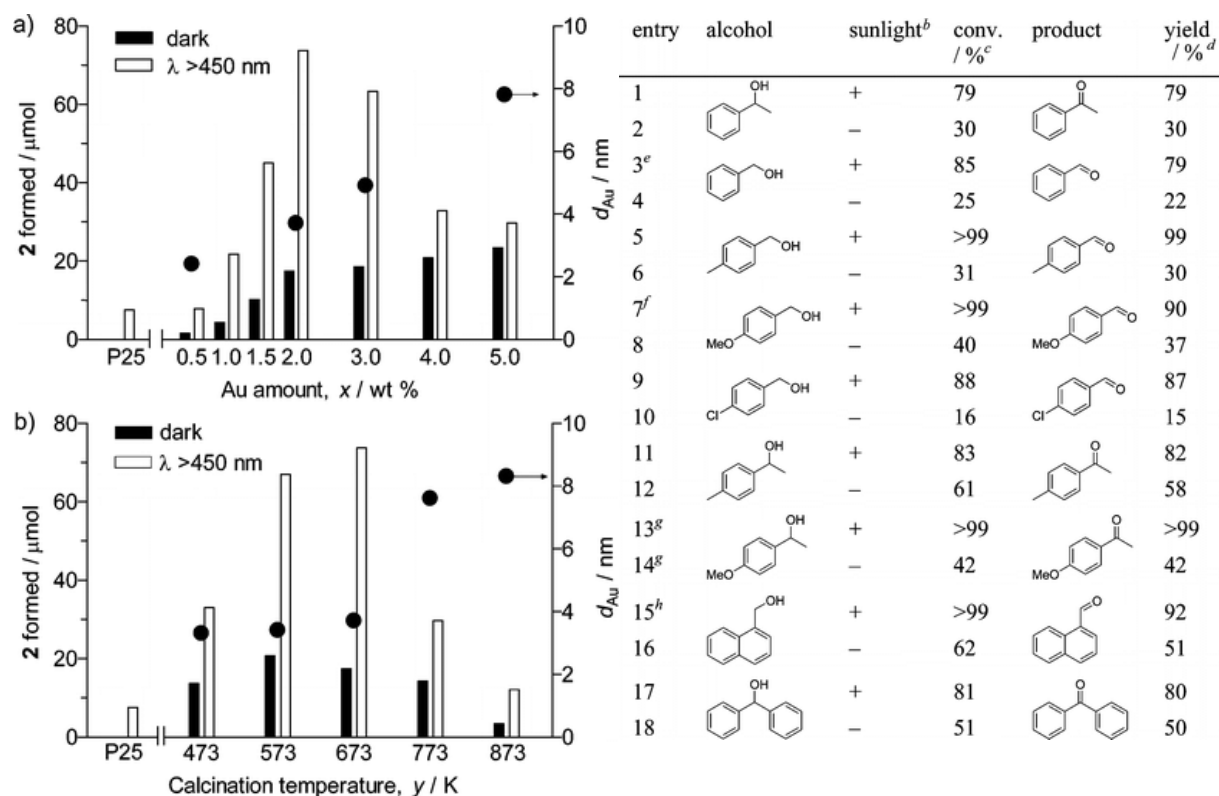


Figure 1.4.3:- (a) The amount of acetophenone formed under thermal (black bar) and photocatalytic (white bar) conditions as a function of Au wt%.

(b) The amount of acetophenone formed by catalysts calcined at different temperatures.

In each graph the black dot shows the average Au particle size for that sample

Table 1.4.1:- The percentage conversion of the alcohol and percentage yield of the carbonyl for various aromatic alcohols. “+” denotes irradiative conditions (photocatalysis), “-” denotes no irradiation (thermal catalysis) [147]

surface hydroxyl species, [109] which Carneiro noted were reduced after the gold deposition procedure. Other inhibitory effects have been highlighted; the effectiveness of Au/TiO₂ photocatalysts is linked to a number of factors that result in an optimal loading. Having too high a metal loading will result layered deposition to occur that will inhibit titania photocatalytic mechanisms and decrease activity. [127] A focal point of gold related oxidative processes is the improvement in selectivity during oxidation with the aim of producing commodity chemicals and fuels. The differing mechanisms present in the oxidation of benzene meant that gold could selectively increase the phenol yield without increasing of other products like resorcinol and benzoquinone. [184] Ide *at al.* reported a similar trend, where 4 wt% Au/TiO₂ decreased the overall benzene conversion but increased the yield and selectivity for phenol from 7.2/21 to 6.5/60.8 % respectively. [185] Other publications reported even higher yields and selectivity for phenol; gold nanoparticles deposited on TiO₂ and titanate, irradiated with visible light ($\lambda > 400$ nm) gave yields and selectivity of 63/91 % [186] and 62/96 % [187] respectively. Both also utilised the

“benzene/phenol recognition ability” which involves including phenol in the reaction mixture to encourage further phenol degradation. Ide also examined phenol oxidation, finding that gold improved selectivity for hydroquinone formation from 7.3% to 12.1 and 8.5%, for 1 and 4 wt% Au/TiO₂, by encouraging hydroquinone desorption and preventing further oxidative degradation. Tsukamoto *et al.* investigated the selective oxidation of phenylethanol to acetophenone, and various other aromatic alcohols, by Au/TiO₂ catalysts prepared by deposition precipitation. [147] **Figure 1.4.3** shows the amount of acetophenone formed in thermal and photo activated catalysis as a function of metal loading **(a)** and calcination temperature **(b)**. A low metal loading had no impact on acetophenone photocatalytic production but allowed a small amount of thermally catalysed production. Increasing metal loading further corresponded to an increase in gold nanoparticle diameter and thermally catalysed acetophenone production however, photocatalysed formation has an optimal weight loading at 2wt% which corresponds to a nanoparticle of ~3.7 nm and an 8-fold increase in acetophenone produced. High temperature calcination (773 and 873 K) resulted in large Au particles which, coupled with the metal loading data, showed Au particles larger than 5nm are inefficient for selective oxidation purposes. Testing on other aromatic alcohols using the optimal catalyst (2 wt% loading, 673 K calcination temp) found even better conversion of substrates and yields of carbonyl equivalents. 4-methylbenzyl ethanol and 4-methoxyphenyl alcohol were both oxidised to their corresponding carbonyl with 99% or greater conversion and yield (**Table 1.4.1**). [147]

Besides selective oxidation of organic compounds, Au/TiO₂ photocatalysts have been tested for the mineralisation of a wide array of organic compounds. A variety of nanoparticle sizes and metal loadings are found to be optimal, depending on the substrate and conditions, so it is worth remembering that the nature of the MS junction is very sensitive to small changes. As such the optimal particle size or metal loadings should generally be considered within the context of the experimental conditions. Although, particles between 3-6 nm appear to commonly be proscribed as the most efficient. [147][187][188] A common compound used to measure photoactivity is methylene blue; [129][188-190] An earlier study by Li *et al.* found that Au/TiO₂ photocatalysts with Au³⁺ states was the most effective catalyst for degrading methylene blue. [129] Whilst Tanabe *et al.* indicated that small Au nanoparticles (5 nm) were the most effective. [188] Zhu *et al.* investigated the degradation of rhodamine B with Au/TiO₂ catalysts and reported a significant improvement in pollutant removal compared to gold free catalysts. [191] The TiO₂ (001) phase was utilised in the study and

determined to be a very beneficial facet due to its rapid charge carrier exchange with the gold nanoparticles and improved adsorption of the pollutant. Other studies into heteroatom containing aromatics, found that gold improved the titania led removal of benzothiophene and dibenzothiophene, where 2.5 wt% Au/TiO₂ was the most proficient catalyst and adding hydrogen peroxide to the reaction mixture greatly increased the removal efficiency.[192] Min *et al.* used dioxane degradation to explore the promoting effect of gold plasmon resonance. [193] The inclusion of gold was, again, shown to positively impact on photocatalytic behaviour, indicating a strong correlation between the nature of the gold nanoparticles and degradation efficiency due to the charging effect of gold enhancing an alternative degradation route.

1.4.3 Pd/TiO₂ Photoreactivity

Palladium, like gold, can increase photocatalysis by introducing Schottky junctions that improve charge separation and allowing some thermal catalysis to occur on the palladium surface. Studies, utilising time resolved microwave conductivity (TRMC), have shown that palladium nanoparticles increase the amount of excess charge carriers detected. However, palladium cannot exhibit plasmonic resonance enhancements, although there are conflicting reports about whether palladium can introduce new energetic states within the titania bandgap, resulting in visible light activity. [194][213]

Palladium has been used extensively for water splitting, methanol reforming and hydrogen production reactions. [25][195-198] Investigation has showed that palladium effectively separates the electron/hole pairs and acts as a decarbonylation centre for the sacrificial agent. [198] Pd/TiO₂ is a more efficient water splitting photocatalyst than Au/TiO₂, evolving H₂ at a faster rate, and that alloyed Au-Pd catalysts displayed synergistic effects. As explained in **section 1.3.4.1**, photogenerated holes can abstract an electron from alcohols to form the alkoxy radical that is oxidised to an aldehyde. Palladium has been shown to thermally decarbonylate methanol at ambient temperatures leaving CO adsorbed on the palladium surface, [199] the CO is then oxidised by photogenerated holes to leave a vacancy that is filled by water subsequently releasing hydrogen. [196] The new pathway is key to the improved reactivity over bare TiO₂ for this reaction.

Pd/TiO₂ Gas Phase Photocatalysis

The gas phase oxidation of a number of volatile organic compounds (VOCs) by Pd/TiO₂ photocatalysts has been studied, target molecules include; benzene, [200] toluene,

[82] propylene, [201] formaldehyde [138], ozone [82][138] and various cyclic/non-cyclic hydrocarbons. [202] Many VOCs are considered to be toxic and carcinogenic so research has often revolved around the total oxidation of the target species. Zhong *et al.* found that adding 0.25 wt% palladium onto TiO₂ increased the maximum conversion of benzene from 28.2% to 65.3%, although the author noted that deactivation by intermediates occurred and the work did not establish what intermediates formed or if CO₂ was released. [200] A few studies have also shown that the use of palladium doped titania catalysts significantly improves conversion, while reducing residence time in the reactor, for the degradation of; toluene, cyclohexane, n-hexane, n-octane, isooctane. [82][202] The improvements in initial degradation was also coupled with improved degradation of intermediates. Loadings were varied between 0.2 and 2 wt% for oxidation of propylene, with 1 wt% giving the highest removal efficiency of 29 % and 71 % for palladium loaded powder and nanotube catalysts. [201] The Pd-nanotube samples also showed impressive photostability, only dropping to 90% conversion after 4 runs. Fu *et al.* examined formaldehyde and ozone oxidation using Pd doped films under intense UV irradiation (254 + 185 nm). [138] Palladium increased the removal rate of formaldehyde and tripled the rate of degradation of ozone, citing increased electron/hole separation as the cause. Hydroxyl radicals were more efficiently produced, and responsible for oxidising formaldehyde, whilst electrons captured by the palladium particles were transferred to the O₃ molecules.

Pd/TiO₂ Selectivity

The bulk of testing for palladium assisted photocatalytic oxidative degradation has been done in the liquid phase. Unlike Au/TiO₂, Pd/TiO₂ is rarely used for selective photo-oxidation procedures, often presenting poor selectivity. Over-oxidation is an issue commonly found with aqueous titania based photo-oxidation. For example, the selective oxidation of benzyl alcohol to benzaldehyde, using bare titania, in water and acetonitrile gave selectivity of 28 [203] and >99 %. [204] Hydroxyl radicals play a large part in degrading aromatic rings, which are very prevalent species in aqueous photocatalysis. Lopez-Tenllado *et al.* illustrated this elegantly in the oxidation of crotyl alcohol to crotonaldehyde in an acetonitrile/water mixture. [205] Increasing the water content from 0 to 0.05% has no impact on the crotonaldehyde yield, but further increases reduced the yield with the yield reducing from ~32 to ~7 %. They also tested an array of metal catalysts on titania for the oxidation of crotyl alcohol and 2-propanol (**Figure 1.4.4 top** and **bottom** respectively) Pd/TiO₂ photocatalysts had a lower conversion of benzyl alcohol, but a higher selectivity for benzaldehyde, in

comparison to plain P25; whilst the same trend was observed for 2-propanol to acetone. Although, Imamura *et al.* did selectively hydrogenate a variety of unsaturated cyclic hydrocarbons, in ethanol, using 0.1 wt% Pd/TiO₂ in the absence of a H₂ stream. [206] The author proposed that the mechanism consisted of photocatalytically reducing H⁺ atoms, to form surface Pd-H, which hydrogenated the alkene bond preferentially to evolving as H₂ gas. These selectivity improvements, however, are often not transferred to aqueous photocatalytic oxidation resulting in a greater focus on total oxidation or mineralisation.

An important aspect of Pd/TiO₂ mineralisation is the oxidation of chlorine containing pollutants. Polyvinyl chloride (PVC) can end up in waterways from plastic piping and the monomer, vinyl chloride (VC), is a carcinogen. [207] As such, the degradation of vinyl chloride without evolving toxic chlorinated gases is an important task. Ideally, VC degradation would mineralise to H₂O, CO₂ and HCl; however it degrades partially to form chlorinated by-products like phosgene that are believed to form from a radical mechanism

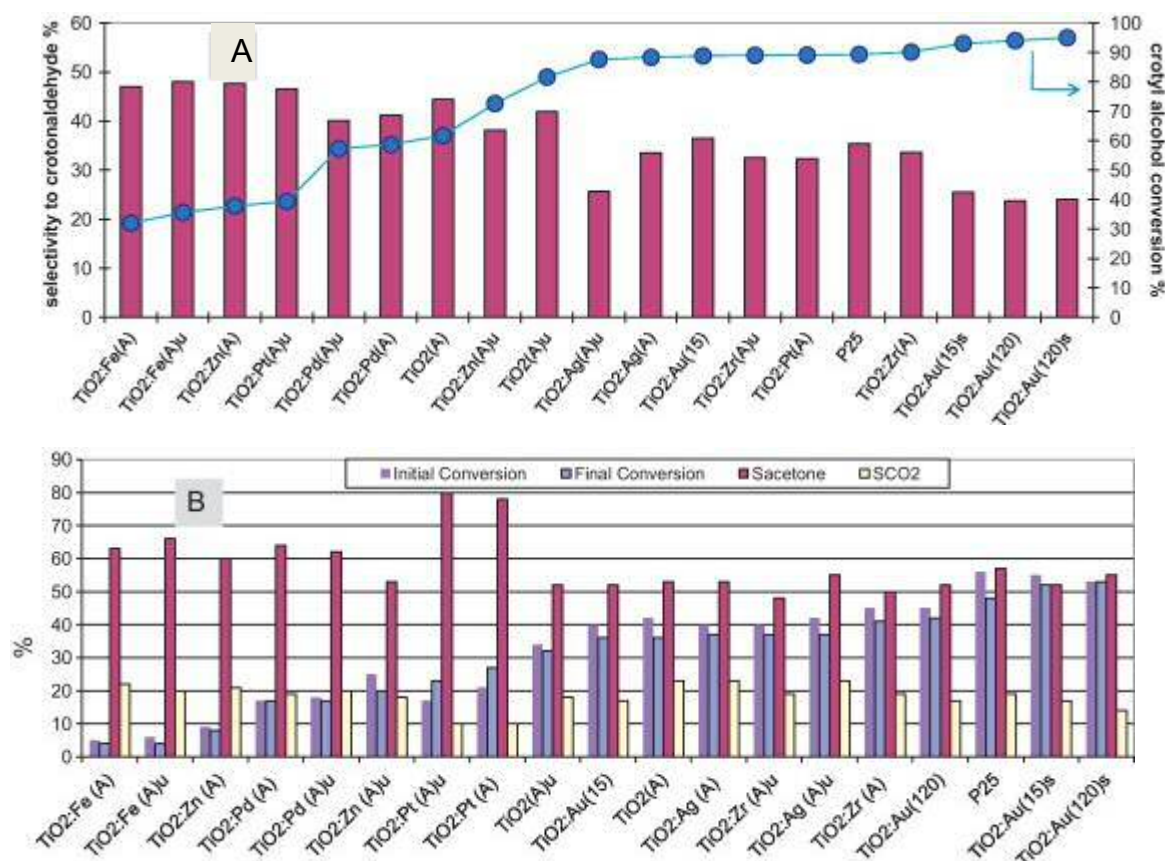


Figure 1.4.4:- (Top) The selectivity for crotonaldehyde (left axis) and conversion of crotyl alcohol (right axis) for a range of metal supported TiO₂ photocatalysts (bottom) The initial conversion, final conversion, selectivity for acetone and selectivity for CO₂ for the metal supported TiO₂ photocatalysts
“(A)” denotes anatase phase
“u” indicates ultrasonication during catalyst preparation [205]

due to Cl^- being oxidised on the TiO_2 surface. [208][209] The introduction of palladium prevents the release of toxic chlorinated by-products due to the trapping of chloro-organics on the palladium surface. [152] Whilst palladium induced a lower conversion, it encouraged total carbon oxidation to CO_2 , rather than partial oxidation to CO , which was attributed to the suppression of electron mediated species due to the electron trapping on palladium.

Total Oxidation of Organic Compounds by Pd/TiO₂

Much of the literature concerning total oxidation over Pd/TiO₂ catalysts, assigns the improvements, over plain TiO₂, to the Schottky barrier enhancing electron-hole separation. The degradation of dyes is a common standard for all photocatalysts, as such Pd/TiO₂ photocatalysts have been tested on; methylene blue, [210][211] rhodamine B, [194] xylene orange [139] and methyl orange. [212] Tahiri *et al.* found palladium improved the rate of degradation of the dye rhodamine B, for all the modified TiO₂ photocatalysts tested. On the other hand, in the case of phenol, improvements in rate were only observed for the lower surface area TiO₂ powders. This difference in behaviour was attributed to differing photocatalytic degradation pathways. The improvements measured were directly correlated to enhanced carrier lifetimes, as measured by TRMC. [194] Testing of methylene blue generally shows improved palladium degradation efficiencies. Tanaka *et al.* produced TiO₂ particles, and embedded Pd/TiO₂, using a novel inkjet process. They found that embedding Pd particles on both the inner and outer surface of the titania showed superior degradation to coating the outer surface with Pd particles. [211] This illustrated that the beneficial Schottky junction, between TiO₂ and Pd, is the most important aspect for methylene blue degradation. The same trends are observed for the other studies into dye degradation, with each ascribing the increased degradation rates to the better electron-hole separation. [210][212]

1.5 Aims of the Studies

The research in this thesis has been divided into three chapters examining various facets of photocatalytic oxidative degradation. Chapter 3, is a kinetic and mechanistic study of the degradation of cinnamic acid by TiO₂ and the impact of inorganic contaminants. The key objective of this work is to elucidate the mechanisms by which cinnamic acid degrades photocatalytically, then explore the kinetic and mechanistic changes induced by likely aqueous contaminants. In particular, the mechanistic changes observed in the presence of chloride are closely examined and discussed within the context of total mineralisation.

Chapter 4 investigates photocatalysis by anodic titania nanotubes and how anodisation time length effects the photocatalytic efficiency. The nanotube arrays were also modified with tungsten and the noble metals gold and palladium by photodeposition to enhance the photoactivity. Measured photocatalytic activity is correlated with the chemical character and, importantly, the topographical nature of the samples. The final experimental chapter, Chapter 5, explores how gold and palladium affect the kinetics and mechanism of cinnamic acid degradation by TiO₂. The study aims to establish whether the noble metals could influence the degradation and improve selectivity of the photocatalyst. Weight loadings are varied to probe the optimal amount of metal co-catalyst.

Chapter 5, the third and final study, enquires into how gold and palladium effect the kinetic and mechanistic aspects of cinnamic acid degradation by TiO₂. The study aims to establish how the noble metals would influence the degradation of cinnamic acid and if selective oxidation to valuable platform chemicals is viable. Weight loadings are varied to probe the optimal amount of metal co-catalyst; the photocatalyst activity and mechanistic preferences were determined in the same manner as for Chapter 3.

Chapter 6, presents conclusions from the work and describes the author's thoughts on where future work should be focussed.

1.6 References

1. PCATDES – Final Report, (2017/04/20), retrieved from <http://www.pcatdes.eu/Publications.asp>
2. *Oil Palm & The Environment, 2014*, Malaysian Palm Oil Board. <http://www.mpob.gov.my/palm-info/environment/520-achievements>
3. Green Palm online, c2016, [accessed: 01 May 2017], www.greenpalm.org/
4. S. Prokurat, *Journal of Modern Science*, 2013, 425 – 423.
5. P. F. Rupani, R. P. Singh, M. H. I. Ibrahim and N. Esa, *World Applied Sciences Journal*, 2010, **11**, 70–81.
6. D. O. Edem, *Plant Foods Hum Nutr*, 2002, **57**, 319–341.
7. P. Jamal, Z. M. Idris and M. Z. Alam, *Food Chemistry*, 2011, **124**, 1595–1602.
8. K. Wong, *Pertanika*, 1980, **3**, 133–141.
9. B. Linke, *Biomass and Bioenergy*, 2006, **30**, 892–896.
10. S. Yacob, M. A. Hassan, Y. Shirai, M. Wakisaka and S. Subash, *Chemosphere*, 2005, **59**, 1575–1581.
11. F.-Y. Ng, F.-K. Yew, Y. Basiron and K. Sundram, *Journal of Oil Palm & the Environment*, 2011, **2**, 1–7.
12. S. Ahmad, M. Z. A. A. Kadir and S. Shafie, *Renewable and Sustainable Energy Reviews*, 2011, **15**, 897–904.
13. Y. V. Paramitadevi and Rahmatullah, *IOP Conference Series: Earth and Environmental Science*, 2017, **65**, 012048.
14. J.-G. Li, T. Ishigaki and X. Sun, *J. Phys. Chem. C*, 2007, **111**, 4969–4976.

15. A. Fahmi, C. Minot, B. Silvi and M. Causá, *Phys. Rev. B*, 1993, **47**, 11717–11724.
16. S.-D. Mo and W. Y. Ching, *Phys. Rev. B*, 1995, **51**, 13023–13032.
17. H. Berger, H. Tang and F. Lévy, *Journal of Crystal Growth*, 1993, **130**, 108–112.
18. L. Kavan, M. Grätzel, S. E. Gilbert, C. Klemenz and H. J. Scheel, *J. Am. Chem. Soc.*, 1996, **118**, 6716–6723.
19. D. L. Hamilton, *Geol. J.*, 1989, **24**, 75–76.
20. A. Fujishima and K. Honda, *Nature*, 1972, **238**, 37–38.
21. G. N. Schrauzer and T. D. Guth, *J. Am. Chem. Soc.*, 1977, **99**, 7189–7193.
22. K. Domen, S. Naito, T. Onishi and K. Tamaru, *Chemistry Letters*, 1982, **11**, 555–558.
23. X. Pan, Q. Xie, W. Chen, G. Zhuang, X. Zhong and J. Wang, *International Journal of Hydrogen Energy*, 2013, **38**, 2095–2105.
24. M. Altomare, M. Pozzi, M. Allieta, L. G. Bettini and E. Selli, *Applied Catalysis B: Environmental*, 2013, **136–137**, 81–88.
25. H. Bahruji, M. Bowker, P. R. Davies and F. Pedrono, *Applied Catalysis B: Environmental*, 2011, **107**, 205–209.
26. H. Bahruji, M. Bowker, P. R. Davies, J. Kennedy and D. J. Morgan, *International Journal of Hydrogen Energy*, 2015, **40**, 1465–1471.
27. H. Bahruji, M. Bowker, P. R. Davies, D. J. Morgan, C. A. Morton, T. A. Egerton, J. Kennedy and W. Jones, *Topics in Catalysis*, 2015, **58**, 70–76.
28. J. R. Jennings, A. Ghicov, L. M. Peter, P. Schmuki and A. B. Walker, *J. Am. Chem. Soc.*, 2008, **130**, 13364–13372.
29. J. Wiszniowski, D. Robert, J. Surmacz-Gorska, K. Miksch and J.-V. Weber, *Journal of Photochemistry and Photobiology A: Chemistry*, 2002, **152**, 267–273.
30. I. K. Konstantinou, V. A. Sakkas and T. A. Albanis, *Applied Catalysis B: Environmental*, 2001, **34**, 227–239.
31. U. I. Gaya and A. H. Abdullah, *Journal of Photochemistry and Photobiology C: Photochemistry Reviews*, 2008, **9**, 1–12.
32. Z. Guo, R. Ma and G. Li, *Chemical Engineering Journal*, 2006, **119**, 55–59.
33. S. Zheng, Y. Cai and K. E. O’Shea, *Journal of Photochemistry and Photobiology A: Chemistry*, 2010, **210**, 61–68.
34. T. T. T. Dang, S. T. T. Le, D. Channei, W. Khanitchaidecha and A. Nakaruk, *Res Chem Intermed*, 2016, **42**, 5961–5974.
35. W. Irawaty, D. Friedmann, J. Scott, P. Pichat and R. Amal, *Catalysis Today*, 2011, **178**, 51–57.
36. T. D. Bui, A. Kimura, S. Higashida, S. Ikeda and M. Matsumura, *Applied Catalysis B: Environmental*, 2011, **107**, 119–127.
37. T. D. Bui, A. Kimura, S. Ikeda and M. Matsumura, *J. Am. Chem. Soc.*, 2010, **132**, 8453–8458.
38. H. Maeda, H. Nakagawa and K. Mizuno, *Journal of Photochemistry and Photobiology A: Chemistry*, 2007, **189**, 94–99.
39. Z. Liu, X. Zhang, S. Nishimoto, T. Murakami and A. Fujishima, *Environ. Sci. Technol.*, 2008, **42**, 8547–8551.
40. A. G. Kontos, A. Katsanaki, T. Maggos, V. Likodimos, A. Ghicov, D. Kim, J. Kunze, C. Vasilakos, P. Schmuki and P. Falaras, *Chemical Physics Letters*, 2010, **490**, 58–62.
41. M. Nischk, P. Mazierski, M. Gazda and A. Zaleska, *Applied Catalysis B: Environmental*, 2014, **144**, 674–685.
42. A. Furube, T. Asahi, H. Masuhara, H. Yamashita and M. Anpo, *J. Phys. Chem. B*, 1999, **103**, 3120–3127.

43. M. A. Henderson, *Surface Science Reports*, 2011, **66**, 185–297.
44. J. Schneider, M. Matsuoka, M. Takeuchi, J. Zhang, Y. Horiuchi, M. Anpo and D. W. Bahnemann, *Chem. Rev.*, 2014, **114**, 9919–9986.
45. D. Lawless, N. Serpone and D. Meisel, *J. Phys. Chem.*, 1991, **95**, 5166–5170.
46. O. I. Micic, Y. Zhang, K. R. Cromack, A. D. Trifunac and M. C. Thurnauer, *J. Phys. Chem.*, 1993, **97**, 7277–7283.
47. D. K. Pallotti, L. Passoni, P. Maddalena, F. Di Fonzo and S. Lettieri, *J. Phys. Chem. C*, 2017, **121**, 9011–9021.
48. G. Fazio, L. Ferrighi and C. Di Valentin, *J. Phys. Chem. C*, 2015, **119**, 20735–20746.
49. D. W. Bahnemann, M. Hilgendorff and R. Memming, *J. Phys. Chem. B*, 1997, **101**, 4265–4275.
50. P. Salvador, *J. Phys. Chem. C*, 2007, **111**, 17038–17043.
51. T. Berger, M. Sterrer, O. Diwald, E. Knözinger, D. Panayotov, T. L. Thompson and J. T. Yates, *J. Phys. Chem. B*, 2005, **109**, 6061–6068.
52. T. Bredow and K. Jug, *J. Phys. Chem.*, 1995, **99**, 285–291.
53. Y. Nosaka and A. Nosaka, *ACS Energy Lett.*, 2016, **1**, 356–359.
54. W. Kim, T. Tachikawa, G. Moon, T. Majima and W. Choi, *Angew. Chem. Int. Ed.*, 2014, **53**, 14036–14041.
55. Y. Li, B. Wen, C. Yu, C. Chen, H. Ji, W. Ma and J. Zhao, *Chemistry - A European Journal*, 2012, **18**, 2030–2039.
56. V. Shapovalov, E. V. Stefanovich and T. N. Truong, *Surface Science*, 2002, **498**, L103–L108.
57. K. Shirai, T. Sugimoto, K. Watanabe, M. Haruta, H. Kurata and Y. Matsumoto, *Nano Lett.*, 2016, **16**, 1323–1327.
58. E. G. Panarelli, S. Livraghi, S. Maurelli, V. Polliotto, M. Chiesa and E. Giamello, *Journal of Photochemistry and Photobiology A: Chemistry*, 2016, **322**, 27–34.
59. A. Litke, E. J. M. Hensen and J. P. Hofmann, *J. Phys. Chem. C*, 2017, **121**, 10153–10162.
60. A. Litke, Y. Su, I. Tranca, T. Weber, E. J. M. Hensen and J. P. Hofmann, *J. Phys. Chem. C*, 2017, **121**, 7514–7524.
61. A. I. Kuznetsov, O. Kameneva, A. Alexandrov, N. Bityurin, P. Marteau, K. Chhor, C. Sanchez and A. Kanaev, *Phys. Rev. E*, 2005, **71**, 021403.
62. A. Yamakata, T. Ishibashi and H. Onishi, *Journal of Molecular Catalysis A: Chemical*, 2003, **199**, 85–94.
63. S. Ikeda, N. Sugiyama, S. Murakami, H. Kominami, Y. Kera, H. Noguchi, K. Uosaki, T. Torimoto and B. Ohtani, *Phys. Chem. Chem. Phys.*, 2003, **5**, 778–783.
64. H. Wang, J. He, G. Boschloo, H. Lindström, A. Hagfeldt and S.-E. Lindquist, *J. Phys. Chem. B*, 2001, **105**, 2529–2533.
65. P. M. Kowalski, M. F. Camellone, N. N. Nair, B. Meyer and D. Marx, *Phys. Rev. Lett.*, 2010, **105**, 146405.
66. S. Leytner and J. T. Hupp, *Chemical Physics Letters*, 2000, **330**, 231–236.
67. Y. Tamaki, A. Furube, M. Murai, K. Hara, R. Katoh and M. Tachiya, *Phys. Chem. Chem. Phys.*, 2007, **9**, 1453–1460.
68. N. Serpone, D. Lawless, R. Khairutdinov and E. Pelizzetti, *J. Phys. Chem.*, 1995, **99**, 16655–16661.
69. T. Luttrell, S. Halpegamage, J. Tao, A. Kramer, E. Sutter and M. Batzill, *Scientific Reports*, 2014, **4**, srep04043.
70. T. Sumita, T. Yamaki, S. Yamamoto and A. Miyashita, *Applied Surface Science*, 2002, **200**, 21–26.

71. W. Xu and D. Raftery, *J. Phys. Chem. B*, 2001, **105**, 4343–4349.
72. S. Paul and A. Choudhury, *Appl Nanosci*, 2014, **4**, 839–847.
73. H. Tang, H. Berger, P. E. Schmid and F. Lévy, *Solid State Communications*, 1994, **92**, 267–271.
74. M. Batzill, *Energy & Environmental Science*, 2011, **4**, 3275–3286.
75. J. L. Giocondi, P. A. Salvador and G. S. Rohrer, *Top Catal*, 2007, **44**, 529–533.
76. D. O. Scanlon, C. W. Dunnill, J. Buckeridge, S. A. Shevlin, A. J. Logsdail, S. M. Woodley, C. R. A. Catlow, M. J. Powell, R. G. Palgrave, I. P. Parkin, G. W. Watson, T. W. Keal, P. Sherwood, A. Walsh and A. A. Sokol, *Nat Mater*, 2013, **12**, 798–801.
77. J. Zhang, P. Zhou, J. Liu and J. Yu, *Phys. Chem. Chem. Phys.*, 2014, **16**, 20382–20386.
78. M. Xu, Y. Gao, E. M. Moreno, M. Kunst, M. Muhler, Y. Wang, H. Idriss and C. Wöll, *Phys. Rev. Lett.*, 2011, **106**, 138302.
79. K. Zhu, N. Kopidakis, N. R. Neale, J. van de Lagemaat and A. J. Frank, *J. Phys. Chem. B*, 2006, **110**, 25174–25180.
80. M. D’Arienzo, J. Carbajo, A. Bahamonde, M. Crippa, S. Polizzi, R. Scotti, L. Wahba and F. Morazzoni, *J. Am. Chem. Soc.*, 2011, **133**, 17652–17661.
81. J. Pan, G. Liu, G. Q. (Max) Lu and H.-M. Cheng, *Angew. Chem. Int. Ed.*, 2011, **50**, 2133–2137.
82. W. Kim, T. Tachikawa, G. Moon, T. Majima and W. Choi, *Angew. Chem. Int. Ed.*, 2014, **53**, 14036–14041.
83. Y. Kakuma, A. Y. Nosaka and Y. Nosaka, *Phys. Chem. Chem. Phys.*, 2015, **17**, 18691–18698.
84. T. Ohno, K. Tokieda, S. Higashida and M. Matsumura, *Applied Catalysis A: General*, 2003, **244**, 383–391.
85. H. Nakajima, T. Mori, Q. Shen and T. Toyoda, *Chemical Physics Letters*, 2005, **409**, 81–84. 1
86. D. C. Hurum, A. G. Agrios, S. E. Crist, K. A. Gray, T. Rajh and M. C. Thurnauer, *Journal of Electron Spectroscopy and Related Phenomena*, 2006, **150**, 155–163.
87. K. V. Baiju, A. Zachariah, S. Shukla, S. Biju, M. L. P. Reddy and K. G. K. Warriar, *Catal Lett*, 2009, **130**, 130–136.
88. J. Zhang and Y. Nosaka, *J. Phys. Chem. C*, 2013, **117**, 1383–1391.
89. J. Zhang and Y. Nosaka, *Applied Catalysis B: Environmental*, 2015, **166**, 32–36.
90. N. M. Dimitrijevic, I. A. Shkrob, D. J. Gosztola and T. Rajh, *J. Phys. Chem. C*, 2012, **116**, 878–885.
91. Y. Tamaki, A. Furube, M. Murai, K. Hara, R. Katoh and M. Tachiya, *J. Am. Chem. Soc.*, 2006, **128**, 416–417.
92. Z. Yu and S. S. C. Chuang, *Journal of Catalysis*, 2007, **246**, 118–126.
93. N. Hykaway, W. M. Sears, H. Morisaki and S. R. Morrison, *J. Phys. Chem.*, 1986, **90**, 6663–6667.
94. D. A. Panayotov, S. P. Burrows and J. R. Morris, *J. Phys. Chem. C*, 2012, **116**, 6623–6635.
95. D. S. Muggli, K. H. Lowery and J. L. Falconer, *Journal of Catalysis*, 1998, **180**, 111–122.
96. F. Arsac, D. Bianchi, J. M. Chovelon, C. Ferronato and J. M. Herrmann, *J. Phys. Chem. A*, 2006, **110**, 4202–4212.
97. W. Xu and D. Raftery, *J. Phys. Chem. B*, 2001, **105**, 4343–4349.
98. G. V. Buxton, M. Bydder, G. A. Salmon and J. E. Williams, *Phys. Chem. Chem. Phys.*, 2000, **2**, 237–245.

99. S. Gligorovski, R. Strekowski, S. Barbati and D. Vione, *Chem. Rev.*, 2015, **115**, 13051–13092.
100. S. Gligorovski and H. Herrmann, *Phys. Chem. Chem. Phys.*, 2004, **6**, 4118–4126.
101. S. Ardizzone, C. L. Bianchi, G. Cappelletti, A. Naldoni and C. Pirola, *Environmental Science & Technology*, 2008, **42**, 6671–6676.
102. J. A. Peres, J. R. Domínguez and J. Beltran-Heredia, *Desalination*, 2010, **252**, 167–171.
103. W. J. McElroy and S. J. Waygood, *J. Chem. Soc., Faraday Trans.*, 1991, **87**, 1513–1521.
104. T. Shi, W. Chang, H. Zhang, H. Ji, W. Ma, C. Chen and J. Zhao, *Environ. Sci. Technol.*, 2015, **49**, 3024–3031.
105. E. Carter, A. F. Carley and D. M. Murphy, *ChemPhysChem*, 2007, **8**, 113–123.
106. M. A. Henderson, *J. Phys. Chem. B*, 2004, **108**, 18932–18941.
107. J. Shang, Y. Du and Z. Xu, *Chemosphere*, 2002, **46**, 93–99.
108. P. Du, J. Moulijn and G. Mul, *Journal of Catalysis*, 2006, **238**, 342–352.
109. A. R. Almeida, J. A. Moulijn and G. Mul, *J. Phys. Chem. C*, 2011, **115**, 1330–1338.
110. X. Pang, W. Chang, C. Chen, H. Ji, W. Ma and J. Zhao, *J. Am. Chem. Soc.*, 2014, **136**, 8714–8721.
111. X. Pang, C. Chen, H. Ji, Y. Che, W. Ma and J. Zhao, *Molecules*, 2014, **19**, 16291–16311.
112. A. Lair, C. Ferronato, J.-M. Chovelon and J.-M. Herrmann, *Journal of Photochemistry and Photobiology A: Chemistry*, 2008, **193**, 193–203.
113. M. Muneer, M. Qamar and D. Bahnemann, *Journal of Molecular Catalysis A: Chemical*, 2005, **234**, 151–157.
114. S. H. Kim, P. C. Stair and E. Weitz, *Chemical Physics Letters*, 1999, **302**, 511–516.
115. S. H. Szczepankiewicz, J. A. Moss and M. R. Hoffmann, *J. Phys. Chem. B*, 2002, **106**, 7654–7658.
116. M. Hayyan, M. A. Hashim and I. M. AlNashef, *Chem. Rev.*, 2016, **116**, 3029–3085.
117. J. J. Warren, T. A. Tronic and J. M. Mayer, *Chem. Rev.*, 2010, **110**, 6961–7001.
118. D. T. Sawyer, M. S. McDowell and K. S. Yamaguchi, *Chem. Res. Toxicol.*, 1988, **1**, 97–100.
119. D. T. Sawyer and J. S. Valentine, *Acc. Chem. Res.*, 1981, **14**, 393–400.
120. M. V. Merritt and D. T. Sawyer, *J. Org. Chem.*, 1970, **35**, 2157–2159.
121. W. C. Danen and R. J. Warner, *Tetrahedron Letters*, 1977, **18**, 989–992.
122. J. L. Roberts, T. S. Calderwood and D. T. Sawyer, *J. Am. Chem. Soc.*, 1983, **105**, 7691–7696.
123. H. Sugimoto, S. Matsumoto and D. T. Sawyer, *J. Am. Chem. Soc.*, 1987, **109**, 8081–8082.
124. M. J. Ryding, A. Debnárová, I. Fernández and E. Uggerud, *J. Org. Chem.*, 2015, **80**, 6133–6142.
125. A. O. Kondrakov, A. N. Ignatev, V. V. Lunin, F. H. Frimmel, S. Bräse and H. Horn, *Applied Catalysis B: Environmental*, 2016, **182**, 424–430.
126. J. Yang, J. Dai, C. Chen and J. Zhao, *Journal of Photochemistry and Photobiology A: Chemistry*, 2009, **208**, 66–77.
127. B. Cojocaru, Ș. Neațu, E. Sacaliuc-Pârvulescu, F. Lévy, V. I. Pârvulescu and H. Garcia, *Applied Catalysis B: Environmental*, 2011, **107**, 140–149.

128. B. Gupta, A. A. Melvin, T. Matthews, S. Dash and A. K. Tyagi, *Renewable and Sustainable Energy Reviews*, 2016, **58**, 1366–1375.
129. F. B. Li and X. Z. Li, *Applied Catalysis A: General*, 2002, **228**, 15–27.
130. S. Oros-Ruiz, J. A. Pedraza-Avella, C. Guzmán, M. Quintana, E. Moctezuma, G. del Angel, R. Gómez and E. Pérez, *Top Catal*, 2011, **54**, 519–526.
131. D. A. Panayotov and J. R. Morris, *Surface Science Reports*, 2016, **71**, 77–271.
132. V. Subramanian, E. E. Wolf and P. V. Kamat, *Langmuir*, 2003, **19**, 469–474.
133. V. Subramanian, E. E. Wolf and P. V. Kamat, *J. Am. Chem. Soc.*, 2004, **126**, 4943–4950.
134. B. Paul, B. Bhuyan, D. D. Purkayastha and S. S. Dhar, *Journal of Photochemistry and Photobiology B: Biology*, 2016, **154**, 1–7.
135. H. Czili and A. Horváth, *Applied Catalysis B: Environmental*, 2008, **81**, 295–302.
136. S. Garg, T. Ma, C. J. Miller and T. D. Waite, *J. Phys. Chem. C*, 2014, **118**, 26659–26670.
137. E. Grabowska, H. Remita and A. Zaleska, *Physiochem. Probl. Miner. Process.*
138. P. Fu, P. Zhang and J. Li, *Applied Catalysis B: Environmental*, 2011, **105**, 220–228.
139. V. Iliev, D. Tomova, L. Bilyarska and L. Petrov, *Catalysis Communications*, 2004, **5**, 759–763.
140. Z. Wu, Z. Sheng, H. Wang and Y. Liu, *Chemosphere*, 2009, **77**, 264–268.
141. D. Eder, M. S. Motta, I. A. Kinloch and A. H. Windle, *Physica E: Low-dimensional Systems and Nanostructures*, 2007, **37**, 245–249.
142. W. Wu, K. Bhattacharyya, K. Gray and E. Weitz, *J. Phys. Chem. C*, 2013, **117**, 20643–20655.
143. B. K. Vijayan, N. M. Dimitrijevic, J. Wu and K. A. Gray, *J. Phys. Chem. C*, 2010, **114**, 21262–21269.
144. C.-H. Huang, I.-K. Wang, Y.-M. Lin, Y.-H. Tseng and C.-M. Lu, *Journal of Molecular Catalysis A: Chemical*, 2010, **316**, 163–170.
145. A. Talebian, M. H. Entezari and N. Ghows, *Chemical Engineering Journal*, 2013, **229**, 304–312.
146. R. Chen, C. Zhang, J. Deng and G. Song, *International Journal of Minerals, Metallurgy and Materials*, 2009, **16**, 220–225.
147. D. Tsukamoto, Y. Shiraishi, Y. Sugano, S. Ichikawa, S. Tanaka and T. Hirai, *J. Am. Chem. Soc.*, 2012, **134**, 6309–6315.
148. V. Iliev, D. Tomova, S. Rakovsky, A. Eliyas and G. L. Puma, *Journal of Molecular Catalysis A: Chemical*, 2010, **327**, 51–57.
149. E. Kowalska, O. O. P. Mahaney, R. Abe and B. Ohtani, *Phys. Chem. Chem. Phys.*, 2010, **12**, 2344–2355.
150. A. J. Bard and M. A. Fox, *Acc. Chem. Res.*, 1995, **28**, 141–145.
151. A. Tanaka, K. Hashimoto and H. Kominami, *Chem. Commun.*, 2011, **47**, 10446–10448.
152. T. Sano, S. Kutsuna, N. Negishi and K. Takeuchi, *Journal of Molecular Catalysis A: Chemical*, 2002, **189**, 263–270.
153. R. T. (• • □ . Tung, *Applied Physics Reviews*, 2014, **1**, 011304.
154. X. Zhang, Y. L. Chen, R.-S. Liu and D. P. Tsai, *Rep. Prog. Phys.*, 2013, **76**, 046401.
155. O. Engström, H. Pettersson and B. Sernelius, *phys. stat. sol. (a)*, 1986, **95**, 691–701.
156. A. Tanabe, K. Konuma, N. Teranishi, S. Tohyama and K. Masubuchi, *Journal of Applied Physics*, 1991, **69**, 850–853.

157. G. J. Hutchings, *Journal of Catalysis*, 1985, **96**, 292–295.
158. M. Haruta, T. Kobayashi, H. Sano and N. Yamada, *Chemistry Letters*, 1987, **16**, 405–408.
159. M. Haruta, N. Yamada, T. Kobayashi and S. Iijima, *Journal of Catalysis*, 1989, **115**, 301–309.
160. A. Corma and H. Garcia, *Chemical Society Reviews*, 2008, **37**, 2096–2126.
161. G. J. Hutchings, M. Brust and H. Schmidbaur, *Chemical Society Reviews*, 2008, **37**, 1759–1765.
162. G. Malta, S. A. Kondrat, S. J. Freakley, C. Davies, L. Lu, S. Dawson, A. Thetford, E. K. Gibson, D. J. Morgan, W. Jones, P. B. Wells, P. Johnston, C. R. A. Catlow, C. J. Kiely and G. J. Hutchings, *Science*, 2017, **355**, 1399–1403.
163. X. Liu, M. Conte, D. Elias, L. Lu, D. J. Morgan, S. Freakley, P. Johnston, C. J. Kiely and G. J. Hutchings, *Catalysis Science & Technology*, 2016, **6**, 5144–5153.
164. M. Comotti, W.-C. Li, B. Spliethoff and F. Schüth, *Journal of the American Chemical Society*, 2006, **128**, 917–924.
165. L. Prati and M. Rossi, *Journal of Catalysis*, 1998, **176**, 552–560.
166. A. Mehri, H. Kochkar, G. Berhault, M. Cómbita and T. Blasco, *Materials Chemistry and Physics*, 2015, **149**, 59–68.
167. S. Meenakshisundaram, E. Nowicka, P. J. Miedziak, G. L. Brett, R. L. Jenkins, N. Dimitratos, S. H. Taylor, D. W. Knight, D. Bethell and G. J. Hutchings, *Faraday Discussions*, 2010, **145**, 341–356.
168. J. Chen, S. J. A. Halin, E. A. Pidko, M. W. G. M. (Tiny) Verhoeven, D. M. P. Ferrandez, E. J. M. Hensen, J. C. Schouten and T. A. Nijhuis, *ChemCatChem*, 2013, **5**, 467–478.
169. A. Chen, Q. Zhu, Y. Zhao, T. Tastumi and T. Iyoda, *Particle and Particle Systems Characterization*, 2013, **30**, 489–493.
170. A. S. K. Hashmi, *Chem. Rev.*, 2007, **107**, 3180–3211.
171. Y. Maeda, M. Okumura, S. Tsubota, M. Kohyama and M. Haruta, *Applied Surface Science*, 2004, **222**, 409–414.
172. W. Hou and S. B. Cronin, *Advanced Functional Materials*, 2013, **23**, 1612–1619.
173. Y. Tian and T. Tatsuma, *Chem. Commun.*, 2004, **0**, 1810–1811.
174. Y. Tian and T. Tatsuma, *J. Am. Chem. Soc.*, 2005, **127**, 7632–7637.
175. S. Mubeen, G. Hernandez-Sosa, D. Moses, J. Lee and M. Moskovits, *Nano Lett.*, 2011, **11**, 5548–5552.
176. A. Furube, L. Du, K. Hara, R. Katoh and M. Tachiya, *J. Am. Chem. Soc.*, 2007, **129**, 14852–14853.
177. W. Ho, *J. Phys. Chem.*, 1996, **100**, 13050–13060.
178. M. J. Kale, T. Avanesian and P. Christopher, *ACS Catal.*, 2014, **4**, 116–128.
179. O. Rosseler, M. V. Shankar, M. K.-L. Du, L. Schmidlin, N. Keller and V. Keller, *Journal of Catalysis*, 2010, **269**, 179–190.
180. M. Haruta, *Catalysis Today*, 1997, **36**, 153–166.
181. J. Fang, S.-W. Cao, Z. Wang, M. M. Shahjamali, S. C. J. Loo, J. Barber and C. Xue, *International Journal of Hydrogen Energy*, 2012, **37**, 17853–17861.
182. C. Gomes Silva, R. Juárez, T. Marino, R. Molinari and H. García, *J. Am. Chem. Soc.*, 2011, **133**, 595–602.
183. J. T. Carneiro, C.-C. Yang, J. A. Moma, J. A. Moulijn and G. Mul, *Catal Lett*, 2009, **129**, 12–19.
184. T. Marino, R. Molinari and H. García, *Catalysis Today*, 2013, **206**, 40–45.
185. Y. Ide, R. Ogino, M. Sadakane and T. Sano, *ChemCatChem*, 2013, **5**, 766–773.

186. Z. Zheng, B. Huang, X. Qin, X. Zhang, Y. Dai and M.-H. Whangbo, *J. Mater. Chem.*, 2011, **21**, 9079–9087.
187. Y. Ide, M. Matsuoka and M. Ogawa, *J. Am. Chem. Soc.*, 2010, **132**, 16762–16764.
188. I. Tanabe, T. Ryoki and Y. Ozaki, *RSC Adv.*, 2015, **5**, 13648–13652.
189. H. Wang, J. L. Faria, S. Dong and Y. Chang, *Materials Science and Engineering: B*, 2012, **177**, 913–919.
190. A. B. Haugen, I. Kumakiri, C. Simon and M.-A. Einarsrud, *Journal of the European Ceramic Society*, 2011, **31**, 291–298.
191. S. Zhu, S. Liang, Q. Gu, L. Xie, J. Wang, Z. Ding and P. Liu, *Applied Catalysis B: Environmental*, 2012, **119**, 146–155.
192. S. Khayyat and L. Selva Roselin, *Journal of Saudi Chemical Society*, 2017, **21**, 349–357.
193. B. K. Min, J. E. Heo, N. K. Youn, O. S. Joo, H. Lee, J. H. Kim and H. S. Kim, *Catalysis Communications*, 2009, **10**, 712–715.
194. O. Tahiri Alaoui, A. Herissan, C. Le Quoc, M. el M. Zekri, S. Sorgues, H. Remita and C. Colbeau-Justin, *Journal of Photochemistry and Photobiology A: Chemistry*, 2012, **242**, 34–43.
195. W. Jones, D. J. Martin, A. Caravaca, A. M. Beale, M. Bowker, T. Maschmeyer, G. Hartley and A. Masters, *Applied Catalysis B: Environmental*, , DOI:10.1016/j.apcatb.2017.01.042.
196. L. S. Al-Mazroai, M. Bowker, P. Davies, A. Dickinson, J. Greaves, D. James and L. Millard, *Catalysis Today*, 2007, **122**, 46–50.
197. M. Bowker, P. R. Davies and L. S. Al-Mazroai, *Catalysis Letters*, 2009, **128**, 253–255.
198. M. Bowker, C. Morton, J. Kennedy, H. Bahruji, J. Greves, W. Jones, P. R. Davies, C. Brookes, P. P. Wells and N. Dimitratos, *Journal of Catalysis*, 2014, **310**, 10–15.
199. A. Dickinson, D. James, N. Perkins, T. Cassidy and M. Bowker, *Journal of Molecular Catalysis A: Chemical*, 1999, **146**, 211–221.
200. J. B. Zhong, Y. Lu, W. D. Jiang, Q. M. Meng, X. Y. He, J. Z. Li and Y. Q. Chen, *Journal of Hazardous Materials*, 2009, **168**, 1632–1635.
201. C. Li, L. Zong, Q. Li, J. Zhang, J. Yang and Z. Jin, *Nanoscale Res Lett*, 2016, **11**, 271.
202. T. M. Fujimoto, M. Ponczek, U. L. Rochetto, R. Landers and E. Tomaz, *Environ Sci Pollut Res*, 2017, **24**, 6390–6396.
203. V. Augugliaro, H. Kisch, V. Loddo, M. J. López-Muñoz, C. Márquez-Álvarez, G. Palmisano, L. Palmisano, F. Parrino and S. Yurdakal, *Applied Catalysis A: General*, 2008, **349**, 182–188.
204. S. Higashimoto, N. Kitao, N. Yoshida, T. Sakura, M. Azuma, H. Ohue and Y. Sakata, *Journal of Catalysis*, 2009, **266**, 279–285.
205. F. J. López-Tenllado, A. Marinas, F. J. Urbano, J. C. Colmenares, M. C. Hidalgo, J. M. Marinas and J. M. Moreno, *Applied Catalysis B: Environmental*, 2012, **128**, 150–158.
206. K. Imamura, Y. Okubo, T. Ito, A. Tanaka, K. Hashimoto and H. Kominami, *RSC Adv.*, 2014, **4**, 19883–19886.
207. R. K. Walter, P.-H. Lin, M. Edwards and R. E. Richardson, *Water Research*, 2011, **45**, 2607–2615.
208. X. Liu, S. Yoon, B. Batchelor and A. Abdel-Wahab, *Chemical Engineering Journal*, 2013, **215**, 868–875.

209. T. Sano, N. Negishi, S. Kutsuna and K. Takeuchi, *Journal of Molecular Catalysis A: Chemical*, 2001, **168**, 233–240.
210. C.-C. Chan, C.-C. Chang, W.-C. Hsu, S.-K. Wang and J. Lin, *Chemical Engineering Journal*, 2009, **152**, 492–497.
211. T. Tanaka, K. Kadota, Y. Tozuka, A. Shimosaka and Y. Shirakawa, *Ceramics International*, 2016, **42**, 9963–9971.
212. M. Anas, D. S. Han, K. Mahmoud, H. Park and A. Abdel-Wahab, *Materials Science in Semiconductor Processing*, 2016, **41**, 209–218.
213. E. A. Obuya, W. Harrigan, D. M. Andala, J. Lippens, T. C. Keane and W. E. Jones, *Journal of Molecular Catalysis A: Chemical*, 2011, **340**, 89–98.

Chapter 2 - Experimental

| | |
|--|----|
| 2.1 Introduction | 42 |
| 2.2 Catalyst Preparation, Methods and Equipment | 42 |
| 2.2.1 Powdered Catalyst Preparation..... | 42 |
| 2.2.1.1 Preparation of Modified P25 (mP25)..... | 42 |
| 2.2.1.2 Pd/TiO ₂ Preparation..... | 42 |
| 2.2.1.3 Au/TiO ₂ Preparation..... | 43 |
| 2.2.2 TiO ₂ Nanotubes Preparation..... | 43 |
| 2.2.2.1 Anodisation equipment..... | 44 |
| 2.2.2.2 TiO ₂ Nanotubes..... | 45 |
| 2.2.2.3 WO ₃ /TiO ₂ Nanotubes..... | 45 |
| 2.2.2.4 Metal Loaded TiO ₂ Nanotubes..... | 45 |
| 2.2.3 Photocatalytic Reactor Experimental Set Up..... | 46 |
| 2.2.3.1 Reactor vessels..... | 46 |
| Liquid Phase Experiment procedure..... | 46 |
| Surface Degradation Experiment Procedure..... | 48 |
| 2.2.3.2 Light Source..... | 48 |
| 2.2.4 UV/Visible Spectroscopy..... | 48 |
| 2.2.5 GC-MS..... | 50 |
| 2.2.6 Gas Chromatography..... | 51 |
| 2.2.7 CO ₂ Calibration..... | 52 |
| 2.3 Catalyst Characterisation | 52 |
| 2.3.1 X-Ray Photoelectron Spectroscopy, XPS..... | 53 |
| 2.3.2 Fourier Transformed Infrared Spectroscopy (FTIR)..... | 55 |

| | |
|---|-----------|
| 2.3.2.1 Attenuated Total Reflection | 56 |
| 2.3.2.2 Diffuse Reflectance Infrared Transform Spectroscopy (DRIFTS)..... | 57 |
| 2.3.3 X-Ray Diffraction | 58 |
| 2.3.5 UV Diffuse Reflectance Spectroscopy | 59 |
| 2.3.6 SEM - EDX..... | 59 |
| 2.3.7 Transmission electron microscopy | 61 |
| 2.4 Characterisation and Analytical Methodology | 63 |
| 2.5 References | 64 |

2.1 Introduction

This experimental chapter describes the procedures followed to obtain all of the data for these studies. Section 1 explains the photocatalyst preparation procedure for both the powder catalysts and the anodised nanotubes. The second section explains the equipment used for experimentation and the reaction methodology. Every reaction was performed in either the PCATDES open flask photoreactor or a 100 mL pyrex round bottom flask, using the PCATDES 365 nm LEDs. The final section describes the basis for the characterisation techniques employed to analyse the photocatalysts before and after use.

2.2 Catalyst Preparation, Methods and Equipment

2.2.1 Powdered Catalyst Preparation

2.2.1.1 Preparation of Modified P25 (mP25)

The primary method for preparing the powdered titania photocatalyst was incipient wetness. P25 was initially planned to be the basic titania photocatalyst employed, however testing found that it was problematic in UV flow cell in that its small particles were difficult to filter out and made UV measurements inaccurate. Additionally, it was found, through atomic emission spectra (AES), that complete removal of titania was cumbersome and so would result in damage to the GC-MS column. P25 was therefore treated by incipient wetness to reduce the mixtures opacity and improve ease of use. Bowker et al found that the optimum amount of water required to reach the incipient wetness point for P25 was 1.5 mL per 2 g of powder. [1] Based on their methodology titanium (IV) oxide (Aeroxide® P25, Sigma Aldrich) was mixed with deionised water, up to the aforementioned incipient wetness point, and ground into a paste. The paste was then dried at 200°C for 2 hours, calcined at 400°C for 3 hours and filtered through a 53µm sieve.

2.2.1.2 Pd/TiO₂ Preparation

Supported Pd on TiO₂ (P25) was produced using the PdCl₂ (99.999%, Sigma Aldrich) precursor. The appropriate amounts of PdCl₂ were added to deionised water with a drop of reagent grade concentrated HCl (37%, Sigma Aldrich) to assist solvation. The mixture was ultrasonicated to complete dissolution, and added dropwise to 2g of TiO₂ (P25). The mixture was then ground into a thick paste in a pestle and mortar and wrapped in foil ready for heat

treatment. The paste was dried at 200°C for 2 hours, calcined at 400°C for 3 hours and pressed through a 53 μm sieve. As an example, the quantity of PdCl_2 required for the preparation of 2g of 0.5 wt% Pd/TiO₂ would be calculated by:

$$\frac{2 \text{ g} \times 0.5 \text{ wt\%}}{100} = 0.0167 \text{ g PdCl}_2$$

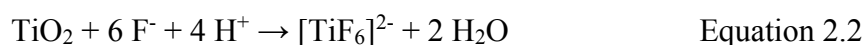
2.2.1.3 Au/TiO₂ Preparation

Supported Au on TiO₂ (P25) was made with exactly the same procedure as described above for Pd/TiO₂, where the gold source used was HAuCl₄ (99.999%, Sigma). The amount required to make 2g of 0.5wt% Au/TiO₂ is calculated as follows:

$$\frac{2 \text{ g} \times 0.5 \text{ wt\%}}{100} = 0.0173 \text{ g HAuCl}_4$$

2.2.2 TiO₂ Nanotubes Preparation

The titania nanotubes used in these studies were produced by an electrochemical technique called anodisation. In this section a brief background to the technique will be explained, however a more exhaustive discussion can be found in the introduction to **Chapter 4**. Anodisation is an electrochemical technique that uses an applied current to oxidise a metal surface. As should be evident from the name, the material of interest is used as the anode whilst the cathode is typically a metal like platinum. Application of a current in an electrolyte will induce oxidation of the top layers of the material, however it wasn't until 1999, when Zwillig *et al* electrochemically oxidised titanium in the presence of HF, that it was realised there was potential to form controlled porous layers in this manner. [2] Ensuing work found that fluoride actively formed a $[\text{TiF}_6]^{2-}$ complex as seen below:



After the initial oxidation to titanium F^- anions readily reacted to form this fluorinated complex, as seen in **equation 2**, that forms tubular structures by digging away at the titania surface. HF, and other highly acidic fluoride sources, were soon replaced by less chemically harsh alternatives like NaF, KF and NH_4F . [3][4][5][6][7] Another key aspect to this technique is the composition of the electrolyte. Early work showed strongly aqueous electrolytes resulted in rippled and defective tubes, so it was determined that organic electrolytes with a small percentage of water provided optimum conditions for nanotube growth. [8][9] Anodisation produces amorphous titania so an annealing step is also required gain crystalline titania nanotubes that are suitable for photocatalytic purposes.

2.2.2.1 Anodisation equipment

This equipment consisted of an electrochemical cell contained in a PTFE container, as seen in **Figure 2.2.1**. The design of the equipment was based on that used by Regonini who made it in conjunction with Bath University. [10] PTFE was the material of choice for the vessel due to its resistance to fluoride ions to prevent the slow dissolution of glassware that would result in sample contamination. Low pH's, especially from acids such as HF, would

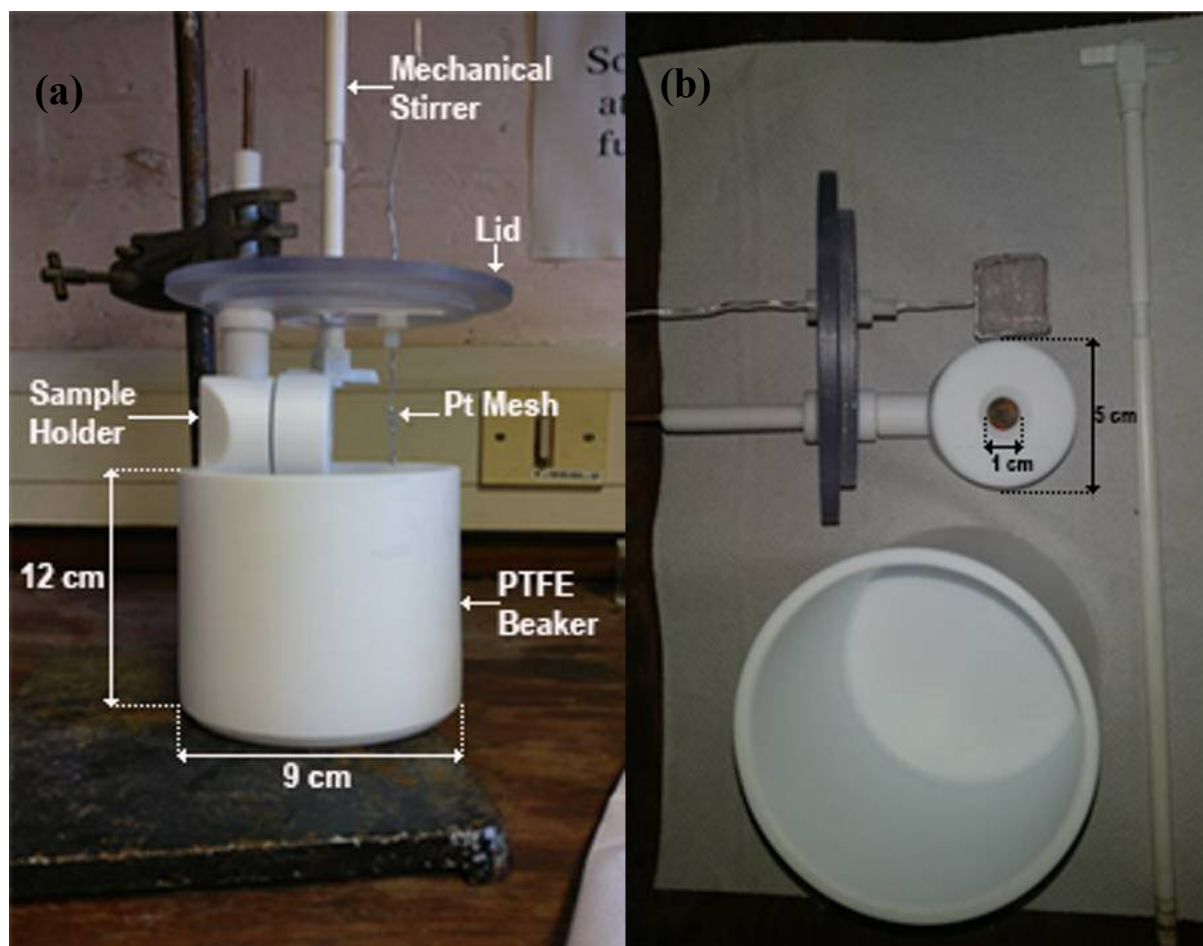


Figure 2.2.1: The electrochemical anodisation set up, (a) shows the front view and (b) shows the beaker, lid and electrodes separately.

also increase the rate of glassware dissolution. The electrochemical cell used a 5cm wide PTFE holder with a 1cm diameter opening to allow exposure of the substrate to the electrolyte. A copper rod and plate is contained within the holder to allow for the completion of the electrical circuit. This holder is where the titanium sheet is placed for anodisation, whilst the cathode is a platinum cathode mesh. Stirring is achieved using a mechanical stirrer that used a custom made PTFE stirrer rod. Voltage is applied using a Techtronics PWS4000 powersupply using crocodile clips and copper wiring.

2.2.2.2 TiO_2 Nanotubes

Titanium sheet (0.5mm, 99% purity, Sigma) was cut into 1.5 cm squares and ultrasonically cleaned sequentially in acetone, isopropyl alcohol and water for 5 minutes each. The sheets were dried under a stream of N_2 and placed into the PTFE holder. The PTFE holder was descended into an electrolyte of ethylene glycol (392 ml), ammonium fluoride (1.33g, 39.95 mmol) and deionised water (8 ml), and a mechanical stirrer is employed to thoroughly mix the solution throughout the reaction. After 5 minutes of stirring a potentiostatic voltage of 60V is applied and the reaction is left to run for 1, 4, 8 or 24 hours. After the allotted time the titanium sheet is removed and rinsed using deionised water before being ultrasonicated in deionised water for 30 seconds and dried under a N_2 stream. Samples were then dried at 80°C overnight and calcined in air at 450°C for 1 hour.

2.2.2.3 WO_3/TiO_2 Nanotubes

To incorporate tungsten into the nanotubes, it was decided that the tungsten precursor should be added into the electrolyte rather than doping post-anodisation. The electrolyte consisted of ethylene glycol (392 mL), ammonium fluoride (1.33g, 35.9 mM), water (8 mL) and sodium tungstate (0.1979 g, 0.6 mM). Titanium sheets were pre-cleaned in the same manner as stated above and anodised for 4 and 8 hours. The electrolyte was reused up to 8 times without additional electrolytes being added.

2.2.2.4 Metal Loaded TiO_2 Nanotubes

Titania nanotubes were doped with gold and palladium after calcination using photodeposition. 5 mmol solutions were prepared for each metal and pipetted (5 mL) into vials. The nanotubes were placed in the vials and vertically irradiated by 365nm LED lights for varying lengths of time (1, 3, 30 and 60 minutes) before being rinsed under DI water and dried in a furnace overnight at 100°C. The samples were then used with no further treatment.

2.2.3 Photocatalytic Reactor Experimental Set Up

2.2.3.1 Reactor vessels

The photoreactor vessel used for all of the experiments in **chapters 3 and 5**, except for the CO₂ capture experiments, was the PCATDES open pyrex vessel seen in **Figure 2.2 (c)**. The reactor vessel has a 250mL capacity and is equipped with a cooling jacket that utilised tap water for cooling. The glass reactor is covered by a purpose fitted black plastic covering with openings designed for several purposes including sample taking, temperature control and gas flow. The LEDs are fitted to the top of the black covering providing top down irradiation unhindered by the PCATDES glassware. The reactor sits on top of a stirrer plate and so stirring is achieved using with a magnetic stirrer. Liquid aliquots are taken with glass pipettes and filtered into sample vials from which they are added to GC-MS sample vials or diluted for UV absorption measurements.

Liquid Phase Experiment procedure

The reactions were all performed at ambient temperatures, which with water cooling averaged at 15°C. All trans-cinnamic acid ($\geq 99\%$, Sigma), or cinnamyl alcohol (98%, Sigma), solutions are prepared beforehand and stirred for 3 hours to ensure complete



Figure 2.2.2: The photoreactor set up. (a) shows the plastic cover, the cooling tubes attached to the LEDs and the control box to the back-right. (b) the 36 LED board, (c) the glass reactor flask showing the entry and exit points for the cooling jacket.

solvation. For the studies pertaining to the effect of inorganic salts the reaction mixture consisted of; deionised water (250 mL), cinnamic acid (12.5 mg), 0.1 g of photocatalyst (TiO_2) and the inorganic salt at the desired concentration (0.05M, 0.1M, 0.5M etc). The salts used were: K_2SO_4 (99.99%, Sigma), Na_2SO_4 ($\geq 99.99\%$, Sigma), KCl (99.999%, Sigma) and NaCl (99.999%, Sigma). The salt was added to the substrate solution and stirred thoroughly before the initial “-30 minutes” sample is taken. The photocatalyst is then added and the reaction mixture is left to stir for 30 minutes in the dark to ensure thorough mixing and reduce mass transfer limitations. Next the LEDs are activated and samples are taken at: 0, 5, 10, 15, 20, 30, 45, 60, 120 and 180 minutes. Samples were taken with glass pipettes, taking a volume of roughly 1.5mL, and filtered before analysis. Cinnamic acid concentration was measured using a Lambda XLS UV spectrometer, whilst the determination of all intermediates was done using a Waters GCT premier TOF-MS system. After the reaction the spent photocatalyst was retrieved by decanting off the solution and drying over night at 80°C . All open flask reactions that included N_2 flow was done so flowing 1 bar N_2 gas continuously, beginning at -30 minutes.

CO_2 capture experiments, in **chapters 3** and **5**, used a 100mL, single necked, pyrex, round-bottom flask sealed with a rubber suba seal. As it was not possible to use the water cooling mechanism included in the PCATDES vessel the 100 mL flask sat in a beaker of tap water that was periodically changed to prevent the solution being heated up by the powerful LEDs. The flask itself sat in a non-upright fashion so the suba seal and neck did not obscure the LED irradiation. Stirring was achieved with a magnetic stirrer. Reactions were performed under ambient air or a N_2 atmosphere, for the latter N_2 gas was flowed during the 30 minute dark period and sealed from “zero” minutes onwards. Gas samples were removed with a gas syringe and analysed in a Perkin Elmer Clarus 480 gas chromatograph.

The liquid phase nanotube experiments were also done in the same single neck, 100 mL round-bottom flask, however the flask was not sealed. Samples were held in a custom made copper wire cage that held the sheet horizontal to the LEDs in the solution and allowed magnetic stirring to take place unhindered. Liquid aliquots were taken and diluted for analysis in a Lambda XLS UV absorption spectrometer.

Surface Degradation Experiment Procedure

These procedures relate to experiments discussed in **Chapter 4**. Nanotube samples were coated with cinnamic acid or stearic acid in chloroform (0.1M, 50 μ L) in a drop wise fashion to ensure the complete coating of the nanotube area. Each sample was left to dry overnight, in the dark, before use. The samples were irradiated under the LEDs, at a distance of approximately 8 cm, and removed to be analysed offline using a DRIFTs FTIR spectrometer.

2.2.3.2 Light Source

The light source utilised in all the experiments is a custom built 32 LED system produced by our partners in Bath University, shown in **Figure 2.2(b)**. The LED board contains 36 3Watt LEDs that are separated into 12 groups where the 3 LEDs are wired in series. At full power each LED produces 112 mW of light in the direction of the sample which equates to 1.9 kW/m² of 365nm (+/-2nm) light at a distance of 0.1M. [11] The PCATDES standard settings set all of the LEDs to 80% of their total power, except for the centre 4 which were set to 20% of the total power to ensure uniform irradiation. The LEDs themselves were housed at the top of the black casing to provide vertical irradiation. Inefficiencies in the LEDs has the consequence that 70% of the energy input being emitted as heat, resulting in the strong requirement for adequate cooling. This system used a Koolance EX2-755 water cooling system, with non-conducting coolant, that was connected via a heat sink to the back of the insulated metal substrate (IMS) LED board. Silica thermal paste was applied in between the LED board and the heat sink for enhanced heat transfer. The LEDs were controlled using a control box provided by Bath University that allowed for temperature and output monitoring. The wavelength of the LEDs were set to 365nm +/- 2nm. This wavelength was chosen as it is the lowest energy photon that can induce the formation of a high density of electrons and holes in pure TiO₂. [12]

2.2.4 UV/Visible Spectroscopy

Ultraviolet-visible spectroscopy is an analytical technique that utilises radiation from 200 to 800 nm and can be referred to as electronic spectroscopy due to its relation to electron excitement. UV irradiation induces an electron to jump from energy level to the next, usually from the highest occupied molecular orbital (HOMO) to the lowest unoccupied molecular orbital (LUMO). Photons in the UV and visible section of the electromagnetic spectrum has energy ranging from 151 to 598 kJ/mol which is enough to excite electrons from a π or non-

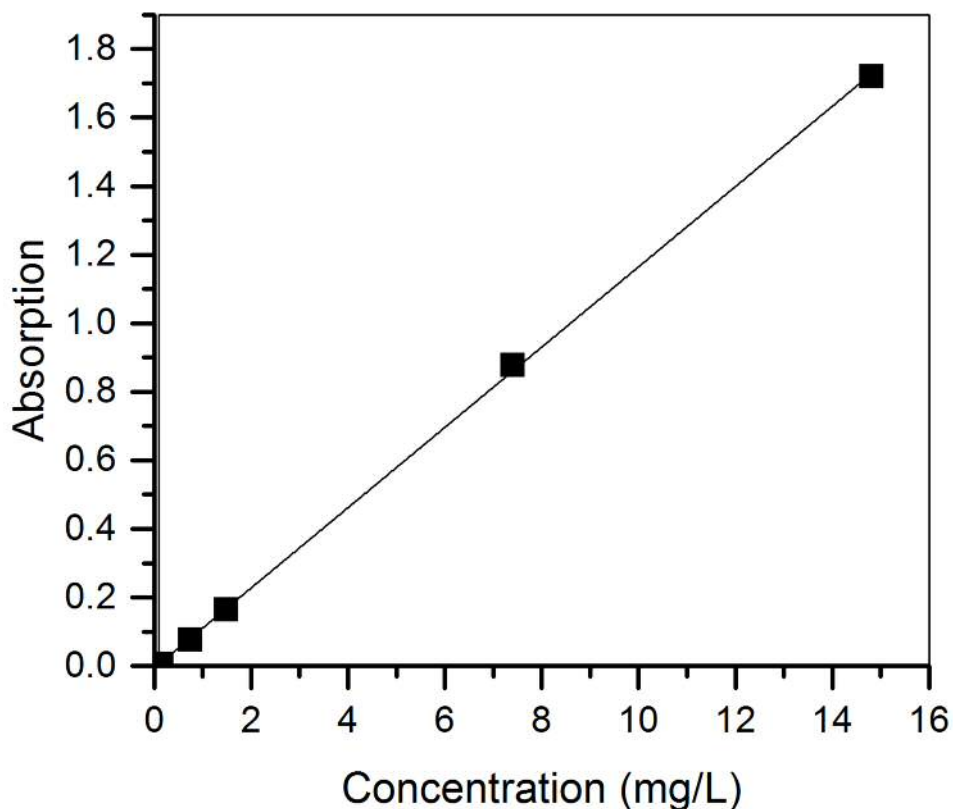


Figure 2.3: Cinnamic acid UV calibration plot

bonding orbital to a π^* anti-bonding orbital. Molecules with double bonds and conjugated π systems will absorb energy within the UV/Vis section of the electromagnetic spectrum, which is the property detected as a UV/Vis spectrophotometer cycles through the wavelengths. UV absorption values can be transformed into real concentrations using the Beer-Lambert law:

$$\text{Equation 2.3}$$

Where A is absorption, I_0 is the incident light intensity, I is the transmitted light, ϵ is extinction coefficient, c is concentration and l is the lights path length. The calibration plot used for all cinnamic acid calculations can be seen in **Figure 2.3**. Cinnamic acid shows a strong absorbance at 272nm which resulted in a saturated signal at any concentration above 15ppm (1.01×10^{-4} moles/L). As such all solutions were diluted by a factor of ten to compensate for this and means the calibration below is suitable. The extinction coefficient is

a function of the strength of absorption of the molecular functionalities. Cinnamic acid, for example, has an aromatic ring conjugated to a double bond and carboxylic acid moiety that strongly absorb UV light.

A Lambda XLS table top UV/Vis spectrophotometer was used for all liquid state UV analysis.

2.2.5 GC-MS

Offline gas chromatography with incorporated mass spectrometry was the main tool used to follow and characterise the intermediates formed and ascertain degradation mechanisms. GC-MS is very commonly used for identification in many fields, such as explosive detection and forensics, due to its accurate and positive identification of specific molecules. Gas chromatography involves the vapourisation of liquid samples, or injection of gaseous samples, that are passed through a column that behaves as the stationary phase and interacts with the analytes. The analytes will have differing affinities for the column, based on the type of column used, that results in them eluting off of the column at different retention times. The eluents are then able to pass through the mass spectrometer separately for analysis. Several types of mass spectrometers are commonly used for endline analysis with gas chromatographs including electron ionisation (EI) and chemical ionisation, however the type found on the system used here was an electron ioniser (EI) with an orthogonal acceleration time of flight (oa-TOF) mass spectrometer. The first step in the process involves the parent molecule entering the ionisation chamber. The ion source bombards the sample with high energy electrons, in a low pressure environment, that causes the sample to lose electrons and fragment. Fragmentation requires higher energies to occur, than loss of electrons, although it is still very common. The charged and fragmented species then leaves the ionisation chamber and enters the TOF analyser, at an angle orthogonal to the magnetic field to improve separation of charges. A magnetic field of a known strength accelerates the molecules, the speed at which the eluent is accelerated depends on both its size and charge where higher charges and light masses result in an increased velocity. Charged species then hit the detector and are logged based on their mass to charge ratio.

A GCT premier gas chromatograph with an oa-TOF (time of flight) mass spectrometer was used for all GC-MS analysis. The system was fitted with an Agilent autosampler and a 30 cm DB-35, (35% phenyl)-methylpolysiloxane, column. This is a mid-polarity column generally suited for terpene analysis. For all samples the injection volume was 10 μ L, except for

calibration solutions where 1 μL was injected. The system is extremely sensitive and was capable of detecting concentrations in the nanogram regime. The GC-MS conditions were as follows:

Carrier gas: Argon

Flow rate: 1 mL/min

Run time: 40 minutes

Initial injector temp: 60°C

Final injector temp: 300°C (9°C/min ramp rate)

Column temp: 80°C

2.2.6 Gas Chromatography

Gas chromatography was utilised to analyse the evolution of CO_2 during reactions. The gas chromatograph used here runs on the same principles as those described above for the GC-MS in 2.2.3. Gaseous samples are injected into the injection port and passed through the column with a helium carrier gas where the column separates the analytes based on the level of interaction with the column. The system here differs from the one in 2.2.3 due to the different detector. A thermal conductivity detector (TCD) was used to detect and quantify the products being released. This detector measures changes in thermal conductivity, in comparison to the carrier gas, where the larger the difference in thermal conductivity the larger the response to each molecule. Helium, as shown in **Table 2.2.1**, has a thermal conductivity around ten times larger than many common products analysed this way, including CO_2 that has a thermal conductivity of 0.017 W/mK. As such, products of known thermal conductivity can be quantified through ratiometric analysis of the peak heights allowing for analysis without calibration.

2.2.7 CO₂ Calibration

A CO₂ calibration was performed to quantify the amount of CO₂ being evolved during the photocatalysed reaction. High purity CO₂ (99.9% purity, BOC gasses) was injected in known volumes of 0.05 mL to 0.25 mL. The peak area were plotted against volume of CO₂ and linearly fitted where the slope was used to give the conversion factor for CO₂ concentration. Using the conversion factor and injection volume it is possible to calculate the volume of CO₂ present in the reactor as follows:

————— **Equations 2.3 and 2.4**

2.3 Catalyst Characterisation

Photocatalysts prepared in these studies were characterised using a number of different techniques including XPS, ATR-FTIR, XRD, AFM, solid state UV spectroscopy, SEM and TEM. This section will explain the theoretical fundamentals behind each technique, the details of the equipment used and the experimental procedures used.

| Gas | Thermal Conductivity at 300°C (W/mK) |
|-----------------|---|
| Air | 0.024 |
| Ar | 0.016 |
| CO | 0.0232 |
| CO ₂ | 0.0146 |
| H | 0.168 |
| He | 0.142 |
| N ₂ | 0.024 |
| Ne | 0.046 |
| O ₂ | 0.024 |

Table 2.2.1: Thermal conductivity values for a series of gases [13]

2.3.1 X-Ray Photoelectron Spectroscopy, XPS

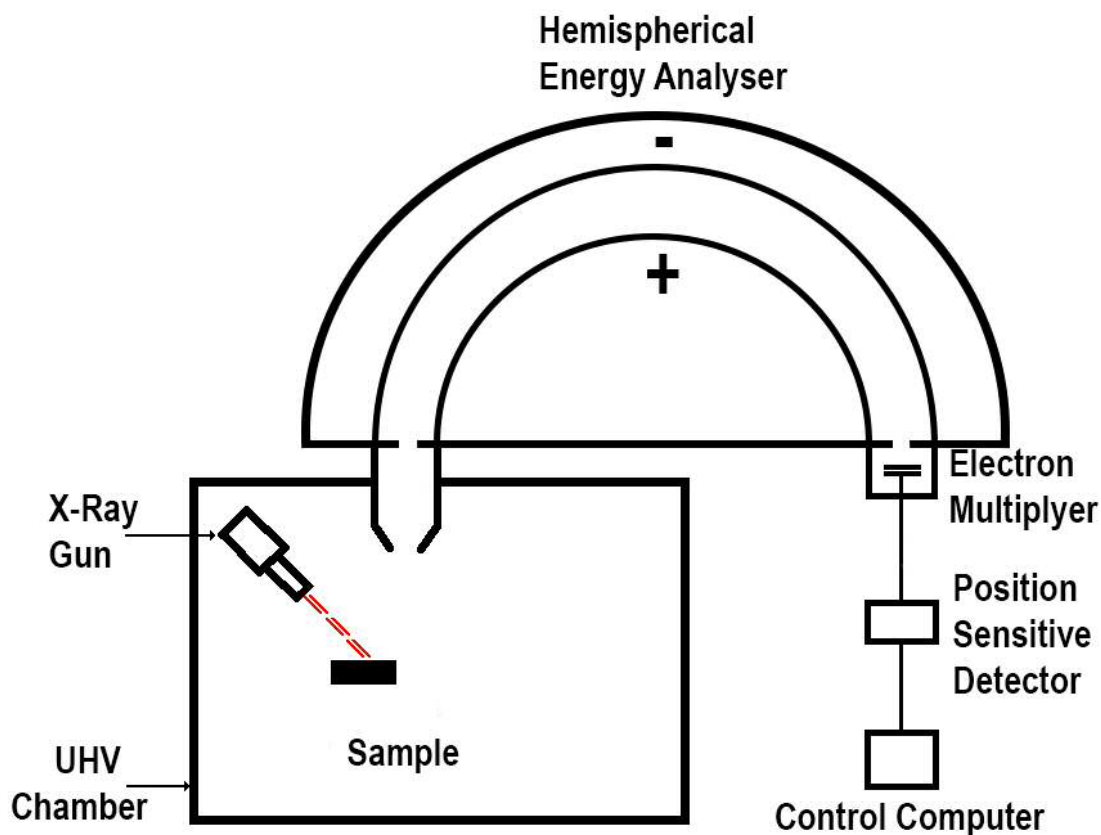


Figure 2.3.2: The layout of an x-ray photoelectron spectrometer

X-ray photoelectron spectroscopy (XPS) is a well-established and widely used analysis technique that allows for surface oriented elemental determination. Fundamentally XPS is based on the photoelectric effect as proposed by Einstein in 1905. When a sample is bombarded with electrons, core shell electrons are ejected from the sample with kinetic energies of E_{kin} as seen in **Figure 2.3.1**. The kinetic energy of the ejected electrons (E_{kin}) will be equal to the sum of the incident x-ray energy ($h\nu$) minus the electrons binding energy (E_b), as depicted in **Equation 2.5**. However, an instrument specific work function (ϕ_{sp}) must also be factored in to describe the energy required to move an electron into a vacuum from its fermi level where $E_{kin} = 0$. This work function is often obtained from instrument calibrations and results in **equation 2.6** that gives the kinetic energy as measured by the analyser for a specific instrument.

Equation 2.5

Equation 2.6

Where:

E_{kin} = Kinetic energy of the emitted electron

E_{bind} = Binding energy of the atomic orbital that the electron

$h\nu$ = Energy of the incident photon

ϕ_{sp} = Instrument work function

Every atomic element has a different number of protons in its nucleus and electrons in its orbitals that leads to differences in the energy by which the electrons are bound. Generally, the greater the number of protons the more positive charge there is and the more tightly bound the atoms' electrons are which causes greater binding energies; and conversely the greater the number of electrons the more negative charge there is for the nucleus to attract which results in a decreased binding energy. This principle means that changes in chemical environment and oxidation will induce small changes in binding energy that allows for the identification of a wide range of compounds. Each atom has a known relative sensitivity factor (RSF) that allows the user to calculate percentage concentrations of species and elements on a sample. As the ejected electrons leave an atom there is also the possibility, in a

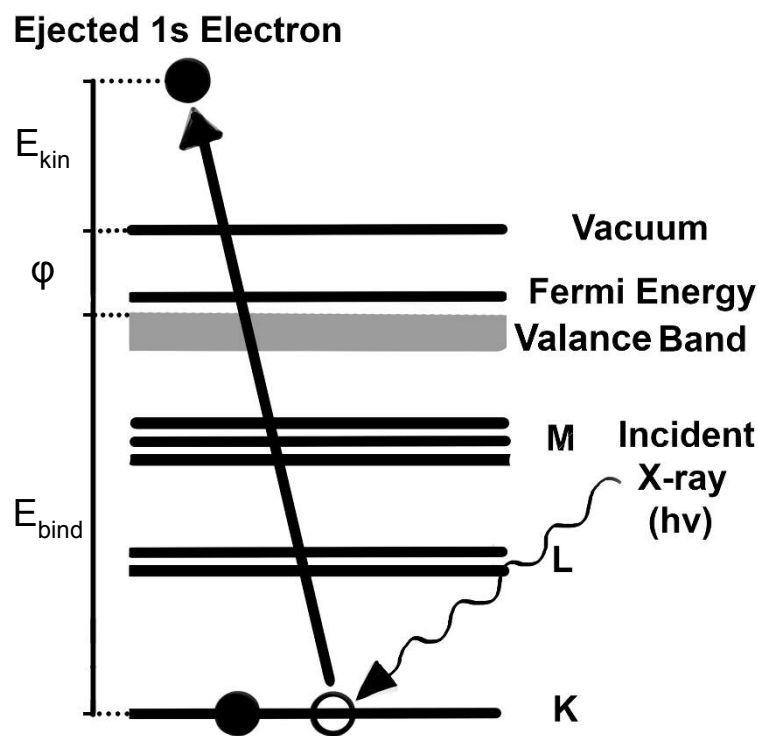


Figure 2.3.1: The energy of the ejected electron (E_{kin}) is a function of the energy of the incident x-ray ($h\nu$) minus the binding energy (E_{bind}) and instrument work function (ϕ)

secondary electron process, for an outer shell electron to fill the hole left in the inner shell and release energy. This is known as the Auger effect and results in an off shoot of XPS known as Auger electron spectroscopy (AES). Auger peaks can be useful for analysis but can also be a hindrance; titanium Auger peaks overlap with the sodium 1s region that causes a large overestimation of the presence of sodium that is problematic to compensate for. The produced photoelectrons can only escape from, at the most, depths of 5 nm due to the kinetic energies involved and this means XPS is essentially a surface based technique. The electrons can potentially be caught in the sample while escaping by various routes including: inelastic collisions, trapping of the electron in an excited state, and recombination of the electron with the hole (h^+).

The basic set up of an x-ray photoelectron spectrometer can be seen in **Figure 2.3.2**. The system is enclosed in an ultrahigh vacuum (UHV), of vacuums between 10^6 to 10^{10} millibars, stainless steel chamber to prevent the resultant electrons interacting with atmospheric molecules that could contaminate the samples and reduce the mean free path of the electrons. High energy electrons bombard a metal anode, typically aluminium or magnesium, resulting in the production of non-monochromatic x-rays. These x-rays then collide with a quartz crystal at an angle of θ and are diffracted according to the Bragg law (**Equation 2.8**). Knowing what wavelength is desired, in this case wavelengths with an energy of 1253.6 eV (Mg) and 1486.6 eV (Al), means the incoming x-rays can be angled so the diffracted x-rays are monochromated to the required wavelength. The x-rays bombard the sample and ejected electrons pass through a channeltron that channels and multiplies the electrons to produce a detectable signal. These electrons then pass through the hemispherical analyser before hitting the detector and is translated into an XP spectra. [14]

Two XPS machines were used for these studies. The first was a Kratos Axis Ultra-DLD XPS system with a monochromated Al $K\alpha$ source. The second machine, and the source of most of the data, was a Thermo Scientific K-Alpha⁺ XP system. An Al $K\alpha$ source is also utilised in the system. CasaXPS was used to analyse and interpret all ensuing data.

2.3.2 Fourier Transformed Infrared Spectroscopy (FTIR)

Infrared spectroscopy is an analysis technique that harnesses the infrared portion of the electromagnetic spectrum, typically 400 to 4000 cm^{-1} , to determine the presence of a variety of bonds and functionalities through absorption of, radiation. Electromagnetic

radiation, in the infrared section of the spectrum, interacts with the resonant energy levels related to the stretching and bending of molecular bonds. The elements involved, and the type of, bond influence the energy of the infrared absorption and can be described by Hooke's law:

$$F = kx \quad \text{Equation 2.7}$$

where F is force, x is displacement, k = force constant, and m is mass

Hooke's law means that the larger the difference in mass between two bonded atoms, the lower the frequency will be. As an example, C-H bonds resonate at 3000 cm^{-1} while C-C resonates at 1000 cm^{-1} . The number of vibrational modes is given by the number of degrees of freedom where a linear molecule has $3N - 5$ degrees of freedom and a non-linear molecule has $3N - 6$ degrees of freedom.

2.3.2.1 Attenuated Total Reflection

ATR FTIR is the combination of the spectroscopic technique or infrared and the sampling method of attenuated total reflectance. ATR removes the issues related to sample thickness that occurs in traditional FTIR and therefore negates the need for careful sample preparation. ATR uses a crystal, in close proximity to the sample surface, which reflects the IR radiation onto the surface before it reaches the detector. **Figure 2.6** shows the setup of a multiple reflection cell, although the number of reflections can be altered and can be as few as one if desired. Materials have a property called total internal reflection that is exploited when the propagated electromagnetic wave hits the sample surface at an angle greater than the critical angle. The IR wave is totally reflected, if the incident wave hits above the critical angle, and produces an evanescent wave that penetrates a few microns into the sample surface. An evanescent wave is a non-propagating electromagnetic wave, whose energy is dependent on the incident wave's wavelength, and can be thought of as analogous to a quantum tunnel. The evanescent wave will be changed by the presence of infrared absorbing molecules in the sample which is the detected change when the wave reaches the detector. As these waves only penetrate a short distance into the surface, up to $5 \mu\text{m}$, the issues with highly absorbing media, like water, flooding the signal is negated. [15][16]

2.3.2.2 Diffuse Reflectance Infrared Transform Spectroscopy (DRIFTS)

DRIFTS is another adaption to standard FTIR that is commonly used due to the ease of sample preparation and the possibility for in-situ measurements. The system utilises a series of mirrors that direct the infrared radiation at the sample surface and subsequently directs the reflected photons towards the detector. There are three classes of reflected radiation that occur from this irradiation, the first two of which are classed under Fresnel Reflection. Fresnel Reflection is the direct reflection of the incident photons and contains zero information about the sample; the first being the photons that are reflected at an angle equal to the incident beam, and the second is caused by the beam reflecting off of sample grains of differing orientations that results in reflection at a different angle to the macroscopic sample. The third class was named Kubelka-Munk Reflectance. This is the reflection of radiation that has transmitted through a minimum of one particle and has been altered by interaction with infrared active molecules in the sample. Due to the set-up of the technique it allows in-situ cells to be harnessed and facilitates online infrared analysis. Additionally samples need not be diluted or prepared into pellets and so DRIFTS offers non-destructive sample preparation. However, as was eluded to earlier, there is a large reliance on surface reflectivity that results in the measured spectra being dependent on particle size that leads to issues of reproducibility, as noted by Fuller *et al.* [17][18]

The FTIR-ATR used in all the studies was a Perkin Elmer Frontier FT-IR spectrometer with a Universal ATR – 1 Reflection Diamond Top Plate attachment. The

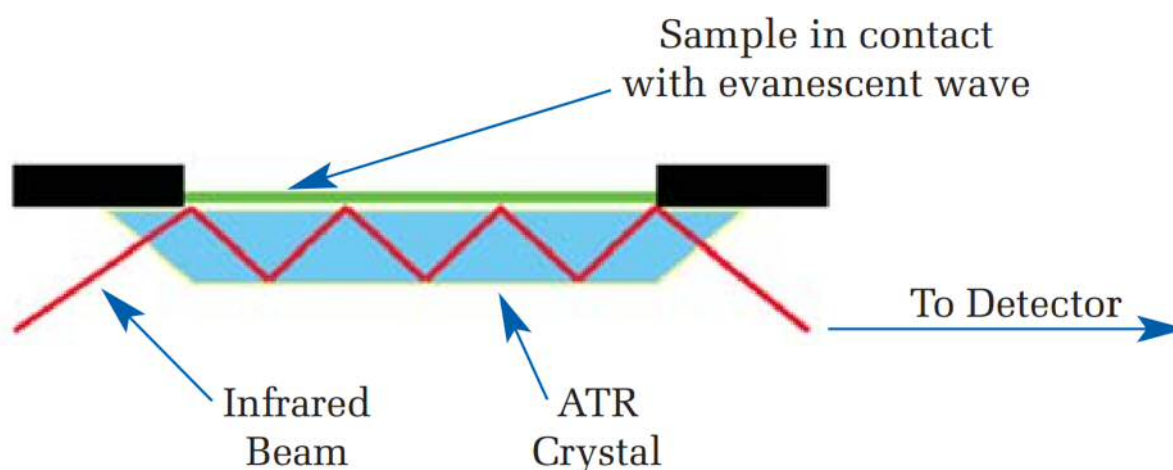


Figure 2.3.3: Diagram of a multiple reflection IR system found in the ATR component [16]

crystal was a dual composition crystal that employs diamond for the internal reflections

whilst using zinc selenide for focusing element. Both crystals offer the same refractive index of 2.4, and penetration depth of 1.66 μm . The combined use of both crystals utilises the chemical resistance of diamond while using the cheaper ZnSe to focus the infrared beam. [16]

2.3.3 X-Ray Diffraction

X-ray diffraction is an important technique for determining the bulk crystal structure of a material and ascertaining what phases are present. Max Von Laue was the first to discover the diffraction of x-rays by crystals and awarded with the Nobel prize in physics in 1914. The following year, 1915, William Henry Bragg and his son William Lawrence Bragg were awarded the Nobel prize for their developments in the crystallographic determination by x-rays. Their work illustrated some of the key concepts and practices behind x-ray crystallography. X-rays are produced in an x-ray tube, a device that converts electrical power into x-rays, and emitted as the required monochromatic x-ray through control of the applied voltage and use of aluminium filters. X-ray tubes are the most convenient lab based x-ray sources although they are very inefficient with only 1% of applied voltage being converted into x-rays, the rest being released as heat. The monochromatic rays that hit the surface are of sufficiently small wavelength that target material acts as a grating that results in the x-rays being diffracted at various angles that are instructive of the present crystal structures. The sample is spun providing a statistical average of the present phases, therefore allowing for the percentage calculation of said phases. The elastically scattered x-rays can interact and cancel out through destructive interference, or if the incident angle satisfies the Bragg equation (**Equation 2.8**) it will form constructive interference that hits a flat detector. This detector measures the counts, or the number of times an x-ray impacts at that angle, which are plotted against degrees of scattering (2θ). Peaks can then be assigned to a materials phase by comparison with empirically determined reference patterns where each peak represents a phase that is labelled according to the associated h,k,l miller indices. [19]

XRD data was obtained using a Panalytical X'Pert Diffractometer.

Equation 2.8

2.3.5 UV Diffuse Reflectance Spectroscopy

UV diffuse reflectance spectroscopy (UV-DRS) operates on the same theoretical principles as the liquid state UV/Vis spectroscopy described in 2.3.3. The UV spectrometer utilises the principle of diffuse reflectance, thus irradiating the sample surface and measuring the decrease in detected light after being reflected off of the surface. Light intensity will decrease if the material is capable of absorbing light in the UV region, due to the excitation of electrons from highest occupied molecular orbital (valence band) to the lowest unoccupied molecular orbital (conduction band). In materials like semiconductors, this absorbance is a measure of the band gap (E_g).

To calculate the bandgap the data can be fitted using an expression derived by Tauc, Grigorivici and Vanacu. [27] They showed that the bandgap and photon energy related to the optical absorption strength via **Equation 2.9**:

$$(\alpha h\nu)^{1/n} = A(h\nu - E_g) \quad \text{Equation 2.9}$$

Where; h = Planck's constant, ν = photon frequency, α = absorption coefficient, E_g = bandgap, A = proportionality constant. The value of the exponent is dependent on if the bandgap transition is; a direct allowed transition ($n = 1/2$), a direct forbidden transition ($n = 3/2$), an indirect allowed transition ($n = 2$), or an indirect forbidden transition ($n = 3$). Plotting $(\alpha h\nu)^2$ versus $(h\nu)$ will give a Tauc Plot where extrapolating from the linear region to the x-axis will give the band gap in eV. [27][28][29]

UV measurements were obtained using an Agilent Cary 4000 UV-Vis-NIR spectrophotometer. Powder samples were analysed in the provided sample holder, similar to that used for DRIFTS, whilst nanotube samples were rested on top of the sample holder.

2.3.6 SEM - EDX

Scanning electron microscopy (SEM) is a surface characterisation technique that utilises electrons to image surfaces. While it is possible for SEM to be run at low pressures, and in wet conditions, it is largely performed in high vacuums to eliminate the interaction of gaseous molecules with the incident electron beam and subsequent species. An electron beam is emitted by an electron gun, typically containing a tungsten filament, and focused by a

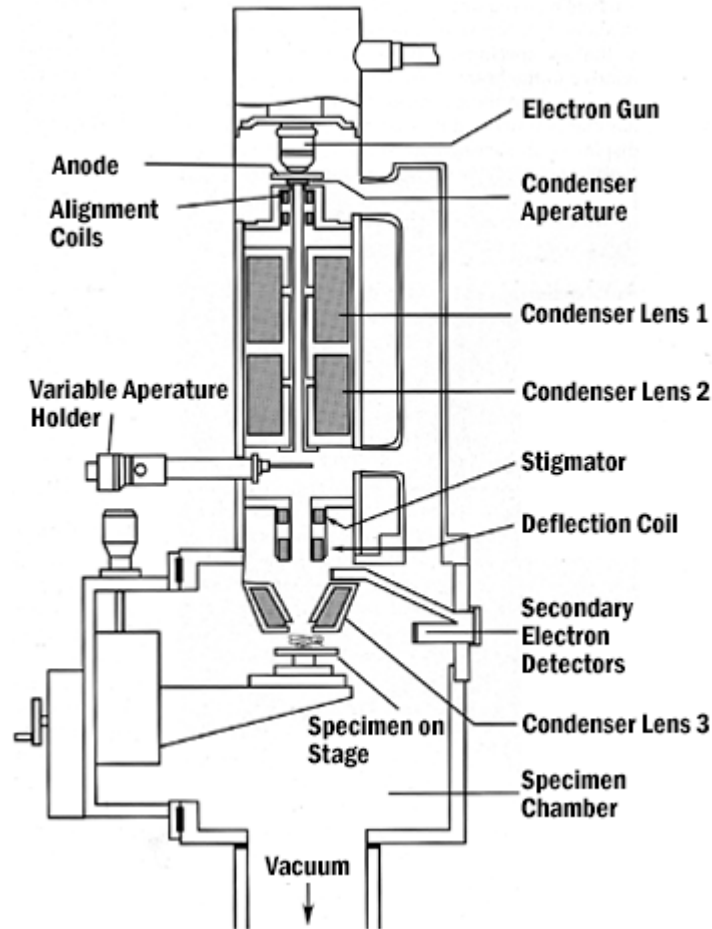


Figure 2.3.4: Schematic showing the layout and components of a scanning electron microscope [25]

series of lenses and apertures before being raster-scanned across the sample surface, as shown in **Figure 2.3.6**. Besides the tungsten filament based electron gun, there is also the field emission electron source which is a “cold” electron source and allows for increased magnification. This source is superior but carries a noticeably larger price tag. The lenses, found inside the short optical column, are magnetic coils that condense the electron beam as it passes through. The focal length of the lenses, or the strength, can be adjusted by altering the voltage passing through the coil. The apertures are metal sheets with holes used for beam refinement. Condenser lens 3, as seen in **Figure 2.3.6**, is the most important of the lenses. It is responsible for controlling the beam so it can raster-scan across the surface and be magnified. Once the electrons have passed the final lens, the incident electrons penetrate the surface and scatter randomly, in a tear drop shape, that extends from depths of 0.1 to 5 μm depending on the electron’s energy and the nature of the sample. Electrons will be of sufficient energy allowing them to induce several processes. Firstly, the electrons can be directly reflected in an inelastic scattering process, that is called back scattering, and

produces highly energetic electrons of essentially the same energy as the incident beam. The heavier the target bombarded element the more likely that backscattering will occur which results in images that effectively display the difference in atomic mass. Capturing these electrons, with a backscatter detector, can be useful for mapping heavy transition metals like platinum on a much lighter support. Secondly there is the emission of secondary electrons (SE), in-elastically scattered electrons of significantly lower energies than the incident electrons. The lower energy of the emitted electrons carries the implication that the only electrons to escape from the sample will be from areas close to the surface, consequently secondary electrons produce highly surface based images very useful for topographical analysis. These are the primary electrons used for surface imaging in typical SEM. Thirdly, electrons can induce the emission of x-rays that, when captured, are highly indicative of the parent atoms electronic structure in a similar manner to XPS. High energy electrons displace core-shell electrons that is filled by an electron from an outer shell. The relaxation of the outer shell electron emits x-rays of characteristic energies, depending on the atom, that allows for elemental analysis. Resolutions of between 1 - 20 nm are possible, with some newer microscopes reaching 0.4nm, [23] using the secondary electron detectors. [24][25]

Powdered samples were mounted on aluminium stubs using carbon tape and checked to ensure no loose photocatalyst was present that could disperse into the SEM chamber. Anodised nanotube samples that were still attached to the titanium sheet were mounted in the same manner, however detached nanotube samples were gently broken up and dispersed on the carbon tape to allow for the top, bottom and intersection to be imaged. Two SEMs were used for these studies: the first was a Hitachi S-4300 LV accompanied with an Oxford Instruments EDX; the second was a Hitachi TM3030 Plus also equipped with an Oxford Instruments EDX. FE-SEM analysis was performed on a Tescan Maia 3 FEG-SEM.

2.3.7 Transmission electron microscopy

Transmission electron microscopy (TEM) is another electron based microscopy that operates on similar fundamentals with a few key differences. A high vacuum is required to prevent the disruption of the beam by gaseous and organic molecules. The electron beam is produced by a tungsten electron gun, as it commonly is in SEM, but is operated at higher currents as the imaging comes from electrons that are transmitted through a sample, rather than reflected or emitted. **Figure 2.3.7** depicts the rough set up of a transmission electron microscope. The electron beam passes through a series of electromagnetic condenser lenses and metal

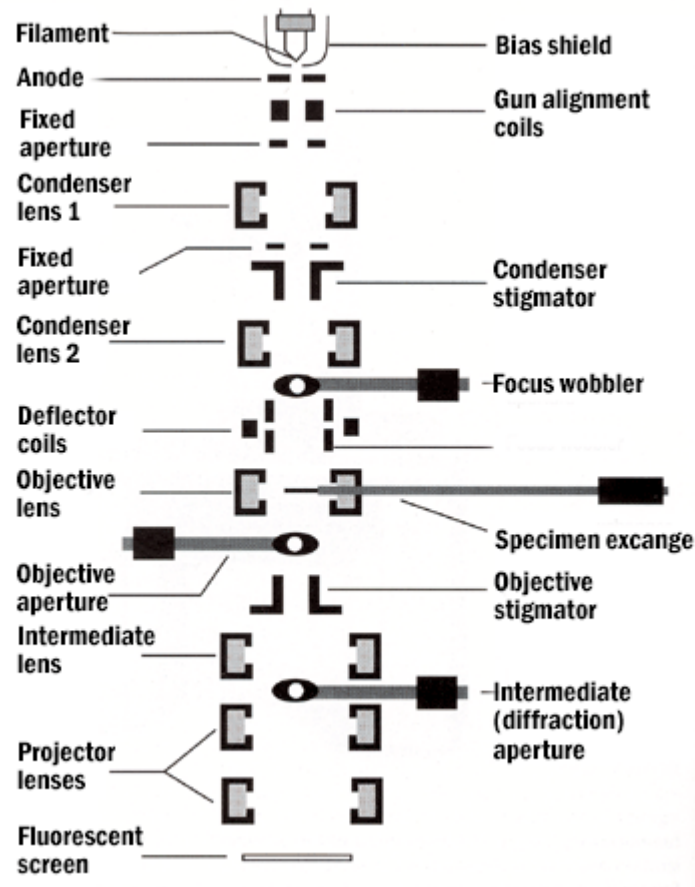


Figure 2.3.5: Schematic showing the main components of a transmission electron microscope

[25]

apertures that are used to focus the beam to a very small size, after which the objective lens focuses the beam and allows for initial magnification. A key difference between SEM and TEM is seen here. A sample stage is inserted directly into the objective lens, after which the electron beam continues through another series of lenses and apertures that enhance the contrast and magnify the image. A stigmator is used to correct a stigmatism, or an irregularity in the beam caused by an uneven lens magnetic field. Final magnification occurs through the projector lens that projects it onto a phosphorescent screen. This screen reacts to the electron beam by phosphorescing and producing a user-friendly display to examine the sample before engaging the camera. Even though the electron beam is more energetic than in SEM, the sample thickness is usually limited to 250nm to allow the electrons to effectively transmit through. As such, sample preparation is key to ensuring thorough dispersion of sample across the carbon grid. Magnification is sufficient that atomic resolution is possible, the most easily

obtainable use of this is to measure atomic spacing that allows for the identification of crystal phases in a sample. [25][26]

All TEM data was acquired using a Joel-2100 LaB6 transmission electron microscope. For powder samples, a few micrograms of the powder were placed in methanol (1 mL) and dispersed by ultrasonication for 2 minutes. The mixture was left to settle for a minute before two drops were placed on the TEM sample grid. The grid was left to dry overnight before use.

2.4 Characterisation and Analytical Methodology

UV/Vis spectroscopy was the primary method used to detect cinnamic acid, the key substrate, due to its very strong absorbance at 272 nm and because analysis with GC-MS found it was not easily detected due to column present in the equipment. The high molar absorption, in comparison to all other expected intermediates, enables UV/Vis to be an effective method in analysing the concentration change of just cinnamic acid. GC-MS was the key analytical method used to examine the formation and destruction of intermediates in the reaction. The high sensitivity, combined with the informative mass spectra, meant that it was very well suited to examine many of the key intermediates. However, the column was not suited to many acids and short chained aliphatic compounds tended to burn off at the beginning of runs. This resulted in difficulties analysing further degradation products which could have been remedied with HPLC analysis. Unfortunately access to HPLC equipment was limited and so it was not possible to incorporate it into the methodology. Lastly, GC-TCD was used to measure CO₂ evolution and ascertain if full mineralisation was occurring.

The characterisation techniques utilised in these studies were chosen for a number of reasons. XPS was the primary route for elemental analysis, supplemented by EDX studies, to provide important information about the chemical makeup of the materials. The most important uses for these studies were the assessment of the chemical states of deposited metals and the analysis of the deposited carbon layer. Functionality of the carbon is not easily obtainable from such elemental techniques, however, so FTIR is widely applied to detect the active surface species present on the surface of the materials. FTIR was important for trying to identify the deposited carbon species that were beyond the detection capabilities of the GCMS. These two techniques were key in supplementing the data from the GCMS and relaying insight into the mechanistic processes. The other techniques were used for strictly material characterising purposes. UV diffuse reflectance spectroscopy gave the bandgap of

the materials, whilst XRD gave important crystallographic information, and the electron microscopy provided valuable topographical analysis.

2.5 References

1. H. Bahruji, PhD thesis, “Photocatalytic Reforming of Oxygenates on Pd/TiO₂ Catalysts” Cardiff University, 2011.
2. V. Zwillig, M. Aucouturier and E. Darque-Ceretti, *Electrochimica Acta*, 1999, **45**, 921–929.
3. J. M. Macak, H. Tsuchiya, and P. Schmuki, *Angewandte Chemie International Edition*, 2005, **44**, 2100–2102.
4. J. M. Macak, H. Tsuchiya, L. Taveira, S. Aldabergerova, and P. Schmuki, *Angewandte Chemie International Edition*, 2005, **44**, 7463–7465.
5. J. M. Macak, S. Aldabergerova, A. Ghicov, and P. Schmuki, *physica status solidi (a)*, 2006, **203**, R67–R69.
6. S. P. Albu, A. Ghicov, J. M. Macak, and P. Schmuki, *physica status solidi (RRL) – Rapid Research Letters*, 2007, **1**, R65–R67.
7. M. Paulose, K. Shankar, S. Yoriya, H. E. Prakasam, O. K. Varghese, G. K. Mor, T. A. Latempa, A. Fitzgerald, and C. A. Grimes, *The Journal of Physical Chemistry B*, 2006, **110**, 16179–16184.
8. H. Yin, H. Liu, and W. Z. Shen, *Nanotechnology*, 2010, **21**, 035601.
9. M. Paulose, O. K. Varghese, L. Peng, K. C. Papat, H. E. Prakasam, G. K. Mor, T. A. Desai, and C. A. Grimes, *Journal of Physical Chemistry C*, 2007, **111**, 14992–14997.
10. D. Regonini, PhD Thesis, “Anodised TiO₂ Nanotubes: Synthesis, Growth Mechanism and Thermal Stability”, University of Bath, 2008.
11. C. Bowen, C. Clarke, D. Allsopp and A. Sergejevs, Deliverable D3.3: – UV LED and photo-catalyst combination, http://www.pcatdes.eu/resimler/20170414__8678857684n.pdf, (accessed 17 May 2017).
12. K. Dai, L. Lu and G. Dawson, *J. of Materi Eng and Perform*, 2013, **22**, 1035–1040.
13. Thermal Conductivity of common Materials and Gases, http://www.engineeringtoolbox.com/thermal-conductivity-d_429.html.
14. P. V. D. Heide, *X-ray Photoelectron Spectroscopy: An introduction to Principles and Practices*, Wiley, 2011.
15. J. Grdadolnik, *Acta Chemica Slovenica*, 2002, **49**, 631–642.

16. www.PerkinElmer.com
17. M. P. Fuller and P. R. Griffiths, *Anal. Chem.*, 1978, **50**, 1906–1910.
18. M. B. Mitchell, in *Structure-Property Relations in Polymers*, American Chemical Society, 1993, vol. 236, pp. 351–375.
19. C. Suryanarayana, *X-Ray diffraction: a practical approach*, Plenum Press, New York ; London, 1998.
20. R. Reifenberger, *Fundamentals of Atomic Force Microscopy: Part I: Foundations*, World Scientific, 2015.
21. N. A. Geisse, *Materials Today*, 2009, **12**, 40–45.
22. Nanoscience Instruments, c2017; [accessed April 2017].
<http://www.nanoscience.com/technology/afm-technology/>
23. Nanotechnology Now - Press Release, http://www.nanotechnology.com/news.cgi?story_id=42612, (accessed 1 June 2017).
24. J. Goldstein, *Scanning electron microscopy and x-ray microanalysis*, Springer, New York, 3rd ed., 2003.
25. <https://cmrf.research.uiowa.edu/>
26. R. J. Keyse and Royal Microscopical Society (Great Britain), *Introduction to scanning transmission electron microscopy*, BIOS Scientific, Oxford, 1998.
27. J. Tauc, R. Grigorovici and A. Vancu, *phys. stat. sol. (b)*, 1966, **15**, 627–637.
28. J. Tauc, *Materials Research Bulletin*, 1970, **5**, 721–729.
29. B. D. Viezbicke, S. Patel, B. E. Davis and D. P. Birnie, *physica status solidi (b)*, 2015, **252**, 1700–1710.

Chapter 3 – The Effect of Salts on the Photocatalytic Degradation of Cinnamic Acid

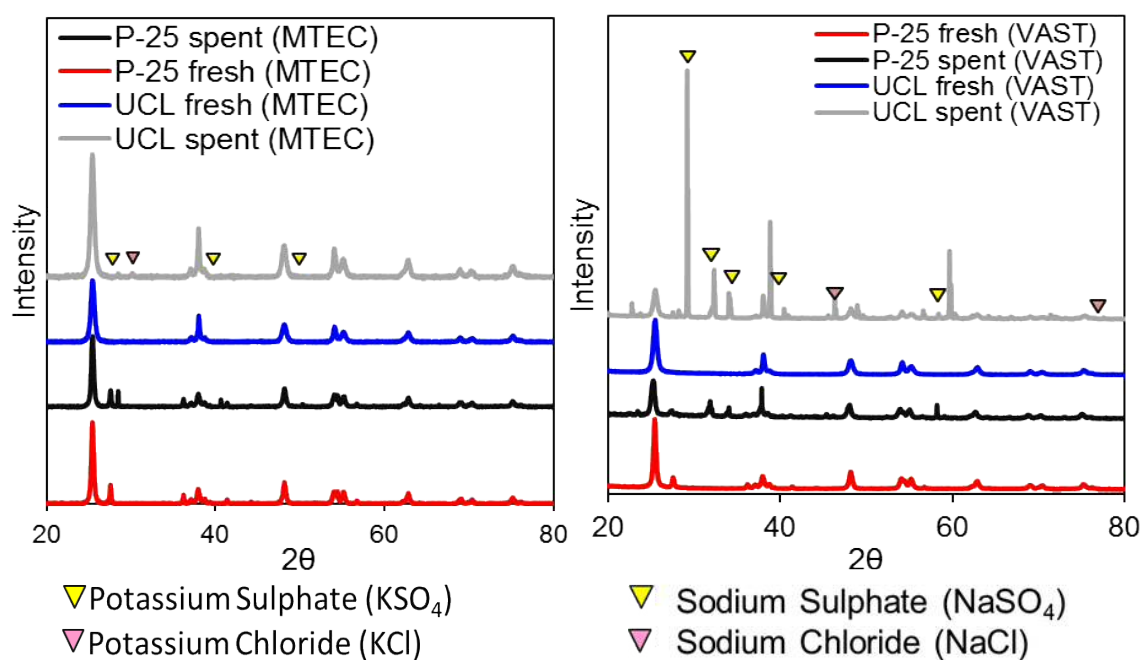
| | |
|--|-----|
| 3.1 Introduction | 68 |
| 3.1.1 Chemistry of Sulfate Radicals | 69 |
| 3.1.2 Chemistry of Chlorine radicals | 70 |
| 3.2 Results and Discussion | 72 |
| 3.2.1 The Degradation of Cinnamic Acid..... | 72 |
| 3.2.1.1 Photocatalytic Degradation of Cinnamic Acid and its Intermediates by Titania..... | 72 |
| 3.2.1.2 Degradation of Cinnamyl Alcohol..... | 74 |
| 3.2.1.3 CO ₂ capture experiments | 75 |
| 3.2.1.4 XPS Analysis of Fresh and Spent Catalysts | 76 |
| 3.2.1.5 Infrared studies of Fresh and Spent Catalysts..... | 80 |
| 3.2.1.6 X-Ray Diffraction Studies of Fresh and Spent Catalysts..... | 86 |
| 3.2.1.7 Proposed Model for the Photocatalytic Degradation of Cinnamic Acid | 86 |
| 3.2.2 The Effect of Sulfates on the Degradation of Cinnamic Acid | 89 |
| 3.2.2.1 Kinetic and Mechanistic Impact of Sulfate on Cinnamic Acid Degradation..... | 89 |
| 3.2.2.2 XPS studies of Spent Photocatalysts from Sulphated Reaction Media | 94 |
| 3.2.2.3 Infrared studies of Spent Photocatalysts from Sulphated Reaction Media..... | 95 |
| 3.2.2.4 XRD studies of Spent Photocatalysts from Sulphated Reaction Media | 98 |
| 3.2.2.5 Discussion of the Impact of Sulfate on the Photocatalytic Degradation of Cinnamic Acid | 99 |
| 3.2.3 The Effect of Chlorides on the Degradation of Cinnamic Acid | 102 |

| | |
|---|-----|
| 3.2.3.1 Kinetic Impact..... | 102 |
| 3.2.3.2 Mechanistic Impact of Chloride..... | 105 |
| 3.2.3.3 Photocatalytic Oxidation of Acetophenone, 2-Chloroacetophenone and 2'Chloroacetophenone | 107 |
| 3.2.3.4 XPS Studies of Spent Photocatalysts from Chlorinated Reaction Media..... | 110 |
| 3.2.3.5 XRD studies of Spent Photocatalysts from Sulphated Reaction Media | 113 |
| 3.2.3.6 Infrared Studies of Spent Photocatalysts from Chlorinated Reaction Media | 114 |
| 3.2.3.7 Discussion of the Impact of Chloride | 117 |
| 3.3 Conclusions | 122 |
| 3.4 References | 123 |

3.1 Introduction

This work aims to describe the mechanistic and kinetic effects of particular ions and molecular oxygen on the photocatalysed degradation of cinnamic acid (CA). CA has been chosen as an ideal substrate in place of the major constituents of various industrial effluents, particularly from the palm oil, olive oil and fishing industries. The effluent from these industries tends to be non-toxic but highly polluting. The Malaysian Palm Oil board reports that palm oil mill effluent (POME) is 100 times more polluting than domestic sewage due to its high chemical and biological oxygen demand[1].

The contaminant ions in this study were chosen for several reasons. Firstly, both sulfates and chlorides are known to be present in the waste waters from the target industries. They are often found as the potassium and sodium salts which commonly get into the effluent during processing steps that include washing, sterilising, and dilution. Sea water is generally



| Sample name | K wt% | Na wt% | S wt% | Cl wt% |
|-----------------------------------|-------|--------|-------|--------|
| P25 spent (MTEC) | 2.3 | / | 0.19 | 1.3 |
| UCL TiO ₂ spent (MTEC) | 1 | / | 0.15 | 0.3 |
| P25 spent (VAST) | / | 4.7 | 2.4 | 1.41 |
| UCL TiO ₂ spent (VAST) | / | 9.3 | 3.7 | 2 |

Figure 3.1.1 (top): XRD analysis of fresh and spent catalysts that have been exposed effluent from the palm oil (MTEC samples) and fishing (VAST samples) industry.

Table 3.1.1 (bottom): XRF elemental analysis of fresh and spent catalysts

used to dilute the effluent, before and during treatments, which is known to have a chloride concentration of roughly 540mM and a sulfate concentration of 28 mM. [2] Levels of each ion are not often recorded, however Cl^- concentration has been measured at: 35.2 mM in olive oil effluent [3], between 59.1 and 758 mM in pharmaceutical effluent [4], and 535 mM in oil field waste water [5]. Additionally, our collaborators in Aston University examined P25 and an anatase TiO_2 catalyst, produced by UCL, which had been exposed to industrial effluent from the palm oil and fishing industries. The spent catalyst characterisation data can be seen in **Figure 3.1.1** and **Table 3.1.1**. Palm oil effluent samples came from MTEC in Thailand and fishing industry samples came from VAST in Vietnam. Each are denoted by the university of origin. Wide angled XRD of the fresh P25 (MTEC) showed the expected anatase diffraction patterns at 2θ values of: 25 (101), 37.3 (004), 47.8 (200), 53.6 (105), 54.9 (211), 62.3 (204), 67.8 (116), 70.1 (220), 74.9 (215). Typical rutile diffraction patterns were seen at 2θ values of: 27.2 (110), 36.7 (101), 41.1 (111). Whilst the TiO_2 from UCL indicated that the only phase present was anatase. Exposure to palm oil effluent, by MTEC, resulted in the appearance of diffraction patterns associated with potassium chloride and sulfate salts as highlighted in **Figure 3.1.1** (left). Whilst spent catalysts from VAST showed patterns relating to sodium sulfates and chlorides. XRF elemental analysis confirmed the presence of; potassium, chlorine and sulphur in spent catalysts from MTEC; and sodium, chlorine and sulphur in spent catalysts from VAST. MTEC's P25 samples were more susceptible, than the anatase from UCL, to potassium salt adhesion. Whereas UCL's anatase was more susceptible to sodium salt adsorption. Based on these data it was decided that KCl , K_2SO_4 , NaCl and Na_2SO_4 would be the primary focus for the contamination studies.

3.1.1 Chemistry of Sulfate Radicals

Presence of sulfate and its influence is often discussed in the context of the radical sulfate ion. SO_4^\bullet is a strong oxidant that is commonly produced from the persulfate ion ($\text{S}_2\text{O}_8^{2-}$) via photolysis, [6] and has been noted for the differing behaviour to that of hydroxyl radicals. Formation of sulfate radicals in photocatalytic systems is possible via 2 routes; the radicalisation of HSO_4^- by HO^\bullet (**Reaction 1**), or by Cl^\bullet (**Reaction 3**) as shown in **Table 3.1.2**. Mendez *et al.* illustrated the differing behaviour between SO_4^\bullet and HO^\bullet in the degradation of dodecylbenzenesulfonate in the presence of fulvic acid. [7] $\text{UV/S}_2\text{O}_8^{2-}$ degraded the target molecule more quickly than $\text{UV/H}_2\text{O}_2$ due to the more specific reactivity of the sulfate radical therefore reducing the ability for dissolved organic carbon species to scavenge it. Some

studies into the influence of sulfates on photo-mineralisation processes have found varying effects. Wiszniowski *et al.* found the degradation of humic acid to be initially inhibited in the presence of sulfate, but promoted in later steps by the formation and reaction of SO_4^\bullet in solution. [8]

3.1.2 Chemistry of Chlorine radicals

As discussed previously, chloride exists in some industrial waste waters at very high concentrations. Generally, chloride ions, in the form of a sodium salt for example, are capable of S_N^2 nucleophilic substitution reactions in preference over an elimination type reaction. In the presence of radicals, chloride anions have been shown to readily form chlorine atoms, or reactive chlorine species (RCS), through several mechanisms, as seen in **reactions 4 – 10**. It appears the literature concerning photogenerated holes on titania and their reaction with Cl^- is minimal and so no direct reference for this rate constant can be cited. However, chloride ions have been measured, by Garg *et al.*, reacting with photogenerated holes on silver chloride in a one electron transfer to give chlorine atoms. [10] Another route to the formation of reactive chlorine species is through the reaction of Cl^- and HO^\bullet , **reactions 5 and 7**. The rate constant

| | | | |
|--------------------|--|--|------|
| Reaction 1 | $\text{SO}_4^\bullet + \text{H}_2\text{O} \rightleftharpoons \text{HSO}_4^- + \text{HO}^\bullet$ | $k_1[\text{H}_2\text{O}] = 460 \text{ s}^{-1}$ | [9] |
| | | $k_{-1} = 6.9 \times 10^5 \text{ M}^{-1} \text{ s}^{-1}$ | [9] |
| Reaction 2 | $\text{HSO}_4^- \rightarrow \text{SO}_4^{2-} + \text{H}^+$ | $K_2 = 1.2 \times 10^{-2} \text{ M}^{-1}$ | [9] |
| Reaction 3 | $\text{SO}_4^\bullet + \text{Cl}^- \rightleftharpoons \text{SO}_4^{2-} + \text{Cl}^\bullet$ | $k_3 = 3.2 \times 10^8 \text{ M}^{-1} \text{ s}^{-1}$ | [11] |
| | | $k_{-3} = 2.1 \times 10^8 \text{ M}^{-1} \text{ s}^{-1}$ | [11] |
| Reaction 4 | $\text{Cl}^- + \text{h}^+ \rightarrow \text{Cl}^\bullet$ | $k_4 = 1 \times 10^7 \text{ M}^{-1} \text{ s}^{-2}$ | [12] |
| Reaction 5 | $\text{HO}^\bullet + \text{Cl}^- \rightarrow \text{ClOH}^\bullet$ | $k_5 = 4.3 \times 10^9 \text{ M}^{-1} \text{ s}^{-1}$ | [12] |
| Reaction 6 | $\text{ClOH}^\bullet \rightarrow \text{HO}^\bullet + \text{Cl}^-$ | $k_6 = 6.1 \times 10^9 \text{ s}^{-1}$ | [13] |
| Reaction 7 | $\text{ClOH}^\bullet \rightarrow \text{Cl}^\bullet + \text{HO}^-$ | $k_7 = 23 \text{ s}^{-1}$ | [13] |
| Reaction 8 | $\text{ClOH}^\bullet + \text{H}^+ \rightleftharpoons \text{Cl}^\bullet + \text{H}_2\text{O}$ | $k_8 = 2.1 \times 10^{10} \text{ M}^{-1} \text{ s}^{-1}$ | [14] |
| | | $k_{-8} = 1.3 \times 10^3 \text{ s}^{-1}$ | [14] |
| Reaction 9 | $\text{ClOH}^\bullet + \text{Cl}^- \rightarrow \text{HO}^- + \text{Cl}_2^\bullet$ | $k_9 = 1 \times 10^5 \text{ M}^{-1} \text{ s}^{-1}$ | [12] |
| Reaction 10 | $\text{Cl}^\bullet + \text{Cl}^- \rightleftharpoons \text{Cl}_2^\bullet$ | $k_{10} = 6.5 \times 10^9 \text{ M}^{-1} \text{ s}^{-1}$ | [13] |
| | | $k_{-10} = 1.1 \times 10^5 \text{ s}^{-1}$ | [14] |

Table 3.1.2: A table of sulphate and chloride radical reaction rates

for the decay of ClOH^\bullet to Cl^\bullet is 10 order of magnitude slower than the rate constant for the reformation of HO^\bullet , meaning that this route cannot feasibly produce enough reactive chlorine

to significantly impact a reaction. [12][13] The most likely source for Cl^\bullet , in our conditions, is seen in **reaction 8**. [14] At pH's lower than 7.2 H^+ rapidly reacts with ClOH^\bullet to give Cl^\bullet , and water, with a significantly slower reverse reaction. ClOH^\bullet can react with excess chloride to give the dichloride radical, Cl_2^\bullet , but this reaction has a rate constant 4 orders of magnitude smaller than the decay of ClOH^\bullet as seen in **reaction 7**. An equilibrium exists between the two radical chlorine species and chloride, as seen in **reaction 10**, with the equilibrium lying closer to the dichloride radical, especially at lower pHs. [15][16]

Work has been done by several groups to analyse and predict the kinetics and reactivity of reactive chlorine species (RCS). Most of the work involves the laser flash photolysis of an organic chloride source, like chloroacetone, to give atomic chlorine; although some work has also investigated the effect of chloride anions in UV/ H_2O_2 advanced oxidation processes (AOPs). [17] RCS are more specific oxidising species, compared to the indiscriminate HO^\bullet , whose reactivity greatly depends on the nature of the substrate. [12] RCS are known to react by single electron oxidation, addition to unsaturated double bonds and hydrogen abstraction. The actual speed of atomic chlorine reactions, in solution, is difficult to ascertain due to them often being diffusion limited, however gas phase testing has found Cl^\bullet reactions to be orders of magnitude faster than HO^\bullet . [18] In general, the measured rate constants of HO^\bullet and Cl^\bullet reacting with oxygenated organic compounds are very similar. Alcohols largely agree, with the previous statement of similarity between radical behaviour, although they are noted as having differing activation energies and mechanistic preference. ESR studies show that Cl^\bullet preferentially reacts with alcohols at the OH group, probably through electron transfer, whilst HO^\bullet preferred hydrogen abstraction. [17][19][20] Ketones and aldehydes were found to be more susceptible to HO^\bullet attack, due to the preference of hydrogens susceptible to abstraction, with rate constants being 10x larger than Cl^\bullet for acetone and acetaldehyde. [21] Carboxylic acids also display different susceptibilities depending on the attacking radical. Cl^\bullet shows a strong preference for attacking a carboxylate over a carboxylic acid because of the ease of electron transfer from the anion in comparison to the neutral acid. Whilst HO^\bullet reactivity is more complicated. In the case of methanoic acid, the deprotonated form reacts 30 times faster due to the increased resonance facilitating an addition-elimination mechanism that occurs more quickly than a hydrogen abstraction. Alternatively with ethanoic acid, the elimination of methanol is not favourable and so both the neutral and anionic form rely on hydrogen abstraction to react. [17][18][19]

The disproportionated form of Cl^\bullet , $\text{Cl}_2^{\bullet-}$, does not show the same level of reactivity. While $\text{Cl}_2^{\bullet-}$ is capable of the same reactions as atomic chlorine, it has been measured to do so at a considerably slower rate. Studies by Jacobi and Wicktor, found the dichloride radical reacted with oxygenated hydrocarbons at rates 5 orders of magnitudes slower than atomic chlorine. [20][22] Whilst excess chloride will move the equilibrium, seen in **reaction 10**, closer to the formation of the dichloride anion, the superior reactivity of atomic chlorine will appreciably contribute to the decay of $\text{Cl}_2^{\bullet-}$ leading Cl^\bullet to be the dominant species.

3.2 Results and Discussion

3.2.1 The Degradation of Cinnamic Acid

3.2.1.1 Photocatalytic Degradation of Cinnamic Acid and its Intermediates by Titania

The photocatalysis utilised here all took place within the PCATDES standardised reactor. Cinnamic acid (CA) did not consistently appear on the GCMS, due to its high boiling point of 300°C , leading us to track cinnamic acid (CA) degradation using UV-visible spectroscopy. All other intermediates were followed using GC-MS.

The photocatalytic degradation of CA by MP25 follows the reaction profile as seen in **Figure 3.2.1.1 (top left)**. A 30 minutes dark period, at the start, is used to ensure thorough mixing so that mass transfer does not limit the reaction when irradiation begins. A small decrease in CA concentration is observed which can be attributed to CA adsorption to titania. Cinnamic acid removal can be plotted using first order rate kinetics to give a rate constant of 0.089 s^{-1} , with a 72% decrease in concentration in the first 15 minutes. P25 was also tested and it gave a slower rate of 0.055 s^{-1} . **Figure 3.2.1.1 (a)** shows a GC chromatogram at the 20 minutes interval after irradiation had begun. The species at 11.09 minutes provided a mass spectrum as seen in **appendix 1.1.1**. The m/z of 106.04 and 77.04 can be attributed to the parent mass peak of benzaldehyde [$\text{C}_6\text{H}_5\text{CHO}$] and [C_6H_5] $^+$ respectively. A benzaldehyde calibration standard provided a matching mass spectrum, as shown in **appendix 1.1.2**, and eluted at the same retention time confirming this assignment. From here on, benzaldehyde will be referred to as **2**. A smaller signal at 13.18 minutes provided a mass spectrum that can be found in **appendix 1.1.3**. Signals at m/z 's of 120.06 and 91.06 can be attributed to the parent mass peak of phenylacetaldehyde [$\text{C}_6\text{H}_5\text{CH}_2\text{CHO}$] and [$\text{C}_6\text{H}_5\text{CH}_2$] $^+$ respectively. A phenylacetaldehyde calibration standard eluted at the same retention time and gave a matching mass spectrum, found in **appendix 1.1.4**, confirming this assignment.

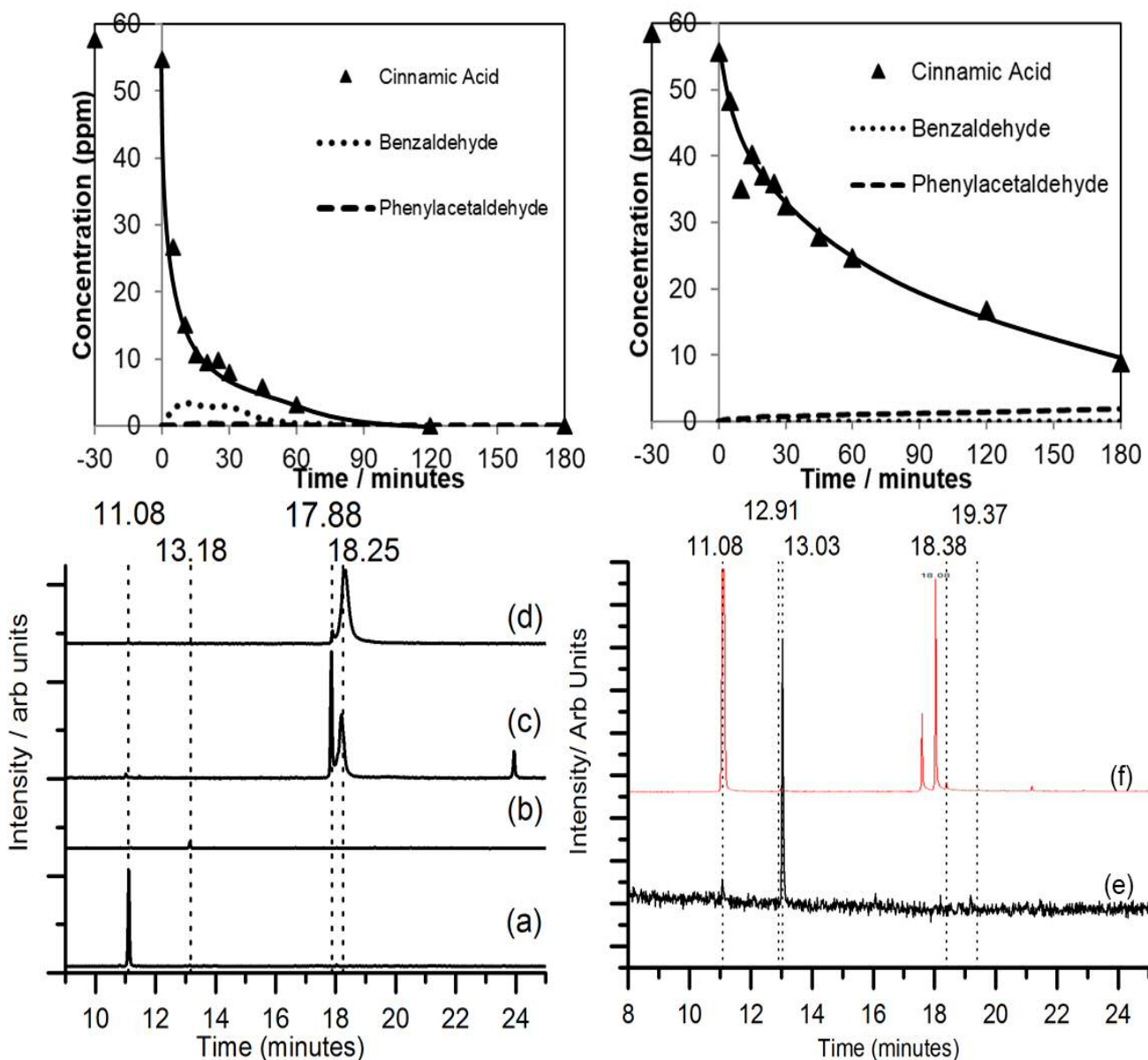


Figure 3.2.1: The reaction profiles for the degradation of CA with TiO_2 (top left) and in the absence of O_2 (top right).

Bottom:- Gas chromatograms after 20 minutes of irradiation for: (a) MP25 + CA, (b) mP25 + CA + N_2 , (c) mP25 + cinnamyl alcohol, (d) mP25 + cinnamyl alcohol + N_2 , (e) mP25 + benzaldehyde, (f) mP25 + phenylacetaldehyde

Phenylacetaldehyde will now be referred to as **3**. A control experiment that tested the reaction of **2** as the substrate, found **2** photocatalytically degraded to the products seen on the chromatogram in **Figure 3.2.1.1 (e)**. It should be noted that the eluents observed at 17.63 and 18.08 minutes were confirmed to be a carbonaceous species being released into solution from the batch of mP25 being used at the time. A catalyst only control experiment found this species was present without any substrate and was absent in all subsequent batches of mP25. Several small peaks were detected in the degradation of benzaldehyde that were only intermittently present in the degradation of CA. They eluted at 13.0 minutes, 18.4 minutes

and 19.4 minutes; and all produced similar mass spectra as shown in **appendices 1.1.5, 1.1.7, and 1.1.9**. The suspected parent mass peak was at an m/z of 122 which agrees with the assessment of a hydroxybenzaldehydes [$C_6H_4(OH)CHO$]. The next largest peak was at an m/z 93 correlates to a hydroxybenzaldehyde fragment minus with the aldehyde group [$C_6H_4(OH)]^+$. Calibration samples for 2-hydroxybenzaldehyde and 3-hydroxybenzaldehyde eluted at 12.9 and 18.4 minutes giving the matching mass spectra in **appendices 1.1.6 and 1.1.8**. The peak at 19.4 minutes was assigned as 4-hydroxybenzaldehyde via the process of elimination. As direct derivatives of **2**, each hydroxylated intermediate will be referred to as **2a**, **2b** and **2c** respectively. Degrading **3** individually gave a chromatographic trace in **Figure 3.2.1.1 (f)**. **3** can be seen at 13.03 minutes and degrades at a first order rate of 0.072 s^{-1} , however no other species were detected.

Dissolved oxygen is a common component utilised in photocatalytic degradation. Oxygen was purged continually, with a 1 bar N_2 flow, during the reaction to examine the effect. The rate of degradation of cinnamic acid was strongly inhibited reducing the first order rate constant to 0.02 s^{-1} , whilst with P25 the rate was reduced to 0.018 s^{-1} . The gas chromatogram in **Figure 3.2.1.1 (top right)** shows the detected species after 20 minutes of irradiation. Under these conditions, **2** was not detected in most of the tests as shown in **Figure 3.2.1.1 (b)**. Whilst **3** was detected at 13.03 minutes with **Figure 3.2.1.1 (top right)** showing the amount formed throughout the reaction. **3** is formed at a fast rate under deoxygenated conditions and its concentration builds throughout the 3 hours irradiation time. No drop in the concentration of **3** is seen and no degradation products are observed.

3.2.1.2 Degradation of Cinnamyl Alcohol

Cinnamyl alcohol was tested as a substrate to examine how a change to an alcohol functionality, instead of a carboxyl group, would affect the degradation by mP25. **Figure 3.2.1 (c)** shows a chromatogram of the oxygenated reaction after 20 minutes irradiation time, the reaction will be labelled “cinnamylA”. The parent compound, cinnamyl alcohol, elutes at 18.2 minutes and is seen to decrease in concentration throughout the reaction. The second largest peak has a retention time of 17.86 minutes and as such overlaps with the parent complex resulting in issues in the deconvolution of the mass spectrums. Analysis of the mass spectra, that is shown in **appendix 1.2.1**, found the eluent at 18.2 minutes gave a mass spectrum with a parent m/z of 134 that matches cinnamyl alcohol. While fragments detected were at m/z s of 117, 105, 91 and 77; which can be assigned as [$C_6H_5C_2H_2CH_2$], [$C_6H_5CH_2CH_2$]⁺, [$C_6H_5CH_2$]⁺ and [C_6H_5]⁺. The next peak is one that elutes at 17.86 minutes.

Its concentration begins to increase by the 0 minute mark, and then increases rapidly until 20 minutes after which it begins to decrease. The mass spectrum (**appendix 1.2.2**) indicates a parent mass peak at an m/z of 132 which can be attributed to the parent mass peak of cinnamaldehyde [$C_6H_5C_2H_2CHO$]. Signals at m/z s of 103, 93 and 77 correspond to the fragmentation products of $[C_6H_5C_2H_2]^+$, $[C_6H_5C_1H_2]^+$ and $[C_6H_5]^+$. A third intermediate was detected at 11.04 minutes and was confirmed to be **2** via analysis of the mass spectrum and the retention time. During the reaction, as the cinnamyl alcohol peak disappears the cinnamaldehyde peak increases. However by 180 minutes both are only present in trace amounts whilst **2** becomes the most prevalent intermediate. When oxygen was purged, cinnamyl alcohol did not show any sign of degrading, besides minor amounts of cinnamaldehyde being formed. This data suggests cinnamyl alcohol is stable to UV irradiation, unlike cinnamic acid, and that oxygen is an important part of the mechanism. This reaction is labelled “CinnamylA (deoxy)”.

5.2.1.3 CO_2 capture experiments

CO_2 evolution for the reactions can be seen in **figure 3.2.1.2**. A no light control indicated no CO_2 was released in the absence of irradiation. Degradation of CA with mP25 releases CO_2 at a rate of $1.29 \mu M^{-1} s^{-1}$ with 100% of the total organic carbon being released as

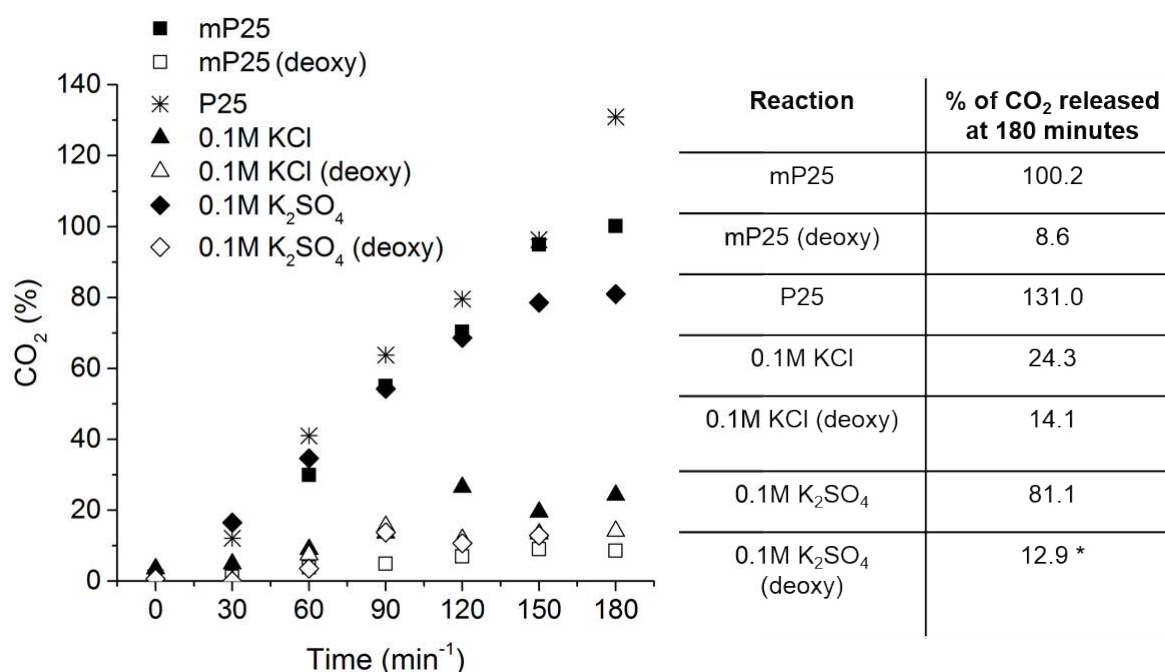


Figure 3.2.1.2:- Left: the amount of CO_2 detected over 180 minutes in the absence and presence of salts

Right: A table showing the percentage of carbon detected after 180 minutes of reaction. (* measurement from 150 minutes)

| Sample ID | XPS Region (Atomic % concentration) | | | | | | | |
|--|-------------------------------------|------|------|-------|------|------|-------|------|
| | Ti 2p | O 1s | C 1s | Na 1s | K 2p | S 2p | Cl 2p | N 1s |
| mP25 | 26.2 | 59.3 | 14.2 | / | / | / | 0.3 | / |
| No substrate blank | 27.4 | 67.8 | 1.2 | / | 1.6 | / | 2.0 | / |
| mP25 spent | 23.6 | 59.4 | 16.9 | / | / | / | / | / |
| mP25 spent (deoxy) | 25.7 | 62.5 | 11.5 | / | / | / | 0.4 | / |
| P25 | 22.1 | 61.4 | 12.5 | / | / | / | / | / |
| P25 spent | 27.5 | 62.9 | 9.4 | / | / | / | / | 0.2 |
| mP25 + cinnamyl alcohol | 28.8 | 66.2 | 5.0 | / | / | / | / | / |
| mP25 + cinnamyl alcohol (deoxy) | 27.3 | 65.8 | 6.6 | / | / | / | / | 0.4 |
| 0.05M Na ₂ SO ₄ | 23.8 | 60.1 | 9.3 | 5.3 | / | 1.5 | / | 0.6 |
| 0.1M Na ₂ SO ₄ | 25.3 | 63.8 | 2.3 | 6.9 | / | 1.8 | / | / |
| 0.1M Na ₂ SO ₄ (deoxy) | 23.9 | 57.2 | 15.6 | 2.4 | / | 0.9 | / | / |
| 0.05M K ₂ SO ₄ | 24.3 | 64.7 | 7.4 | / | 1.9 | 1.2 | / | 0.6 |
| 0.1M K ₂ SO ₄ | 25.0 | 63.2 | 7.7 | / | 2.6 | 1.6 | / | / |
| 0.1M K ₂ SO ₄ (deoxy) | 21.7 | 59.5 | 14.8 | / | 2.6 | 1.3 | / | / |
| 0.005M KCl | 29.0 | 64.3 | 6.0 | / | 0.2 | / | 0.5 | / |
| 0.05M KCl | 26.3 | 63.8 | 5.4 | / | 2.1 | / | 2.4 | / |
| 0.1M KCl | 28.3 | 63.2 | 6.7 | / | 0.7 | / | 1.1 | / |
| 0.5M KCl | 28.0 | 62.2 | 5.4 | / | 2.0 | / | 2.4 | / |
| 0.1M NaCl | 29.6 | 59.2 | 6.4 | 3.9 | / | / | 0.9 | / |
| 0.1M NaCl (deoxy) | 28.4 | 55.2 | 3.6 | 7.2 | / | / | 5.6 | / |
| 1M NaCl | 28.0 | 55.6 | 8.1 | 5.7 | / | / | 2.5 | / |

Table 3.2.1.1: Percentage elemental concentrations from XP spectra

CO₂, whilst for P25 it is 1.45 $\mu\text{M}^{-1} \text{s}^{-1}$ 130% of the total CO₂ released. Whereas under deoxygenated conditions the rate of CO₂ evolution is 0.0981 $\mu\text{M}^{-1} \text{s}^{-1}$ that results in just 8.57% of the total CO₂ being released after three hours of reaction.

3.2.1.4 XPS Analysis of Fresh and Spent Catalysts

XP spectra of the fresh and spent catalyst provided percentage concentrations that can be seen in **Table 3.2.1.1**, with the curve fitted carbon 1s spectra for **3.2.1** shown in **Figure 3.2.1.3** and the corresponding component breakdown in **Table 3.2.1.2 (top)**. None of the analysed samples showed any change in the Ti2p region. Each showed a Ti2p signal at 458.6 eV that had a spin orbit splitting 5.7 eV clearly indicating Ti in the +4 oxidation state. The Ti2p region was fitted with a Shirley background and an SGL line shape which provided the best fit for the fresh catalyst. This lack of change from fresh to spent indicates that the mP25 is neither significantly oxidised or reduced. Oxygen 1s analysis shows a peak at 529.8 eV in all samples and a smaller component at roughly 531-531.5 eV. The peak at 529.8 eV is typical of the oxide of titania, and the second component is likely to be organic C-O. **Table 3.2.1.2 (bottom)** gives the binding energy and percentage concentration for the oxygen species. In general, the amount of C-O oxygen present is linked to the amount of carbon

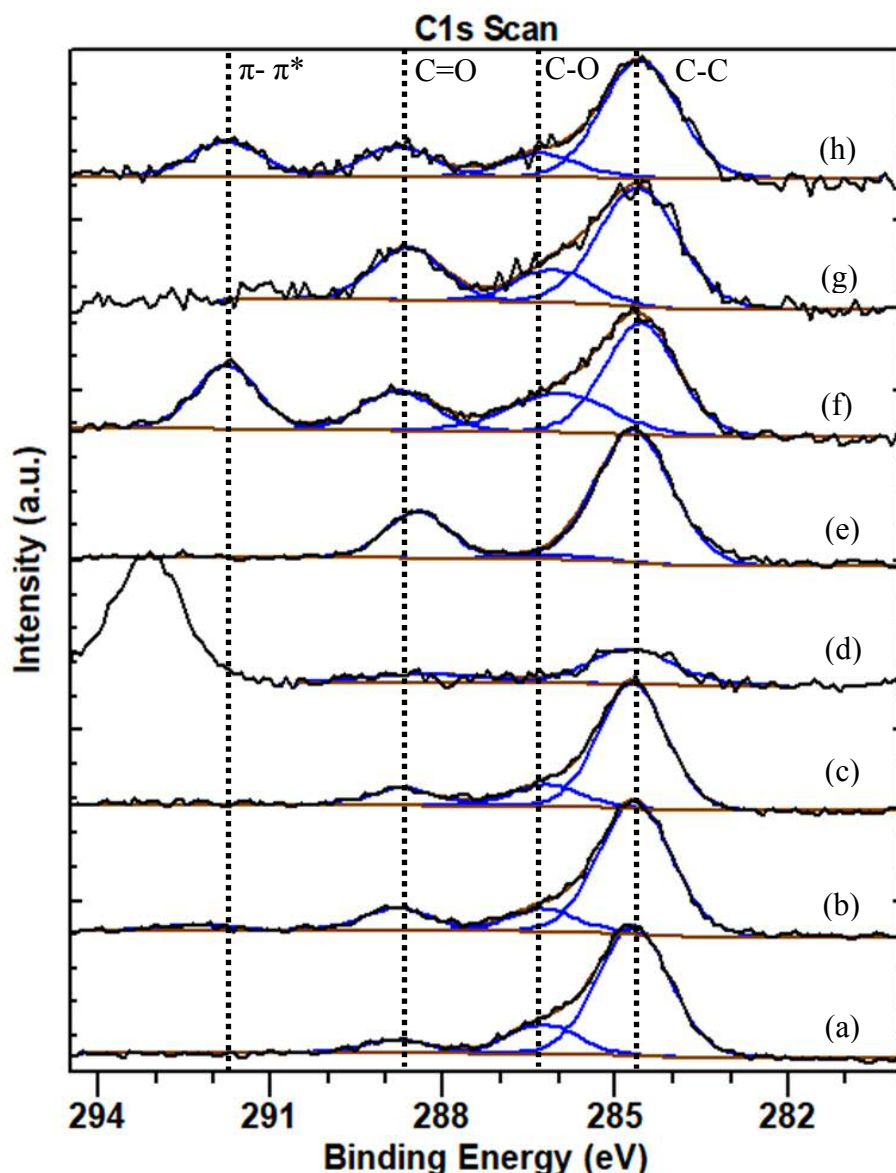


Figure 3.2.1.3: Changes in C1s XP spectra for: (a) mP25 fresh, (b) mP25 spent, (c) mP25 spent (deoxy) (d) mP25 no substrate control, (e) P25 fresh, (f) P25 spent, (g) mP25 + cinnamyl alcohol spent, (h) mP25 + cinnamyl alcohol (deoxy)

detected in each sample. For example, the percentage of carbon increases from fresh mP25 to spent mP25 which is coupled with an increase in C-O oxygen percentage. This trend is present throughout this batch of samples, except for “mP25 spent (deoxy)” that see a decrease in detected carbon but an increase in the percentage of C-O oxygen. Curve fitting of the carbon region indicates that there are two environments, peaks at 284.7 eV and 288.7 eV, which are common to all samples. An additional peak at 286.2 eV is also detected in the majority of samples whilst a peak at 291.7 to 292.3 eV is only present in 3 of the 8 samples. Fresh mP25 has an adventitious carbon layer that mostly consists of C-C species and roughly 25% C-O, most of which is C-O in nature. The “no substrate” blank sample sees a significant

| Sample Name | C1s (C-C) | C1s (C-O) | C1s (C=O) | C1s (π - π^*) |
|---------------------------------|---------------|---------------|---------------|-------------------------|
| mP25 fresh | 284.1 (74.0%) | 286.3 (17.5%) | 288.8 (8.5%) | / |
| mP25 spent | 284.7 (72.6%) | 286.3 (12.4%) | 288.8 (12.4%) | 292.3 (2.6%) |
| mP25 spent (deoxy) | 284.7 (74.5%) | 286.2 (14.1%) | 288.7 (11.4%) | / |
| mP25 no substrate control | 284.7 (76.1%) | / | 288.2 (24.0%) | / |
| P25 fresh | 284.7 (76.8%) | / | 288.4 (23.2%) | / |
| P25 spent | 284.6 (42.1%) | 286.0 (21.2%) | 288.9 (15.6%) | 291.8 (21.2%) |
| mP25 + Cinnamyl alcohol | 284.6 (60.1%) | 286.1 (16.3%) | 288.6 (23.6%) | |
| mP25 + Cinnamyl Alcohol (deoxy) | 284.6 (56.8%) | 286.3 (12.1%) | 288.8 (14.5%) | 291.8 (16.6%) |

| Sample Name | O1s (O ²⁻) | O1s (C-O) |
|---------------------------------|------------------------|--------------|
| mP25 fresh | 529.9 (92.8%) | 531.5 (7.2%) |
| mP25 spent | 529.9 (90.1%) | 531.5 (9.9%) |
| mP25 spent (deoxy) | 530.0 (91.4%) | 531.5 (8.6%) |
| mP25 no substrate control | 529.9 (96.3%) | 531.5 (3.7%) |
| P25 fresh | 529.9 (90.4%) | 531.6 (9.6%) |
| P25 spent | 529.9 (94.1%) | 531.5 (5.9%) |
| mP25 + Cinnamyl alcohol | 529.8 (94.4%) | 531.5 (5.6%) |
| mP25 + Cinnamyl Alcohol (deoxy) | 529.9 (95.1%) | 531.5 (4.9%) |

Table 3.2.1.2:- Top: A table showing the percentage concentration of the carbon 1s environments

Bottom: A table showing the percentage concentrations of the oxygen 1s environments drop in carbon present, as well as C-O oxygen. With no substrate present the photocatalyst appears to be oxidising what carbon is left, effectively cleaning the surface, and leaves carbonaceous species that consist of C-C and C=O character. The spent catalyst sample sees a small increase in carbon present that now has evidence of π - π^* interactions, a satellite that is usually indicative of delocalised carbon species like those found in aromatic systems or graphite. The XPS data could be indicating the result of further oxidation occurring, since it appears oxygen is required to efficiently oxidise the substrate, where CA is being largely oxidised to carbonaceous species of an aromatic and oxygenated nature. Furthermore, the formation of benzaldehyde is proposed by Maeda *et al.* as a surface orientated reaction that eliminates 2 carbons and three oxygens from the substrate, [29] or as Costa *et al.* indicate, as carbon dioxide and formaldehyde. [24] This process could also add to this carbon build up although, as the no substrate blank has shown, deposited carbon is liable to be oxidised and cleaned off of the surface. Under deoxygenated conditions a slight decrease in the carbon, that has no π - π^* character, is observed. GC-MS and CO₂ capture data indicated that **3**, the main intermediate detected in these conditions, is not efficiently degraded in the absence of oxygen. This suggests that the π - π^* character is a result of significant degradation taking

place and so furthers the argument that dissolved oxygen is an important factor in the photocatalysed degradation of cinnamic acid. The fresh P25 sample has a symmetrical peak at 284.7 eV with no shoulder, unlike the fresh mP25 sample, and a C=O peak at 288.4 eV. It is usually more characteristic of P25 to have an asymmetric peak that contains a C-O component. Spent P25 was found to have a lowered carbon content that also exhibited a π - π^* satellite, however it was a much greater constituent of the carbon content than in spent mP25. This data is in agreement with the lowered oxygen 1s C-O component that was found to have dropped significantly from before the reaction. This could suggest an increased preference to degrade CA via the benzaldehyde route and deposit graphitic residue. The last two XPS samples relate to reactions with cinnamyl alcohol. Both exhibit lowered carbon concentrations, potentially for the same reason. For cinnamylA, a more significant loss of carbon is observed, as shown in **Table 3.2.1.1**. A carbon atomic percentage of 5% is detected, potentially due to the lack of surface based degradation and the presence of oxygen available to help oxidise carbon to CO₂. With CinnamylA (deoxy), the carbon content drops to 6.6% and the detected species contains a large amount of π - π^* character at 16.6% of the carbon present. Since no degradation is observed, the π - π^* component is very likely to be a result of the extended conjugation from the aromatic ring, C=C double bond and O-H on the unreacted cinnamyl alcohol. π - π^* character is not observed for cinnamylA, presumably because the substrate largely degrades to benzaldehyde and cinnamaldehyde that are both not capable of the extended conjugation required.

3.2.1.5 Infrared studies of Fresh and Spent Catalysts

| Infrared Frequency (cm ⁻¹) | Assignments | Fresh mP25 | mP25 - no CA control | mP25 spent | mP25 spent (deoxy) | Fresh P25 | P25 spent |
|--|---|------------|----------------------|---------------|--------------------|-----------|----------------------|
| 3068 | Aromatic v(C-H) -s | / | / | / | weak | / | v.weak |
| 2975 | CH ₃ antisym-s | / | / | strong | | / | weak |
| 2923 | CH ₂ antisym-s | v.weak | / | strong | weak | weak | strong |
| 2855 | CH ₃ sym-s | v.weak | / | medium | weak | weak | medium |
| 1750 | v(C=O) H-Bonded aldehyde | / | / | / | v.weak | / | / |
| 1713 | v(C=O) Ti-O=C-CH ₂ -Ph | / | / | v.weak | weak | / | medium |
| 1698 | v(C=O) aldehyde | / | / | / | / | / | strong |
| 1680 | v(C=O) V ₂ O ₅ -O=C-CH ₂ -Ph | / | / | / | v.weak | / | weak |
| 1659 | v(C=O) | / | / | / | / | / | medium |
| 1633/1643 | v(O-H) H ₂ O bend | medium | medium | strong, broad | strong | strong | medium |
| 1602 | v(C=C) -s aromatic skeletal | / | / | / | v.weak | / | v.weak |
| 1578 | | / | / | weak | v.weak | / | v.weak |
| 1542 | | / | / | weak | v.weak | / | weak |
| 1470 | CH ₂ scissoring | / | / | strong | / | / | weak |
| 1451 | v(C-H) bend O=C-C-H ₂ -Ph | / | / | / | weak | / | weak |
| 1418 | CH ₃ antisym-b | / | / | weak | medium | / | weak |
| 1398 | | / | / | / | / | / | medium |
| 1383 | CH ₃ sym-b | / | / | strong | / | / | weak |
| 1344 | | / | / | weak | / | / | v.weak |
| 1304 | CH ₂ wagging | / | / | medium | / | / | weak |
| 1194-1264 | v(C-C), v(C-O) -s | / | / | / | / | / | weak, multiple peaks |
| 1164 | | / | / | strong | / | / | / |
| 1158 | | / | / | / | weak | / | medium |
| 1132 | | / | / | strong | / | / | v.weak |
| 1109 | | / | / | weak | v.weak | / | weak |
| 1091 | | / | / | / | / | / | weak |

Table 3.2.1.3:- Infrared frequencies and the associated assignments for fresh and spent mP25 photocatalyst

Assignments followed by -s = stretching mode, -b = bending mode

ATR spectra analysis of fresh titania showed several characteristic peaks, as seen in **Figure 3.2.1.4 (a)**. A wide band is observed at 3200-3600 cm⁻¹, weak stretches at 2850-3000cm⁻¹ and 1633 cm⁻¹ which correspond to v(H₂O) stretching mode, C-H stretching modes and a v(H₂O) bending mode respectively. The no substrate blank, **Figure 3.2.1.4(b)**, shows an increase in strength of the H₂O bending and stretching modes as well a very weak signal at

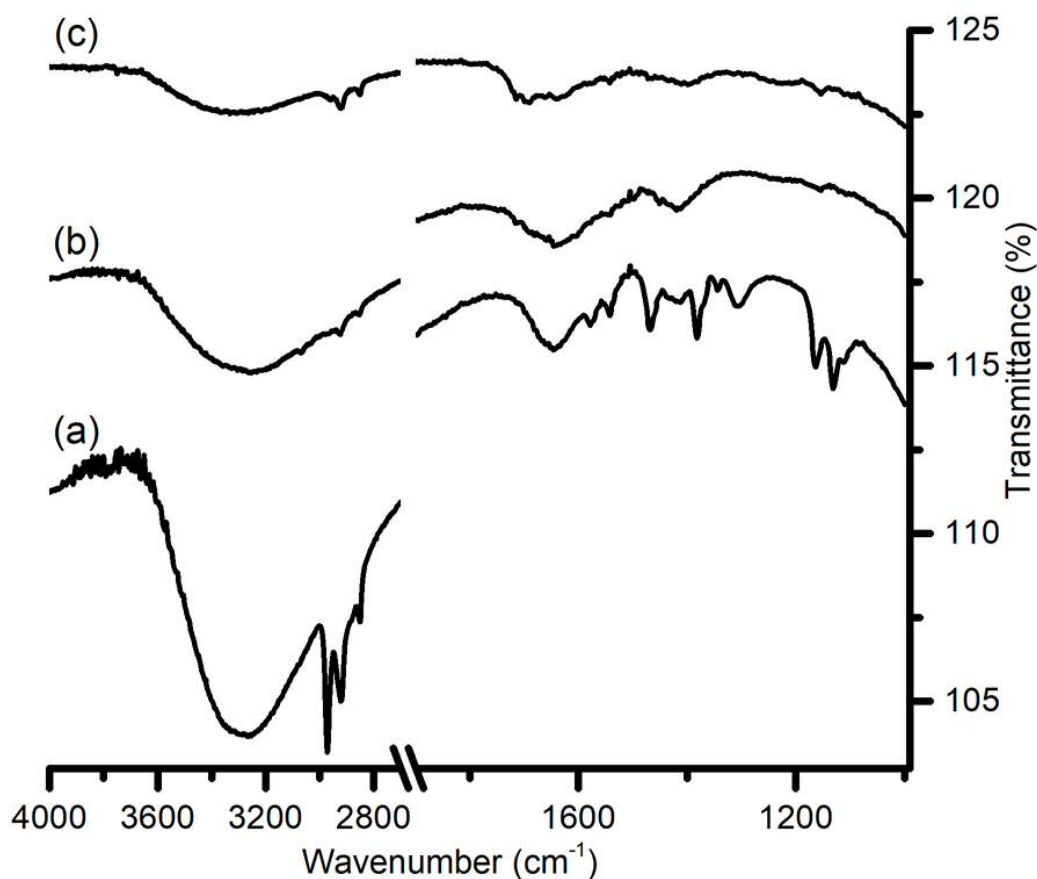


Figure 3.2.1.4: ATR spectra of a fresh mP25 and spent mP25 from CA acid reactions: (a) spent mP25, (b) mP25 spent (deoxy), (c) spent P25

3701 cm^{-1} that possibly relates to a hydroxylated TiO_2 species from UV irradiation. [24] No other bands are observed and the, already weak, C-H stretches are now almost undetectable. In conjunction with the XPS it is clear that most of the carbon has been removed during irradiation. Numerous new signals are observed in the spent mP25 sample, a compiled list of peaks and assignments are shown in **Table 3.2.1.3**. The alkyl C-H stretches are considerably stronger and the H_2O bend at 1633 cm^{-1} has shifted up slightly to 1640 cm^{-1} . Three bands at 1109, 1132 and 1164 cm^{-1} can be seen that sit in a region often characterised as C-O and C-C stretches of alcohol functionalities bound to the titania surface. [25][26][27] Assignment of the peaks is difficult with the unknown nature of the adsorbed molecules, however, the stretches at 1132 and 1164 cm^{-1} are of similar wavenumber to those detected during acetaldehyde degradation by Topliani *et al.*, who assigned them to C-C stretches of

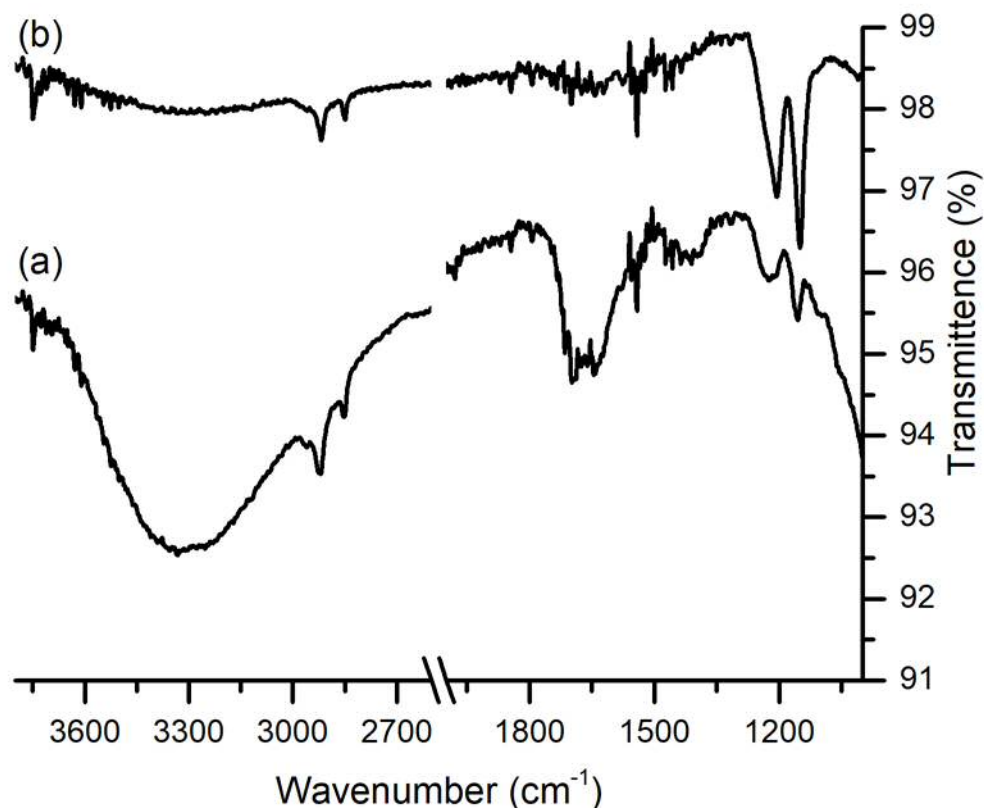


Figure 3.2.1.5: ATR IR spectra of the spent mP25 from : (a) CinnamylA and (b) CinnamylA (deoxy) reactions

acetaldehyde and crotonaldehyde. [27] Given that there are no signs of any carbonyl groups in the typical region, $1670 - 1820 \text{ cm}^{-1}$, it is fair to assert that the oxygen based functionalities that remain post-photocatalytic degradation are not of a carbonyl character. The peaks in the next region of this IR spectrum, $1280 \text{ to } 1500 \text{ cm}^{-1}$, are likely to be caused by aliphatic CH_2 and CH_3 bending. The peak at 1304 cm^{-1} is within the region for a carboxylic C-O stretch but the lack of associated C=O and O-H frequencies rules out the possibility of a residual carboxylic species. It is more feasible that these frequencies are caused by the numerous small chained hydrocarbons that are known to be produced from the mineralisation of aromatic compounds such as phenol. [49][50] Therefore, the frequencies could be tentatively assigned, based on their increasing wavenumber, as: 1304 cm^{-1} (CH_2 wagging), 1344 cm^{-1} , 1382 cm^{-1} (CH_3 symmetric bending), 1417 cm^{-1} (CH_3 antisymmetric

| IR Frequency (cm ⁻¹) | Assignments | CinnamylA | CinnamylA (deoxy) |
|----------------------------------|--|------------------|-------------------|
| 3747 | v(O-H) | medium | medium |
| 3332 | v(O-H) -s | broad | / |
| 2959 | CH ₃ antisym-s | weak | / |
| 2920 | CH ₂ antisym-s | strong | medium |
| 2849 | CH ₃ sym-s | medium | medium |
| 1982 | v(C=C) assym-s | weak | / |
| 1715 | v(C=O) coordinated CO ₂ | weak | / |
| 1697 | v(C=O)-s O=C-H-Ph | strong | / |
| 1663 | aliphatic v(C=C) sym-s | weak | / |
| 1639 | v(O-H) H ₂ O bend | medium | / |
| 1546 | Aromatic v(C=C) -s | medium | medium |
| 1460 | Aromatic v(C=C) -s | weak | weak |
| 1398 | v(C-H)-b H-CO-Ph | weak | / |
| 1225 | v(C-O) coordinated CO ₂ | medium, broad | / |
| 1206 | v(C-O) | / | strong |
| 1153 | v(C-O)-b HO- CCHCH ₂ -Ph | medium | strong |

Table 3.2.1.4: - Infrared frequencies and the associated assignments for the spent mP25 from the cinnamyl alcohol reactions

bending), 1469 cm⁻¹ (CH₂ scissoring). The next set of peaks, 1541 and 1576 cm⁻¹, are in a region often associated with aromatic C=C and so suggest that there is still some aromaticity present, despite the extensive mineralisation of the substrate. The final set of peaks (2855, 2923, 2974 cm⁻¹) are very characteristic of aliphatic C-H stretching and can be assigned as; 2855 cm⁻¹ (CH₃ symmetrical stretching), 2923 cm⁻¹, (CH₂ antisymmetric stretching) and 2974 cm⁻¹ (CH₃ antisymmetric stretching). [27] These data exclude the possibility of several functionalities being deposited post reaction. Firstly, the lack of C=O vibration excludes the possibility of any carbonyl forming here with the more feasible oxygen moiety being alcoholic in nature. Carbonates are potentially present however the XP spectra do not support their presence. XP spectra also indicate the presence of delocalisation, but the IR data eliminates aromaticity of a benzene ring or graphene as a contender. Instead the

delocalisation must be due to conjugated unsaturated hydrocarbons. The spent catalyst, from the reaction under deoxygenated conditions, provided IR spectra with a few key changes. Peaks in the region of 2850 – 3000 cm^{-1} again signify aliphatic CH_2/CH_3 stretches; but the peak at 3072 cm^{-1} , which is mostly hidden under the water band, is symptomatic of aromatic C-H stretching. The aliphatic C-H frequencies probably relate to a variety of carbonaceous species on the surface. Unfortunately, the large band at 1644 cm^{-1} makes it difficult to make out the convoluted peaks in that region. From GC-MS analysis we know that **3** is the only detectable intermediate formed and it doesn't appear to degrade after 3 hours. Based on the assignments of acetaldehyde on titania, by Topliani *et al.*, [27] one could suggest: 1749 cm^{-1} ($\nu(\text{C}=\text{O})$ Hydrogen bonded (**3**)) 1714 cm^{-1} ($\nu(\text{C}=\text{O})$ $\text{Ti}-\text{O}=\text{C}-\text{CH}_2-\text{Ph}$), 1680 cm^{-1} ($\nu(\text{C}=\text{O})$ $\text{V}_\text{O}-\text{O}=\text{C}-\text{CH}_2-\text{Ph}$), 1643 cm^{-1} ($\nu(\text{O}-\text{H})$ H_2O bend) and 1602 cm^{-1} ($\nu(\text{C}=\text{C})$ aromatic skeletal stretches). 1602 cm^{-1} is the typical stretches of an aromatic ring $\text{C}=\text{C}$, whilst the frequencies in the region of 1680 to 1749 cm^{-1} are variations of the aldehyde component of **3** bonded to TiO_2 . Topliani observed the acetaldehyde frequency shift up by 10 cm^{-1} from the free carbonyl to the adsorbed hydrogen bonded species, which is consistent with our measured peak shifting from 1740 cm^{-1} to 1749 cm^{-1} . Whereas **2** has a reference carbonyl frequency of 1701 cm^{-1} that would be unlikely to shift by 50 wavenumbers. [appendix 2.2] The 1451 cm^{-1} peak is observed in acetaldehyde and can be assigned to the C-H bending of the CH_2 group that links the aldehyde to the phenyl group. These assignments appear to conclusively show that the only molecule deposited on the surface after reaction is **3** and that the aromatic ring does not provide the delocalisation required to give a $\pi-\pi^*$ component in XP spectra. Notably, the strength of all the vibrations relating to adsorption of **3** are very weak.

Fresh P25 shows the same range of vibrations as fresh TiO_2 , which are the $\nu(\text{O}-\text{H})$ stretching and $\nu(\text{H}_2\text{O})$ bending modes at 3200-3500 cm^{-1} and 1639 cm^{-1} , respectively. Spent P25 appears to show signs of both carbonyls and aromaticity present, unlike spent TiO_2 . The usual aliphatic C-H stretches are seen at 2962 cm^{-1} (CH_3 antisymmetric stretching), 2923 cm^{-1} (CH_2 antisymmetric stretching), 2850 cm^{-1} (CH_3 symmetrical stretching); which are accompanied by a weak peak at 3069 cm^{-1} ($\nu(\text{C}-\text{H})$ aromatic C-H stretch). A variety of peaks are visible in the carbonyl region at: 1716, 1694, 1660, and 1639 cm^{-1} . 1639 cm^{-1} will be the $\nu(\text{H}_2\text{O})$ bend, whilst the other frequencies are indicative of a TiO_2 bound aldehyde as seen in the mP25 (deoxy) sample. The key intermediates, **2** and **3**, are both aromatic aldehydes that could be present. However, deconvolution of the spectra to accurately examine the peaks is unrealistic, considering the strength of the signals. At best one could indicate a very weak

peak at 1453 cm^{-1} to hint at the presence of $\nu(\text{C-H})$ bending of a CH_2 . Since these carbonyls are detected it suggest that 100% mineralisation did not occur here.

Figure 3.2.1.5 shows the stacked ATR spectra for the used catalysts from the cinnamylA and cinnamyl B reactions. The detected frequencies and the related assignments can be found in **Table 3.2.1.4**. Both spectra have the peak at 3747 cm^{-1} that can only be assigned to a photocatalytically induced O-H species. [26] The broad and intense peak centred of 3332 cm^{-1} , that is only seen in cinnamylA, is caused by $\nu(\text{O-H})$ stretching; whilst the region from $2850\text{-}3000\text{ cm}^{-1}$ indicates the same aliphatic C-H stretching modes as explained previously for both reactions. A very weak vibration at 3015 cm^{-1} for cinnamylA, is again suggestive of aromatic C-H stretching mode, although the strength of the peak makes it questionable. Additionally, it would be expected to see this aromatic C-H band with CinnamylA (deoxy) but it is not visible. Despite the convolution of the peaks from $1750\text{-}1550\text{ cm}^{-1}$, a $\nu(\text{C=C})$ symmetric stretch can be made out at 1663 cm^{-1} for cinnamylA and one could weakly assert that it is also present at the same wavenumbers for CinnamylA (deoxy). CinnamylA also has $\nu(\text{C=C})$ asymmetric stretch at 1982 cm^{-1} that is not visible for CinnamylA (deoxy), presumably due to the weak nature of the associated vibrations. CinnamylA is the only spent catalyst that showed strong signs of carbonyls being present with a peak at 1697 cm^{-1} . Given that GCMS showed **2** as the primary intermediate, still present in solution after 3 hours, it is probable that the peak corresponds to $\nu(\text{C=O})$ stretching frequency of **2**. Of the remaining peaks for cinnamylA, 1398 cm^{-1} could be assigned to $\nu(\text{C-H})$ bending of a bound aldehyde. 1225 cm^{-1} , unique to the spent catalyst from cinnamylA, sits in a region often representative of $\nu(\text{C-O})$ bending which is a bending mode that is not predicted based on the species believed to be present. The broadness, and appearance, of the peak suggests there may also be a peak at 1206 cm^{-1} . CO_2 is expected from the reaction however, and reports have found CO_2 bound to TiO_2 to resonate at a similar wavenumber. [27] As such, 1225 and 1715 cm^{-1} have been assigned to $\nu(\text{C-O})$ and $\nu(\text{C=O})$ of coordinated CO_2 . The final peak at 1153 cm^{-1} , as well as the peak obscured by the CO_2 bending mode at 1225 cm^{-1} , is common to both cinnamylA and B, could be assigned to C-O bending on an sp^3 carbon of the alcohol functionality of the starting material. This accounts for the greater intensity seen with both peaks in the CinnamylA (deoxy) reaction, due to the lack of degradation of the starting material. This indicates that photocatalyst from cinnamylA has an aromatic aldehyde bound to the surface, most likely **2**, accompanied by some of oxidised carbon from the parent molecule. Additionally, some cinnamyl alcohol remains unreacted

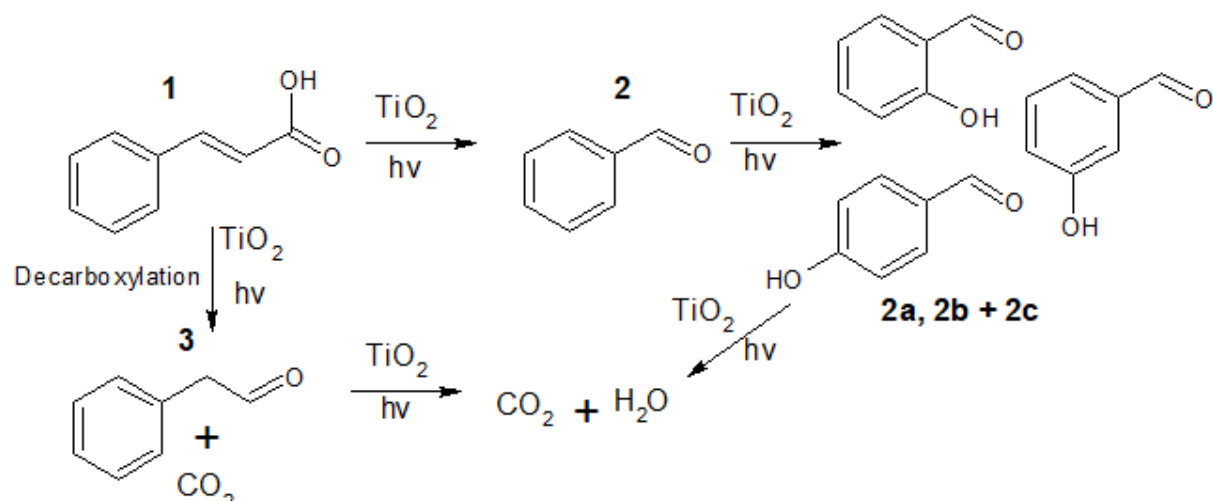
and bound to the surface after 3 hours of reaction. For CinnamylA (deoxy) the IR data shows minor signs of aromaticity and no sign of a carbonyl. GC-MS data showed the substrate did not degrade under these conditions so the expected molecules adsorbed would be the substrate itself. Comparison of the spectra to the reference spectra in **appendix 2.4** found several similar peaks. XP spectra agree with this hypothesis as a strong π - π^* component is observed that could be created by extended conjugation in cinnamyl alcohol. This interaction is probably not detected in the cinnamylA reaction as the majority of the carbon left on the catalyst surface is found to be CO₂ and **2**.

1.2.1.6 X-Ray Diffraction Studies of Fresh and Spent Catalysts

XRD of the fresh TiO₂ photocatalyst, that can be found in **Figure 3.2.2.5**, gave peaks at 2θ values of: 25.44 (A 101), 27.56 (R 110), 36.25, 37.12 (R 101), 38.00 (A 004), 38.77 (), 41.37 (R 111), 48.22 (A 200), 54.21 (A 105), 54.39 (A 211), 55.21 (), 62.89 (A 204), 69.06 (A 116), 70.42 (A 220) and 75.27 (A 215). This diffraction pattern is typical of a mixed phase titania pattern, as would be expected from a sample made from P25. Application of the Debye-Scherrer equation gave an anatase crystallite size of 21.75 nm and a rutile crystallite size of 31.52 nm from the anatase 101 and rutile 110 reflections respectively.

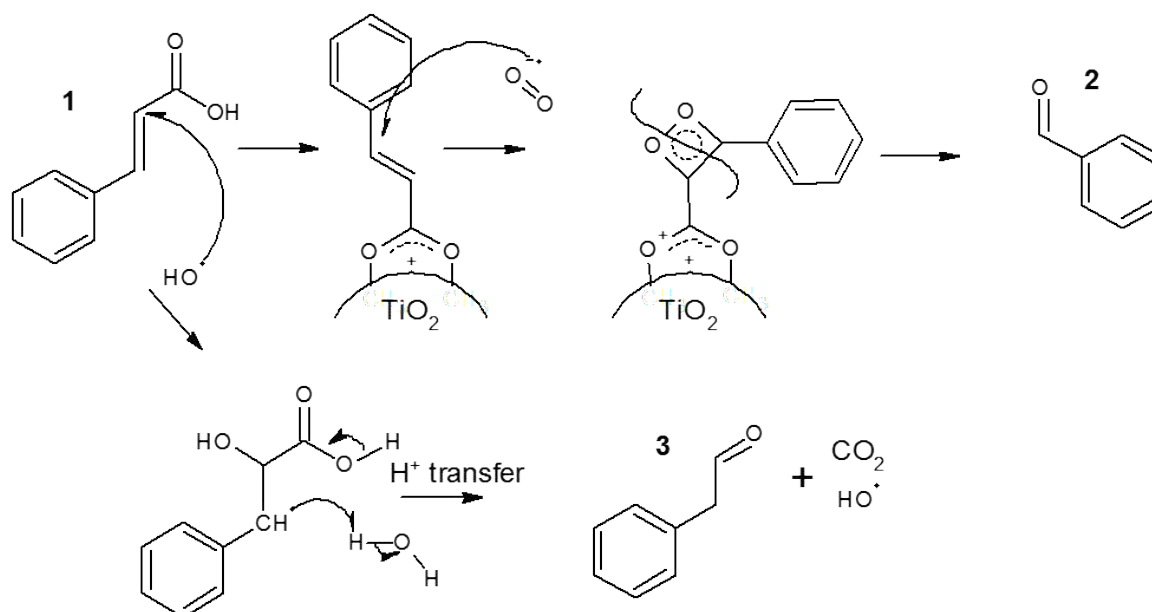
3.2.1.7 Proposed Model for the Photocatalytic Degradation of Cinnamic Acid

Based on the above data, it is evident that dissolved oxygen plays a vital role in the degradation of CA. The flowing of N₂ gas causes a clear inhibition of the removal of CA that is accompanied with the loss of **2** as a detectable intermediate, as well as the continued formation of **3**. Assuming that the majority of dissolved O₂ is removed the most available radical oxygen species would be a hydroxyl radical. Although hydroxyl radicals are capable for forming superoxide radicals, the kinetics do not favour significant superoxide levels by this route. As such, the data indicates that dissolved oxygen, in the superoxide radical state, is a required component for the formation of **2**. These data agree with the findings of Maeda *et al.* who described the role that oxygen radicals play in the degradation of CA. [29] Maeda *et al.* proposed that CA binds to the surface of titania to form a bound radical cation species that is attacked by a superoxide/hydroperoxyl radical. The oxygen radical binds across the double bond of CA resulting in the cleavage of the double bond and the formation of benzaldehyde. Several groups have reported the superoxide led oxidation of halogenated aromatic systems



Mechanism 3.2.1.1: The general route for the photocatalytic degradation of cinnamic acid by titania, showing the key intermediates and double bonds that occurs in a similar manner to that described above. [30][31] CO₂ detection found that 100% of the expected carbon was released during the reaction containing just TiO₂ strongly indicating total oxidation had occurred, whilst under deoxygenated conditions just 8.6% was released. This tells us that the benzaldehyde route is vital for total oxidation to occur and that dissolved oxygen is essential. Further reaction of benzaldehyde, resulted in the detection of the intermediates **2a**, **2b**, and **2c**. The substitution of the hydroxyl moiety is evidently due to the hydroxyl radical attack on the ortho, para and meta positions of the aromatic ring. Where aromatic rings are present, hydroxyl radicals are known to substitute aromatic rings in preference to hydrogen abstraction. [32] Considering the non-specific nature of this radical it is not surprising to detect all three hydroxybenzaldehydes. The natural step after this is likely to be a second hydroxylation and the subsequent ring opening. The species we'd expect to evolve after ring opening are likely to be small molecule organics like methanol that would be burned off rapidly in the GC meaning they would be undetectable by the analysis method. Given the work cited and our data it is reasonable to assert that CA degrades primarily via the mechanism seen in **Mechanism 3.2.1.2**. The surface bound reaction of CA would result in the deposition of some carbonaceous species which is observed in the spent catalyst analysis.

The formation of the other breakdown product, **3**, is very likely to be via a different mechanism to **2** since it still forms under deoxygenated conditions and so the involvement of dissolved oxygen can be ruled out. The next option for potential photocatalytically formed species would be hydroxyl radicals. Superoxide is formed via the reaction of molecular oxygen with a conduction band electron, whilst hydroxyl radicals are typically formed from the reaction of a hydroxide ion or water molecule with a photogenerated hole. As such,



Mechanism 3.2.1.2: Proposed mechanism depicting the formation of benzaldehyde (**2**) and phenylacetaldehyde (**3**)

hydroxyl radicals would be abundant in our system as long as e^-/h^+ recombination rates do not exceed the deactivation of h^+ , and would be readily available for reaction. One possible mechanism is a decarboxylation such as the Photo-Kolbe decarboxylation. This however, would produce a carboxylic acid, not an aldehyde, and it is widely understood to occur using molecular oxygen. These reasons run contrary to our data so it is not a realistic option. The more feasible option is one presented by Santos *et al.* [33] Santos utilised gamma radiolysis to generate hydroxyl radicals to react with CA and found **3** formed in the absence of dioxygen radical species. Their proposed mechanism involves the hydroxylation of the position α to the carboxylic acid moiety on the exocyclic C=C, and the subsequent decarboxylation to give a styryl alcohol that tautomerises to **3**. **3** is only one carbon shorter than CA leading to the prediction that the carboxyl group would be release carbon dioxide. CO₂ capture experiments indicated that roughly 9% of the total carbon of CA was released, after three hours, under deoxygenated conditions which is less than the expected 11% carbon if every CA molecule were to be decarboxylated. A slightly lower CO₂ detection can be attributed to its solubility in aqueous media, however it also indicates that total oxidation is not favoured by just radical hydroxylation. Previous research by Bui *et al.* noted two potential mechanisms for benzene oxidation that utilise hydroxyl radicals, although no testing was done under oxygen free conditions so it cannot be confirmed that hydroxyl radicals alone can completely mineralise an aromatic system. [34] It should be noted that the concentrations of **3** detected do not match the expected amounts. This is potentially because of the poor solubility

of **3** in aqueous media leading its concentration to steadily increase over the course of the reaction.

The data collected from the cinnamyl alcohol reaction cinnamylA shows that the key route for degradation involves the oxidation of the primary alcohol to the corresponding aldehyde, cinnamaldehyde, and benzaldehyde (**2**). Previous research has shown that cinnamyl alcohol readily oxidises to cinnamaldehyde and then cinnamic acid upon exposure to air. [35] It is therefore suspected that cinnamyl alcohol is oxidised through to CA, however CA does not readily appear in GC-MS and UV spectroscopy was not performed in this case, so it is not known if CA did form. **2** forms slowly from the beginning of irradiation and accumulates throughout the reaction. It cannot be ascertained if **2** forms directly from cinnamyl alcohol or one of its oxidation products. Rossi *et al.* found that cinnamyl alcohol could be selectively oxidised to cinnamyl aldehyde, by catalytic Ag-Au oxidation, so long as a radical trap was present. They suggested that **2** formed via a radical cleavage of the C=C of cinnamaldehyde in solution. This could also mean that in our reaction **2** forms only from cinnamaldehyde. These processes were not observed in the reaction where oxygen was purged (CinnamylA (deoxy)). The aldehyde was observed in the initial aliquot (-30 minutes) before irradiation indicating the oxidation has begun in the short time between preparation of the solution and beginning to flow N₂ gas and purge the dissolved oxygen. The concentration of the aldehyde is not observed to increase throughout the reaction, and the concentration of the alcohol does not show signs of decreasing, implying that dissolved oxygen is required for the aqueous oxidation to the aldehyde and the photocatalysed oxidation. Additionally, this data also suggests that the hydroxyl radicals do not readily react with the alcohol. One could postulate that it is because the hydroxyl radical attack has a transition state that requires an appropriate leaving group, like carbon dioxide, that is not present. Future work need to determine if total oxidation of the substrate, within the 3 hour reaction time, is using UV measurements and CO₂ capture.

3.2.2 The Effect of Sulfates on the Degradation of Cinnamic Acid

3.2.2.1 Kinetic and Mechanistic Impact of Sulfate on Cinnamic Acid Degradation

Table 3.2.2.1 summarises the effect of sulfates on the photocatalytic degradation of cinnamic acid. Both potassium and sodium sulfate caused similar inhibitions of degradation rates. 0.05 and 0.1 molar concentrations of either salt resulted in a 4X reduction in CA

| Reaction Conditions | 1 st Order rate (s ⁻¹) | + N ₂ Flow |
|--|---|-----------------------|
| mP25 | 0.089 | 0.020 |
| mP25 + 0.05M Na ₂ SO ₄ | 0.027 | / |
| mP25 + 0.1M Na ₂ SO ₄ | 0.021 | 0.008 |
| mP25 + 0.5M Na ₂ SO ₄ | 0.022 | / |
| mP25 + 0.05M K ₂ SO ₄ | 0.022 | / |
| mP25 + 0.1M K ₂ SO ₄ | 0.020 | 0.006 |
| mP25 + 0.5M K ₂ SO ₄ | 0.020 | / |

Table 3.2.2.1: The effect of sulphate and oxygen-removal on the photocatalysed degradation of cinnamic acid

removal rates, as seen in **Table 3.2.2.1**, where rates fell to below 0.028 s⁻¹. Increasing salt concentrations 0.5M did not result in further slowing of degradation. Flowing nitrogen through the reaction caused a further inhibition of CA degradation rate; in both cases, flowing nitrogen had an accumulative effect where the rate was reduced to 0.008/0.006 s⁻¹ for Na₂SO₄/K₂SO₄ respectively. Similar to the no catalyst control (0.008s⁻¹), the measured rates suggest the reaction is entirely inhibited and reduced to just the light-activated degradation. CO₂ capture experiments, **Figure 3.2.1.2**, shows that the rate of CO₂ evolution is the same in the presence of 0.1M K₂SO₄ as in its absence. Although, the rate of evolution did slow down, in the final 60 minutes of reaction, 81.10 % of carbon was released as CO₂. In the absence of oxygen, just 12.87 % of carbon was released after 150 minutes and it produced a profile similar to that in the absence of the sulfate.

An analysis of intermediate formation, using GCMS, found that sulfates do not initiate new degradation pathways or produce new sulfated intermediates. Data shows that, even with lower concentration, that the presence of sulfate correlates to a decreased rate of **2** production. Addition of 0.05M of either the Na or K sulfate caused a halving of the maximum benzaldehyde concentration as well as a decrease in the rate of benzaldehyde removal, as seen in **Figure 3.2.2.1 (a)** and **(b)**. Sulfate concentration of 0.1M showed minimal change to the formation of **2**; however, a tenfold increase in potassium/sodium sulfate concentration saw a large decrease in **2** formation with 0.18/0.52 mgL⁻¹ being detected after 20 minutes, respectively. Whilst flowing N₂ throughout the reaction was coupled with the complete inhibition of the formation of **2**. Concentrations of **2** were significantly

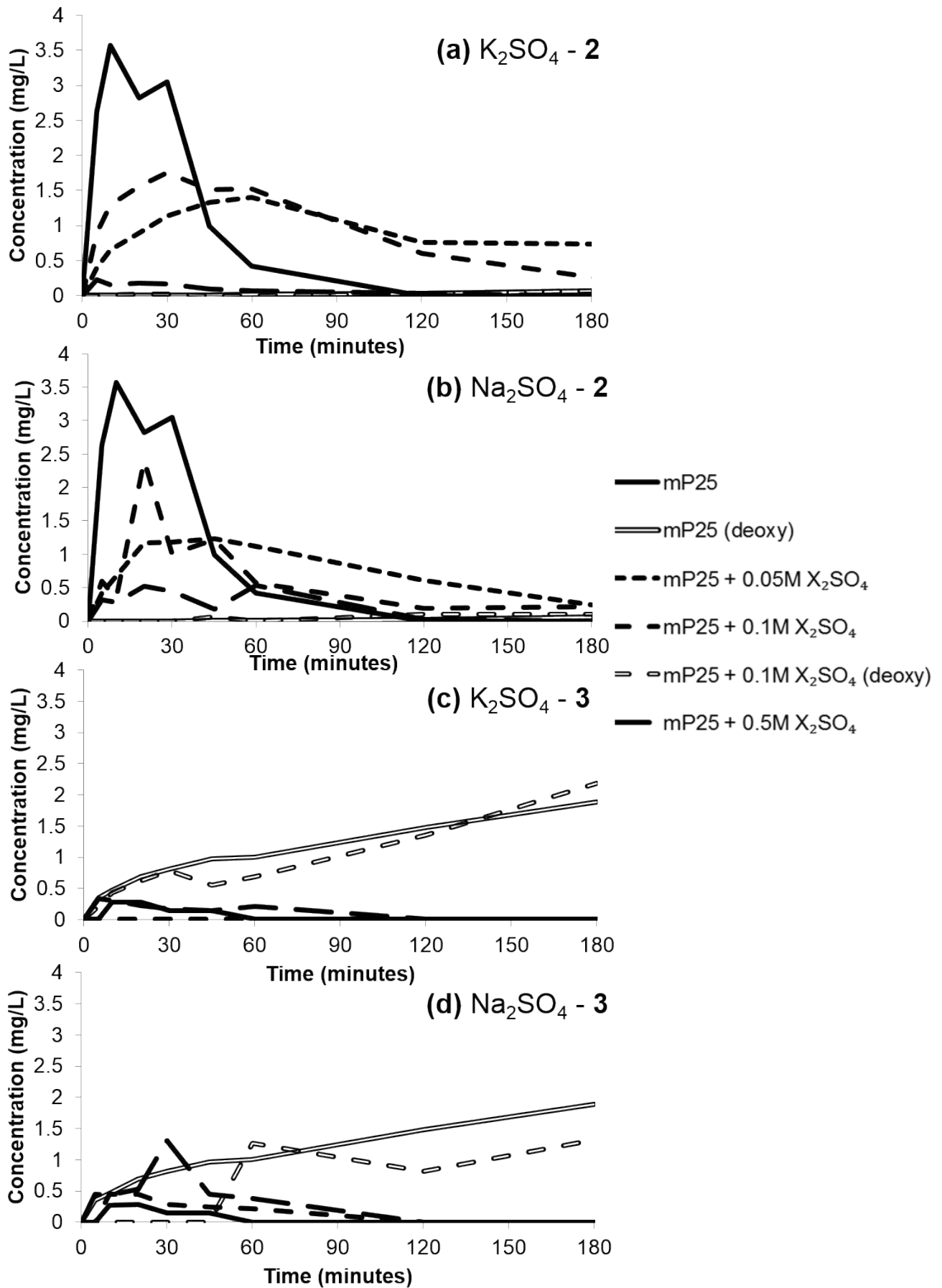


Figure 3.2.2.1: Concentration profiles showing the change in concentration of benzaldehyde (2) and phenylacetaldehyde (3) in the presence of increasing concentrations of potassium sulphate (a) and (c) and sodium sulphate (b) and (d)

The legend (to the right) shows the reaction conditions, where “X” refers to potassium (K) or sodium (Na)

decreased with concentrations rarely exceeding 0.03 mgL^{-1} in the presence of either sulfate. **3** displayed small changes to production in the presence of sulfate. **3** wasn't detected when 0.05M sulfate, sodium or potassium, was dissolved in solution. In almost all cases, in oxygenated conditions, the formation of **3** was near identical to under standard conditions. Although it should be noted that removal of **3** was slower.

Intermediates **2a**, **2b** and **2c** were all occasionally detected during the reactions. During reactions containing sulfate, an eluent was intermittently observed at 20.13 minutes that had a parent mass peak of 138 which matches the molecular mass of dihydroxybenzaldehyde (**appendix 1.3.1**). Peaks at m/z s of 109 and 92 correspond to $[\text{HOC}_6\text{H}_3\text{OH}]^+$ and $[\text{C}_6\text{H}_3\text{OH}]^+$, respectively. Deoxygenated conditions also gave similar production levels of **3**, as was found in the standard reaction under deoxygenated conditions. Assuming the potential mechanisms for formation of **2** and **3** from cinnamic acid are correct, this data implies that sulfates have a greater effect on the O_2 driven mechanism. However,

| Sample Name | C1s (C-C) | C1s(C-O) | C1s (C=O) |
|---------------------------------------|-------------------------|----------------|---------------|
| 0.05M Na_2SO_4 | 284.7(45.1%) | 286.4 (35.9%) | 288.5 (19.0%) |
| 0.1M Na_2SO_4 | 285.0 (81.2%) | / | 288.7 (18.9%) |
| 0.1M Na_2SO_4 (deoxy) | 284.8 (80.3%) | 286.4 (11.5%) | 288.8 (8.2%) |
| 1M Na_2SO_4 | 284.5(56.1%) | 286.1 (25.9%) | 288.3 (18.1%) |
| 0.05M K_2SO_4 | 284.7 (53.4%) | 286.3 (26.7%) | 288.5 (20.0%) |
| 0.1M K_2SO_4 | 284.8 (68.7%) | 286.4 (16.7%) | 288.7 (14.6%) |
| 0.1 M K_2SO_4 (deoxy) | 284.8 (79.4%) | 286.4 (11.4%) | 288.7 (9.2%) |
| Sample Name | O1s (O^{2-}) | O1s (C-O) | |
| 0.05M Na_2SO_4 | 529.8 (81.6%) | 531.53 (18.5%) | |
| 0.1M Na_2SO_4 | 529.8 (72.3%) | 531.1 (27.2%) | |
| 0.1M Na_2SO_4 (deoxy) | 530.0 (87.8%) | 531.7 (12.2%) | |
| 1M Na_2SO_4 | 529.8 (93.4%) | 531.5 (6.6%) | |
| 0.05M K_2SO_4 | 529.8 (87.1%) | 531.5 (12.9%) | |
| 0.1M K_2SO_4 | 529.8 (83.5%) | 531.5 (16.3%) | |
| 0.1 M K_2SO_4 (deoxy) | 529.8 (82.7%) | 531.5 (17.4%) | |

Table 3.2.2.2:- Top: A table showing the percentage concentrations of the carbon 1s components for spent photocatalysts from the sulphated reactions.

Bottom: A table showing the percentage concentrations of the oxygen 1s components for spent photocatalysts from the sulphated reactions.

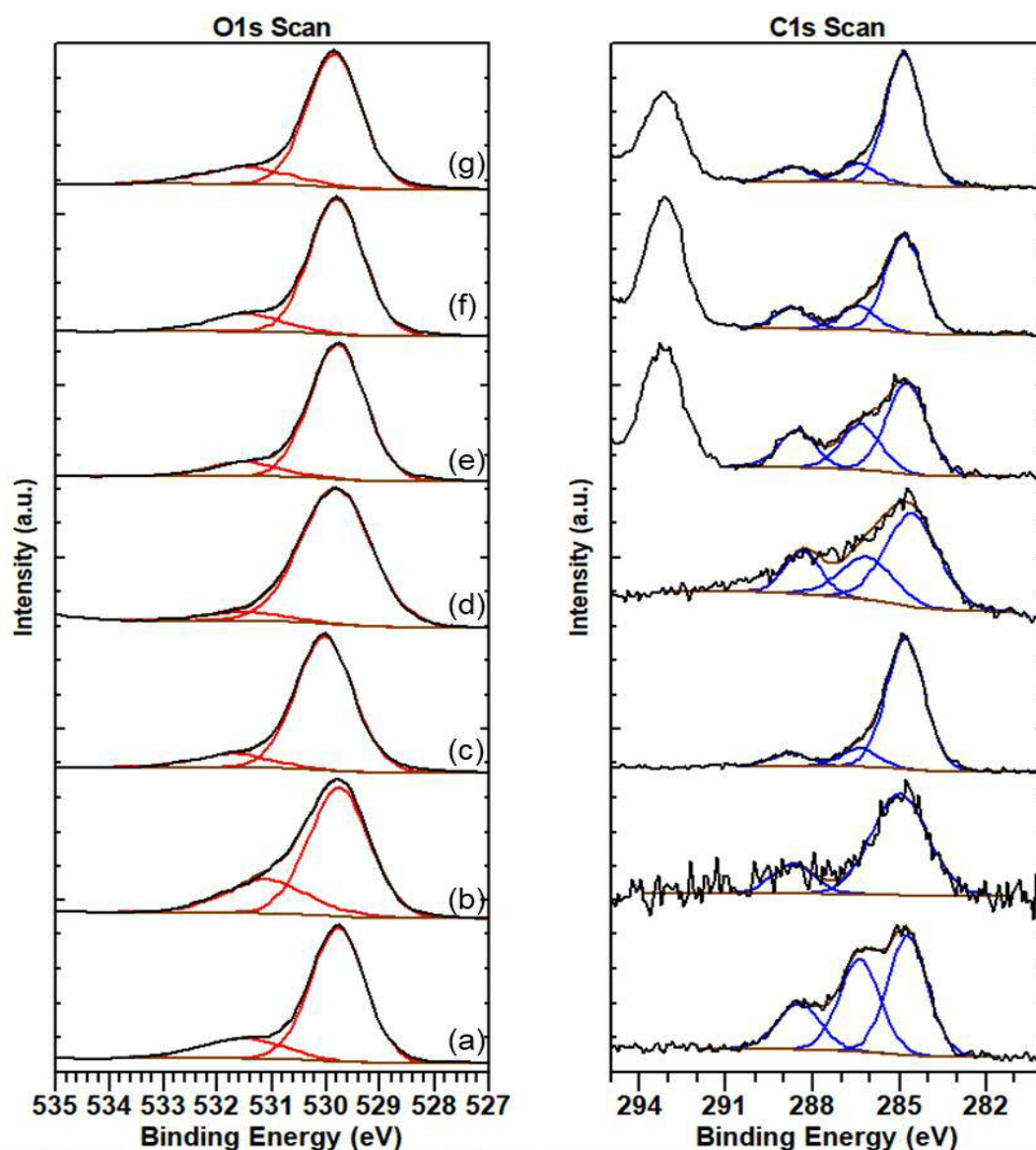


Figure 3.2.2.2: Deconvoluted oxygen 1s (left) and carbon 1s (right) spectra for: **(a)** 0.05M Na_2SO_4 , **(b)** 0.1M Na_2SO_4 , **(c)** 0.1M Na_2SO_4 (deoxy), **(d)** 1M Na_2SO_4 **(e)** 0.05M K_2SO_4 , **(f)** 0.1M K_2SO_4 , **(g)** 0.1M K_2SO_4 (deoxy).

data in section 3.2.1 indicates that **2** degrades via its hydroxylated intermediates most likely implicating hydroxyl radicals as the oxidative species. **3** also appears to form using a hydroxylation mechanism yet its direct formation from cinnamic acid is not affected by sulfates. An explanation for this data is that the formation of **3** is not happening entirely on the surface, but may also occur in solution.

3.2.2.2 XPS studies of Spent Photocatalysts from Sulphated Reaction Media

Percentage concentrations for the spent catalysts from the sulfate reactions can be found in **Table 3.2.1.1**, with the curve fitted C1s and O1s spectra for **3.2.2** in **figure 3.2.2.2**. The Ti 2p region was, again, most appropriately fitted with a Shirley background and an SGL line shape. The presence of sulfate in the reaction showed no effect on the chemical state of the titania at any concentration. Analysis of the S 2p region for all samples showed two peaks at 168.50 eV and 169.66 eV that correspond to S2p_{3/2} and S2p_{1/2} respectively. The O 1s region was only peak fitted with two components, as seen in **Figure 3.2.2.2**, and it can be seen that the shoulder at 531.5 eV is significantly larger than in the absence of sulfates. These apparently elevated levels of C-O oxygen can actually be attributed to the presence sulfate oxygen that has been reported to appear around 531.2 eV. [36][37][38] Lower carbon levels are observed for all oxygenated sulfate reactions in comparison to catalysts from non-sulfated conditions. Examination of the C 1s environments, which can be found in **Table 3.2.2.2**, indicated a marked increase in the ratio of oxygenated carbon chemical states. Levels of C-O carbon were higher on all accounts in comparison to both fresh and spent TiO₂ samples, whereas C=O carbon was observed to be up to double the percentage of that found in fresh TiO₂. Notably, the no π - π^* interaction was observed for any of the samples. Powders analysed after reactions with nitrogen flow had surface carbon concentrations double that of the oxygenated equivalents. While increasing sulfate concentrations appears to correlate to decreasing carbon content, flowing nitrogen resulted in concentrations of around 14 – 16 atomic %. Narrow scans showed this carbon was of a highly C-C character, as seen in **Table 3.2.2.2**. The C-C peak at 284.8 eV, for both sodium and potassium sulfate, constituted 80% of the carbon peak, with both C-O and C=O character seeing a marked fall in total composition.

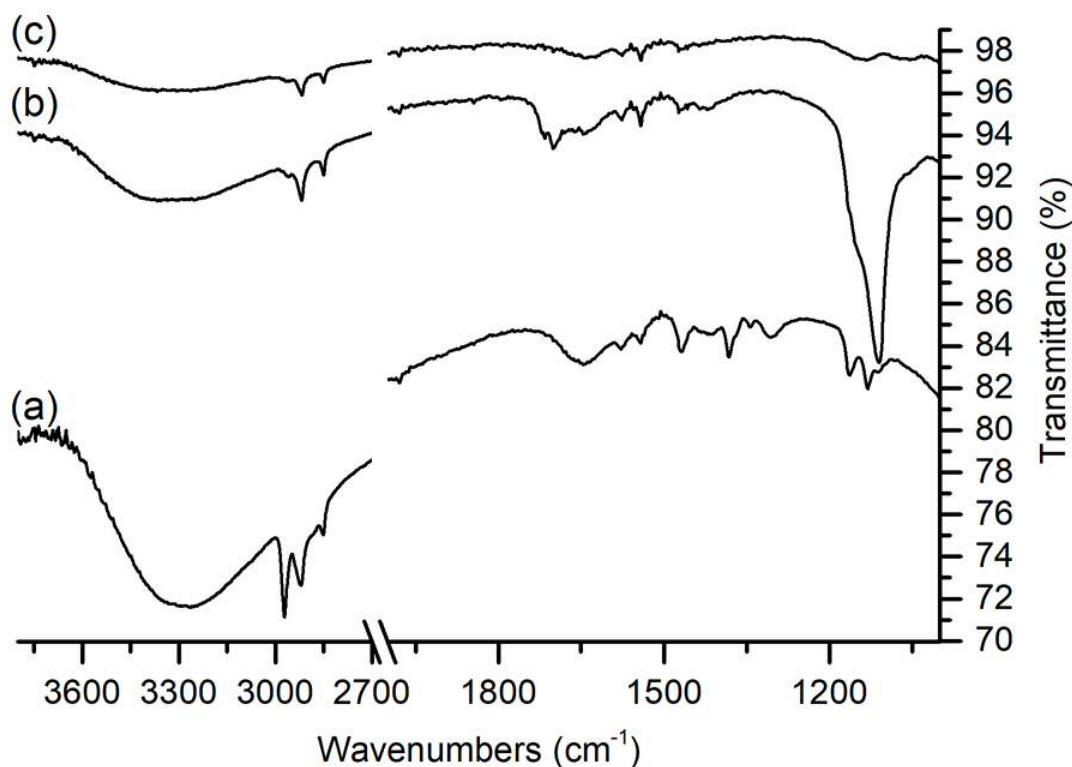


Figure 3.2.2.3: ATR IR spectra for (a) mP25 spent, (b) mP25 + 0.1M K₂SO₄, (c) mP25 + 0.1M Na₂SO₄

3.2.2.3 Infrared studies of Spent Photocatalysts from Sulphated Reaction Media

ATR spectra of the 0.1M K₂SO₄ and 0.1M Na₂SO₄ spent catalysts can be seen in **Figure 3.2.2.3** and the compiled peak lists with their assignments can be found in **Table 3.2.2.3**. Catalysts from the 0.05M and 0.1M K₂SO₄ reactions both exhibit the same IR vibrations with different intensity. The peaks between 2850-3000 cm⁻¹, on all three spectra, are likely to be the aliphatic C-H stretches as described in **3.2.1**. In both 0.1M sulfate spectra however, the peak ratios are very different from the TiO₂ spent sample analysed previously. The peak at 2960 cm⁻¹ is significantly weaker, compared to the other two found in the region, and both the other peaks are shifted down by 5 wavenumbers. This difference suggests a difference in environment compared to sulfate free spent catalysts. From the GC-MS data, in the presence of oxygen the two aldehydes, **2** and **3**, are produced in similar amounts leading us to expect a mix of aldehydes in the carbonyl region. A new dimension is added by the presence of sulfate; Topalian *et al.* showed that dosing the TiO₂ surface with sulfate provides new vibrational modes for aldehydes. [27] Based on their findings it is feasible that the strongest vibrations at 1700 and 1680 cm⁻¹, in 0.1M K₂SO₄, could be assigned as $\nu(\text{C}=\text{O})$ for an aldehyde interacting with adsorbed sulfate species and so these two vibrations are

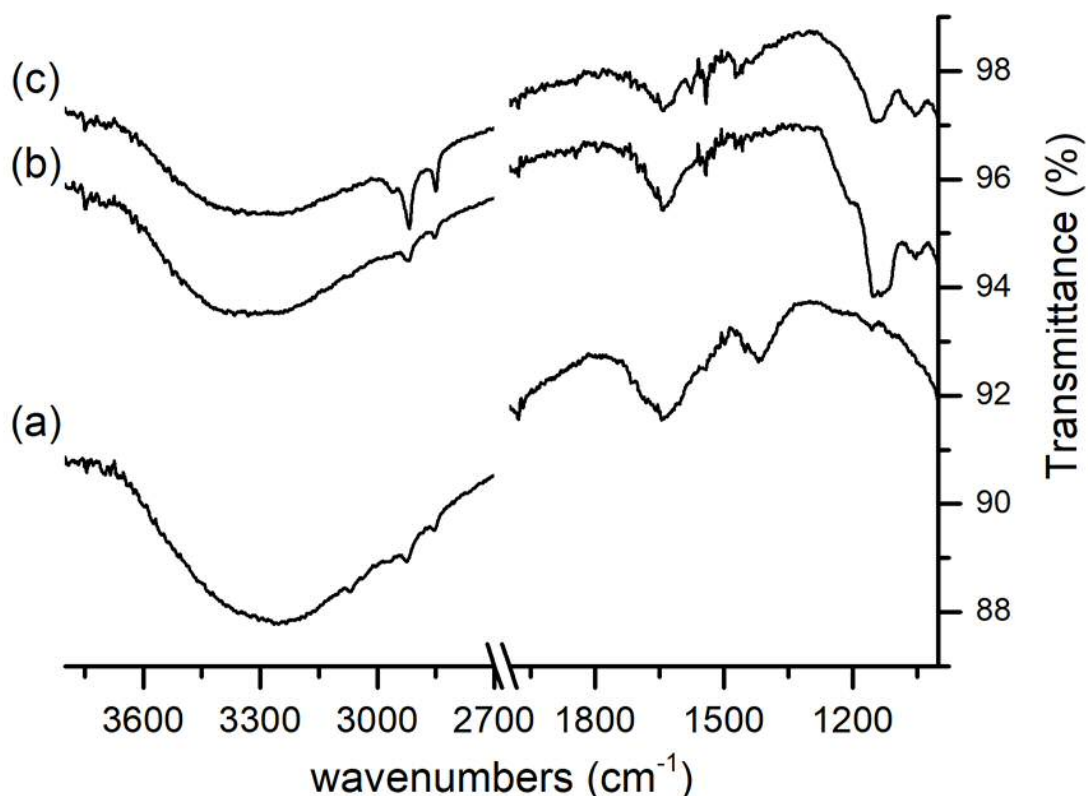


Figure 3.2.2.4:- ATR IR spectra for (a) mP25 spent (deoxy), (b) mP25 + 0.1M K₂SO₄ (deoxy), (c) mP25+ 0.1M Na₂SO₄ (deoxy).

connected to the presence of **2** on the surface. **2** is the most prevalent intermediate and its formation, from cinnamic acid, is believed to occur on the surface followed by a destruction pathway that retains the aldehyde functionality as hydroxylation occurs. One would also expect to see aldehyde interactions directly with the surface which are found at 1746 and 1716 cm⁻¹. These can be assigned as $\nu(\text{C}=\text{O})$ of a hydrogen bonded aldehyde and a $\nu(\text{C}=\text{O})$ of a directly bonded aldehyde respectively. These peaks are similar to those seen previously in mP25 (deoxy), where it was rationalised that they belonged to the interaction of **3** and surface sites. There is only a slight discrepancy between one of the vibrations, 1746 cm⁻¹ here and

| IR Frequency (cm ⁻¹) | Assignment | 0.1M K ₂ SO ₄ | 0.1M Na ₂ SO ₄ | 0.1M K ₂ SO ₄ (deoxy) | 0.1M Na ₂ SO ₄ (deoxy) |
|----------------------------------|---|-------------------------------------|--------------------------------------|---|--|
| 2960 | CH ₃ antisym-s | medium | v.weak | / | weak |
| 2918 | CH ₂ antisym-s | v.strong | v.strong | weak | strong |
| 2849 | CH ₃ sym-s | strong | medium | weak | medium |
| 1746 | v(C=O) Ti-H-CO-R | weak | v.weak | weak | v.weak |
| 1736 | v(C=O) | / | / | weak | / |
| 1716 | v(C=O) Ti-O=CH-R | strong | weak | weak | weak |
| 1700 | v(C=O) SO ₄ coordinated aldehyde | strong | weak | weak | weak |
| 1680 | | weak | / | / | / |
| 1661 | | weak | v.weak | weak | medium |
| 1645 | v(O-H) H ₂ O bend | medium | strong | medium | strong |
| 1577 | v(C=C) stretching | medium | strong | / | medium |
| 1555 | | weak | weak | weak | weak |
| 1541 | | strong | strong | medium | strong |
| 1525 | | v. weak | weak | weak | weak |
| 1498 | | / | weak | / | weak |
| 1473 | v(C-H) bending modes | medium | medium | v.weak | strong |
| 1458 | | medium | medium | weak | medium |
| 1434 | | weak | weak | v.weak | weak |
| 1144 | v(S=O) SO _x | medium | v.strong | medium | v.strong |
| 1111 | v(S=O) SO ₄ ²⁻ (free) | v.strong | / | / | / |
| 1089 | | / | weak | / | / |
| 1051 | v(S=O) SO ₄ ²⁻ (ads) | weak | medium | medium | medium |

Table 3.2.2.3:- A list of the detected IR peaks found on spent photocatalyst from sulfate containing reactions. Included are the proposed assignments and the relative strength of the peaks

1749 cm⁻¹ previously, however the difference in peak strength leads to the possibility that there could be **2** present in a hydrogen bound state that is covering the peak relating to **3**. It is logically more likely that the strongest peaks here, 1716 and 1700 cm⁻¹, correlate to the most prevalent intermediate **2**. 1645 cm⁻¹ can again be assigned to v(O-H) H₂O bend. The region, 1610-1490 cm⁻¹ corresponds to aromatic C=C stretching which is also seen in spectra of photocatalyst from non-sulfated reactions. The most noticeable difference of these spent catalysts from the sulfate experiments is the lack of v(C-H) bends except for the peak at 1456 cm⁻¹ that can be assigned as v(C-H) bending mode of a methylene group, indicating some **3** is

in fact present, as well as the vibration at 1473 cm^{-1} that would most likely also correspond a CH_2 $\nu(\text{C-H})$ bending mode. Lastly, sulfate is expected to give a strong peak at around 1110 cm^{-1} , [52] however only the sample from the reaction with $0.1\text{M K}_2\text{SO}_4$ has a peak at this wavenumber. It is probably that this shows the presence of crystalline sulphate, although the reason for why this appears in only one sample is difficult to explain. The two bands at 1144 and 1051 cm^{-1} are peaks common to all spectra where sulfate is present and probably relate to a chemically altered sulfate species and adsorbed SO_4^{2-} . [28][53] Whilst the peak at 1051 cm^{-1} can be assigned as $\nu(\text{S=O})$ for an adsorbed sulfoxide species.

In the absence of oxygen the intermediate distribution pattern is the same as when sulfate is absent. **3** is the most prevalent intermediate which is suspected to have a weak interaction with the surface which is displayed by the distinct lack of new and large peaks in comparison to the oxygenated reactions. Similar $\nu(\text{C-H})$ stretching frequencies are observed, as seen in the previous reactions shown in **Figure 3.2.2.3**, with roughly the same peak ratios. The carbonyl region looks to be as complicated as when O_2 was present, however there are no distinctively strong vibration modes. Peaks at 1716 and 1700 cm^{-1} are still likely to signify the $\nu(\text{C=O})$ of a surface bound **2** and the aldehyde component interacting with surface sulfate, but their decrease in strength corroborates with the decrease in production of **2** observed in the GC traces. Additionally, 1716 cm^{-1} is of a relatively equal strength in **figure 3.2.2.4 (a)** whilst the sulfate peak at 1700 cm^{-1} is absent. 1661 cm^{-1} is present throughout **(a)** to **(c)** indicating it could be caused by a vibrational mode of **3** but the assignment is not definitive. Due to the complicated nature of this region, the peaks have been loosely assigned to aldehyde bending modes. Again, the peak at 1645 cm^{-1} represents $\nu(\text{O-H})$ bending mode of water and it dominates the lower carbonyl region. The decrease in strength of the 1577 and 1542 cm^{-1} peaks indicate these frequencies could be present because of an aromatic system like **2**.

3.2.2.4 XRD studies of Spent Photocatalysts from Sulphated Reaction Media

XRD of the spent sulfate reaction catalysts gave the same characteristic titania diffraction patterns that are symptomatic of a mixed anatase and rutile phase titania material. These were at 2θ values of: 25.44 (A 101), 27.56 (R 110), 36.25 , 37.12 (R 101), 38.00 (A 004), 38.77 , 41.37 (R 111), 48.22 (A 200), 54.21 (A 105), 54.39 (A 211), 55.21 , 62.89 (A 204), 69.06 (A 116), 70.42 (A 220) and 75.27 (A 215). Additionally two peaks appeared in the $0.1\text{M K}_2\text{SO}_4$ sample at 29.96 and $31.03\ 2\theta$ that indicate the presence of K_2SO_4 crystallographic phases. There does not appear to be any visible diffraction patterns that

indicate the presence of Na_2SO_4 . **Figure 3.2.2.5** shows the diffraction patterns and the crystallite sizes that were calculated using the Scherrer equation.

3.2.2.5 Discussion of the Impact of Sulfate on the Photocatalytic Degradation of Cinnamic Acid

The above data strongly indicates that the presence of any amount of sulfate inhibits the photocatalysed degradation of cinnamic acid through blocking the formation of **2** while not introducing any new reaction pathways. Kinetic data showed that the mere presence of sulfate, in amounts as low as 0.05M, were detrimental to the removal of CA. As discussed in **3.2.1**, **2** is suspected to form via a surface mediated degradation route where a radical oxygen species reacts with the adsorbed CA and cleaves the double bond to form **2**. Formation of **2** is discouraged by increasing sulfate concentrations, but degradation of **2** still occurs generally leaving some **2** in the reaction mixture after 3 hours. In contrast, **3** formation is unaffected by the presence of sulfate regardless of the presence of oxygen due to sulfate having a low affinity for scavenging hydroxyl radicals. [39] The inhibition of **2** formation is probably due to sulfate occupying surface vacancies as it is known for its affinity for TiO_2 surfaces, as well as its interaction with adsorbed carbonyl species. [28][40] The occupation of these surface

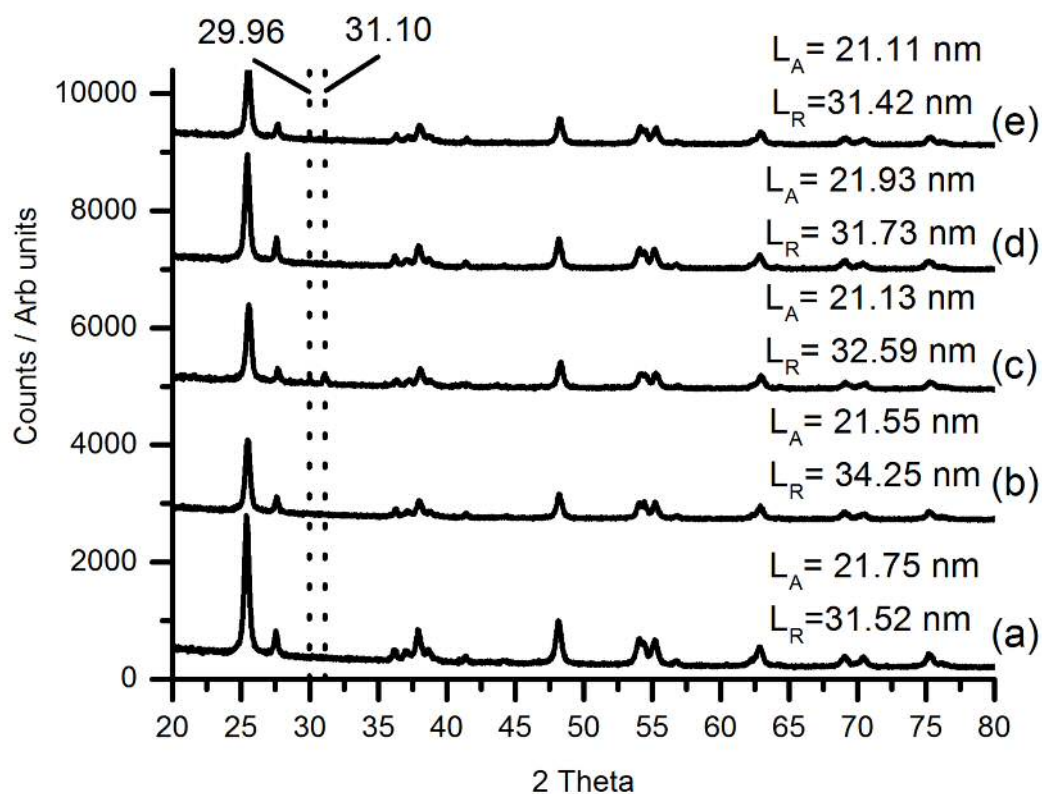


Figure 3.2.2.5:- XRD diffraction patterns and the associated anatase (L_A) and rutile (L_R) crystallite size for: (a) mP25, (b) mP25 + 0.05M K_2SO_4 , (c) mP25 + 0.1M K_2SO_4 , (d) mP25 + 0.05M Na_2SO_4 , (e) mP25 + 0.1M Na_2SO_4

vacancies reduces the available sites for CA to bind to the surface, an important step in CA degradation as discussed in 3.2.1, which subsequently reduces the rate of formation for **2**. Whilst the formation of **3** might be unaffected by sulfate, sulfate does also slow the removal of **3**. One might suggest the removal of both **2** and **3** was being inhibited due to sulfate scavenging hydroxyl radicals, whilst **2** is understood to degrade further via hydroxyl radical attack. [10] However, this would also impact on **3**'s formation, which not observed, and there is no evidence of sulfate radicals forming. This rules out hydroxyl radical scavenging as the primary cause of slowed intermediate removal. Instead, it is probable that sulfate contamination effects aldehyde degradation through surface interactions.

Sulfate was confirmed on the surface post reaction by XRD, XPS and IR spectroscopy. IR suggested the interaction of sulfate with adsorbed carbonyl groups with the prevalence of a strong vibrational modes at 1700 and 1680 cm^{-1} that was not observed in the absence of sulfates and corroborated with IR data of other groups. [28] A number of carbonyl species were detected on the surface using ATR-IR spectroscopy. Their presence indicates the possibility that the intermediates, **2** and **3**, could degrade via surface oriented processes. The number of peaks detected in the carbonyl region make it difficult to accurately assign the peaks. However, the weakness of the peaks from the deoxygenated reactions suggests that the strong peaks in the oxygenated reaction are likely to be from **2** and its degradation products. Furthermore, CO₂ capture experiments found that 81.15% of carbon had been released after 3 hours of reaction and GCMS studies showed that **2** was still present in the solution at the end of the experiment whereas **3** was not. Based on this data it is reasonable to conclude that the IR data, for the oxygenated sulfate reactions, are shaped by **2** and its degradation products. **2a**, **2b**, and **2c** are understood to be the immediate products after **2** and would provide a partial explanation for the complicated state of the carbonyl region. However, little evidence is present in the IR spectra for aromatic OH groups or aromatic C-H bands. There were no detectable phenolic $\nu(\text{O-H})$ bending modes from 1300 to 1400 cm^{-1} and the region known for alcoholic C-O/C-C stretching is mostly saturated with the sulfate peak. An increase in carbon in the C-O and C=O chemical states, from XPS, does however hint that the substrate is in an advanced state of oxidative degradation. A lack of π - π^* transition for all samples indicates an absence of extended conjugation in the remaining species. As was illustrated in the cinnamyl alcohol reactions in 3.2.1, π - π^* interactions were only observed when the extended conjugation of cinnamyl alcohol was present, which means a lack of π - π^* character in the C1s region does not eliminate the presence of molecules such as **2** and **3**. Although there are

some IR peaks that could be assigned to **3** such as the methylene C-H bend (1458 cm^{-1}), there is little sign of aromaticity and the vibration at 1458 cm^{-1} , and likely 1473 cm^{-1} , could easily be attributed to an aliphatic CH_2 group. These data suggest that, at best, there are only trace amounts of **3** present on the photocatalyst surface and that **3** does not have a great affinity for the titania surface.

In the absence of oxygen, measured rates indicated a significant inhibition of cinnamic acid degradation to rates equivalent to photocatalyst free photolysis. This decreased rate was accompanied the near complete blocking of the degradation pathway that produced **2**, whilst the formation of **3** was left unaffected and gave a concentration profile matching oxygen free conditions in the absence of sulfate. This is a very strong indication of the significance of the benzaldehyde pathway for the destruction of CA and therefore the importance of superoxide radicals. Whereas the pathway to form **3** does not rely on superoxide or access to the surface. From the GC data it is also apparent that **3** does not show signs of degrading further in the absence of oxygen as the concentration profile shows a steady formation that does not plateau within the 3 hour reaction time. Given that after 150 minutes of reaction just 12.87% of the expected carbon had been released, slightly higher than the 8.56% of the sulfate and O_2 free conditions. Or, roughly the amount of CO_2 one would expect from the decarboxylation of CA to form **3**. The IR spectrum, seen in **Figure 3.2.2.4**, shows only very weak vibrations across the spectrum despite **3** being the major intermediate under these conditions. This is an indicator that **3** has a low affinity for the titania surface and also suggests that widespread degradation of **3** is not occurring and depositing carbon species on the surface. It is clear that **3** is forming and does not undergo complete mineralisation further enforcing the conclusion that dissolved oxygen is a requirement for complete degradation as seen in **3.2.1**. XP spectra also support this sentiment. Wide scans showed carbon levels remain above 10% during deoxygenated reactions, contrary to what is found after oxygenated sulphated reactions that all had carbon content drop below 10% and even as low as 2%. This highlights a difference in surface behaviour when sulfate is present or absent. Whereas, in the absence of sulfate a build-up of carbon occurs which is attributed to the benzaldehyde mechanism depositing carbon that has not yet been removed; in the presence of sulfate no such build up occurs. The remaining carbon often exhibits strongly carbonyl character, according to XPS and IR, with several potential interactions with sulfate on the surface. What this suggests, is that sulfate could be catalysing the removal of carbon from the surface, a process that is now inhibited by deoxygenation. The build-up of

carbon was found to be of largely C-C character for 0.1M K₂SO₄ and 0.1M Na₂SO₄ (deoxy), as shown in **Table 3.2.2.2**, with levels of this component reaching 80% of the total carbon present. This was a stark difference to the oxygenated sulphated reactions that were found to have significantly higher C-O and C=O concentrations. Evidently, the deposited carbon shows little oxygen functionality, as is clear from XPS and the IR spectra that show no sign of any carbonyl moiety, and after 3 hours of reaction the titania has not incorporated substantial amounts of oxygen into the carbon. Increasing amounts of carbon on the surface could be result in catalyst deactivation, however it is unlikely reactors would run under anaerobic conditions due to the poor degradation seen in oxygen-free conditions.

3.2.3 The Effect of Chlorides on the Degradation of Cinnamic Acid

3.2.3.1 Kinetic Impact

Potassium and sodium chloride are two other salts that are commonly found in industrial waste water due to the effluent being diluted with sea water. Introduction of either to the reaction mixture causes an acceleration of cinnamic acid removal; the rate increases from 0.089 s⁻¹ to 0.099 s⁻¹ in the absence of chloride and the presence of 0.1M KCl, respectively. A progressive increase in degradation rate is observed as the KCl concentration increases (**Table 3.2.3.1**). Inclusion of NaCl demonstrated a similar promotion of CA removal, although with noticeably less impact. The reaction in the presence of 0.1M NaCl did not appear to improve degradation rates with the measured rate being just 0.0881 cm⁻¹, however increasing sodium chloride concentrations to 0.5M and 1M gave removal rates of 0.0949 cm⁻¹ and 0.103 cm⁻¹, respectively. Introducing a N₂ flow to the reaction displayed rate

| Reaction Conditions | 1 st Order rate (s ⁻¹) | + N ₂ flow |
|---------------------|---|-----------------------|
| mP25 | 0.089 | 0.020 |
| mP25 + 0.025M KCl | 0.080 | / |
| mP25 + 0.05M KCl | 0.090 | 0.016 |
| mP25 + 0.075M KCl | 0.095 | / |
| mP25 + 0.1M KCl | 0.099 | 0.024 |
| mP25 + 0.25M KCl | 0.107 | / |
| mP25 + 0.5M KCl | 0.115 | / |
| mP25 + 0.1M NaCl | 0.088 | 0.020 |
| mP25 + 0.5M NaCl | 0.095 | / |
| mP25 + 1M NaCl | 0.103 | / |

Table 3.2.3.1:- First order rate constants for chloride containing reactions

inhibition behaviour like that seen under standard conditions. Removal rates fall to 0.016 cm^{-1} , 0.024 cm^{-1} and 0.020 cm^{-1} for 0.1M KCl 0.5M KCl and 0.1M NaCl respectively. These rates are similar rates to the rate of CA degradation with just TiO_2 and flowing N_2 . Measurement of the carbon dioxide released indicate significantly slower evolution, as seen in **Figure 3.2.1.2**. 24.2% and 14.1 % of the total carbon is released after 3 hours of reaction for 0.1M KCl and the corresponding deoxygenated reaction, respectively. These percentages equate to roughly 2 and 1 equivalents respectively of the total carbon in CA being evolved after 3 hours.

The presence of chloride also instigates mechanistic changes. Benzaldehyde production and removal rates fall, as seen in **Figure 3.2.3.1** (top right), where there does not seem to be a clear correlation between chloride concentration and the rate of production or removal. The true levels of intermediates produced is difficult to ascertain due to the continuous photocatalytic degradation. As a result, there is no correlation between the maximum detected concentration and the amount of chloride present, the concentration profiles will be a function of the speed of formation against the speed of destruction. Therefore, it can be assumed that the longer it takes to reach the maximum concentration, the slower the production of the intermediate is in comparison to its removal. Here it can be seen that the maximum detected concentration, for **2**, shifts as the chloride concentration increases. Under standard conditions, and 0.05M KCl, the concentration maximum is observed at the 5 minute mark. Increasing the KCl concentration to 0.1M pushes it to 30 minutes where it stays even at 0.5M KCl. Notably, the conditions where **2** is the slowest to be removed is 0.5M KCl. The flowing of N_2 appears to induce the same behaviour in the presence of chloride as it does in its absence, where the formation of **2** is almost completely inhibited. NaCl was found to have the same impact on the production of **2**, except for the case of 1M NaCl where the concentration of **2** does not begin to decrease within the 3 hour reaction length and the experiment ended with **2** having a

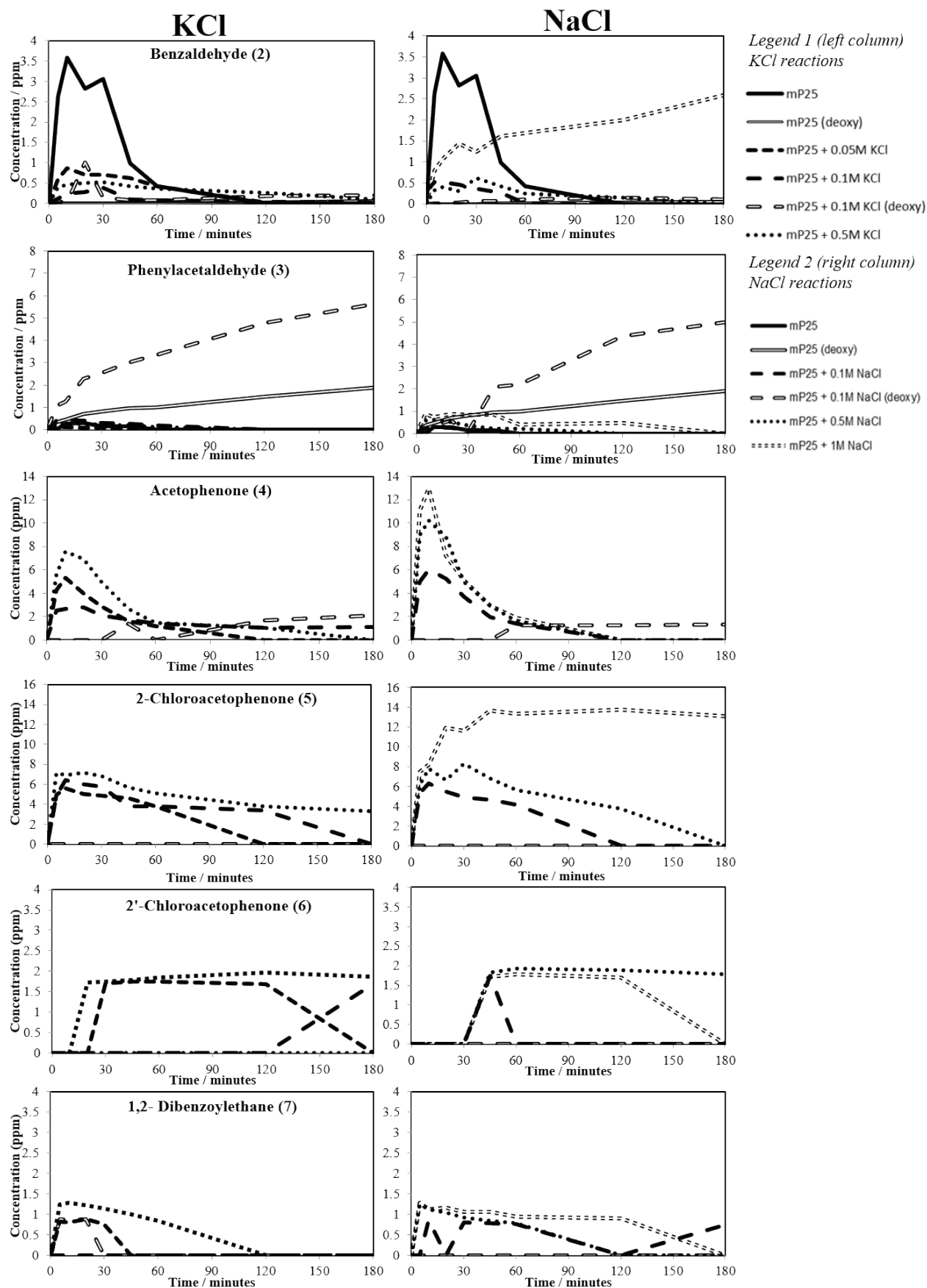


Figure 3.2.3.2:- Concentration profiles for the main intermediates in the chlorinated reaction. **Left column;** KCl. **Right column;** NaCl

concentration of 2.58ppm. Analysis of the formation of **3** throughout the reaction shows that introducing chloride does not significantly impact its production, for all concentrations of potassium or sodium chloride. The only change that does occur in the presence of chloride is in a deoxygenated atmosphere. Over the initial 20 minutes of reaction the rate of formation of **3** is 0.014, 0.038, and 0.1203 mg L⁻¹ min⁻¹ for mP25, mP25 (deoxy) and mP25 (deoxy) + 0.1M KCl, respectively. The rate of formation triples each time whilst for 0.1M NaCl (deoxy), the rate of formation of **3** increases to 0.087 mg L⁻¹ min⁻¹. No degradation of **3** is measured in the absence of oxygen when chloride is present or not.

3.2.3.2 Mechanistic Impact of Chloride

A number of new intermediates were detected via GCMS that are only detected in reactions where chloride was present. Acetophenone (**4**) only appears at a retention time of 13.6 minutes in **Figure 3.2.3.3 (i)**. It was identified via analysis of its mass spectrum (**appendix 1.3.1**) and confirmed with a calibration standard (**appendix 1.3.2**). The mass spectrum shows a peak at an m/z of 120 that has been assigned as the parent mass peak. Other key peaks are at 105 and 77 which have been assigned as [C₆H₅CO]⁺ and [C₆H₅]⁺, respectively. Its formation shows links to chloride concentration in that the maximum detected concentration generally increases with chloride concentration. With KCl, the concentration of **4** at 10 minutes is 5.3 mg/L, 2.8 mg/L and 7.5mg/L for 0.05M, 0.1M and 0.5M KCl respectively. Whilst formation of **4** in the presence of NaCl was 6.0mg/L, 10.2 mg/L and 12.9 mg/L for 0.1M, 0.5M and 1M NaCl reactions respectively. These figures illustrate that, for the most part, the maximum concentration of **4** detected positively correlates with chloride concentration. The rate of disappearance of **4** does not, however, appear to be directly linked chloride concentration. Instead, the higher the maximum concentration of **4**, the quicker it degrades. Flowing N₂ during the reaction results in the near complete inhibition of the production of **4**. **4** is not detected immediately after irradiation, as it is in oxygenated environments, and is only detected at levels of less than 2mg/L.

2-Chloroacetophenone (**5**) appears in the GC trace at 18.1 minutes in **Figure 3.2.3.3 (i)**. The mass spectrum indicated a parent mass peak at 154 that matches the molecular weight of **5** (**appendix 1.3.3**) and its presence was confirmed by calibration standard (**appendix 1.3.4**). The signals at m/z of 120 and 105 are likely to correspond to [C₆H₅COCH₂]⁺ and [C₆H₅CO]⁺. The chlorine atom is first to be broken off during fragmentation leading to no visible isotope patterns. As shown in **Figure 3.2.3.2 d**, **5** forms immediately after irradiation at rates that increase slightly with regards to chloride concentration with regards to both NaCl

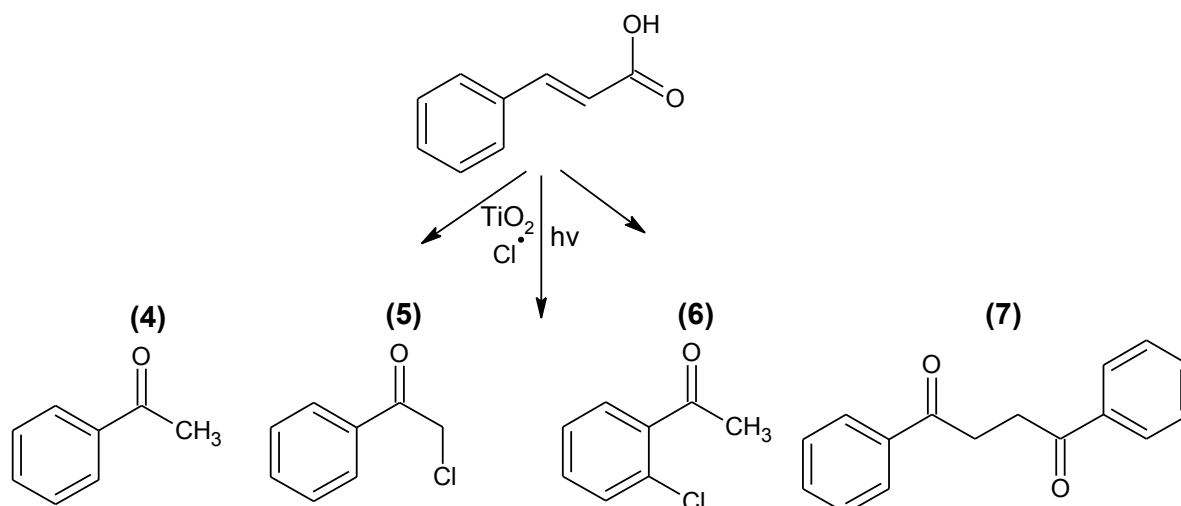


Figure 3.2.3.1:- New intermediates detected during the photocatalytic degradation of cinnamic acid in chlorinated conditions

and KCl. Degradation of **5** is slower the higher the concentration of chloride, presenting a potential reason for the larger concentration maximums seen for **5**. Increasing NaCl concentration from 0.5M to 1M causes **5** to continue to form after the initial 5 minutes, reaching a maximum of 13.7 mg/L after which it degrades by just 0.5mg/L in 2 hours and 15 minutes. The purging of O_2 inhibits the formation of **5** and it is not detected at all throughout the reaction. **Figure 3.2.3.2 (e)** shows the formation and degradation of 2'-chloroacetophenone (**6**), that eluted at 16.1 minutes as seen in **Figure 3.2.3.3 (i)**. Its mass spectrum showed parent mass peaks at 154 and 156, in a ratio of 3:1, that corresponds to the molecular mass of a chloroacetophenone species displaying a typical chlorine isotopic pattern (**appendix 1.3.5**). Peaks at 141 and 139 can be assigned as $[\text{C}_6\text{H}_4\text{Cl}^{37}\text{CO}]^+$ and $[\text{C}_6\text{H}_4\text{Cl}^{35}\text{CO}]^+$; whilst peaks at 113, 111 and 75 can be assigned to $[\text{C}_6\text{H}_4\text{Cl}^{37}]^+$, $[\text{C}_6\text{H}_4\text{Cl}^{37}]^+$, and $[\text{C}_6\text{H}_3]^+$ respectively. These assignments confirmed the eluent at 16.11 minutes to be a ring substituted chloroacetophenone, with the calibration standards confirming it as 2'-chloroacetophenone (**appendix 1.3.6**). **6** does not form at the beginning of irradiation and only reaches concentrations ≤ 2 mg/L, showing no relationship with chloride concentration. As in the case of **5**, **6** was not detected when O_2 was purged from the reaction mixture.

Figure 3.2.3.2 f shows the evolution and destruction of the final intermediate, 1,2-dibenzoyl ethane (**7**) which eluted at 31.3 minutes. The mass spectrum gave the parent mass peak as 238, which contained no isotopic patterns indicating it did not contain chlorine (**appendix 1.3.7**). Further analysis of the mass spectrum showed peaks at m/z 's of 219, 203, 133 and 105; that can be assigned as $[\text{C}_6\text{H}_5\text{COCH}_2\text{CH}_2\text{CC}_6\text{H}_5]^+$, $[\text{C}_6\text{H}_5\text{CCH}_2\text{CH}_2\text{CC}_6\text{H}_5]^+$, $[\text{C}_6\text{H}_5\text{COCH}_2]^+$, $[\text{C}_6\text{H}_5\text{CO}]^+$. This assignment was confirmed with the calibration standard

that had a retention time of 31.3 minutes and produced a matching mass spectrum that can be found in **appendix 1.3.8**. Intermediate **7** forms immediately after irradiation. However it does not show any sensitivity to $[Cl^-]$ as its formation and destruction shows no correlation to chloride concentration. The only correlation is that chloride must be present for it to form.

3.2.3.3 Photocatalytic Oxidation of Acetophenone, 2-Chloroacetophenone and 2'-Chloroacetophenone

Further photocatalytic oxidation of intermediate **4** gave the chromatogram as seen in **Figure 3.2.3.3 (ii)**. New species were detected at 15.5, 20.0, 20.9 and 22.0 minutes (**appendices 1.4.1 to 1.4.4**). The eluents at 15.5, 20.0 and 20.9 all gave similar mass spectra with peaks at m/z 's of; 136, 121, 93 and 65. The parent mass peak at 136 indicates the species to be ortho/para or meta substituted hydroxyacetophenones, and the peaks at m/z s of 121 and 93 can be assigned as $[C_6H_5C(OH)CH_3]$ and $[C_6H_4OH]^+$. The eluent at 22.0 gave a mass spectrum with peaks at m/z s of; 152, 137, 109 and 81. The parent mass peak at 152 suggests a dihydroxyacetophenone $[(OH)_2C_6H_3COCH_2]$ whilst the remaining peaks can be assigned as $[(OH)C_6H_3C(OH)CH_3]$, $[(OH)_2C_6H_3]^+$ and $[(OH)_2C_6H_4]^+$, respectively. **5** was photocatalytically oxidised further, in the presence and absence of KCl, and gave a main product at a retention time of 16.1 and minor product at 17.0 minutes in both reactions. Comparison of the mass spectrum signals indicates the eluent at 16.1 was **6**. The m/z of 154 corresponds to the mass peak for 2'-chloroacetophenone, whilst the m/z 's of 139 and 111 are likely to correspond to $ClC_6H_4CCH_3$ and ClC_6H_4 species due to the matching masses and the presence of the 3:1 isotopic abundance that is characteristic of chlorine. Additionally, the retention time matched the calibration standard. The product at 16.89 minutes also produced a mass spectrum that matched the one obtained for **6** (**appendix 1.5.1**), and the intermediate at 16.11 minutes, suggests that it must be 3'/4'-chloroacetophenone. A control experiment confirmed no reaction occurs without UV irradiation, however a no mP25 control showed signs of degradation and yielded several products. Species at eluent times of 16.1 and 17.0 minutes were detected again and assigned as 2-chloroacetophenone (**6**) and 3'/4'-chloroacetophenone respectively, due to the similar retention times and matching fragmentation patterns. A third species at 15.4 minutes was also found that produced a mass spectrum with a parent mass peak of 136, and peak fragments at $m/z = 121, 105$ and 93. The peak at $m/z = 136$ matches the molecular mass for a hydroxyacetophenone

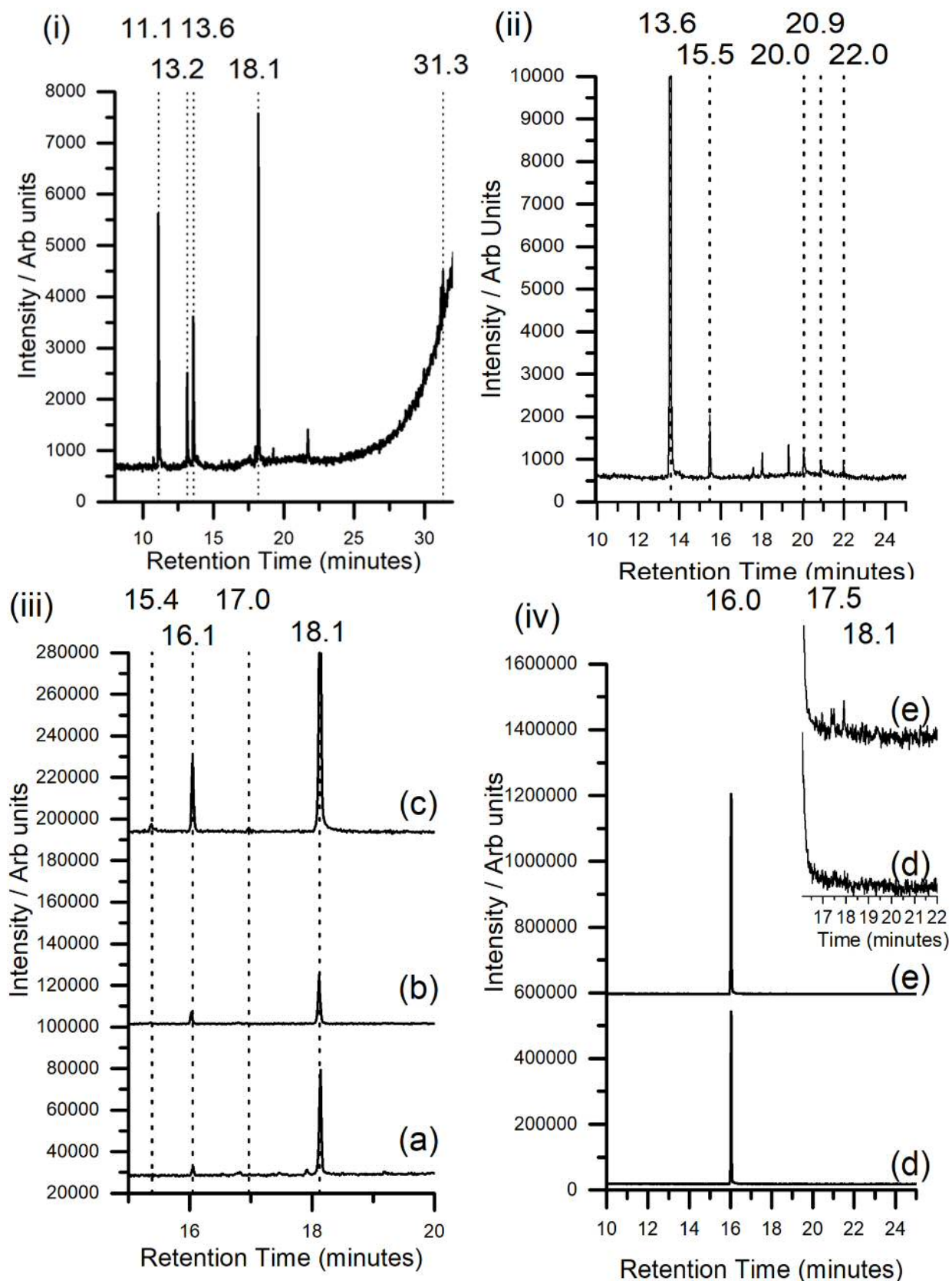


Figure 3.2.3.3:- Gas chromatograms for the degradation of cinnamic acid and the individual reaction of intermediates 4, 5 and 6.

(i) Cinnamic acid + KCl

(ii) Acetophenone + KCl

(iii) (a) 2-chloroacetophenone, (b) + 0.1M KCl, (c) No mP25 or KCl

(iv) (d) 2'-chloroacetophenone, (e) + 0.1M KCl

$[(\text{OH})\text{C}_6\text{H}_4\text{COCH}_3]$; whilst $m/z = 121, 105$ and 93 could be $[(\text{OH})\text{C}_6\text{H}_4\text{CO}]^+$, $[\text{C}_6\text{H}_4\text{CO}]$ and $[(\text{OH})\text{C}_6\text{H}_4]^+$ respectively. After 60 minutes the reactions with KCl, without KCl and without mP25 gave **5** removal at; 75.25 %, 67.11% and 24.85%. Greater amounts of **6** were detected, as well as more intermediates, in the absence of TiO_2 . **6** was reacted individually in the presence and absence of KCl and the chromatograms can be seen in **Figure 3.2.3.3 (iv)**. In the presence of chloride no degradation is observed with no intermediates (**Figure 3.2.3.3 (ii)(d)**), whilst in the absence of chloride some degradation is observed as well as several small peaks at retention times of 16.9, 17.5 and 18.7 minutes. The peak at 16.9 minutes produced a mass spectrum with the same parent mass peak fragmentation pattern of the substrate (**6**), indicating it is an isomer of **6** where the Cl moiety is attached to the 3/4 position of the aromatic ring. The peak at a retention time of 17.5 minutes (**appendix 1.6.2**) produced a mass spectrum with the main mass peaks at m/z s of 170 and 155 which correspond to $[(\text{Cl}^{35})(\text{OH})\text{C}_6\text{H}_3\text{COCH}_3]$ and $[(\text{Cl}^{35})\text{C}_6\text{H}_4\text{COCH}_3]$. These peaks each have sister peaks, two mass units above, at a ratio of 3:1, due to the chlorine isotopic effect which is lost in all masses below 155. The peak at 18.7 minutes gave a mass spectrum (**appendix 1.6.3**) with a set of peaks at $mz = 192, 190$ and 189 which can be assigned to $[(\text{Cl}^{37})_2\text{C}_6\text{H}_3\text{COCH}_3]$, $[(\text{Cl}^{37})(\text{Cl}^{35})\text{C}_6\text{H}_3\text{COCH}_3]$ and $[(\text{Cl}^{35})_2\text{C}_6\text{H}_3\text{COCH}_3]$ respectively. The next set of peaks at 177, 174 and 173 are most likely due to $[(\text{Cl}^{37})_2\text{C}_6\text{H}_3\text{CO}]^+$, $[(\text{Cl}^{37})(\text{Cl}^{35})\text{C}_6\text{H}_3\text{CO}]^+$ and $[(\text{Cl}^{35})_2\text{C}_6\text{H}_3\text{CO}]^+$. This complicated fragmentation pattern can only be caused by two chlorine atoms being present. The loss of a methyl group, without also losing a chlorine atom, indicates that both chlorine atoms are attached to the aromatic ring confirming that this intermediate is a dichloroacetophenone species.

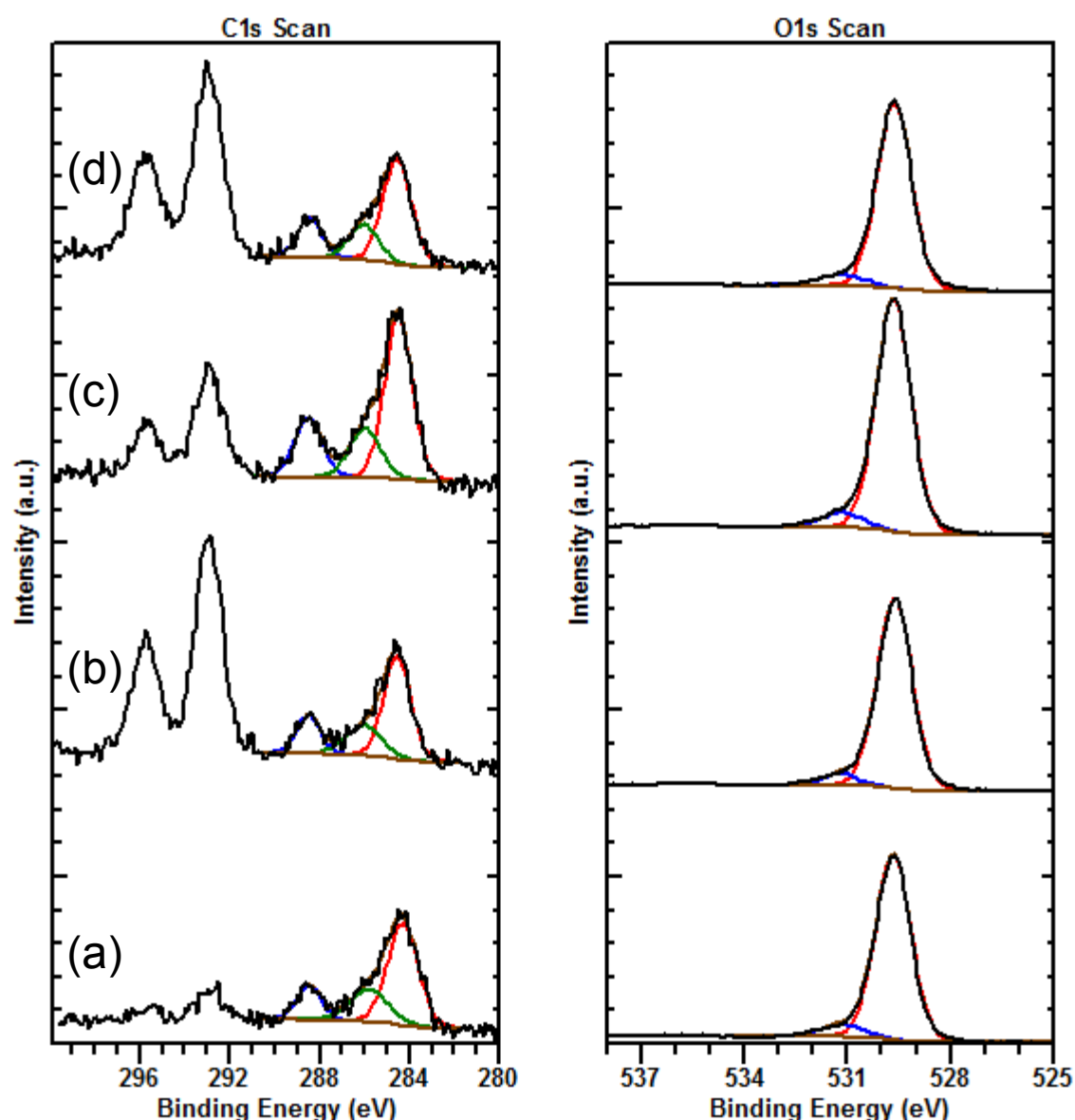


Figure 3.2.3.4:- Carbon (left) and oxygen (right) 1s XP spectra for (a) 0.05M KCl, (b) 0.1M KCl, (c) 0.1M KCl (deoxy), (d) 0.5M KCl

3.2.3.4 XPS Studies of Spent Photocatalysts from Chlorinated Reaction Media

XP spectra of the carbon and oxygen regions for the spent catalysts, after reaction in the presence of KCl and NaCl, can be found in **Figures 3.2.3.4** and **3.2.3.5** and **Table 3.2.3.1**. Examination of the Ti 2p region for both salts found no change after reaction. Deconvolution of the Cl 2p peaks showed a single chlorine species with a spin orbit coupling value of 1.6 eV. Although this confirms that the detectable chloride exists in its salt form; it does not necessarily rule out the possibility of organic chloride being formed due to the low amounts

| Sample Name | C1s (C-C) | C1s(C-O) | C1s (C=O) |
|--------------------------|------------------------|-------------|-------------|
| mP25 + 0.005M KCl | 284.3 (60%) | 285.8 (24%) | 288.5 (16%) |
| mP25 + 0.05M KCl | 284.5 (58%) | 286.0 (23%) | 288.4 (19%) |
| mP25 + 0.1M KCl | 284.5 (58%) | 286.0 (21%) | 288.4 (21%) |
| mP25 + 0.5M KCl | 284.5 (59%) | 286.0 (21%) | 288.4 (19%) |
| mP25 0.1M NaCl | 284.5 (55%) | 286.0 (28%) | 288.7 (18%) |
| mP25 + 0.1M NaCl (deoxy) | 284.6 (52%) | 286.0 (24%) | 288.7 (24%) |
| mP25 1M NaCl | 284.5 (60%) | 286.1 (23%) | 288.5 (17%) |
| Sample Name | O1s (O ²⁻) | O1s (C-O) | |
| mP25 + 0.005M KCl | 529.7 (93%) | 531.2 (7%) | |
| mP25 + 0.05M KCl | 529.6 (94%) | 531.2 (6%) | |
| mP25 + 0.1M KCl | 529.7 (93%) | 531.2 (7%) | |
| mP25 + 0.5M KCl | 529.6 (93%) | 531.2 (7%) | |
| mP25 0.1M NaCl | 529.7 (90%) | 531.22(10%) | |
| mP25 + 0.1M NaCl (deoxy) | 529.7 (94%) | 531.2 (6%) | |
| mP25 1M NaCl | 529.7 (92%) | 531.2 (8%) | |

Table 3.2.3.2:- Top: A table showing the percentage concentrations of the carbon 1s components for spent photocatalysts from the chlorinated reactions.

Bottom: A table showing the percentage concentrations of the oxygen 1s components for spent photocatalysts from the chlorinated reactions.

formed in comparison to dissolved chloride. The oxygen 1s region for all samples showed two peaks whose binding energies and percentage concentrations can be found in **Table 3.2.3.2 (bottom)**. The first environment at 529.7 eV is due to the oxide component of TiO₂, whilst the second component at 531.2 eV is often ascribed to a surface hydroxide species. 531.2 eV does sit within the carbonates region however there is no conclusive evidence from the carbon 1s region or the IR spectra to indicate that carbonates formed. The carbon 1s regions, for the sodium and potassium salt spent catalysts, show a general decreased carbon content on the surface, as seen in (**Table 3.2.1.1**), where the percentage concentration generally dropped to around 6%. The lowest percentage, 3.6% for 0.1M NaCl (deoxy), is

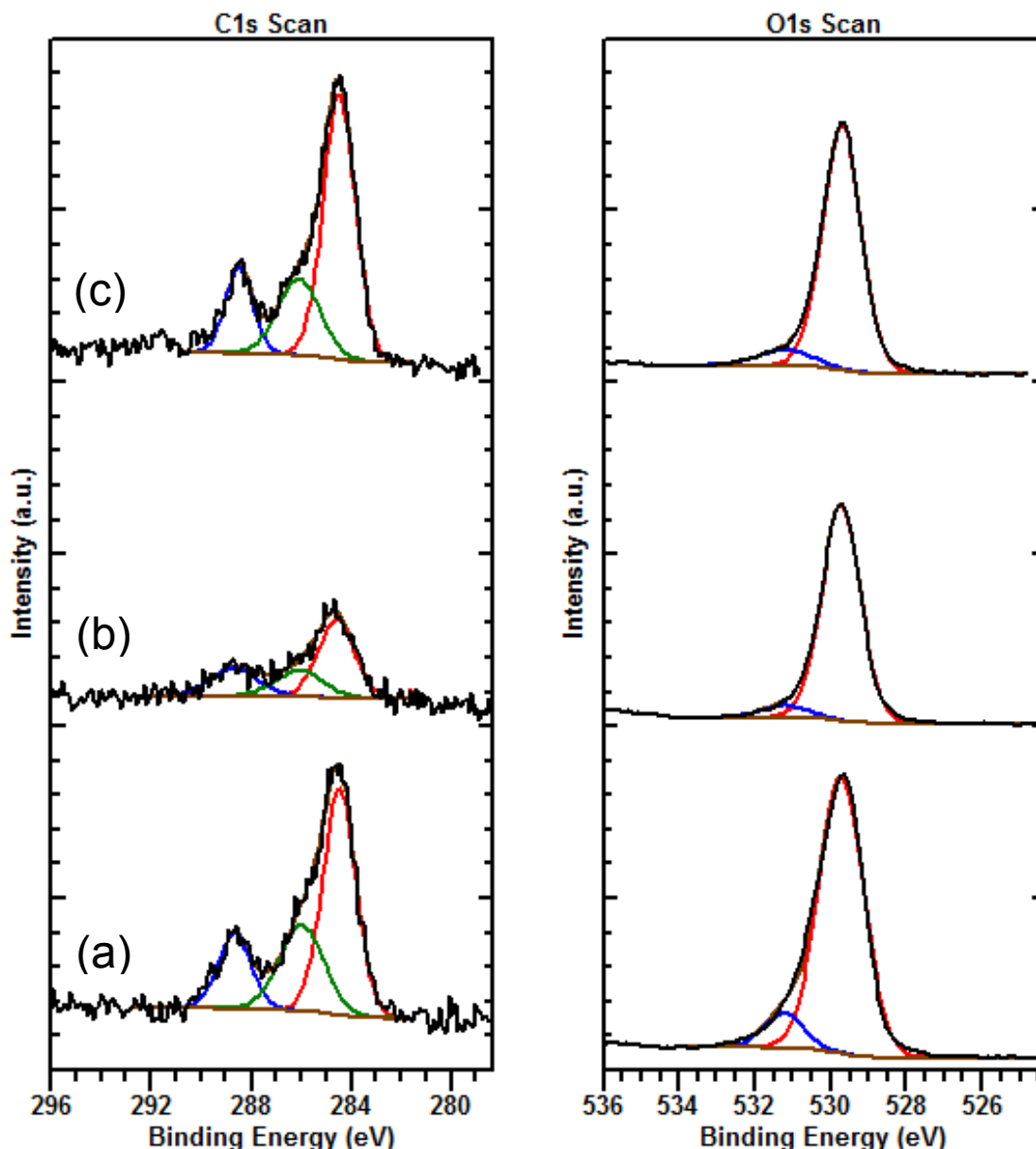


Figure 3.2.3.5: Carbon (left) and oxygen (right) 1s XP spectra for: **(a)** 0.1M NaCl, **(b)** 0.1M NaCl (deoxy), **(c)** 1M NaCl coupled with very high levels of Na and Cl that is likely distorting the true value. Despite the decrease in carbon content there is a stark increase on the amounts of suspected C-O and C=O carbon present. Almost all chloride containing samples had >20% for both carbon environments indicating an increased level of oxygenated molecules present, even when O₂ was purged throughout the reaction. Interestingly, none of the samples showed evidence of a π - π^* interaction as seen in **Figures 3.2.3.4** and **3.2.3.5**. The K 2p peaks would obscure a π - π^* satellite but it is also not detected in the NaCl samples either so it is fair to assume there is no interaction.

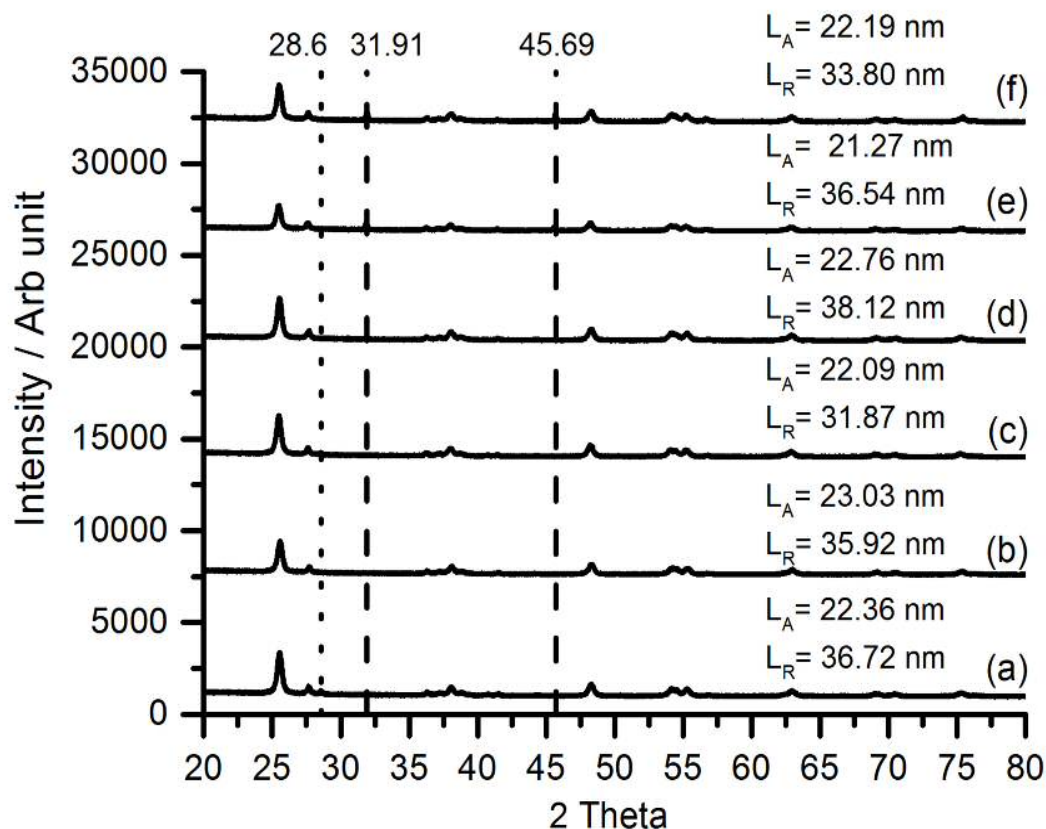


Figure 3.2.3.6: XRD diffraction patterns and the associated crystallite size for: **(a)** 0.05M KCl, **(b)** 0.1M KCl, **(c)** 0.5M KCl, **(d)** 0.1M NaCl, **(e)** 0.1M NaCl (deoxy), **(f)** 1M NaCl
Dotted line = KCl, dashed line = NaCl diffraction pattern

3.2.3.5 XRD studies of Spent Photocatalysts from Sulphated Reaction Media

XRD of the spent chloride-exposed catalysts exhibit the same anatase and rutile diffraction patterns seen in 3.2.1 and 3.2.2. Crystallite sizes calculated using the Scherrer equation, where the anatase (101) phase and the rutile (110) phase were used to calculate the crystallite sizes, seen in **Figure 3.2.3.6**. Crystallite size showed an increase from the fresh mP25 anatase and rutile sizes of 21.75 nm and 31.52 nm respectively. The anatase phase showed a pattern that didn't seem to be directly linked to salt concentrations, whilst the rutile phase clearly showed a large increase of size with small amounts of salt present and the subsequent decrease in size as salt concentration increased. Additional to the titania diffraction patterns was a peak at $2\theta = 28.6^\circ$ for KCl; and peaks at 31.91° and 45.69° for NaCl spent catalysts. Reference spectra indicate that the pattern at 28.6° is the KCl (200) phase. Whereas the peaks at 31.91° and 45.69° are the NaCl (200) and (220) phases respectively.

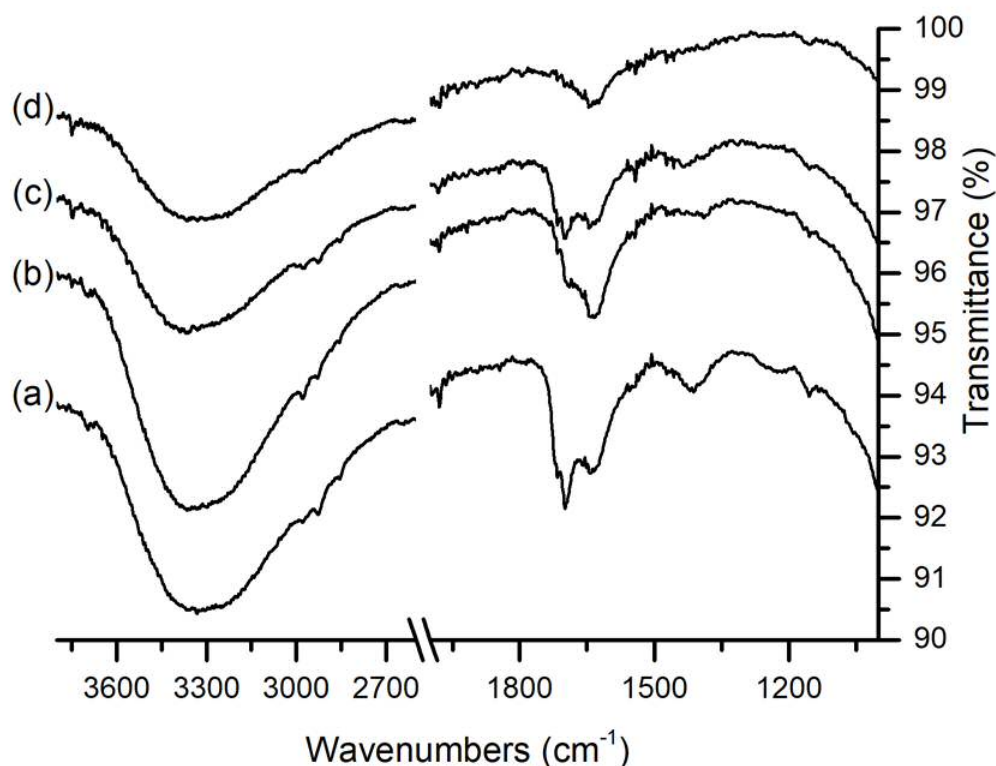


Figure 3.2.3.7: ATR IR spectra of the spent titania photocatalyst from the reactions containing (a) 0.1M KCl, (b) 0.1M KCl (deoxy), (c) 0.1M NaCl, (d) 0.1M NaCl (deoxy)

3.2.3.6 Infrared Studies of Spent Photocatalysts from Chlorinated Reaction Media

ATR of the spent chloride photocatalysts indicate that photocatalysis in the presence of NaCl and KCl reactions produced similar ATR spectra irrespective of the cation. Additionally, changing the concentration of KCl gave no change in spectra either. As such, just photocatalysts from the 0.1M NaCl/KCl and 0.1M NaCl/KCl (deoxy) reactions will be analysed here and can be found in **Figure 3.2.3.7**, the corresponding peaks and their assignments can be found in **Table 3.2.3.3**. The remaining spectra can be found in the supporting data. Based on the GC-MS data of the reactions containing oxygen, it is predicted that all of the intermediates are very likely to be present on the photocatalyst surface. Whilst in the absence of oxygen, **2**, **3** and **4** are the only detectable intermediates with **3** being the most prevalent. Previous data however suggests that **3** does not interact strongly with the titania surface which may result in many of the peaks being obscured. Due to the structural similarities of many of the intermediates, particularly **4** to **7**, assigning peaks to exact vibrations is a very precarious job. As such, the peaks assigned to specific vibrational modes are only done so with sufficient evidence. **Table 3.2.3.3** shows that all four spent photocatalysts share the majority of the peaks detected, many of them being weak. In the $\nu(\text{C-H})$ stretching region each sample has three or four weak vibrational modes that all

| IR Frequency (cm ⁻¹) | Assignment | 0.1M KCl | 01M NaCl | 01M KCl (deoxy) | 01M NaCl (deoxy) |
|----------------------------------|------------------------------------|----------|----------|-----------------|------------------|
| 2997 | CH ₃ antisym-s | / | v.weak | / | / |
| 2980 | | v.weak | weak | weak | weak |
| 2926 | CH ₂ antisym-s | weak | weak | v.weak | v.weak |
| 2881 | CH ₃ sym-s | / | / | v.weak | v.weak |
| 2856 | | v.weak | v.weak | v;weak | v.weak |
| 1790 - 2000 | Aromatic overtones | weak | v.weak | v.weak | v.weak |
| 1750 | v(C=O) H-Bonded aldehyde | v.weak | v.weak | v.weak | v.weak |
| 1734 | | / | / | v.weak | weak |
| 1716 | v(C=O) Ti-O=C-CH ₂ -Ph | weak | weak | v.weak | weak |
| 1699 | v(C=O) H ₃ C-(CO)-R | strong | strong | v.weak | weak |
| 1688 | v(C=O) | / | / | weak | weak |
| 1674 | v(C=O) Ti-O=C(CH ₃)-Ph | v.weak | v.weak | v.weak | v.weak |
| 1657 | v(C=O) | weak | weak | v.weak | weak |
| 1640 | v(OH) H ₂ O-b | strong | strong | strong | strong |
| 1555 | v(C=C) aromatic | v.weak | v.weak | weak | weak |
| 1543 | | v.weak | medium | weak | weak |
| 1511 | | v.weak | v.weak | v.weak | v.weak |
| 1473 | v(C-H) -b | v.weak | v.weak | v.weak | v.weak |
| 1456 | | v.weak | v.weak | v.weak | weak |
| 1433 | | weak | medium | weak | weak |
| 1410 | | medium | v.weak | weak | weak |
| 1390 | | / | v.weak | weak | weak |
| 1315 | | v(C-O) | v.weak | weak | weak |
| 1153 | medium | | weak | v.weak | weak |
| 1132 | v.weak | | / | / | / |

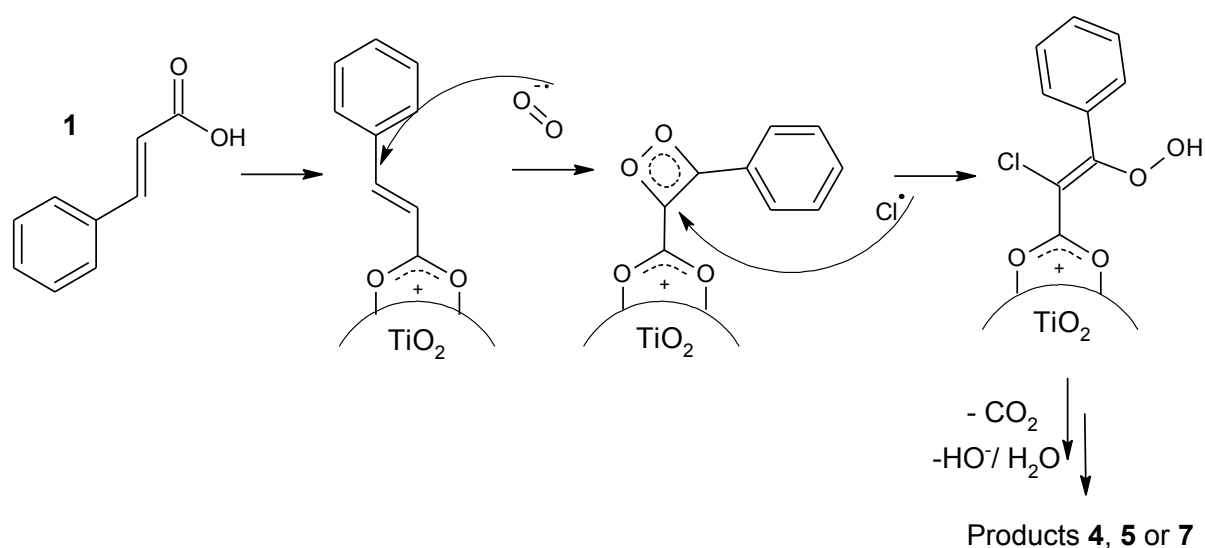
Table 3.2.3.3:- Infrared frequencies and the proposed assignments for spent photocatalysts from chloride containing reaction media

resonate at a wavenumber indicative of aliphatic C-Hs. The vibrations at 2997 and 2979 cm^{-1} can be assigned to a CH_3 antisymmetric stretch, whilst 2927 cm^{-1} is probably the CH_2 antisymmetric stretch. Peak at 2881 and 2856 have been assigned to CH_3 symmetric stretches. A mixture of peaks is expected due to the presence of methyl groups in **4** and **6**, and methylene groups in **3**, **5** and **7**. **4**, **5**, **6** and **7** are all potentially present after oxygenated reactions, while **3** and **4** are both expected after deoxygenated reactions. This means a mixture of various methyl and methylene containing species are expected under both conditions which would result in a complicated region. To further obscure potential assignments, acetophenone has also been found to enolise when bound to titania. [41][42] Evidence, of enolization occurring, is seen in the tentative assignment of 1153 cm^{-1} to $\nu(\text{C-O})$ of the enolised form bound to the surface. Aromatic C-H vibrations were either not present or potential peaks so weak that they could provide little confirmation. However, all samples have numerous potential peaks in the aromatic overtones region of 2000 to 1800 cm^{-1} where the most intense vibration is at 1979 cm^{-1} . However, the peak at 1979 cm^{-1} could also be the carbonyl peak for **7**, the free molecule having a peak at 1805 cm^{-1} shown in **appendix 2.8**, exhibiting a downwards shift due to ligation to titania. A shift that large is possible but would imply very strong adsorption to titania, which is unlikely given that the other acetophenone derived intermediates only exhibit weak adsorption. Based on the data, the safer conclusion is to assign this frequency to an aromatic overtone, rather than the carbonyl frequency for **7**. The carbonyl region for both samples is very full. Broadly, the oxygenated reaction has stronger peaks in the upper carbonyl region of 1655 to 1750 cm^{-1} , where 1699 cm^{-1} is the most intense. A peak at this position was previously attributed to an aldehyde interacting with surface bound sulfate, and a signal was not observed in “standard” conditions leading to the conclusion that it must be due to one of the newly formed products. The vibration at 1699 cm^{-1} could be caused by the ketone in any of the new intermediates. Considering the intermediates all degrade through intermediates that retain the ketone functionality it is difficult to assign the 1699 cm^{-1} frequency with absolute certainty; however it is reasonable to say that it may be caused by **4**, **5** or **6**. The literature indicates **4** would have a vibration at 1674 cm^{-1} , and a shift downwards from liquid phase wavenumber of 1685 cm^{-1} , due to the ligation to titania. [41] This peak is observed, although weakly, in all samples. General principles would suggest that an adjacent chlorine atom would inductively strengthen the carbonyl double bond, therefore resulting in an upwards shift in wavenumber. As both **5** and **6** have a strong carbonyl peak at around 1705 cm^{-1} (**appendices 2.6 and 2.7**), the minor shift to 1699 cm^{-1} suggests weak ligation is occurring. All four samples had three peaks between

1560 and 1510 cm^{-1} that can be attributed to $\nu(\text{C}=\text{C})$ stretching of an aromatic ring. Peaks sitting resonating between 1500 and 1350 cm^{-1} have been assigned to the aliphatic C-H bending modes. 1456 cm^{-1} was previously assigned to $\nu(\text{C}-\text{H})$ bending for the methylene group of **3**, an assignment that still probably holds true. Whilst the greater strength of the peaks at 1410 and 1433 cm^{-1} , from KCl and NaCl respectively, suggest that could be caused by **5**, **6** or **7**. The major differences, when oxygen is purged, is the loss of strength in the carbonyl region at 1699 cm^{-1} . The vibration is still there but is significantly weaker. Overall, the main conclusion from this IR data is the confirmation that many of the intermediates are adsorbed to the photocatalysts surface. Additionally, despite the large increase in detected concentrations of **3** when oxygen is purged we still do not see an accompanying increase in its presence on the surface. This, again, reinforces the conclusion that **3** either does not adsorb to the surface effectively or is formed in solution rather than the photocatalyst surface.

3.2.3.7 Discussion of the Impact of Chloride

The data above indicates that the inclusion of chloride in the reaction mixture introduces new photocatalytically driven mechanistic pathways. While the previously discussed mechanisms use just reactive oxygen species, these new pathways also rely on reactive chlorine species (RCS). As discussed in the introduction it is likely that the radical species is a chloride radical in the form of Cl^\bullet or $\text{Cl}_2^{\bullet-}$. The data we have collected here was not intended however to differentiation which RCS was responsible and so cannot ascertain



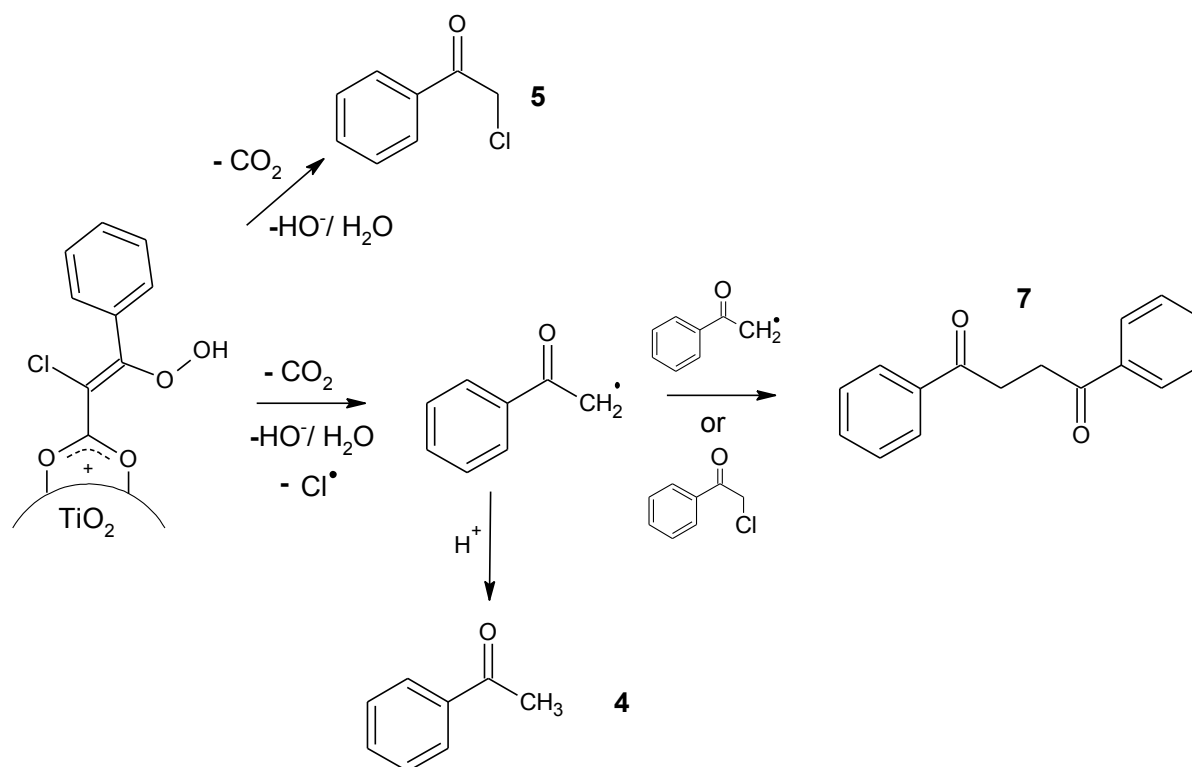
Mechanism 3.2.3.1:- A proposed mechanism for the initial steps of cinnamic acid degradation in the presence of Cl^-

which radical it is. The initial rate of degradation of CA is observed to increase with the concentration of chloride, as seen in **table 3.2.3.1**. The lack of degradation in the no light control showed that Cl^- ions do not have the capacity to react in these conditions; whilst during a no titania control the rate of degradation was not increased by the inclusion of chloride. This indicated that 365nm UV light is not capable of oxidising Cl^- to Cl^\bullet and therefore that the reactivity of the chlorine species must occur due to photocatalysed processes induced by both TiO_2 and UV light. As discussed in **section 3.1**, most mechanisms of forming Cl^\bullet and Cl_2^\bullet do not favour the production of RCS, however **equations 6** shows that chloride scavenges hydroxyl radicals to form the hypochlorous acid radical at a rapid pace that can, even more rapidly, react with H^+ to give H_2O and Cl^\bullet as shown in **equation 8**. The degradation rates, seen in **table 3.2.3.1**, display a link to chloride concentration where CA degrades more rapidly the more chloride is present. Both KCl and NaCl induce this acceleration of CA degradation although KCl appears to be more effective at catalysing the break down with the 0.5M KCl and NaCl reactions having 1st order rate constants of 0.12 s^{-1} and 0.095 s^{-1} respectively. The presence of chloride in wastewater would initially appear to be beneficial from this data. However the CO_2 measurements show that chloride is also a major inhibitor of complete mineralisation due to the majority of the carbon remaining locked in the reaction mixture after 3 hours. Whereas with TiO_2 we found 100% of the CA carbon was released, just 24.3% of the carbon was detected in the presence of 0.1M KCl. Purging of oxygen resulted in the inhibition of CA degradation to similar values when both oxygen and chlorine are absent. This behaviour was observed for both NaCl and KCl and strongly suggests that the mechanistic changes induced by the presence of chloride require dissolved oxygen. CO_2 capture experiments echoed this conclusion; purging the reaction of oxygen reduced the detected CO_2 to 14.1%. This value is only marginally higher than in the absence of chlorine and is expected due to the detection of **4** and **7** in GC-MS.

Firstly, the presence of chloride induces changes that competes with formation of **2** but not the formation of **3**. The concentration profiles in **Figure 3.2.3.2** show that, at any concentration of chloride, both the formation and removal of **2** is affected. Lower maximum concentrations are observed and the rate of disappearance is clearly lowered. Considering the formation of **2**, in the absence of Cl^- , consists of a radical O_2 species bonding across the double bond of an adsorbed CA species it follows that Cl^\bullet likely interrupts this mechanism. The placement of the oxygen in both **2** and **4** is the same, whereas the hydroxyl driven production of **3** places an oxygen α to the carboxyl functionality, combined with the mutual

reliance of dissolved oxygen it suggests the initial steps of the mechanism are the same. As such it follows that the lowered production of **2** is rationalised by the introduction of competing mechanisms. Chloride radicals have often been measured to have extremely rapid reaction times, often diffusion limited, which can compete with hydroxyl and superoxide radicals. [20][21][22] There does not appear to be a direct correlation between $[Cl^-]$ and the production of **2**, just that the presence of Cl^- results in a stark drop in formation. The observed drop in **2** removal is presumably due to the scavenging of hydroxyl radicals, the primary radical species as noted in 3.2.1, by chloride. Under oxygenated conditions, and similarly to sulfated media, chloride exhibits little to no influence on the production of **3**; whilst in deoxygenated conditions a very distinct increase in the production of **3** was found. It is assumed that, in the presence of oxygen, the lack of change is for the same reasons as in sulfated solution; that **3** is generally formed in solution by hydroxyl radicals. This assumption would predict no direct competition with chloride based mechanisms and so no change in intermediate formation with increasing chloride concentration. The next question is how chloride increases the production of **3** in the absence of oxygen? Increasing the ionic strength of aqueous solutions is reported to decrease the solubility of organic compounds so that does not explain the increase. [43] One could theorise that the presence of chloride extends the lifetime of hydroxyl radicals by scavenging the radical charge and later releasing it by photolysis after complexation with water. [44][45][46]

Analysis of the GC-MS indicated why the increase of degradation and inhibition of CO_2 release was occurring. Several new intermediates were detected; acetophenone (**4**), 2'-chloroacetophenone (**5**), 2-chloroacetophenone (**6**) and 1,2-dibenzoylthane (**7**). Just by visual inspection all of these intermediates are related in that they are all derivatives of acetophenone, including **7** which looks like a dimerization product. **4** and **5** are the intermediates with the highest preference for formation, as seen in the reaction profiles of **Figure 3.2.3.2**, where they each reach concentrations between 7 and 8 ppm after the first 5 minutes of irradiation for 0.5M KCl. The same chloride concentration dependence was seen for NaCl reactions, although significantly higher concentrations were detected for **4** and **5**, for the equivalent $[Cl^-]$. Whereas the purging of oxygen caused the inhibition of the production of these new intermediates, clearly illustrating the importance of dissolved oxygen in the reaction mechanism. The key question here is, how does the presence of chloride facilitate the production of **4**, **5**, **6** and **7**? Our data indicated that **6** is merely a product of the degradation of **5** and so it can be disregarded for now. Atomic chlorine is known to react via



Mechanism 3.2.3.2:- Proposed mechanism showing in detail how intermediates **4**, **5** and **7** could form

hydrogen abstraction, addition or addition/elimination mechanisms. [19][47][48] Assuming the initial step is similar to the one proposed in **Mechanism 3.2.1.1**, the most likely mechanism involves Cl[•] attacking at the position α to the carboxylic acid after, or at the same time, the radical oxygen species has bound across the double bond, as seen in **Mechanism 3.2.3.1**. From this theoretical state, the molecule can decarboxylate and dehydrate to give either **4**, **5** or **7**. **Mechanism 3.2.3.2** then depicts the two key routes required to form these intermediates. The molecule can simply lose a CO₂ and OH⁻/H₂O and form **5**. Or it can additionally lose the chlorine moiety leaving it with a resonance stabilised carbocation that can do one of three things: abstract a hydrogen from H₂O to form **4**, radically add to a free molecule of **5** to kick out a Cl[•] and form **7**, or radically dimerise with another radical acetophenone species to give **7**. Intuitively it follows that the most abundant intermediates, **4** and **5**, form via the simpler mechanisms where the radical reacts with a solvent molecule or an abundant ion; therefore increasing the likelihood of their formation. Whilst the formation of **7** depends on the probability of colliding with a molecule of **5** or another radical acetophenone intermediate species.

The removal of **4** was observed to be independent of chloride concentration, whereas **5** was not. The reasons for this can be found in the mechanism of how each degrades. Further reaction of **4** found that it was not susceptible to Cl[•] attack or addition to give a chlorinated

aromatic ring. Instead it preferentially degraded via HO• radical attack to the aromatic ring. Its degradation likely relies on the hydroxyl radical driven ring opening [49][50] **5**, however, displays degradative behaviour that is linked to chloride concentration. The higher the concentration of chloride the slower **5** is degraded with only 53.8% of **5** removed from 5 to 180 minutes in the 0.5M KCl reaction. Whilst in the presence of 1M NaCl the concentration of **6** does not begin to fall with the 3 hour reaction time. The further reaction of **5** showed its transformation to **6** occurred in the absence of both chloride and titania. The formation of **6** in the absence of titania is expected due to UV photolysis being a known route to the homolytic cleavage of the chlorine moiety [18] The absence of TiO₂ gives the slowest degradation of **5**, but the greater amounts of detected intermediates. This is clearly because the degradation relies entirely on the homolytic cleavage of the Cl atom, as does the formation of all of the products, which has no semiconductor replenishing the radical species that have been neutralised. Whilst reacting **5** in the presence of mP25 and mP25/Cl⁻ resulted in increased degradation, 67.1% and 75.3% respectively. From our data it is clear that, during the formation of **5**, the RCS most favourably attacks CAs double bond leaving it attached in the position α to the ketone functionality, if it remains at all. During the further reaction of **4**, in the presence of chloride, it was evident that chlorine addition/elimination was not occurring suggesting the direct addition of Cl• to the aromatic ring is not favoured. This presents the dilemma of how chlorine is added to the ring. It does not appear feasible starting from **4**, so perhaps the homolytic cleavage of the chloride in **5** activates the ring? A potential mechanism may involve the homolytic cleavage of the C-Cl bond that leaves a radical delocalised across the molecule that therefore makes the addition/elimination by Cl• to the aromatic system more viable. [51] The degradation of both **2** and **3** do not a susceptibility to chlorination on the aromatic ring either, an observation that is consistent with the assertion that ring chlorination here requires a disruption of delocalisation.

We know, from CO₂ capture experiments, that most of the carbon is retained in the reaction mixture with the assumption that it exists mostly in an intermediary form. The GC-MS data illustrated the expansion of the available reaction pathways and subsequent prolonging of total mineralisation. Whereas, under standard conditions complete mineralisation occurs within three hours that results in more deposited carbon with less oxygen functionality; degradation with chloride resulted in less carbon with a greater ratio of oxygen present. IR data showed the organic species on the photocatalyst surface displayed characteristic vibrations of a variation of carbonyl functionalities, including ketones and

aldehydes, which can easily be attributed to one of the many intermediates detected in the reaction and through further experimentation. The greater ratio of oxygen bearing carbon is a symptom of the partial degradation, also observed in sulfated conditions, that results in the widespread oxidation and hydroxylation of the aromatic species. The presence of aromatic species on the spent catalysts corroborates with the GC-MS data that showed aromatic intermediates remained in solution.

3.3 Conclusions

In conclusion, the main mechanism for cinnamic acid degradation heavily relies on superoxide radicals for effective removal and purging of oxygen reduces the advanced oxidation processes to those involving hydroxyl radicals. 2 is formed by the strictly surface based mechanism (mechanism 3.2.1.2) that is switched off in the absence of oxygen, inhibited in the presence of sulfate and runs in competition with mechanisms where chloride partakes. 3 is produced via the participation of hydroxyl radicals and could occur in solution or on the surface. The inclusion of sulfate had no impact on the production of 3, whilst chloride only caused a change when oxygen was removed. Sulfates generally slowed the rate of degradation, however it only has minor effects on the rate of total mineralisation. There was no evidence that sulfate radicals formed during the reaction and no mechanistic changes were observed. The introduction of chloride instigated an acceleration of the initial steps of cinnamic acid degradation that was accompanied with the retardation of total mineralisation. Chloride is assumed to have formed Cl^{\bullet} radicals that reacted in conjunction with a ROS to give 4, 5 and 7. Mechanism 3.2.3.2 shows the suggested reaction path that can explain the appearance of these new intermediates. The evidence suggests Cl^{\bullet} radically adds to the adsorbed species described in 3.2.1, that is responsible for formation of 2, to give an intermediary chlorinated-peroxy species (Mechanism 3.2.3.2). Whilst alongside this reaction Cl^{\bullet} also performs an addition/elimination that leaves a radical acetophenone species that either abstracts a hydrogen from H_2O to form 4 or dimerises to give 7 (Mechanism 3.2.3.2). 6 was shown to only form from 5, irrespective of if chloride or titania was present, from which it was theorised chlorination of the aromatic ring was only feasible whilst the aromaticity had been disrupted. Overall both sulfate and chloride have inhibitory effects on the degradation of cinnamic acid that would reduce the mineralisation efficiency in real waste water systems.

3.4 References

- 1 “Oil Palm & The Environment (updated March 2014).” Malaysian Palm Oil Board. Accessed January 2, 2016. <http://www.mpob.gov.my/palm-info/environment/520-achievements>.
- 2 K. K. Turekian, *Oceans*, Prentice-Hall, 1968.
- 3 M. D. Victor-Ortega, J. M. Ochando-Pulido, D. Airado-Rodríguez and A. Martínez-Férez, *Journal of Industrial and Engineering Chemistry*, 2016, **34**, 224–232.
- 4 A. A. Lima, A. F. Montalvao, M. Dezotti and G. L. S. Jr, *Ozone: Science & Engineering*, 2006, **28**, 3–8.
- 5 G. Li, T. An, J. Chen, G. Sheng, J. Fu, F. Chen, S. Zhang and H. Zhao, *Journal of Hazardous Materials*, 2006, **138**, 392–400.
- 6 L. Dogliotti and E. Hayon, *J. Phys. Chem.*, 1967, **71**, 2511–2516.
- 7 J. Méndez-Díaz, M. Sánchez-Polo, J. Rivera-Utrilla, S. Canonica and U. von Gunten, *Chemical Engineering Journal*, 2010, **163**, 300–306.
- 8 J. Wiszniowski, D. Robert, J. Surmacz-Gorska, K. Miksch and J.-V. Weber, *International Journal of Photoenergy*, 2003, **5**, 69–74.
- 9 P. Neta, R. E. Huie and A. B. Ross, *Journal of Physical and Chemical Reference Data*, 1988, **17**, 1027–1284.
- 10 S. Garg, T. Ma, C. J. Miller and T. D. Waite, *J. Phys. Chem. C*, 2014, **118**, 26659–26670.
- 11 G. V. Buxton, M. Bydder and G. A. Salmon, *Phys. Chem. Chem. Phys.*, 1999, **1**, 269–273.
- 12 J. E. Grebel, J. J. Pignatello and W. A. Mitch, *Environ. Sci. Technol.*, 2010, **44**, 6822–6828.
- 13 U. K. Klänig and T. Wolff, *Berichte der Bunsengesellschaft für physikalische Chemie*, 1985, **89**, 243–245.
- 14 G. G. Jayson, B. J. Parsons and A. J. Swallow, *J. Chem. Soc., Faraday Trans. 1*, 1973, **69**, 1597–1607.
- 15 X.-Y. Yu and J. R. Barker, *J. Phys. Chem. A*, 2003, **107**, 1313–1324.
- 16 X.-Y. Yu and J. R. Barker, *J. Phys. Chem. A*, 2003, **107**, 1325–1332.
- 17 G. V. Buxton, M. Bydder, G. A. Salmon and J. E. Williams, *Phys. Chem. Chem. Phys.*, 2000, **2**, 237–245.
- 18 L. Nelson, O. Rattigan, R. Neavyn, H. Sidebottom, J. Treacy and O. J. Nielsen, *Int. J. Chem. Kinet.*, 1990, **22**, 1111–1126.
- 19 B. C. Gilbert, J. K. Stell, W. J. Peet and K. J. Radford, *J. Chem. Soc., Faraday Trans. 1*, 1988, **84**, 3319–3330.
- 20 H.-W. Jacobi, F. Wicktor, H. Herrmann and R. Zellner, *Int. J. Chem. Kinet.*, 1999, **31**, 169–181.
- 21 H. Herrmann, B. Ervens, P. Nowacki, R. Wolke and R. Zellner, *Chemosphere*, 1999, **38**, 1223–1232.
- 22 F. Wicktor, A. Donati, H. Herrmann and R. Zellner, *Phys. Chem. Chem. Phys.*, 2003, **5**, 2562–2572.
- 23 J. C. S. Costa, P. Corio and L. M. Rossi, *Nanoscale*, 2015, **7**, 8536–8543.
- 24 S. H. Szczepankiewicz, A. J. Colussi and M. R. Hoffmann, *J. Phys. Chem. B*, 2000, **104**, 9842–9850.
- 25 W. Wu, K. Bhattacharyya, K. Gray and E. Weitz, *J. Phys. Chem. C*, 2013, **117**, 20643–20655.
- 26 W.-C. Wu, C.-C. Chuang and J.-L. Lin, *J. Phys. Chem. B*, 2000, **104**, 8719–8724.
- 27 Z. Topalian, B. I. Stefanov, C. G. Granqvist and L. Österlund, *Journal of Catalysis*, 2013, **307**, 265–274.
- 28 Z. Topalian, G. A. Niklasson, C. G. Granqvist and L. Österlund, *ACS Appl. Mater. Interfaces*, 2012, **4**, 672–679.

Chapter 3 – The Effect of Salts on the Photocatalytic Degradation of Cinnamic Acid

- 29 H. Maeda, H. Nakagawa and K. Mizuno, *Journal of Photochemistry and Photobiology A: Chemistry*, 2007, **189**, 94–99.
- 30 H. Sugimoto, S. Matsumoto and D. T. Sawyer, *J. Am. Chem. Soc.*, 1987, **109**, 8081–8082.
- 31 K. Matsunaga, M. Imanaka, K. Kenmotsu, J. Oda, S. Hino, M. Kadota, H. Fujiwara and T. Mori, *Bull. Environ. Contam. Toxicol.*, 1991, **46**, 292–299.
- 32 G. V. Buxton, *Journal of Physical and Chemical Reference Data*, 1988, **17**, 513–886.
- 33 P. M. P. Santos and A. J. S. C. Vieira, *J. Phys. Org. Chem.*, 2013, **26**, 432–439.
- 34 T. D. Bui, A. Kimura, S. Higashida, S. Ikeda and M. Matsumura, *Applied Catalysis B: Environmental*, 2011, **107**, 119–127.
- 35 I. B. Niklasson, T. Delaine, M. N. Islam, R. Karlsson, K. Luthman and A.-T. Karlberg, *Contact Dermatitis*, 2013, **68**, 129–138.
- 36 C. D. Wagner, D. A. Zatko and R. H. Raymond, *Anal. Chem.*, 1980, **52**, 1445–1451.
- 37 J. G. A. Terlingen, J. Feijen and A. S. Hoffman, *Journal of Colloid and Interface Science*, 1993, **155**, 55–65.
- 38 L. V. Duong, B. J. Wood and J. T. Klopogge, *Materials Letters*, 2005, **59**, 1932–1936.
- 39 J. Farnier Budarz, A. Turolla, A. F. Piasecki, J.-Y. Bottero, M. Antonelli and M. R. Wiesner, *Langmuir*, 2017, **33**, 2770–2779.
- 40 M. Abdullah, G. K. C. Low and R. W. Matthews, *J. Phys. Chem.*, 1990, **94**, 6820–6825.
- 41 I. Ahmad, J. A. Anderson, T. J. Dines and C. H. Rochester, *Spectrochimica Acta Part A: Molecular and Biomolecular Spectroscopy*, 1998, **54**, 319–326.
- 42 D. M. Griffiths and C. H. Rochester, *J. Chem. Soc., Faraday Trans. 1*, 1978, **74**, 403–417.
- 43 C. Bretti, R. M. Cigala, F. Crea, C. D. Stefano, C. Foti, A. Pettignano and S. Sammartano, *Monatsh Chem*, 2016, **147**, 1481–1505.
- 44 V. Nagarajan and R. W. Fessenden, *J. Phys. Chem.*, 1985, **89**, 2330–2335.
- 45 M. D. Sevilla, S. Summerfield, I. Eliezer, J. Rak and M. C. R. Symons, *J. Phys. Chem. A*, 1997, **101**, 2910–2915.
- 46 A. Treinin and E. Hayon, *J. Am. Chem. Soc.*, 1975, **97**, 1716–1721.
- 47 E. W. Kaiser and T. J. Wallington, *J. Phys. Chem.*, 1996, **100**, 9788–9793.
- 48 M. J. Ezell, W. Wang, A. A. Ezell, G. Soskin and B. J. Finlayson-Pitts, *Physical Chemistry Chemical Physics*, 2002, **4**, 5813–5820.
- 49 Z. Guo, R. Ma and G. Li, *Chemical Engineering Journal*, 2006, **119**, 55–59.
- 50 T. T. T. Dang, S. T. T. Le, D. Channei, W. Khanitchaidecha and A. Nakaruk, *Res Chem Intermed*, 2016, **42**, 5961–5974.
- 51 B. W. McCann, H. Song, H. B. Kocer, I. Cerkez, O. Acevedo and S. D. Worley, *J. Phys. Chem. A*, 2012, **116**, 7245–7252.
- 52 F. A. Miller and C. H. Wilkins, *Analytical Chemistry*, 1952, **24**, 1253–1294.
- 53 A. M. Shor, A. A. Dubkov, A. I. Rubaylo, N. I. Pavlenko, O. M. Sharonova and A. G. Anshits, *Journal of Molecular Structure*, 1992, **267**, 335–339.

Chapter 4 –Metal Doped Titania Nanotubes for the Photocatalytic Degradation of Organic Contaminants

| | |
|--|-----|
| 4.1 Introduction | 127 |
| 4.1.1 The Development of Anodic Nanotubes..... | 128 |
| 4.1.1.1 First Generation Nanotubes | 128 |
| 4.1.1.2 Second Generation Nanotubes..... | 129 |
| 4.1.1.3 Third Generation Nanotubes..... | 130 |
| 4.1.2 Titania Nanotubes in Photocatalytic Processes..... | 131 |
| 4.2 Characterisation of Nanotube Photocatalysts | 132 |
| 4.2.1 Topographical Studies of Nanotube Arrays..... | 132 |
| 4.2.1.1 Titania Nanotubes | 132 |
| 4.2.1.2 Ti/W Mixed Oxide..... | 138 |
| 4.2.1.3 Deposition of Gold and Palladium – Topography..... | 139 |
| 4.2.2 X-Ray Diffraction Studies | 141 |
| 4.2.3 UV Measurements of Nanotube Samples..... | 144 |
| 4.2.4 XPS Studies | 144 |
| 4.2.4.1 Titania Nanotube Arrays..... | 144 |
| 4.2.4.2 Ti/W Nanotube Arrays..... | 146 |
| 4.2.4.3 Gold and Palladium Decorated Nanotubes | 148 |
| 4.3 Photocatalytic Testing | 152 |
| 4.3.1 Reactivity of Plain Nanotube Arrays | 153 |
| 4.3.1.1 Liquid Phase Degradation of Cinnamic Acid | 154 |

| | |
|---|------------|
| 4.3.1.2 Surface Degradation of Cinnamic Acid | 155 |
| 4.3.1.3 Surface Degradation of Stearic Acid | 156 |
| 4.3.2 Reactivity of Au/Pd Nanotube Arrays | 160 |
| 4.3.2.1 Liquid Phase Degradation of Cinnamic Acid | 160 |
| 4.3.2.2 Surface Degradation of Stearic Acid | 163 |
| 4.4 Conclusions | 167 |
| 4.5 References | 169 |

4.1 Introduction

An important aspect in the mineralisation of organic recalcitrant material, and other industrial photocatalytic processes, is the structure of the photocatalyst utilised. Powdered catalysts are easy to make but often avoided, if possible, due to the inconvenient and expensive step of retrieving the catalyst from the reaction mixture. Immobilisation of catalysts is a favourable step in catalyst design that facilitates the use of constant flow reactors, that reduces costs and has the potential to improve a reactors overall efficiency. Titania, besides being an obvious choice for photocatalytic purposes, is an extremely adaptable material that can be forged into many forms on the nanoscale. Nanostructured titania, is a material where the production allows the strict control of the resulting dimensions. It is produced by many techniques and found in many forms, including: homogeneously formed anatase particles; [1][2] electrophoretic deposition of colloidal titania onto anodic alumina membrane template to form nanowires; [3] the hydrothermal synthesis of nanoparticles, [4][5] nanorods, [6][7][8][9] and nanotubes; [10][11][12][13] and the anodisation formation of vertically ordered nanotubes. [16 - 24] The type of nanostructured titania investigated in this chapter is anodic titania nanotubes. Anodised titania nanotubes were chosen for their reproducible structures that have potential for incorporation into photocatalytic reactor design.

In this chapter we aim to investigate, principally, how changes in anodisation length affects the photocatalytic properties of the materials. Additionally, the impact of decorating the tubes with gold and palladium in the area of advanced oxidation processes will be explored. The first section is a non-exhaustive literature analysis of the anodisation of titania to form nanotubes and the use of anodic nanotubes in photocatalytic processes. The second part of the chapter is the beginning of the results and discussion where we initially catalogue the topographical changes from varying anodisation time and subsequently deals with the deposition of gold and palladium. Tungsten was also incorporated to ascertain if a Ti/W mixed metal oxide offered improved degradation properties, the physical changes of which are described. In the third section, the elemental, crystallographic and absorption changes are discussed before an evaluation of the photocatalytic degradative efficiency. Liquid phase testing was performed using cinnamic acid to simulate the removal of organic waste as performed in chapters 3 and 5. Whilst arrays were coated with stearic acid and cinnamic acid

to assess the nanotubes self-cleaning abilities, an important attribute for materials being used in real world reactors.

4.1.1 The Development of Anodic Nanotubes

4.1.1.2 First Generation Nanotubes

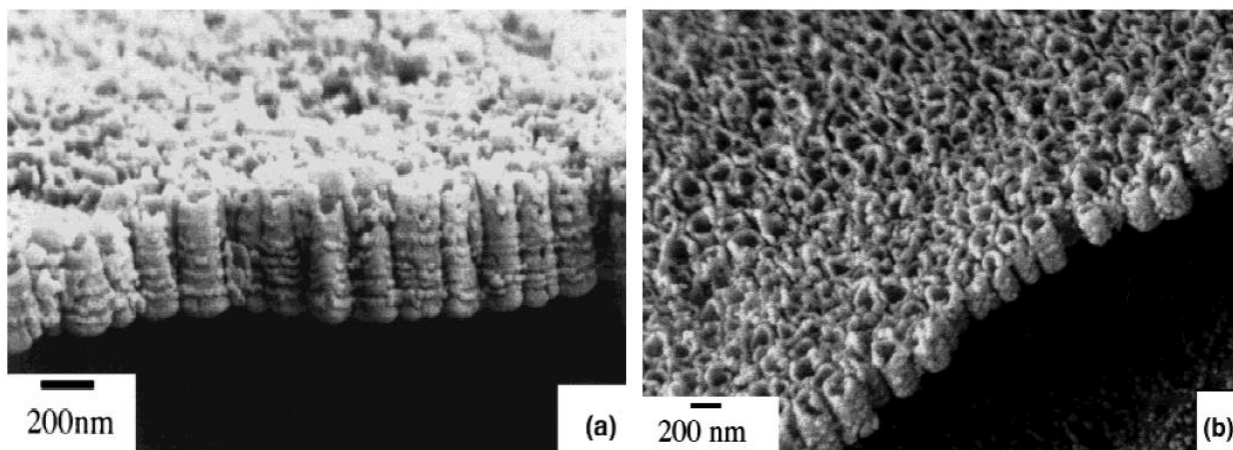


Figure 4.1 FE-SEM images of anodised titania nanotubes, anodised in aqueous 0.5wt% HF solution at 20V for 20 minutes. [14]

Anodisation has, for some time, been used on titanium for protective applications, but in 1999, Zwillling *et al.* discovered that the inclusion of fluoride into the acidic electrolyte produced a self-ordered porous titania film. [14] Earlier research found the presence of fluoride did not impact on the anodic oxidation of aluminium, the porosity of which is induced through chemical etching with strong acids and bases, [15] and it was soon realised that fluoride initiated a new chemical process. Oxide growth on titania can be simply described by **Equation 4.1**. If unaided, an oxide barrier layer forms which will grow until the thickness of the layer prevents migration of water molecules to the titanium sheet below. When fluoride is present, the F⁻ ion is attracted to the titanium anode and chemically dissolves the metal to form the thermodynamically stable, water soluble titanium hexafluoride ion, as shown in **Equation 4.2**.



Nanotubes grown in this highly acidic, fluorinated electrolyte could only reach lengths of 500 nm. It was concluded that the strong acidity of HF, and the experimental conditions, were

responsible for the stunted growth observed. This development spurred on research into the next phase of nanotube growth.

4.1.1.2 Second Generation Nanotubes

Second generation TiO₂ nanotubes were developed using an alternative fluoride source to hydrogen fluoride. Different groups branched out trying different electrolyte compositions. In 2005 Cai *et al.* [16] utilised various potassium and sodium fluoride solutions with great success, tubes of length 4.4 μm could be synthesised by variation of applied voltage, anodisation time and pH. 25 V was found to be the optimum voltage, while it was discovered that the longest tubes developed at higher pHs so long as the aqueous solution remained acidic. Macak *et al.* used NaF in neutral aqueous Na₂SO₄ solution achieving tubes of 2.4 μm in length and 100 nm in diameter with dissolution rates of 38 nm min⁻¹ at a pH of 2 and 1.5 nm min⁻¹ at a pH of 5. [17] A characteristic of an electrolyte with a high water content

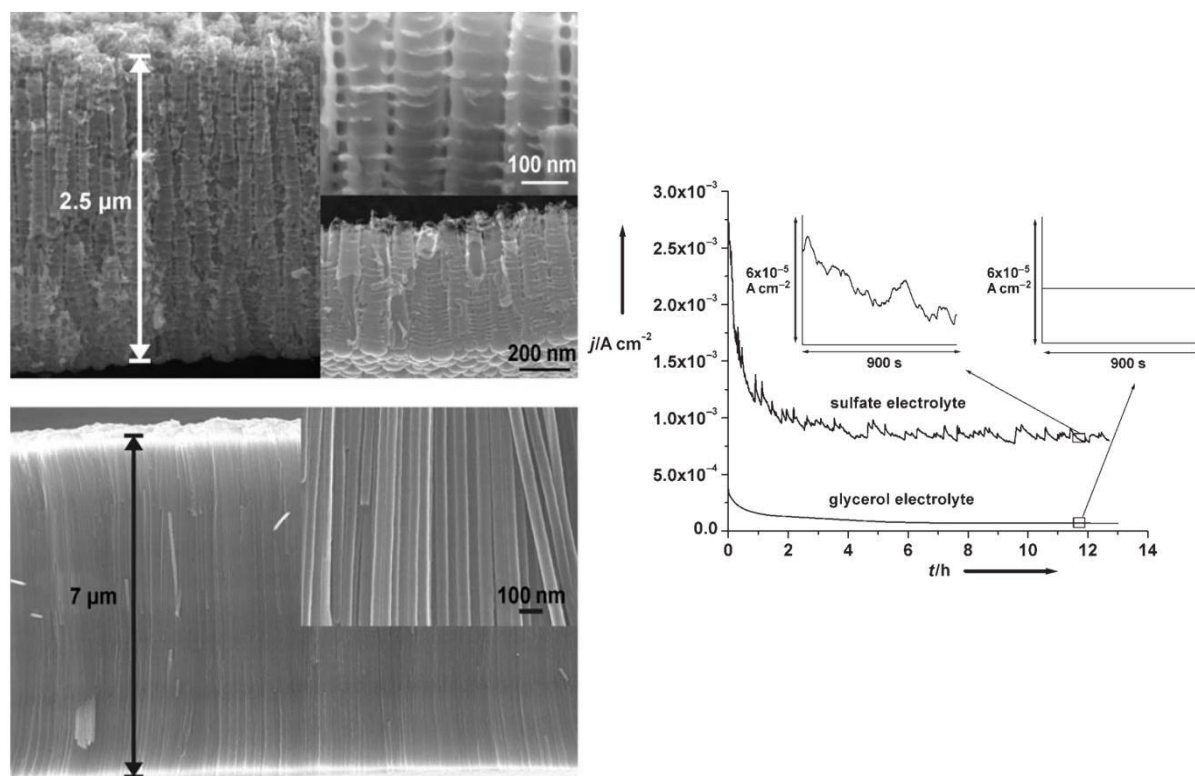


Figure 4.2: Left images. (a) SEM images of nanotubes produced in 1M H₂SO₄ solution and 0.15% HF. **(b)**SEM images of 7μm long, smooth nanotubes produced in a glycerol and 0.5 wt % NH₄F electrolyte.

Right Image. (c) Current-Time behaviour of samples anodised at 20V for 13 hours. Electrolyte composition was glycerol or 1M (NH₄)₂SO₄ both with 0.5 wt% NH₄F. [18]

and fluoride ions is the presence of ripples, or ribs, on the tube walls. These marks are only present in aqueous or high water content solutions (>3%) (as seen in **Figure 4.2 (a)**). It was realised that as the fluoride etched into the TiO₂ surface created a pH gradient where the pore bottom (pH = 2) was more acidic than the pore mouth (pH = 5) that was buffered by the (NH₄)₂SO₄ electrolyte. The regular ripples in the nanotube wall were regulated by periodic current oscillations that were caused by local acidification from the oxidation of elemental titanium via hydrolysis (**Equation 4.1**).

4.1.1.3 Third Generation Nanotubes

The synthesis of smooth nanotubes that stretched for tens to hundreds of micrometers in length were classed as 3rd generation TiO₂ nanotubes. Macak showed that smooth TiO₂ nanotubes were produced in the more viscous electrolyte, glycerol, at lengths of up to 7 μm. [18] A current-time transient, **Figure 4.2 c**, compares the current fluctuations of the glycerol electrolyte compared to that of a sulphate electrolyte and it is evident the use of glycerol has suppressed the current fluctuations. This led to entirely smooth nanotubes due to the lower diffusion coefficients that more effectively contained the acidification to the pore tips, as well as a markedly lower current density. The switch to more viscous, organic electrolytes allowed considerably longer tubes with higher aspect ratios. The pore diameter was determined to be roughly 40nm with a wall thickness of 12 nm greatly differing from the dimensions of aqueous electrolyte nanotubes where the diameter was roughly 100nm. In 2007 Macak's group explored the use of HF in anhydrous ethylene glycol with much greater success than earlier experiments with HF. [19] Using a relatively high voltage of 120 V, HF concentration of 0.2M and anodising for 15 hours tubes of 251 μm were formed. These tubes had an inner diameter of 70 nm and an outer diameter of 160nm at the top of the tubes, indicating a very high aspect ratio, while at the pore bottom the inner diameter was smaller creating a conical shape to the tubes. This suggested the top of the tubes are subjected to more chemical etching than the base and this thins the walls. The study showed that increasing concentrations of fluoride and anodisation potential increased the length of tubes to an upper limit of 261 μm. In the same year Grimes *et al.* reported the complete consumption of 250 μm sheet of titanium to give a self-standing 720 μm thick nanotube membrane. [20] A true bench mark was set by Grimes *et al.* who grew tubes of lengths of 2000μm by double sided anodisation of 1mm thick Ti sheet at 60V for 9 days using 0.6wt% NH₄F and 3.5% water in ethylene glycol. [21] BET measurements indicated a surface area of 38 m²/g which was mostly constant

regardless of anodisation voltage. Besides the control of tube length, allowed by the technique, pore size has also been shown to be controllable with pore diameters of 190nm, [22], 350nm, [23] and later up to 600nm with a growth rate of 100 $\mu\text{m}/\text{h}$. [24]

Another key aspect of the process is the annealing step. Anodically formed nanotubes are naturally amorphous, a state that is not conducive to high photocatalytic activity, and so heat treatment is required to alter the crystallinity and promote hole-charge separation during irradiation. Anatase is typically the phase of choice for photocatalytic processes, [25] amorphous nanotubes will crystallise to anatase at temperatures as low as 280°C but will begin forming rutile at temperatures above 450°C. Studies have found that annealing at higher temperatures reduces structural defects and enhances crystallinity; enhancements that correlate to an improved charge-hole separation and a reduction in bandgap. [25][26][27] Temperatures above 600°C have been shown to promote higher levels of rutile phase; a feature that becomes detrimental to nanotube functionality as the rutile phase tends to form at the metal-metal oxide barrier eventually resulting in the destruction of the nanotubes as the rutile crystals grow. [28]

4.1.2 Titania Nanotubes in Photocatalytic Processes

The area of titania nanotube photocatalysis has rapidly expanded over the last decade to the point where research is beginning to examine how effective nanotubes are in many areas. Dye sensitized solar cells utilise dyes to capture electrons and pass them on to a semi conducting material, like TiO_2 or ZnO , the former is then regenerated by the electrolyte and the system generates electricity without being changed itself. [29] Powdered TiO_2 was used first but suffered from issues related to long, random electron escape paths and defect induced trapping that encourages recombination processes. [30] Titania nanotubes have been explored as nanostructured supports and research has shown hugely improved electron diffusion pathlengths regardless of nanotube film thickness. [31] Current testing has shown solar cell efficiencies reaching up to 10%. [32][33] Titania nanotubes have also shown promise in various other applications including: gas sensing of NO_2 , [34] H_2O , [35], and H_2 ; [36] and in photocatalytic watersplitting to produce H_2 and O_2 . [37] Nanotubes have also been studied for biomedical applications such as protein binding; [38].

Anodised nanotubes have been tested for their photocatalytic degradation of many aqueous organic molecules. Studies have investigated: azodyes such as methyl orange;

[39][40][41] phenol; [42] nitrophenols; [43] chlorinated heteroatom molecules like paraquat, [44] pentachlorophenol [45][46] and 2,3-dichlorophenol; [47] and formic acid. [59] The current data suggests that there are several key factors that control the degradation of organic pollutants. As with all titania based catalysts, organic degradation relies on the non-specific advanced oxidation by hydroxide radicals and other reactive oxygen species (ROS). Whilst there is some capability for these species to diffuse into solution, there is still a strong dependence on surface adsorption resulting in a Langmuir-Hinshelwood mechanism often being sufficient to describe degradation rates, particularly at low pollutant concentrations. However, the top tube morphology has been found to be crucial in understanding nanotube array photocatalytic efficiency. [28][44][48] Open tubes with thin walls have been shown to have improved penetration of irradiating light where light typically only penetrates 1-2 μm into the nanotube layer. [48] This revelation sheds light onto the variation of values found for the most efficient tube length for photocatalytic degradation, which has been variously suggested to be 6 μm [49] 17 μm , [42] and even as high as 47 μm . [59] The exact length of the tube is not the crucial factor; instead the nanotube anodisation length which results in wall thinning as times increase, as well as increased tube length, is the more pertinent variable. Thinner and longer tubes facilitate deeper light penetration, whilst also improving pollutant diffusion kinetics and decreasing electron diffusion paths to pollutant molecules. However, increased tube length has also been correlated to a negative impact on degradation as the distance between pollutant and titania increases, therefore reducing the chance of the reactive species reaching the target molecules before reacting elsewhere. [44]

4.2 Characterisation of Nanotube Photocatalysts

4.2.1 Topographical Studies of Nanotube Arrays

4.2.1.1 Titania Nanotubes

Titania nanotubes used in these studies were produced, using the electrochemical technique called anodisation, in an electrolyte of ethylene glycol (392 mL), water (8 mL) and ammonium fluoride (1.33 g); at a potentiostatic voltage of 60 V with no voltage ramp rate. Anodisation times were varied to form nanotubes of differing lengths and pore sizes, with the chosen reaction times being; 1 hour, 4 hours, 8 hours and 24 hours. These anodisation times

| Sample | Tube Width (nm) | Pore Width (nm) | Wall Thickness (nm) | Tube Length (μm) | Aspect ratio | Crystallite size (nm) | E_g (eV) |
|---------------|-----------------|-----------------|---------------------|-------------------------------|--------------|-----------------------|------------------|
| 1hr Nanotube | 94.6 \pm 2.8 | 77.8 \pm 3.5 | 13.3 \pm 1.6 | 9.59 \pm 0.6 | 1 : 101.4 | 30.6 | 3.08 \pm 0.022 |
| 4hr Nanotube | 102.2 \pm 2.7 | 76.3 \pm 1.3 | 12.1 \pm 2.2 | 27.2 \pm 3.8 | 1:265.8 | 31.4 | 3.03 \pm 0.12 |
| 8hr Nanotube | 158.2 \pm 2.7 | 127.2 \pm 1.7 | 13.4 \pm 1.4 | 18.3 | 1 : 115.5 | 36.3 | 2.97 \pm 0.064 |
| 24hr Nanotube | 176.3 \pm 2.2 | 139.4 \pm 2 | 18.4 \pm 0.5 | 63.1 \pm 2.2 | 1 : 358 | 32.3 | 3.13 \pm 0.083 |
| Ti/W NT | 101.2 \pm 1.5 | 75.4 \pm 1.4 | 12.9 \pm 0.5 | / | / | 31.1 | 2.86 \pm 0.014 |

Table 4.2.1: Physical and electronic characteristics measured for nanotube samples. Nanotube measurement error is given as absolute error values, bandgap error is given as were used to provide an insight into how tube length and width might influence the degradation of organic contaminants. From a production point of view, the shorter the anodisation time the better, as smaller timescales naturally improve production efficiencies. The summarised attributes of the nanotubes formed can be found in **Table 4.2.1**. Firstly, under all reaction lengths the first nanotube sample produced in a fresh electrolyte tended to become detached from the titanium sheet either immediately after anodisation or during the ultrasonic cleaning process. Analysis, using several microscopic techniques, showed a clean break from the titanium sheet below with defined tubular bottoms being observed. **Figure 4.2.1 (left)** is a TEM image of the rear side of a one hour anodised nanotube array that was formed in fresh electrolyte. Measurements indicated a wall thickness of roughly 20 nm, which is 7nm thicker than at the tube openings measured via FESEM; a difference expected due to tube openings being exposed to the corroding effect of the fluoride for a greater time period. The SEM image, **Figure 4.2.1 (right)** shows the rear side of a 24 hour anodised nanotube array and the tube openings are very visible, again showing the well-defined and tube bottoms. This detachment phenomenon, which occurs in fresh electrolyte, has been previously documented and is due to the increased current densities associated with higher water and F^- content in comparison to “aged” electrolytes. [50] Lower current densities result in larger barrier layers forming during anodisation which improves adhesion of the nanotubes to the parent titanium sheet. The surface topology of the nanotube arrays was initially

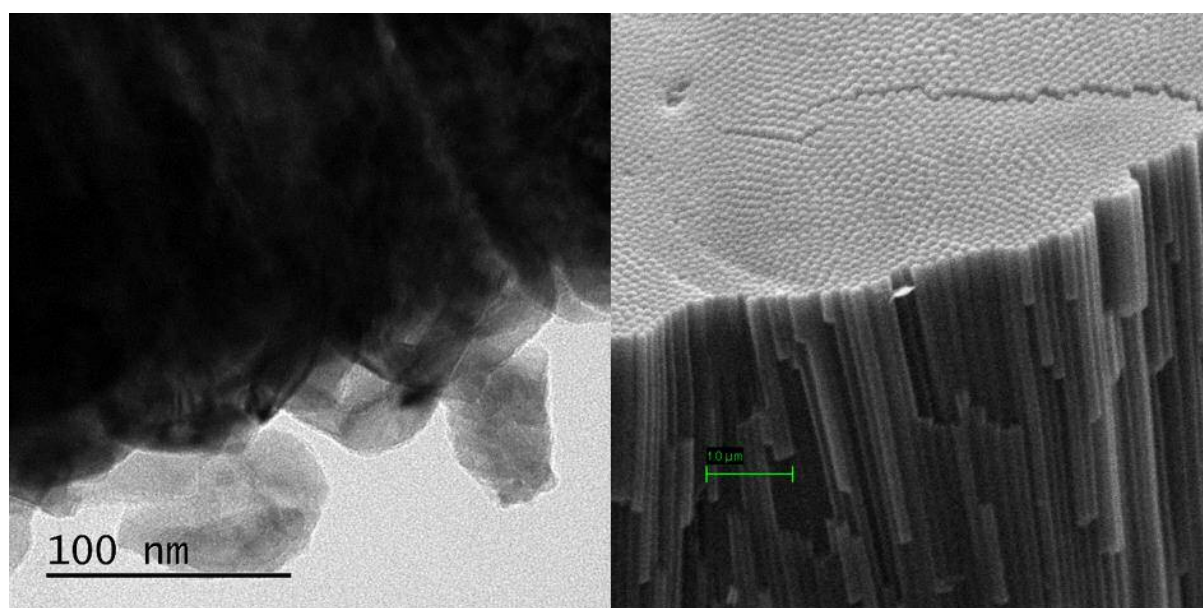


Figure 4.2.1:- Microscopy images of the underside of nanotube sheets. Left is a TEM image of a 1 hour nanotube, Right is an SEM image of the underside of a 24 hour nanotube array established with a standard scanning electron microscope, and later imaged in greater detail with a field emission scanning electron microscope. FESEM images (a) and (b) in **Figure 4.2.2** show a typical cross section and surface topology of nanotube arrays that had been anodised for 1 hour. The surface had a generally homogeneous appearance with open tubes with an average pore diameter and wall thickness of 77.8 ± 2.8 nm and 13.3 ± 1.6 nm respectively. These tubes were the smallest in width and shortest in length with a calculated aspect ratio of 1:101.4. TEM analysis of the samples indicated average pore and tube diameters that were notably smaller than average measurements calculated from FESEM imaging, suggesting the tubes forming were of a V-shape. **Figure 4.2.3** shows a transmission electron microscope image of a section of tubes anodised for one hour; measurements taken along a single tube show the tube and pore diameter increasing along the tube. This is a consequence of the anodisation process where the tube bottoms have been exposed to the corrosive fluoride species for less time than the top ends. Increasing the anodisation time to 4 hours yielded significantly longer tube lengths, the average of which was determined to be 27.2 ± 3.8 μm. The near fourfold increase in length indicates growth had entered a steady state and continued at a constant speed of roughly 110 nm/min. The pore diameters and wall thicknesses were measured to be of very similar dimensions to 1 hour nanotubes which resulted in an increased aspect ratio of 1 to 265.8. SEM analysis did however identify the appearance of valley-like structures and the presence of a barrier layer that had formed atop

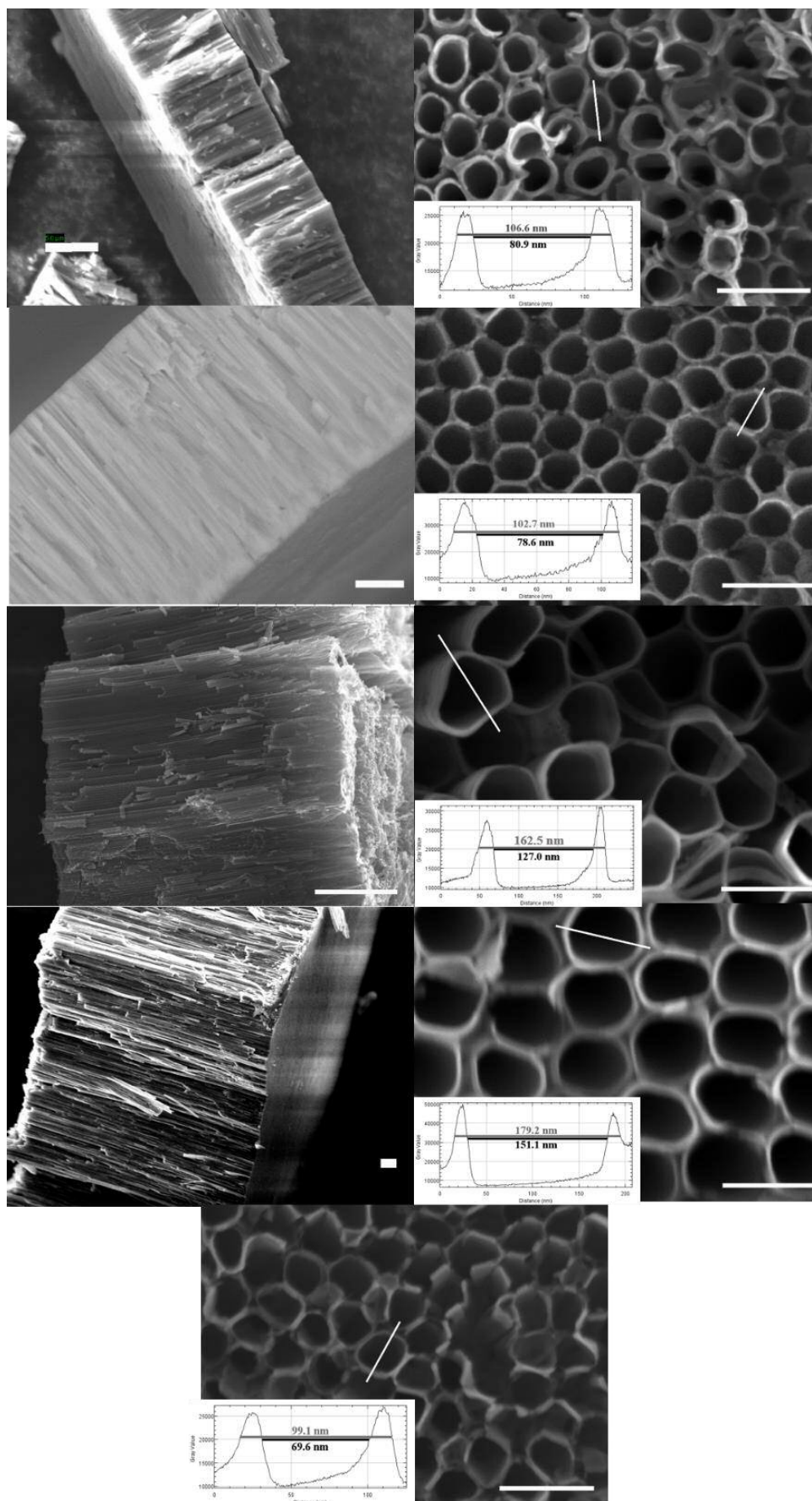


Figure 4.2.2: SEM and FESEM images showing the cross-section and surface morphology for nanotubes anodised for 1 hour [(a) and (b)], 4 hours [(c) and (d)], 8 hours [(e) and (f)], 24 hours [(g) and (h)], and for 4 hours in the presence of tungsten (i) White scale bars represent 5µm (cross sections) and 200 nm (top morphology)

the nanotube array in some areas. Other work has identified this issue previously as an oxidised TiO₂ layer that can be removed by ultrasonication or by HF treatment. [51][52] Nanotubes anodised for 8 hours had tube widths averaging at 158.2±2.7 nm, pore diameters of 127.2±1.7 nm and a wall thickness averaging 13.4±1.4 nm. The large increase, in both tube and pore diameter, is a symptom of the extended anodisation time enlarging the total diameter whilst maintaining a similar wall thickness. Data for tube lengths for these samples was however poor. No samples detached easily from the titanium sheet, as was found with all other samples, which resulted in part of an array being scraped off using a scalpel. From this sample, the average tube length was measured at 18.3 µm, a significant decrease from 4 hours. **Figure 4.2.4** shows a low magnification image of a typical sample, and three insets showing three different regions. (i) is a region where a thin layer of, what looks like, tubular detritus on top of the nanotube layer. This feature was found on tubes anodised for 4 and 8 hours, appearing more frequently on the longer anodised samples. This layer is consistent

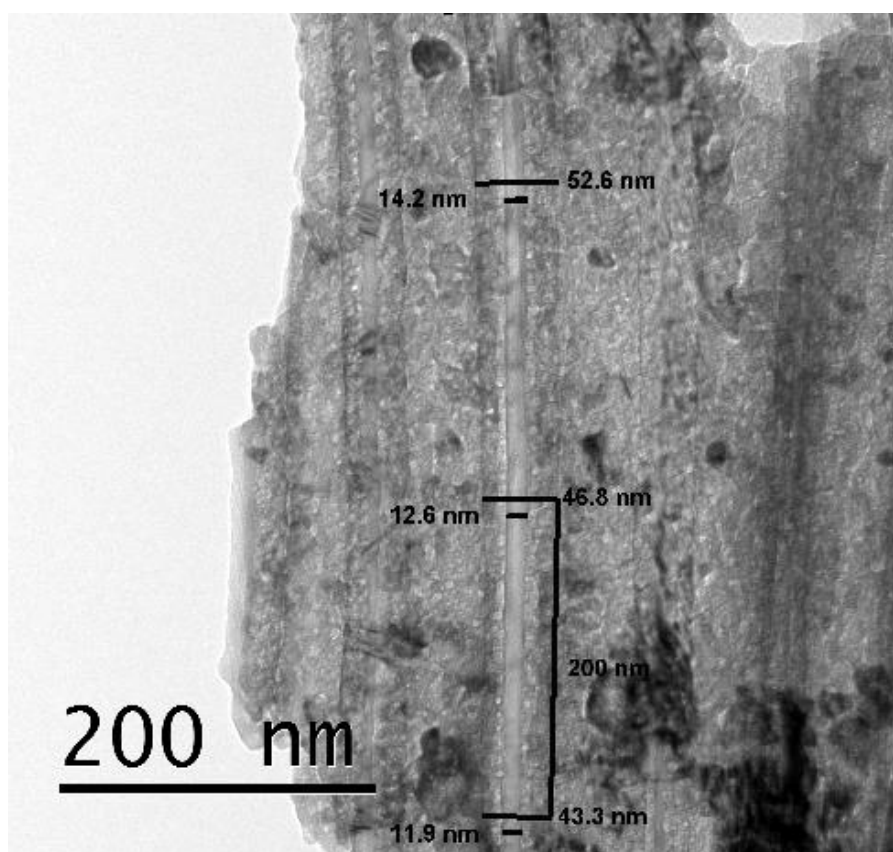


Figure 4.2.3:- TEM image showing a section of a nanotube array at the bottom of tubes that were anodised for 1 hour. Measurements up the tube, at 200 nm intervals, show an increase in tube diameter and pore width

with a symptom of long anodisation times that results in the collapse of elongated, thinned tubes. [48] (ii) shows a section of the nanotube layer that is partially covered by a porous layer of titania. The pores of the layer appear to line up with the mouths of the tubes below suggesting this feature may not cause too much of hindrance to photocatalytic efficiency. The third region, (iii) shows an area with a large number of tubes entirely open and unhindered. From the lower magnification image, one can see that region (iii) is the most common followed by (ii) and then (i). This suggests the majority of the surface is likely to be open to irradiation. For nanotubes anodised for 24 hours we observe an increase in all dimensions and subsequently the aspect ratio. FESEM found the tube and pore width to be 176.3 ± 2.2 nm and 139.4 ± 2 nm, respectively, whilst the tube length was measured to be 63.1 ± 2.2 μ m. This provides a higher aspect ratio, once again, of 1 to 358. Tube diameter measurements from TEM gave different values, to those from FESEM, in the same manner to that for 1 hour

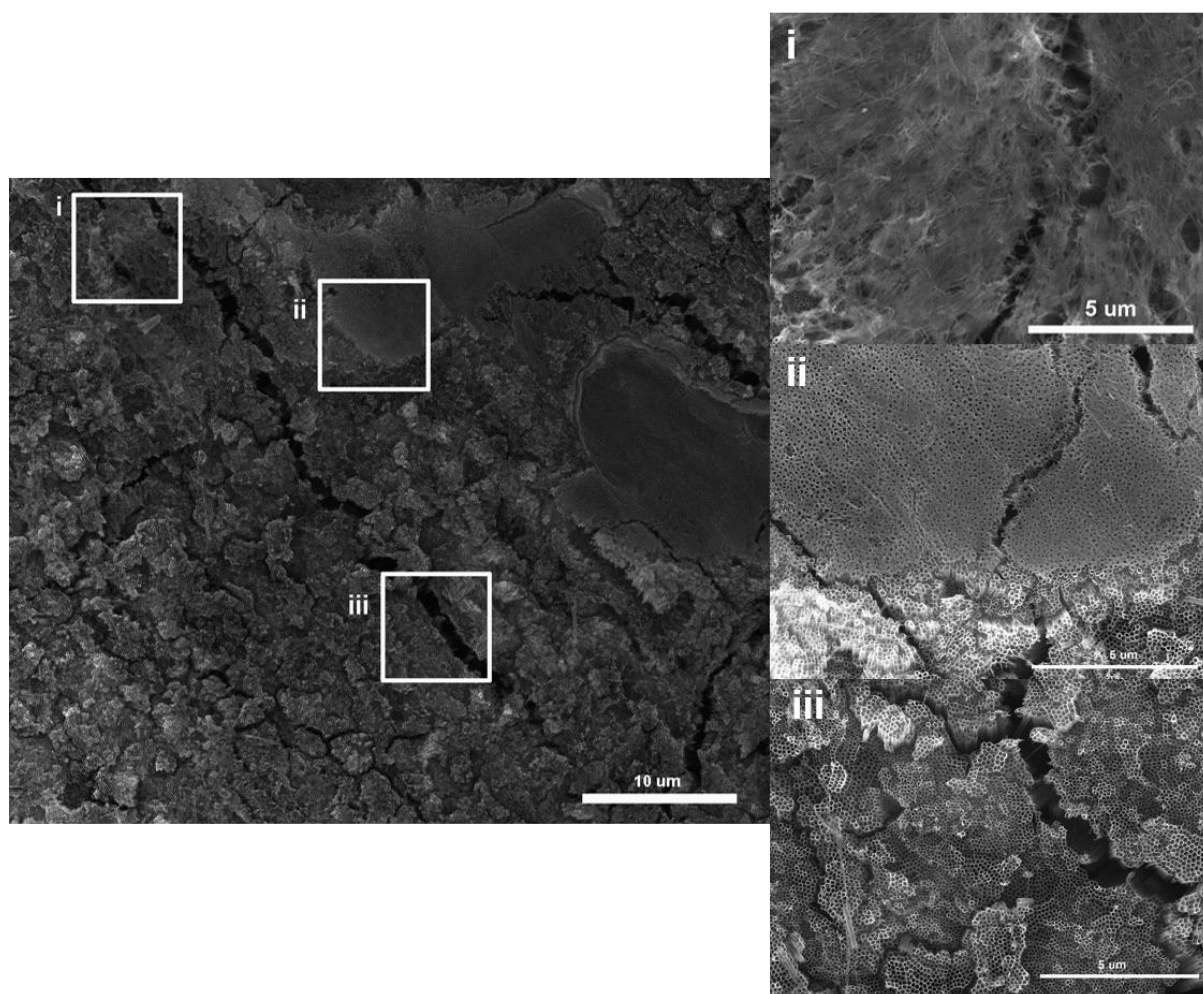


Figure 4.2.4: Low magnification FESEM image with highlighted regions: (i) detritus covered tubes, (ii) porous layer partially covers tubular layer below, (iii) open mouth tubes.

anodised tubes. Tubes were again measured along various sections of tubes and found to have smaller diameters, in both tube and pore diameter, but thicker walls which is ascribed to the tubes having conical shapes. Topographical studies, using FESEM and SEM found that anodisation for 24 hours resulted in less detritus but also less relatively flat planes of tubes; the latter is due to the presence of valley-like features formed by longer tubes with thinner walls.

4.2.1.2 Ti/W Mixed Oxide

The inclusion of tungsten in the anodisation process did not prevent in the formation of nanotubes after four hours of anodisation. Measurements found pore widths and wall thicknesses of 101.2 ± 1.5 nm and 12.9 ± 0.5 nm respectively. These values are consistent with

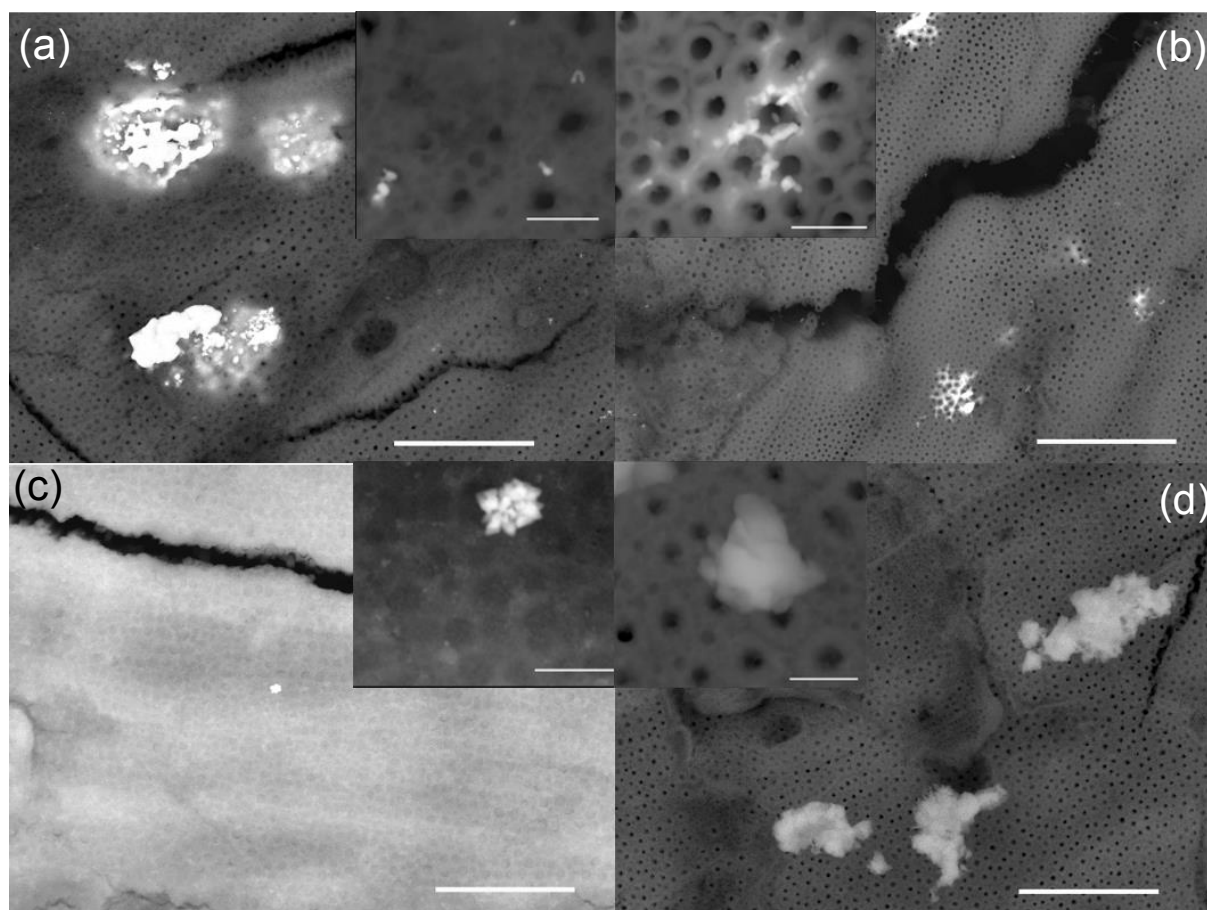


Figure 4.2.5: Back scattered FESEM images of nanotubes anodised for 8 hours and decorated with gold and palladium by photodeposition, with insets showing higher magnification Images show nanoparticles photo deposited from solutions of: HAuCl_4 after - (a) 1 minute (8hr Au1), (b) 3 minutes (8hr Au3); PdCl_2 after - (c) 1 minute (8hr Pd1), (d) 3 minutes (8hr Pd3) White scale bar represent 2 μm in main images, and 200 nm in inset images

those of tubes anodised for four hours in the absence of tungsten suggesting that the metal did not impact on the core growth mechanisms. However, as seen in **Figure 4.2.2 (i)**, the tubes formed were not as perfectly tubular as those in tungsten free conditions. Tubes were often seen to be malformed or broken and bear a closer resemblance to squares than circles at the pore openings. Tube length measurements could not be collected so the aspect ratio was not calculated although, as discussed previously, pore diameter and wall thickness is more pertinent to photocatalysis than tubelength. [24][44][48]

4.2.1.3 Deposition of Gold and Palladium – Topography

Titania nanotubes, which had been anodised for 4 and 8 hours, were doped with gold or palladium via a photo assisted deposition technique. Deposition was performed for 1, 3, 30 and 60 minutes in 5 mM solutions of PdCl₂ and HAuCl₄, for 4 hour nanotubes, and 1 and 3 minutes for 8 hour nanotubes. These nanotube samples were chosen for deposition, as will be discussed later, because initial testing indicated that they had the best photocatalytic performance. Due to time and funding constraints, FESEM images were only collected for 8 hour nanotubes doped with palladium and gold for 1 and 3 minutes. Examples of these images can be found in **Figure 4.2.5**. Images **(a)** and **(b)** are backscattered electron images that show how gold deposition occurred after 1 and 3 minutes, the insets of each showing higher magnification backscattered images. In both cases, gold accumulates in three different manners: as small scattered particles, as is evident in both images; as agglomerated clusters that are most obvious in **Figure 4.2.5 (a)**; and around the pore openings of the tubes most clearly seen in **(b)** and **(b) inset**. For 8hr Au1 and 8hr Au3 this results in an average gold particle size ($A_{v_{np}}$) of 40.1±3 nm and 30.7±3 nm. Palladium tended to deposit as smaller particles that had a high tendency to agglomerate as shown in **Figure 4.2.5 (c) inset**. A large agglomeration of palladium is visible as well as many small nanoparticles scattered across the surface. The small nanoparticles were of sizes near the detection limit of the instrument and meant the quoted value ($A_{v_{np}} \approx 15.3$ nm) contained a large degree of uncertainty in the measurement. Individual particles were even harder to locate on the 8hr Pd3 samples which prevented the calculation of an average measurement. Of the agglomerated particles found on the surface a rough average was found of 400 nm.

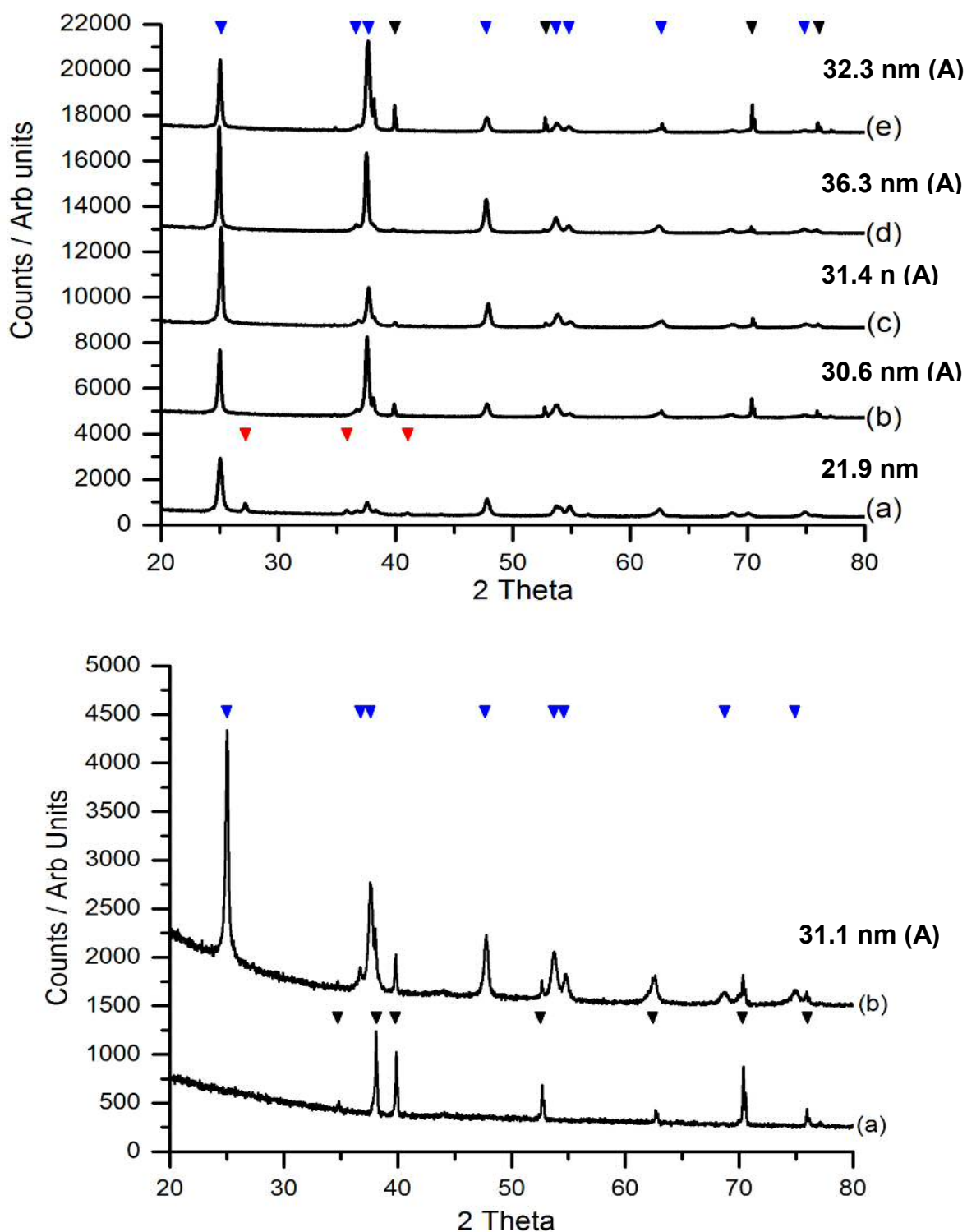


Figure 4.2.6 X-Ray diffraction patterns for nanotube samples: Top – (a) modified P25 powder, (b) 1hr NT, (c) 4 hr NT, (d) 8hr NT, (e) 24hr NT; Bottom – (a) Ti/W NT as formed, (b) Ti/W NT after annealing at 400°C
 Triangle phase markers: anatase (blue), rutile (red), metallic titanium (black)
 Attached values are the associated crystallite sizes, as determined using the Scherrer equation

4.2.2 X-Ray Diffraction Studies

As anodisation produces amorphous titania nanotubes, an annealing step was required to obtain a crystalline phase. XRD confirmed that annealing at 400°C for 1 hour formed purely anatase nanotubes, as shown in **Figure 4.2.6 (top)**. A comparison to our titania powder showed the lack of rutile diffraction peaks indicating no rutile had formed, whereas the very clear diffraction patterns of anatase can be observed, marked with a blue triangle, including the anatase 101 phase at a 2θ of 25. Additionally, metallic titanium diffraction patterns can be seen, denoted with a black triangle, at 2θ values of; 34.8, 38, 39.9, 52.8, 62.6, 70.4 and 76. [60] The titanium phase can be detected in all four nanotube samples with a

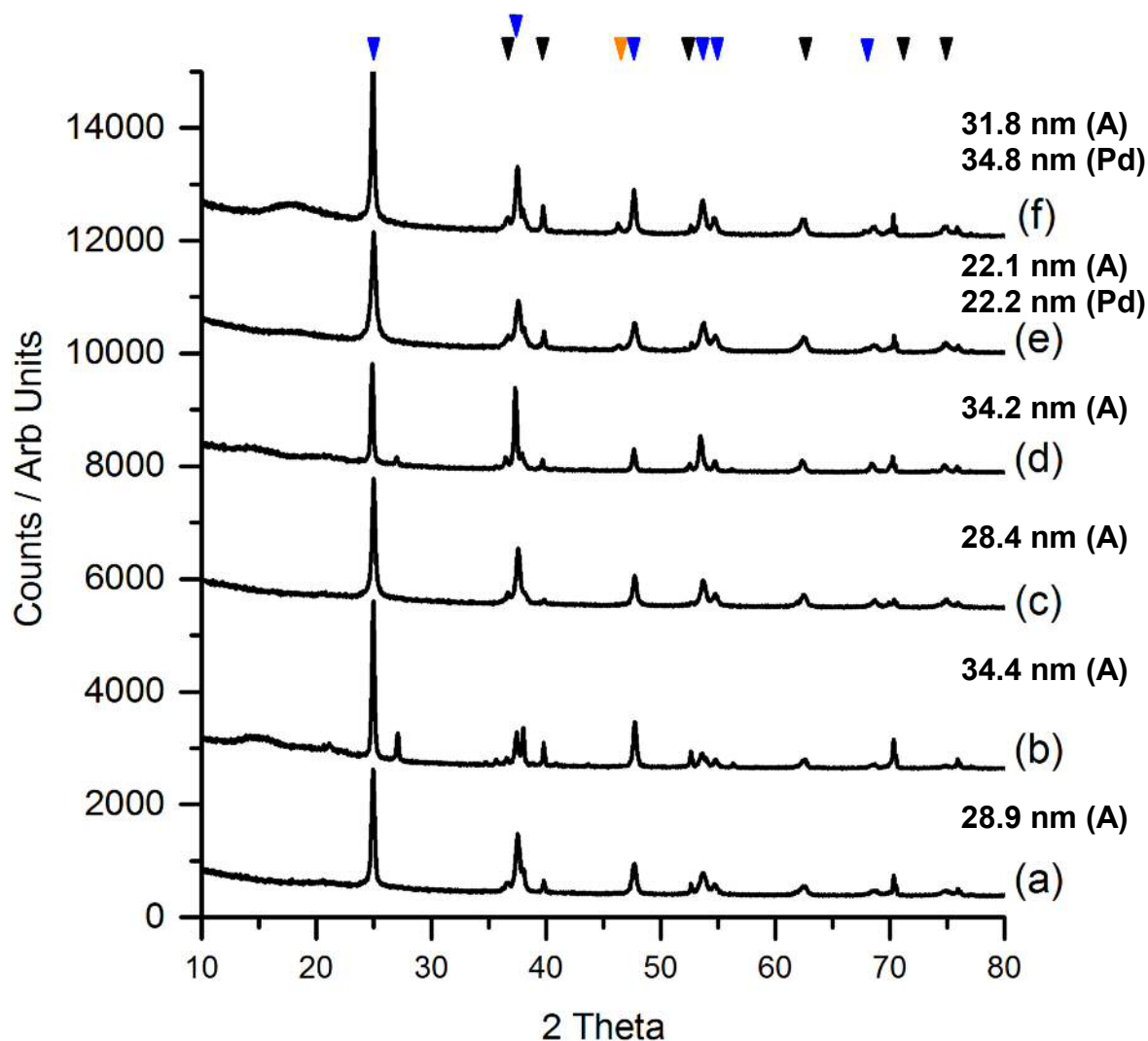


Figure 4.2.7:- X-Ray diffraction patterns for: (a) 4hr Pd1, (b) 8hr Pd1, (c) 4hr Pd3, (d) 8hr Pd3, (e) 4hr Pd30, (f) 4hr Pd60
Triangle phase markers: anatase (blue), metallic titanium (black), palladium (orange)

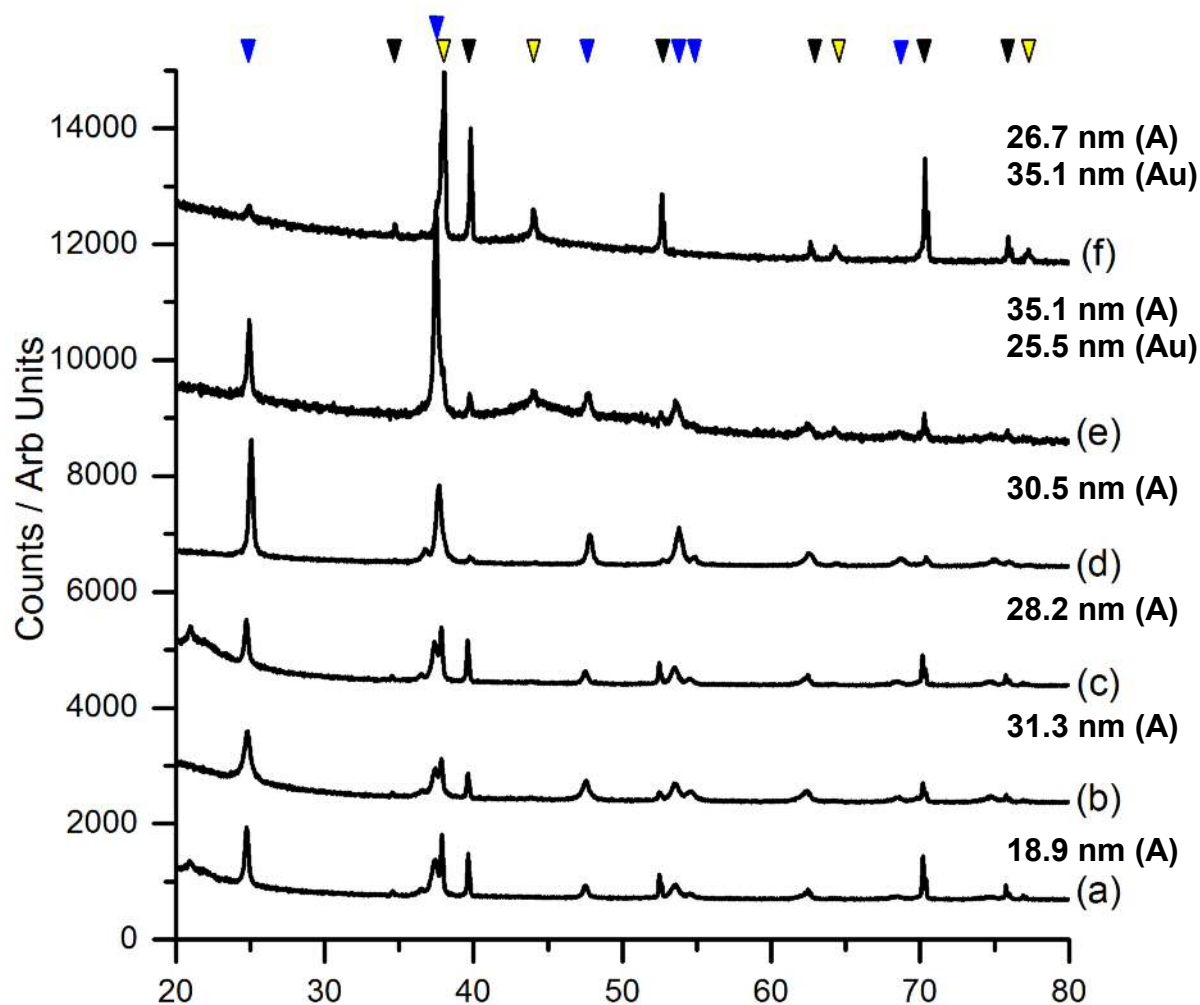


Figure 4.2.8:- X-Ray diffraction patterns for: (a) 4hr Au1, (b) 8hr Au1, (c) 4hr Au3, (d) 8hr Au3, (e) 4hr Au30, (f) 4hr Au60
 Triangle phase markers: anatase (blue), metallic titanium (black), gold (yellow)

variable intensity that is not linked to tube length, suggesting that rotation during acquisition may have caused some of the titanium sheet to be irradiated. Average crystallite size was determined, using the Scherrer equation, the values of which can be seen in **Table 4.2.1**. The modified P25, used in Chapters 3 and 5, had a crystallite size of 21.9 nm whilst all anodised nanotubes had larger calculated crystallite sizes. From arrays anodised for 1 to 8 hours the anatase crystallite sizes increased from 30.6 nm to 36.3 nm after annealing and subsequently dropped to 32.3nm for annealed 24 hour nanotubes. Tungsten containing nanotubes showed

no crystallinity, besides metallic titanium, and after annealing a purely anatase phase is observed (**Figure 4.2.6 bottom**). The anatase (101) phase had average crystallite size of 31.1 nm, a similar size to the tungsten free arrays formed for the same length of time. No diffraction patterns relating to tungsten were detected.

Xray diffraction patterns for palladium and gold decorated nanotubes can be seen in **Figures 4.2.7** and **Figures 4.2.8**. For palladium decorated arrays, the addition of palladium caused a general increase in anatase crystallite size from 1 minute to 30 minutes, followed by an increase to 31.8 nm for 60 minute deposition. The most notable change is the presence of a palladium diffraction pattern at $46.3\ 2\theta$ for the 30 and 60 minute treatments indicating significant deposition of palladium had occurred. In contrast, deposition of gold resulted in an unexpected changes in anatase crystallite size that saw a marked increase at 60 minutes of deposition. It is difficult to explain why these changes are occurring because photodeposition should not impact on crystallite size and the samples underwent no further thermal treatment that could account for the crystal growth. Either the gold is catalysing crystallite growth at room temperature or it's interfering in the XRD pattern in some way. However, neither model is very convincing and further investigation is required to provide an adequate explanation. The marked increase is very likely due to the significant decrease in strength of the anatase (101) phase due to the levels of gold deposited at this length of treatment. It can be seen that anatase and titanium metal diffraction patterns are the only visible signals for 1 to 3 minutes

| Sample name | E_g (eV) | Deposition time (minutes) | $E_g + Pd$ (eV) | $E_g + Au$ (eV) |
|-------------|------------|---------------------------|------------------|------------------|
| 4hr NT | 3.08 | 1 | 2.87 ± 0.05 | 3.11 ± 0.014 |
| | | 3 | 3.14 ± 0.035 | 2.92 ± 0.05 |
| | | 30 | / | 3.06 ± 0.007 |
| | | 60 | / | 2.77 ± 0.021 |
| 8hr NT | 2.97 | 1 | 3.01 ± 0.018 | 3.12 ± 0.099 |
| | | 3 | 3.02 ± 0.004 | 3.03 ± 0.004 |

Table 4.2.2: Bandgap energies obtained by extrapolation of the linear region of the respective Tauc plots

of photo-assisted deposition. At 30 minutes patterns pertaining to gold appear at 38.2 (111), 44.1 (200), 64.3 (220) and 77.3 (311) 2θ . [61] The (200) phase was used to calculate crystallite size, as it was the most intense and least convoluted phase. For both palladium and gold the crystallite size increased with deposition time.

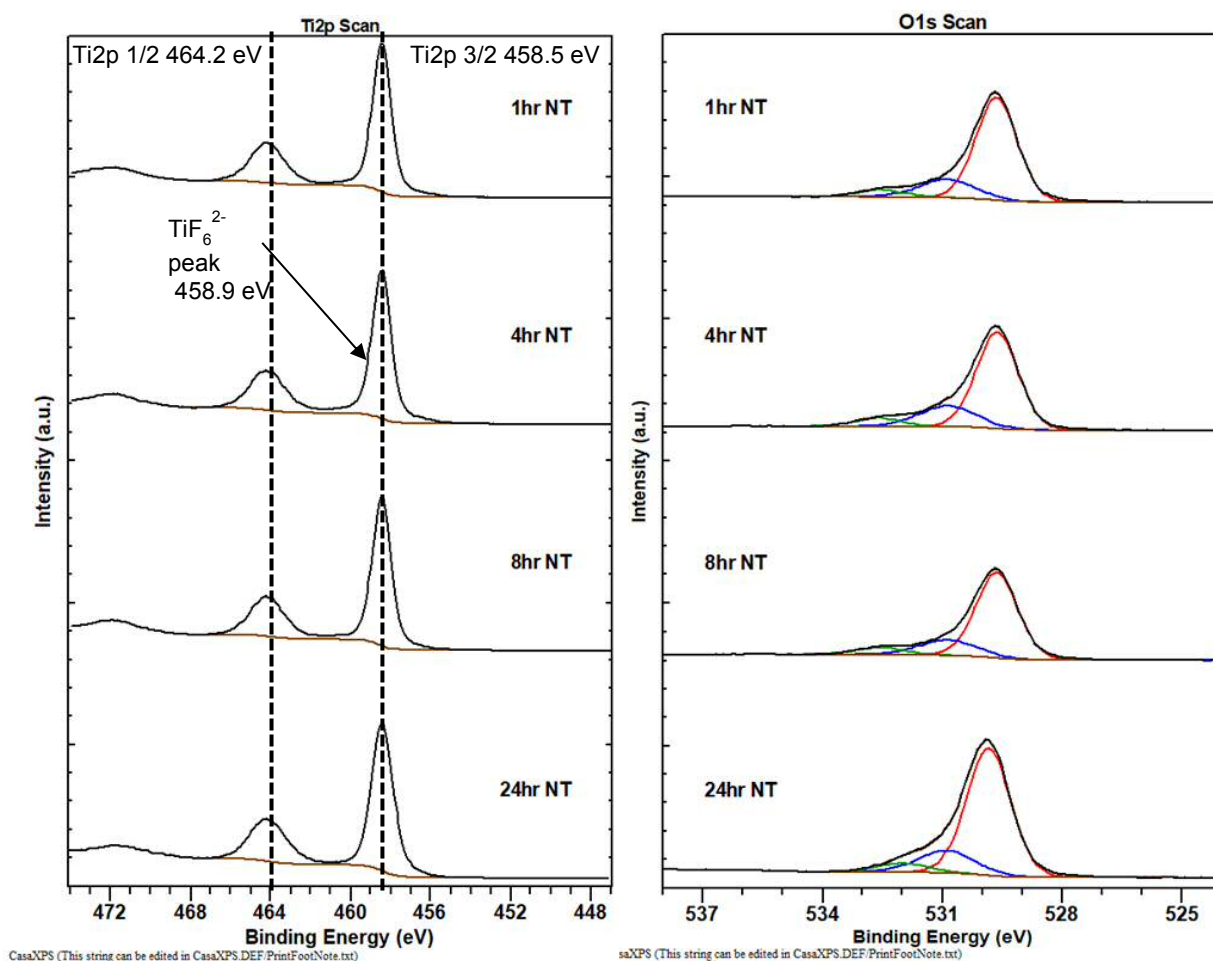
4.2.3 UV Measurements of Nanotube Samples

UV-Vis spectra were measured for the samples and Tauc plots used to ascertain the bandgaps of the materials. The values for the plain nanotube arrays can be found in **Table 4.2.1**, whilst for the decorated arrays the E_g values can be found in **Table 4.2.2**. All bare nanotube arrays had measured bandgaps of around 3.1 eV, values that sit between the typical rutile and anatase bandgaps, except for 8 hour anodised tubes that have a smaller bandgap of 2.97 ± 0.064 eV. 4 hour anodised tubes had the second smallest bandgap with a value of 3.03 ± 0.12 eV, whilst 1 and 24 hour anodised nanotubes had the largest bandgaps with values of 3.08 ± 0.022 and 3.13 ± 0.083 eV, respectively. The inclusion of tungsten in the arrays had the, expected, effect of decreasing the bandgap to 2.86 ± 0.014 eV. Doping with gold nanoparticles had mixed effects; photodeposition for one minute increased the bandgap to 3.11 ± 0.014 eV and 3.12 ± 0.099 eV for 4 hour and 8 hour nanotubes respectively, whilst after 3 minutes the bandgaps had decreased to 2.92 ± 0.05 eV and 3.03 ± 0.003 eV, respectively. The smallest bandgap measured being gold samples being irradiated for 60 minutes. Only palladium samples that were photo-deposited for 1 and 3 minutes had measurable bandgaps. One minute of deposition gave bandgaps of 2.87 ± 0.05 and 3.01 ± 0.018 , whilst 3 minutes of deposition gave values of and 3.14 ± 0.035 eV for samples irradiated in PdCl_2 for 1 and 3 minutes respectively. For the 30 and 60 minute samples, a linear response was detected suggesting there was no measurable bandgap.

4.2.4 XPS Studies

4.2.4.1 Titania Nanotube Arrays

Elemental analysis was performed for all samples using XPS and for most of the samples using EDX, with **Tables 4.2.3** showing the atomic percentage measured from XPS. Firstly, the as formed nanotubes only differed from the calcined tubes in the concentrations of carbon and fluorine. Atomic concentrations of carbon often exceeded 20% with greater C-O and C=O composition, whilst fluorine concentrations were usually measured between 6 and 10% of the atomic percentage. The annealing step, also used to form crystallite phases from the amorphous arrays, eliminates the fluoride content to 0.2% or less as described previously



| Sample name | Ti 2p | O 1s | C 1s | F 1s |
|-------------|-------|-------|-------|------|
| 1hr NT | 23.4 | 61.9 | 14.8 | 0 |
| 4hr NT | 23.9 | 64.2 | 11.7 | 0.2 |
| 8hr NT | 24.3 | 61.3 | 14.2 | 0.1 |
| 24hr NT | 22.28 | 55.19 | 18.22 | 0.1 |

Figure 4.2.9: Ti2p and O1s XP spectra showing changes in each region as anodisation length increases

Table 4.2.3: The atomic percentage concentrations of each nanotube sample

in many publications. [51][52] XP spectra of the annealed nanotubes shows no correlation between the length of the tubes and the composition. **Table 4.2.3** shows that nanotubes, anodised for the four chosen times, had similar compositions that indicates an expected

amount of titanium and oxygen with a layer of adventitious carbon. The carbon layer is a result of a few different factors: the ethylene glycol used in the anodisation process will deposit carbon even after the drying and annealing process; and exposure to air is widely understood to deposit carbon on catalyst surfaces, . A ratio of roughly 1:3, between titanium and oxygen, is found because of contributions to the oxygen signal from hydroxylation and organic contaminants. High resolution XP spectra for the titanium and oxygen regions can be seen in **Figure 4.2.9**. The stacked titanium spectra show that, regardless of anodisation time, only TiO₂ is formed during the process. A Ti2p 3/2 peak sits at 458.5 eV with the corresponding spin orbit coupled 1/2 at 464.2 eV, therefore providing a spin orbit splitting of 5.7 eV. A slight asymmetry is observed in the Ti2p 3/2 peak due to the presence of TiF₆²⁻, a very stable product formed during the anodisation process, that creates an observable chemical state at the slightly higher binding energy of 458.9 eV. [52] It is possible that a small fraction of the titanium exists in the Ti³⁺ oxidation state, the Ti2p 5/2 peak of which would appear at 1 to 1.5 eV lower than Ti⁴⁺, however the amounts appear to be so low that their presence is difficult to discern due to the band tailing of the Ti⁴⁺ peak. The oxygen region has a mostly uniform appearance except for a 0.5 eV downwards shift of the organic oxide peak for the 24-hour anodised sample. Peaks were deconvoluted using a Shirley background and a Gaussian-Lorentzian peak shape. The largest component of the oxygen signal is at 329.6 eV, which is typical of a metal oxide, and represents the titania lattice oxygen. The remaining oxygen components at 531 and 532.5 eV are often assigned as “hydroxide” oxygen and organic oxygen, respectively, an assignment that is fitting here considering the likely presence of surface organic species in the adventitious carbon layer.

4.2.4.2 Ti/W Nanotube Arrays

High resolution XP spectra for the O 1s, Ti 2p and Ti 3p + W 4f regions of the mixed metal oxide, nanotubes can be seen in **Figure 4.2.10**. The spectra show scans from 3 samples made sequentially from the same batch of electrolyte, the stage being denoted by the numbers 1, 2 or 3. Firstly, the confirmation of the presence of tungsten was initially ascertained from the W 4d region in the survey scan, because the W 4f region heavily overlaps with the Ti 3p 3/2 peak. The survey scan indicated the concentration of tungsten incorporated into the nanotube array was linked to the stage of reuse of the anodisation electrolyte. Over three uses the concentration of tungsten increases from 0.03% to 0.46%, a trend also shown in the W 4f narrow scan in **Figure 4.2.10 (right)**. The narrow scan shows the development of a shoulder

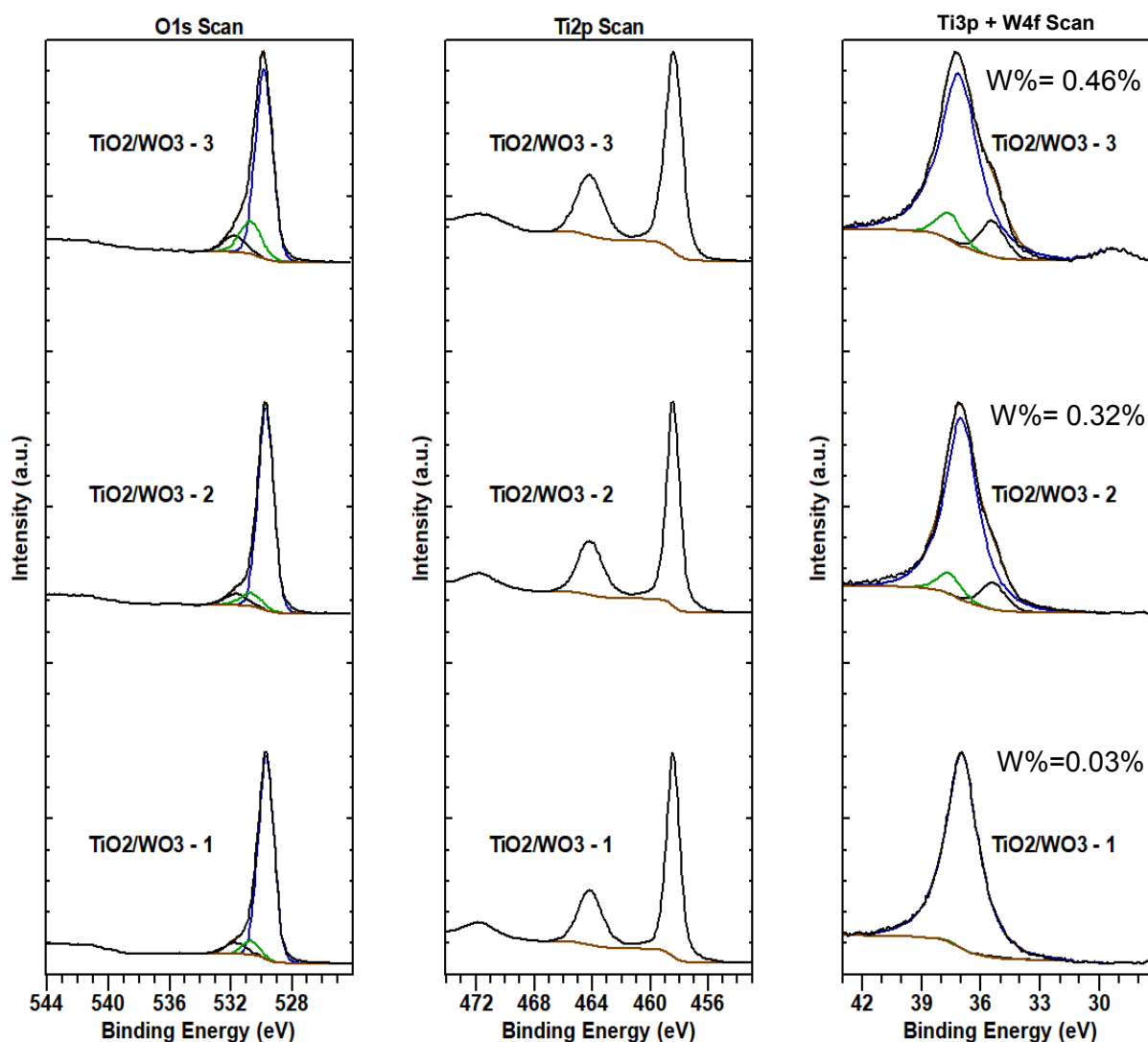


Figure 4.2.10: XP spectra of the O1s, Ti2p and Ti3p + W4f regions across three uses of the anodisation electrolyte

The percentage concentrations relate to the atomic concentration of tungsten calculated from the W4f region

at the lower binding energies of the Ti 3p 3/2 peak. The Ti 3p 3/2 peak was deconvoluted by introducing a pair of peaks with a spin orbit splitting of 2.2 eV, the known splitting of tungsten oxide, and gave concentration values that matched those from the W 3d region. No changes were observed in the Ti 2p region indicating the presence of tungsten in the electrolyte did not impact on the oxidation of titania. Besides the presence of the titania lattice oxide at 529.6 eV and the “hydroxylated” signal at 531.5 eV; deconvolution of the O1s region also indicated the presence of the metal oxide associated with tungsten. The shoulder of the O 1s peak becomes increasingly visible as the tungsten concentration increases. As such, the third component of the region was placed at 530.5 eV, a known binding energy for oxygen in tungsten oxide, where the best fit was accompanied with an increase in the size of

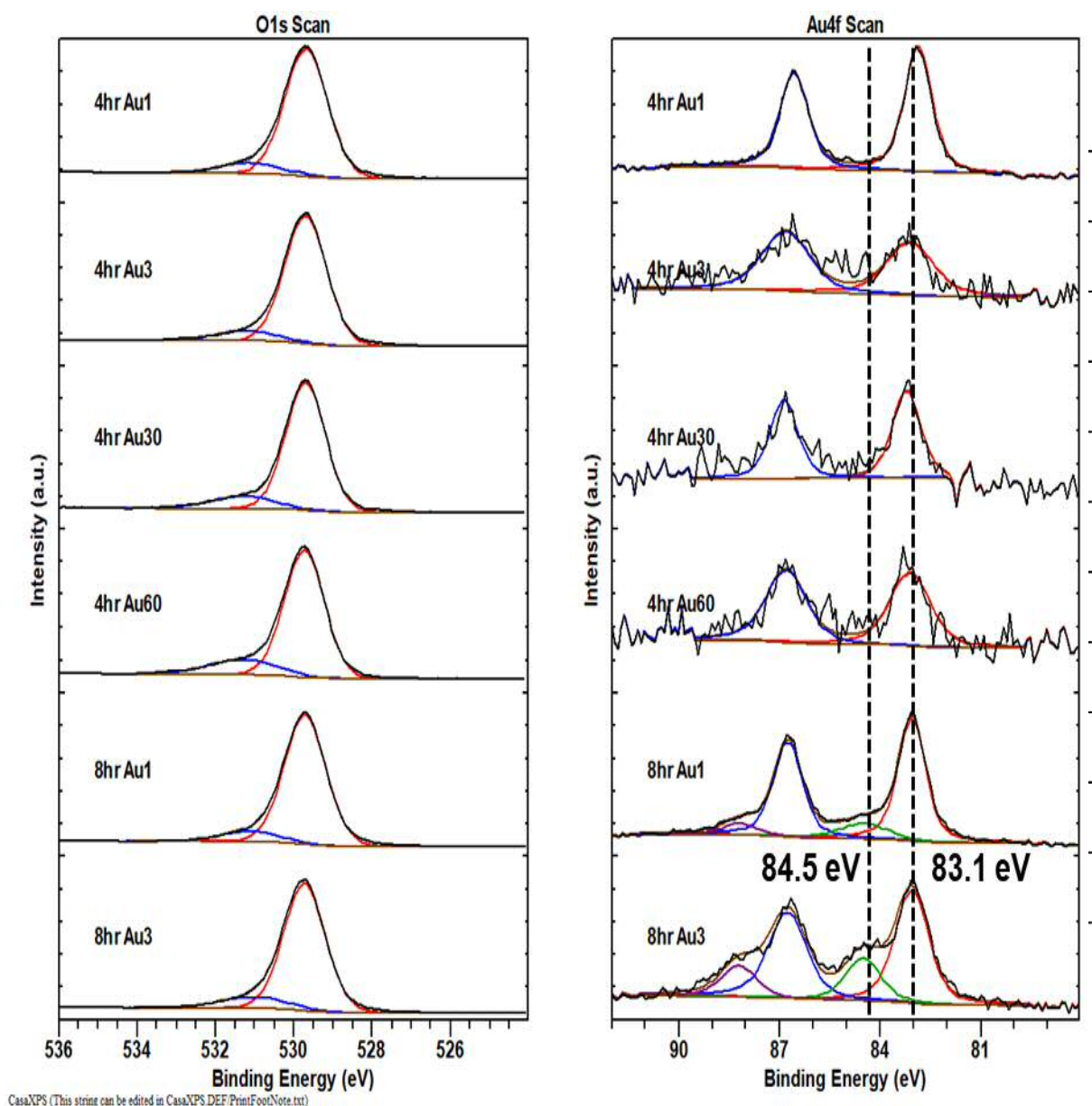


Figure 4.2.11: XP spectra of the O1s and normalised Au4f regions of the gold coated nanotube samples. showing the change in gold species across different nanotube samples

this component. It is difficult to use the ratio of the detected tungsten and tungsten related oxygen to confirm the presence of tungsten trioxide, however the binding energy of the tungsten peak is strongly suggestive of tungsten trioxide. [53]

4.2.4.3 Gold and Palladium Decorated Nanotubes

XPS analysis of samples that had undergone palladium and gold deposition indicated that deposition of the metals did not significantly impact the chemical makeup of the nanotube surface. As **Table 4.2.4** shows, fluoride was detected at higher concentrations than

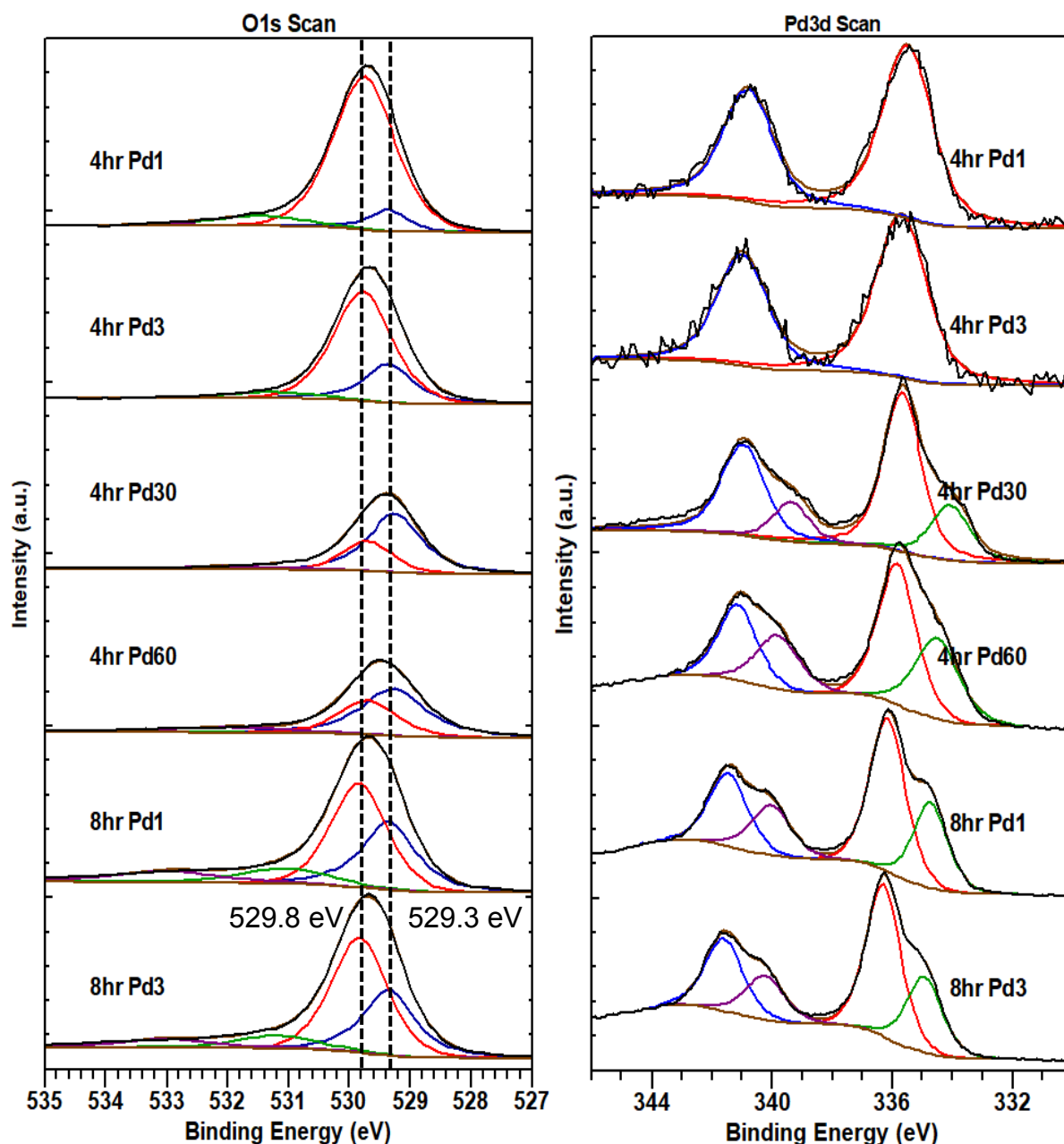


Figure 4.2.12: XP spectra showing the O1s (left) and Pd3d (right) regions for the palladium doped nanotube samples. The line colours for each set represent:-
 O1s: lattice oxygen (red), hydroxyl oxygen (green), palladium 3p (blue)
 Pd 3d: Pd²⁺ 5/2 and 3/2 (red and blue), Pd⁰ 5/2 and 3/2 (green and purple)

in the undoped samples. Neither of the metal precursors contained significant amounts of fluoride so the ion must have been present at this concentration before metal deposition. EDX of the 8-hour metal doped samples, seen in **Table 4.2.5**, shows either zero or lower amounts of fluoride suggesting that the fluoride is surface oriented, potentially being drawn to the

surface during photodeposition. There also appears to be a correlation between the carbon concentration and the length of deposition. The highest carbon percentage for each set is 17.5 and 18% for palladium and gold respectively, however the correlation does not hold when compared to the amount of metal actually detected using XPS. All samples showed significant amounts of chlorine, indicating the washing step, after photodeposition, was not sufficient in eliminating this contaminant. The Ti 2p region retains its majority Ti^{4+} character where the Ti 2p_{1/2} peak sits at 458.5 eV with a slight asymmetric shape from the TiF_6^{2-} . For the O 1s region some changes are observed for palladium deposition, although not for gold. In the case of gold, the oxygen peak shows no signs of shifting or any changes to the peak shape. Deconvolution, shown in **Figure 4.2.11** (left), was best fitted with two peaks using a Shirley background and Gaussian-Lorentzian peak shapes. The two peaks were assigned to the titania lattice oxygen (529.7 eV) and hydroxide oxygen (531.1 eV). The oxide element of gold oxide should appear at 530.1 eV, [73] however there is no evidence that this peak is present. Considering that amount of detected gold does not exceed 1%, from XP spectra and EDX, then the contribution of gold oxide to the peak would be minimal resulting in the high likelihood of it being obscured by the TiO_2 lattice oxygen. Quantification of gold was achieved using the narrow scan performed before acquisition of the remaining elements, to minimise the impact of beam induced photo-reduction. Gold atomic concentrations, found in **Table 4.2.4**, suggests increasing photodeposition time did not increase the amount of gold deposited and actually had a negative correlation. However, this is in conflict with XRD data that detected gold diffraction patterns for both Au30 and Au60, the presence of which only occurs when a substantial amount of an element is present forming repeating crystal units that diffract the incident x-rays. The discrepancy could be explained as a surface/bulk effect. The available data on gold particle size tentatively implies increasing photodeposition time results in smaller nanoparticles. If this trend continues then it would be expected that the nanoparticles would more effectively penetrate the nanotubes, depositing beyond the detection capabilities of XPS and EDX. The movement of the gold solution through the tubes may be slowed by the water surface tension. Long deposition times could therefore help facilitate deposition deeper in the tubes, presenting a possible explanation for the detection of gold diffraction patterns contradicting the low concentration of metals detected on the surface. Further work, in the form of careful weight measurements in the deposition methodology, is required to determine the validity of this explanation. From a qualitative perspective, the data does show the shifting values of the Au 4f 7/2 peak, a phenomena

associated with nanoparticle size. [54][55] The normalised XP spectra in **Figure 4.2.11**, show the Au 4f region for the six samples. Au⁰ normally appears at 84 eV, with oxidised forms having higher binding energies. In **Figure 4.2.11** the peaks sit between 82.9 and 83.5 eV, with the deconvolution of the 8hr (Au1 and Au3) nanotube spectra also showing another smaller doublet starting at 84.5 eV. Both doublets have a spin orbit splitting of 3.7 eV and can be assigned as Au⁰ and Au¹, respectively. Photodepositing palladium resulted in greater amounts of palladium, in comparison to gold, on the surface. **Table 4.2.4** shows that minor differences in deposition time, one to three minutes for both 4 and 8 hour nanotubes, results in a reduction of detected palladium. EDX, for 8hrPd1 and 8hrPd3, indicated atomic concentrations of 0.04 and 0.12% of Palladium, respectively (**Table 4.2.5**). The greater penetration depth of EDX, compared to the surface sensitive XPS, means EDX will reveal more information about bulk. Based on FESEM images captured it seems increasing deposition time may increase the amount of agglomeration occurring which could prevent some of the deposited metal from being detected via XPS. Curiously, FESEM images do not give off the impression that the 8hr Pd1 and Pd3 have a surface coverage of 9.9 and 7.4 %, respectively. It was noted that many of the particles measured on 8hrPd3 were of sub 10nm sizes, sizes easily possible when photodepositing palladium, that would be beyond the resolution of the FESE microscope. The production of ultra-small palladium particles would explain the lack of visible particles whilst XP spectra show atomic concentrations as high as 10%. [56] Analysis of the high-resolution scans for the oxygen and palladium regions can be seen in **Figure 4.2.12**. The oxygen 1s region overlaps with the palladium 3p region, an issue that is accounted for during deconvolution with the palladium 3p peak being represented by the purple line. As the concentration of palladium increases a shift downwards in binding

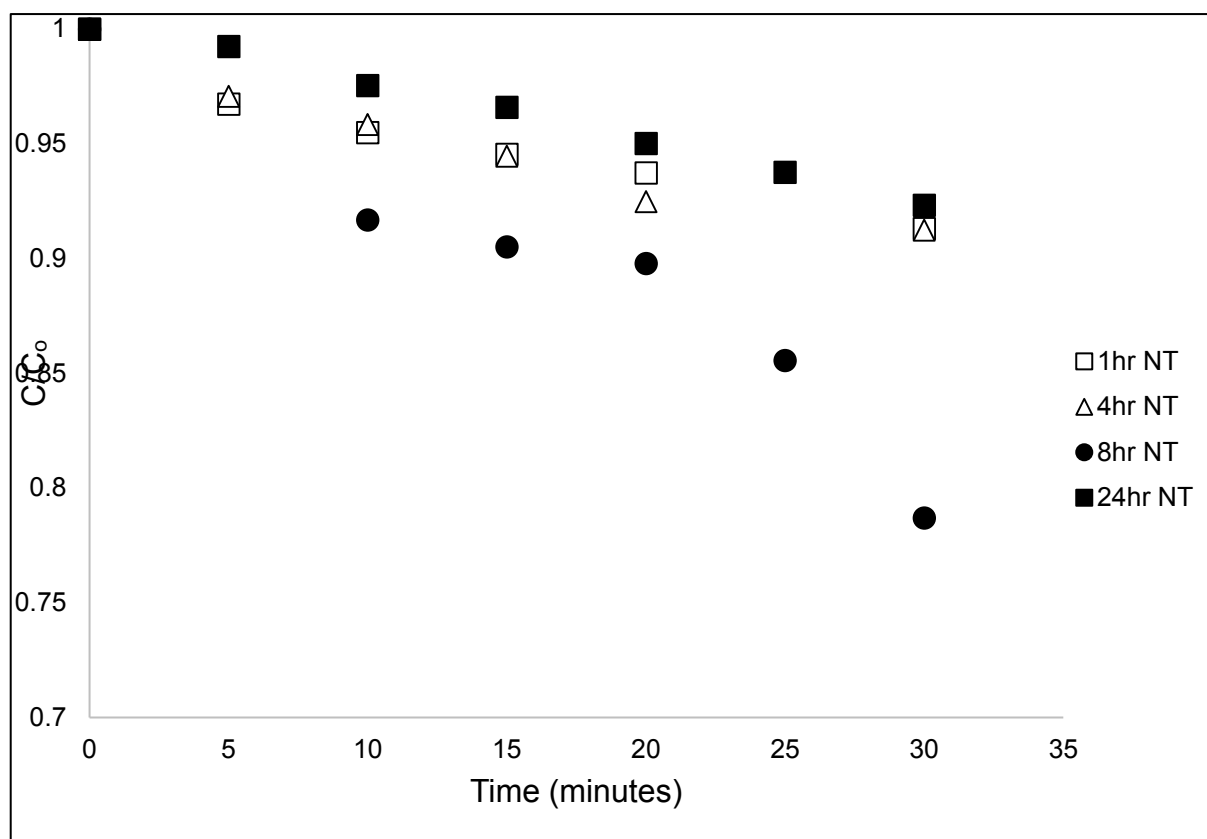
| | Ti | O | C | F | Cl | Pd | Au | W |
|--------|-------|-------|---|------|------|------|------|---|
| 8hrAu1 | 32.39 | 67.5 | / | / | 0.08 | / | 0.07 | / |
| 8hrAu3 | 30.3 | 69.96 | / | 0.37 | 0.06 | / | 0.31 | / |
| 8hrPd1 | 70.08 | 29.89 | 0 | 0 | 0 | 0.04 | / | / |
| 8hrPd3 | 32.18 | 67.65 | / | / | 0.04 | 0.12 | / | / |

Table 4.2.5: Atomic percentages obtained from EDX analysis for the nanotube samples anodised for 8 hours and doped with gold or palladium

energies is observed, a trend that is accompanied with the peak composition becoming increasingly dominated by the PdO component at 529.3 eV (blue line). Notably, a greater degree of shifting is observed for the longer deposition times, the maximum shifting from 529.7 to 529.4 eV, implying a higher amount of Pd 3p character is detected. A preliminary analysis from the peak fitting of the region suggests that 4hr Pd30 and Pd60 could have a palladium concentration exceeding 10%, whilst the other samples contained less than 7.5% on the surface. This conflict implies the concentration, based on the Pd3d region, may contain inaccuracies which would also account for why diffraction patterns related to palladium are detected for 4hrPd30 and Pd60 even though 8hr Pd1 and Pd3 were found to have higher concentrations by XPS. Analysis of the Pd 3d region found the palladium in two environments. The first appears between 334 - 335 eV that is assigned as metallic palladium (Pd^0), and the second between 335.6 – 336.2 eV that is assigned as the native oxide (Pd^{2+}). Both appear as doublets with spin orbit splitting values of 3.7 eV. All six spectra show signs of PdO, whilst the samples with concentrations exceeding 1 atomic percent also show metallic palladium character.

4.3 Photocatalytic Testing

Nanotube arrays were tested for their efficiency in degrading organic material in the liquid phase and as solid deposited on the surface of the arrays. The degradation of cinnamic acid in solution is used, as in **Chapter 3** and **5**, to model the presence of recalcitrant organic waste as found in palm oil mill effluent. While, the deposition of a substrate onto films has been used to assess the self-cleaning ability of a material where stearic acid is considered a suitable model for organic pollutants that build up on the exterior of windows. While it is useful to try to assess how effective nanotubes are in this situation, it is unlikely that nanotubes would be employed as a window coating due to visibility issues. As such we have also tested how the efficiency of the nanotubes in destroying cinnamic acid to ascertain how well the nanotubes can clean themselves between reaction runs.



| Sample | 1 st Order Rate Constant (min ⁻¹) |
|----------------|--|
| Titanium Sheet | 0.0024 |
| 1hr Nanotube | 0.0037 |
| 4hr Nanotube | 0.0049 |
| 8hr Nanotube | 0.0054 |
| 24hr Nanotube | 0.0032 |

Figure 4.3.1: Liquid phase photocatalytic degradation behaviour of the plain nanotube samples to cinnamic acid

Table 5.3.1: 1st order rate constants for the reactions seen in **Figure 4.3.1**

4.3.1 Reactivity of Plain Nanotube Arrays

The benefits of using a fixed catalyst like a thin film of nanotubes means the catalyst does not need to be retrieved from the mixture. However, this comes with the issue of poorer mixing in comparison to a loose powder. Leaving time for a reaction mixture to equilibrate, temporarily negates mixing issues, but once the substrate adsorbed to the surface is

mineralised the probability of a substrate molecule colliding with the catalyst surface is lower than for a powder. As such the first order rate constants stated here are lower than those of **Chapter 3**. A nanotube array is also not equivalent in mass to the 0.1g of TiO₂ powder used in that chapter. Weight measurements, of detached arrays, placed those anodised for 24 hours at roughly 20 mg per array. To reflect this weight difference the amount of substrate used was decreased by a factor of 5 to keep the catalyst to substrate ratio at a similar value.

4.3.1.1 Liquid Phase Degradation of Cinnamic Acid

Figure 4.3.1 shows a plot of the normalised concentration of cinnamic acid over time in the presence of the four plain titania nanotube arrays, and **Table 4.3.1** below it hold the first order rate constants for each, including the titanium sheet control (equivalent to a no catalyst control). The most effective, at destroying cinnamic acid, is plainly the arrays anodised for 8 hours. After 30 minutes of reaction just under 22% of CA has been degraded giving it the largest rate constant of 0.0054 s⁻¹, a value double that of the control. The 4 hour nanotubes are slightly less effective with a rate constant of 0.0048 s⁻¹ followed by 1 hour and

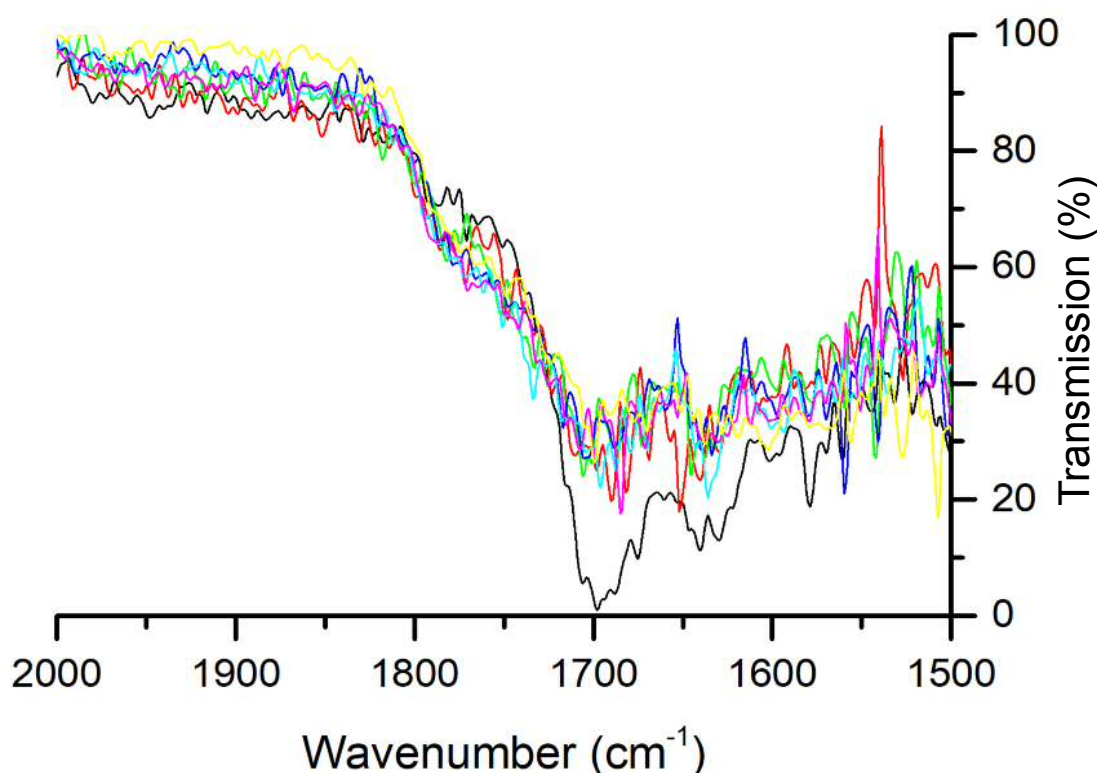


Figure 4.3.2:- A typical set of IR spectra showing the decrease in intensity for the carbonyl region during the photocatalytic degradation of cinnamic acid on titania nanotubes

then 24 hour nanotubes. 1 and 24 hour anodised nanotubes are notably slower than the other two samples, with the 24 hour sample offering a rate constant not far above the no catalyst control.

4.3.1.2 Surface Degradation of Cinnamic Acid

The experiments described in this section are intended as a qualitative insight into the efficiency of nanotube arrays in the degradation of surface deposited cinnamic acid. In contrast to the established quantitative methodology for determining stearic acid degradation, which uses the C-H stretching vibration, for cinnamic acid the intensity of the carbonyl band has been used to ascertain substrate destruction (shown in **Figure 4.3.2**). As we evaluated in **Chapter 3**, in the liquid phase the primary route for degradation of CA is believed to be the cleaving of the C=C by a reactive oxygen species and the subsequent loss of CO₂. In the case of performing the reaction in air over the nanotubes, the assumption was made that the formation of superoxide could still occur and so was likely to remain the primary route for degradation. This would still lead to the loss of CO₂ first and therefore, following the loss of the carbonyl stretching vibration was the most effective manner in which to follow the initial degradation step.

Cinnamic acid deposited on the nanotube arrays appeared to show the same trends, in the undoped samples, as was observed in the liquid phase. **Figure 4.3.3 (a)** and **(d)** show that samples anodised for one hour and 24 hour were no more active than the titanium sheet control, in the degradation of CA. The reactions followed a similar rate to the control and resulted in a 16.5% and 10% loss, respectively, in intensity in the carbonyl region of 1690 to 1700 cm⁻¹. 4 hour nanotubes showed a slight improvement, above the control sample, and after 3 hours an 18.5% loss in intensity is observed. Whilst 8 anodised hour arrays were the most efficient with a 28% loss in transmission after 3 hours. The data indicate that the factors determining the proficiency for photocatalysed degradation in the liquid phase also apply to the self-cleaning ability observed here. Some reports have shown [57][58] that larger anatase crystallite sizes are beneficial in the degradation of phenol and this may provide a possible explanation for the superior degradative capability of 8 hour anodised arrays in both surface oriented and liquid phase degradation. However, 24 hour anodised tubes have, thus far, proven to be the most ineffectual photocatalysts and yet have a larger measured crystallite size than 4 hour tubes, indicating there must be more to the picture. The bandgap of the material correlates with the efficiency of the nanotubes. The trend for bandgap size, from

smallest to largest, was 8hr NT < 4hr NT < 1hr NT < 24hr NT; which is also the proficiency of the nanotube arrays for degradation from the most active to the least. However, the LEDs used here were tuned to 365nm (3.4 eV), greater in energy than all measured bandgaps, and so should have no impact on photocatalytic efficiency. A likely factor is the morphology of the top 2 to 3 μm of the tubes. 8 hour nanotubes have considerably larger pore widths than those anodised for shorter time scales, whilst having walls of an equivalent thickness; an attribute that is believed to improve pollutant diffusion within the nanotubes and allow deeper penetration of irradiating light. [44] This is only true to a certain degree, as displayed by the poor activity of the wider and longer 24 hour anodised tubes. Reaction mixture will flow to the bottom of the tubes, where substrate molecules adsorb and desorb on the tube surface, which will move the target molecules deep below the region where irradiation occur. However, this does not explain why nanotubes anodised for 24 hours have performed so poorly in these studies. A feature of the surface morphology, of 24 hour anodised tubes, was the over-etched tubes that did not have the structural strength and formed valleys. The slumping is very likely preventing the top-side irradiation from penetrating into a large portion the tubes and therefore negating the point in the titania nanostructure containing tubular moieties. The arrays anodised in the presence of a tungsten precursor were also tested however it was found that, despite 4 hour anodised TiO_2 only nanotubes showing some activity, the samples containing tungsten showed zero activity and mirrored the titanium sheet control.

4.3.1.3 Surface Degradation of Stearic Acid

The next batch of results tests the nanotube arrays in the self-cleaning of stearic acid from the surface. Two metrics have been employed to examine the materials efficiency. The first is that described by Paz *et al.* and Mills *et al.* (metric 1); where a conversion factor is used to convert the integrated area underneath the C-H stretching band ($2700\text{--}3000\text{ cm}^{-1}$) to a number of stearic acid molecules. [62][63][64] The conversion used was 9.75×10^{15} molecules of stearic acid per cm^{-2} equates to 1 cm^{-1} , an adjusted conversion factor based on work by Mills *et al.*. [63] The second metric (metric 2) was the normalised transmission of the carbonyl frequency found between 1680 and 1700 cm^{-1} . An example of typical degradation spectra for both metrics is seen in **Figure 4.3.4**. Stearic acid is understood to degrade photocatalytically in a stoichiometric, zero order manner, as described by the

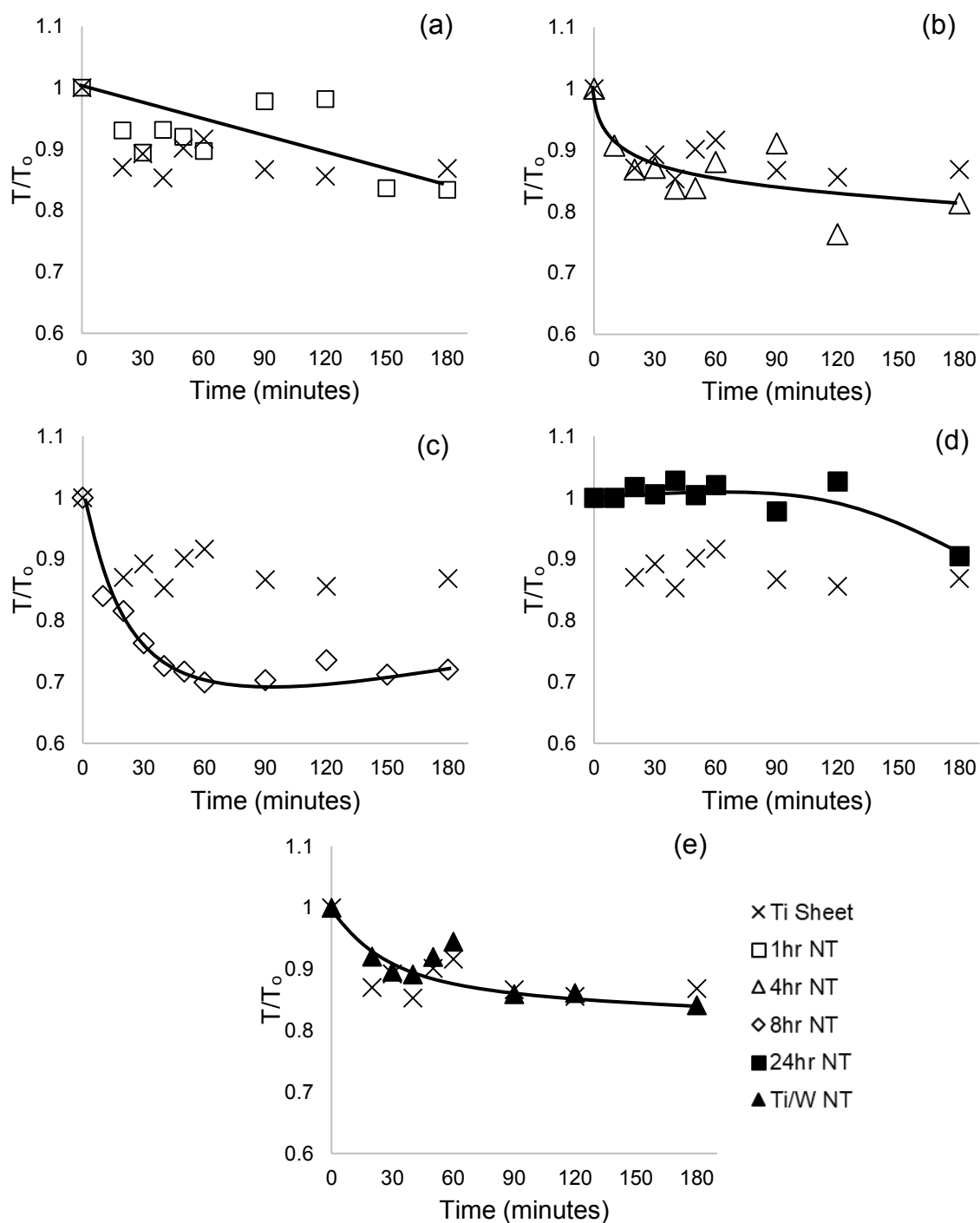


Figure 4.3.3: Plots showing the changing degradation behaviour of cinnamic acid on nanotube samples where; (a) = 1hr NT, (b) = 4hr NT, (c) = 8hr NT, (d) = 24hr NT, (e) = Ti/W NT

Normalised transmission of the carbonyl region (1690 to 1700 cm^{-1}) is plotted against time, where the black line depicts the trend of the degradation associated with the nanotube array. The control test (Ti sheet) is included in each spectrum, marked by the cross, for comparison

equation below:

Equation 4.3.1

Although it is believed that full mineralisation of SA, to CO_2 and H_2O , does not usually occur due to intermediates interfering in the reaction mechanism, the general mechanism is believed to consist of the sequential chain shortening via loss of CO_2 . [65][66] Based on this assumption one can tentatively evaluate the loss of C-H moieties alongside the loss of the carboxyl feature for qualitative purposes.

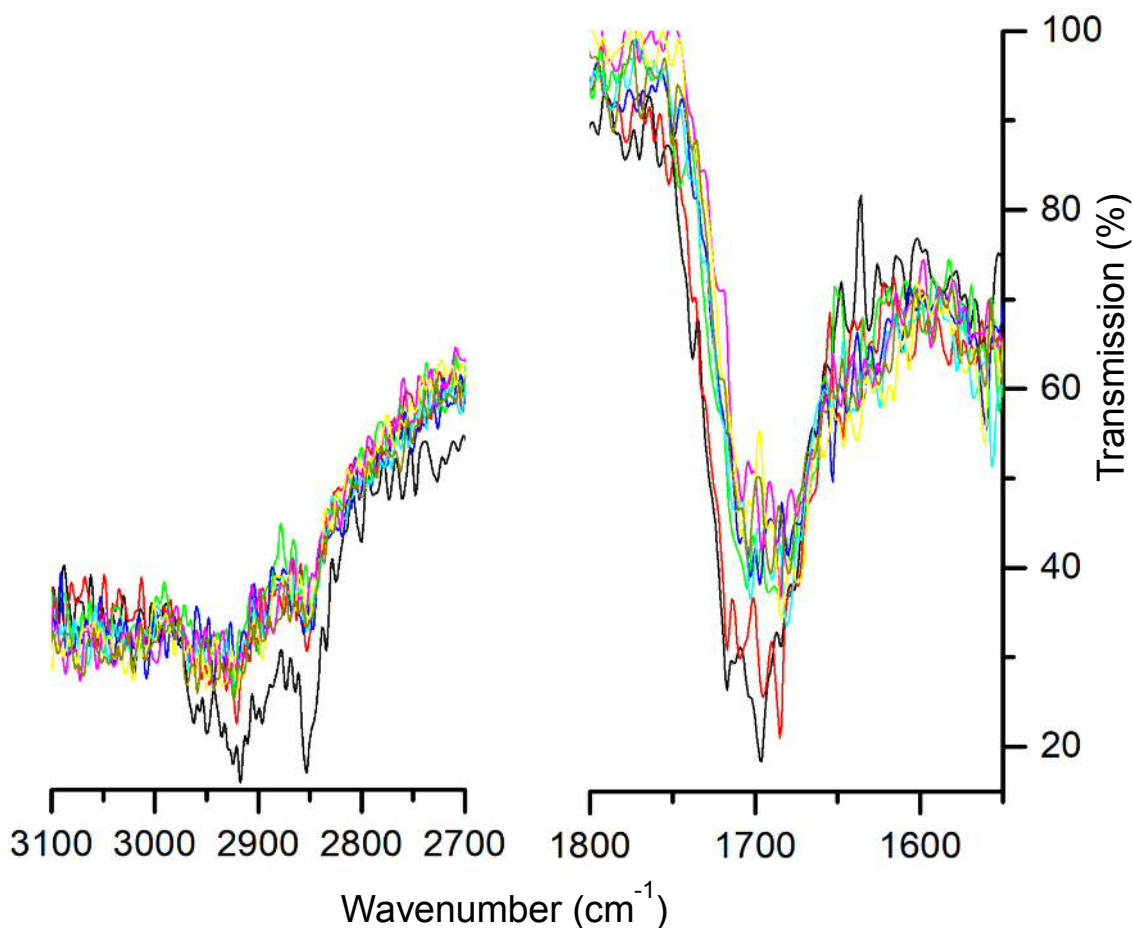


Figure 4.3.4:- A typical example of IR spectra of stearic acid showing the decrease in intensity for the C-H (left) and the carbonyl regions (right) during the photocatalytic degradation of stearic acid on the titania nanotubes

Figure 4.3.5 contains plots showing the degradation of SA depicted in the two previously described metrics, whilst **Table 4.3.2** shows the percentage change of metric 1 and 2 after 180 minutes for all stearic acid reactions. For the remainder of the chapter the hollow triangles will represent the normalised intensity of the carboxyl band and the square represents the normalised concentration of the C-H stretching bands. Testing indicated that the use of a titanium sheet, as a no catalyst control, resulted in less than 5% in both metric 1 and 2 after 3 hours of reaction. As can be seen in **Figure 4.3.5**, nanotube arrays can be split into two groups based on degradation proficiency. 4 and 8 hour nanotubes both show signs of

| Sample Name | Change In C-H band after 180 minutes (%) | Change In Carboxyl Band after 180 minutes (%) |
|---|--|---|
| Titanium Sheet | 0.1 | 7.8 |
| 1 hour NT | 15.6 | 2.6 |
| 4 hour NT | 32.6 | 13.1 |
| 8 hour NT | 33.1 | 30.8 |
| 24 hour NT | 2.3 | -0.2 |
| 4 hour TiO ₂ /WO ₃ NT | 8.4 | 0 |
| 4 hour Au1 | 5.2 | 0 |
| 4 hour Au3 | 15.5 | 9.8 |
| 4 hour Au30 | 12.9 | 2.7 |
| 4 hour Au60 | 8.7 | 7.8 |
| 8 hour Au1 | 25.9 | 1.9 |
| 8 hour Au3 | 26.3 | 15.7 |
| 4 hour Pd1 | 13.1 | 9.2 |
| 4 hour Pd3 | 19.6 | 4.7 |
| 4 hour Pd30 | -0.6 | - 0.9 |
| 4 hour Pd60 | 13.4 | 6.5 |
| 8 hour Pd 1 | 35.7 | 10.8 |
| 8 hour Pd3 | 24.3 | 6.7 |

Table 4.3.2: Percentage changes in infrared C-H and carboxyl band after 3 hours of reaction for each nanotube array

The C-H band is correlated to real concentrations, whilst the carbonyl band is based purely on intensity

degradative ability, as seen in previous tests. The concentration in metric 1, based on SA C-H band area, drops rapidly in the first 30 minutes of reaction time which is followed by a period where the concentration remains constant. Whilst metric 2, the normalised intensity of the carboxyl band, decreases at a slower, more constant rate, and the 8 hour nanotubes display superior activity. After 3 hours, using 8 hour anodised arrays, metric 1 holds a comparative value to metric 2. The second group contains the remaining, non-decorated arrays, that show little to no degradative activity. 24 hour nanotubes show zero degradation, after 3 hours, whilst both the 1 hour and tungsten containing samples display a small amount of loss under the C-H regime. The stopping of the C-H degradation could be a symptom of inert stearic acid intermediates blocking reactive surface sites, as stated by Minabe *et al.* [65]

4.3.2 Reactivity of Au/Pd Nanotube Arrays

4.3.2.1 Liquid Phase Degradation of Cinnamic Acid

From the initial results with TiO₂ only nanotubes, it was decided to use 4 hour and 8 hour anodised nanotubes as the support for gold and palladium. Gold and palladium were separately deposited to determine whether either metal would improve the photocatalysed degradation of cinnamic acid. Two sets of samples were chosen for deposition: tubes anodised for 8 hours were chosen as they were found to show the greatest proficiency in the liquid phase and in self-cleaning tests; whilst tubes anodised for 4 hours were shown to have the second best activity and also have the benefit of taking half the time to produce. **Figure 4.3.4** shows a plot of the degradation of cinnamic acid in the presence of gold and palladium decorated nanotube arrays, the corresponding first order rate constants can be found in **Table 4.3.3** below. The measured rate constants show both gold and palladium did not improve the photocatalytic proficiency under these conditions. The inclusion of either metal resulted in a significant slowing of CA removal. Palladium at both preparation times effectively killed off any photocatalysis and caused the degradation rate to fall to the baseline level. Whilst, gold was slightly less detrimental at the short preparation time of 1 minute of deposition, the longer 3 minute preparation time appeared to cause a complete inhibition of the arrays' photocatalysing capability. The cause of this could be for several reasons. Chloride, for example, was detected in XP spectra and may inhibit degradation by trapping photogenerated holes or deactivating the surface by occupying important surface sites and blocking cinnamic acid adsorption. However, as was found in **Chapter 3**, the presence of chloride does not necessarily result in photocatalytic slowing. In solution testing showed chloride was

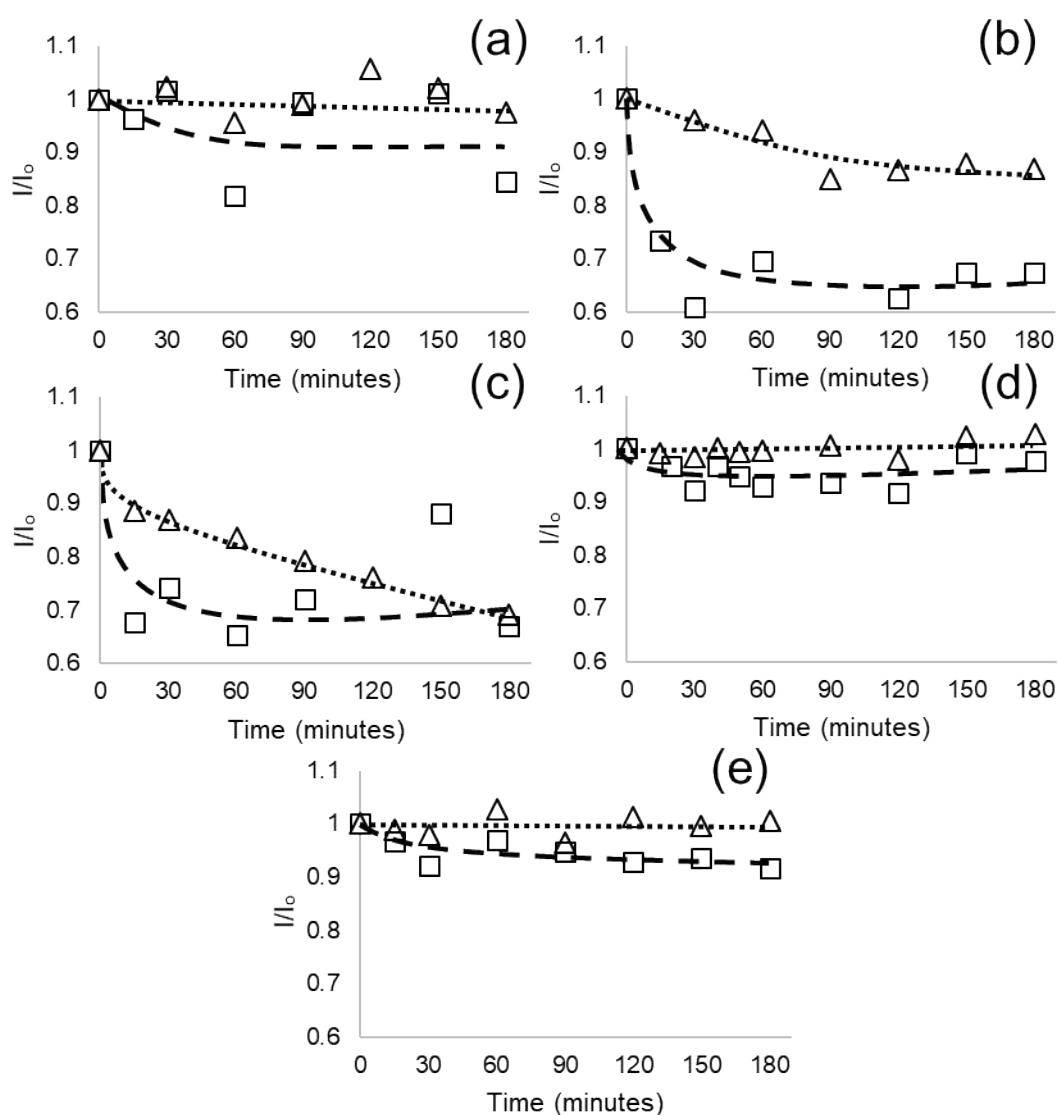
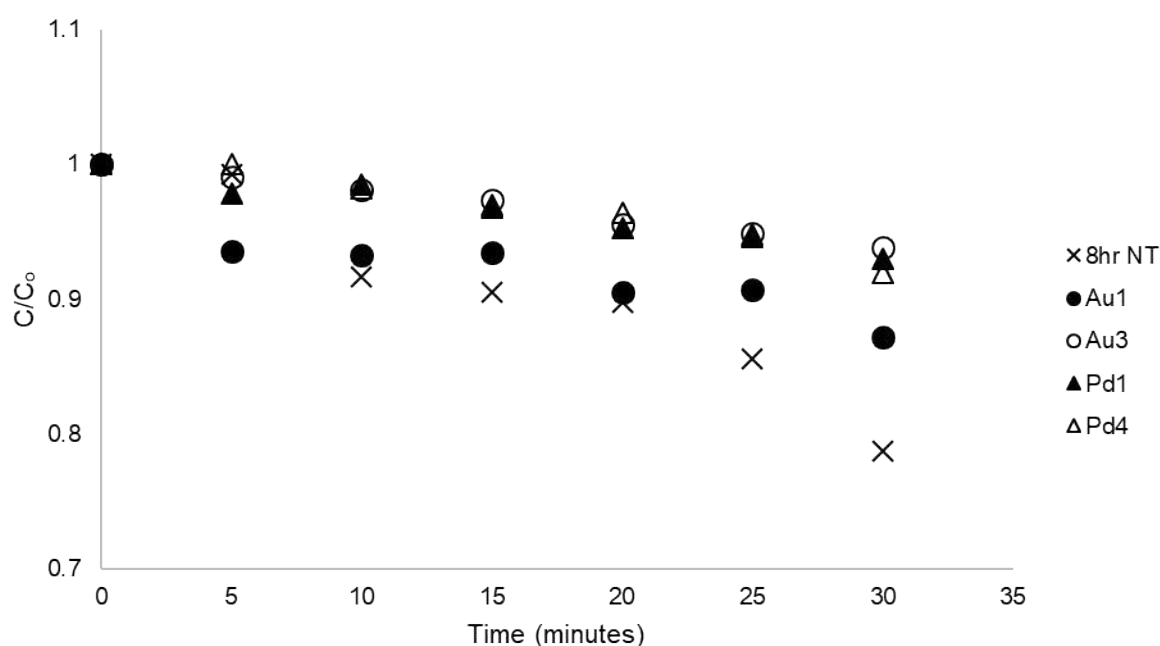


Figure 4.3.5: Plots showing the change in intensity of the C-H band (squares) and the carbonyl band (triangles) in the degradation of stearic acid by: **(a)** 1hr NT, **(b)** 4hr NT, **(c)** 8hr NT, **(d)** 24hr NT, **(e)** Ti/W NT
The dashed line shows the trend for C-H band, the dotted line shows the trend for the carbonyl band

beneficial in initial degradation steps, but resulted in the complication of the degradation mechanism and a subsequent slowing of overall mineralisation rate. Whether chloride directly deposited on a photocatalyst surface has a positive affect is unknown however. The correlation could be drawn here that the greater amounts of gold observed on the palladium samples could be responsible for the reduction in the photoactivity, in comparison to the gold analogues that have less chloride on the surface. For the gold doped arrays, both samples had

similar anatase crystallite sizes and similar compositions according to XPS. TEM images indicated that photodeposition for 1 minute resulted in gold particles 10 nm larger than for 3 minutes, and EDX indicated a higher concentration of gold after 3 minutes. These data suggest the smaller gold particles, formed after 3 minutes deposition time, are gaining deeper penetration depth. Given that these results in a poor photocatalytic performance this could indicate that depositing the gold deeper in the tubes has a negative impact on photocatalysed degradation. A possible explanation for this could be that the presence of chloride is poisoning photocatalytic steps, such as the transfer of holes or electrons on the surface, whilst any benefits of the presence of gold are lost when it is so deeply deposited in the nanotubes.



| Sample | 1 st Order Rate Constant (min ⁻¹) |
|----------|--|
| 8hr Au 1 | 0.0037 |
| 8hr Au 3 | 0.0022 |
| 8hr Pd1 | 0.0023 |
| 8hr Pd3 | 0.0027 |

Figure 4.3.6: A plot showing the normalised change in concentration of cinnamic acid of the gold and palladium decorated 8 hour nanotubes

Table 4.3.3: 1st order rate constants for the reactions plotted in **Figure 4.3.4**

Palladium, on the other hand appears to deposit poorly with a low dispersion and high tendency to agglomerate. TEM shows agglomerated particles reached sizes of 400 nm, significantly larger than the 127.2 nm tube size. A large discrepancy between the atomic percentage of palladium detected in XPS and EDX suggests that palladium deposition, in the 8-hour anodised samples, could be highly surface based leading to the conclusion that agglomeration prevents the palladium from penetrating the nanotubes. XP spectra show that the palladium is deposited mostly in its PdO form, with some in the metallic state at higher deposition times. Studies show that Pd²⁺ ions can have a positive impact on the oxidation of NO, [67] whilst data often suggests the presence of palladium inhibits degradation pathways like the degradation of trichloroethylene and the vinyl chloride monomer. [68][69] However, as reported by Sano *et al.*, the partial inhibition of the VC monomer had the benefit of trapping chloride on the catalyst surface and preventing the release of harmful chlorinated by products. This preference to adsorb chloride is also the likely cause of the higher amount of chloride on the surface of palladium doped arrays, in comparison to those doped with gold. So it appears that the photodeposition of palladium here forms palladium in an unsuitable oxidation state that results in a negative impact on the degradation process.

4.3.2.2 Surface Degradation of Stearic Acid

Plots of the degradation of SA by gold decorated nanotubes can be found in **Figure 4.3.6**, with the percentage change in signal shown in **Table 4.3.2**. The data shows that, again, gold does not improve the degradation efficiency of the nanotube arrays and largely has a negative impact. All of the 4 hour anodised arrays doped with gold showed a significant reduction in activity. 4hr Au3 displayed a marginally better activity, with SA concentration based on metric 1 decreasing by 15.5% after 3 hours and metric 2 decreasing in intensity by 9.8%. Whilst the remaining three arrays showed <10% decrease under both metrics. Both 8hr Au1 and 8hr Au3 were slightly hindered, in comparison to the undoped equivalent, although still resulted in a 25% drop in metric 1. 8hr Au3 gave a trend in percentage change of metric 2 that matched metric 1, whereas 8hr Au1 produced a much slower change in the carboxyl metric 2. Perhaps a reason for the poor performance of the 4 hour gold doped samples is the presence of solely metallic gold according to XP spectra. A lack of active gold species does not necessarily lead to bad activity or a low quantum efficiency. Metal nanoparticles catalysis is governed by redox processes and studies have found that, while a mixture of Au³⁺ and Au⁰ is optimal, metallic gold can easily be oxidised by photogenerated holes to form active gold

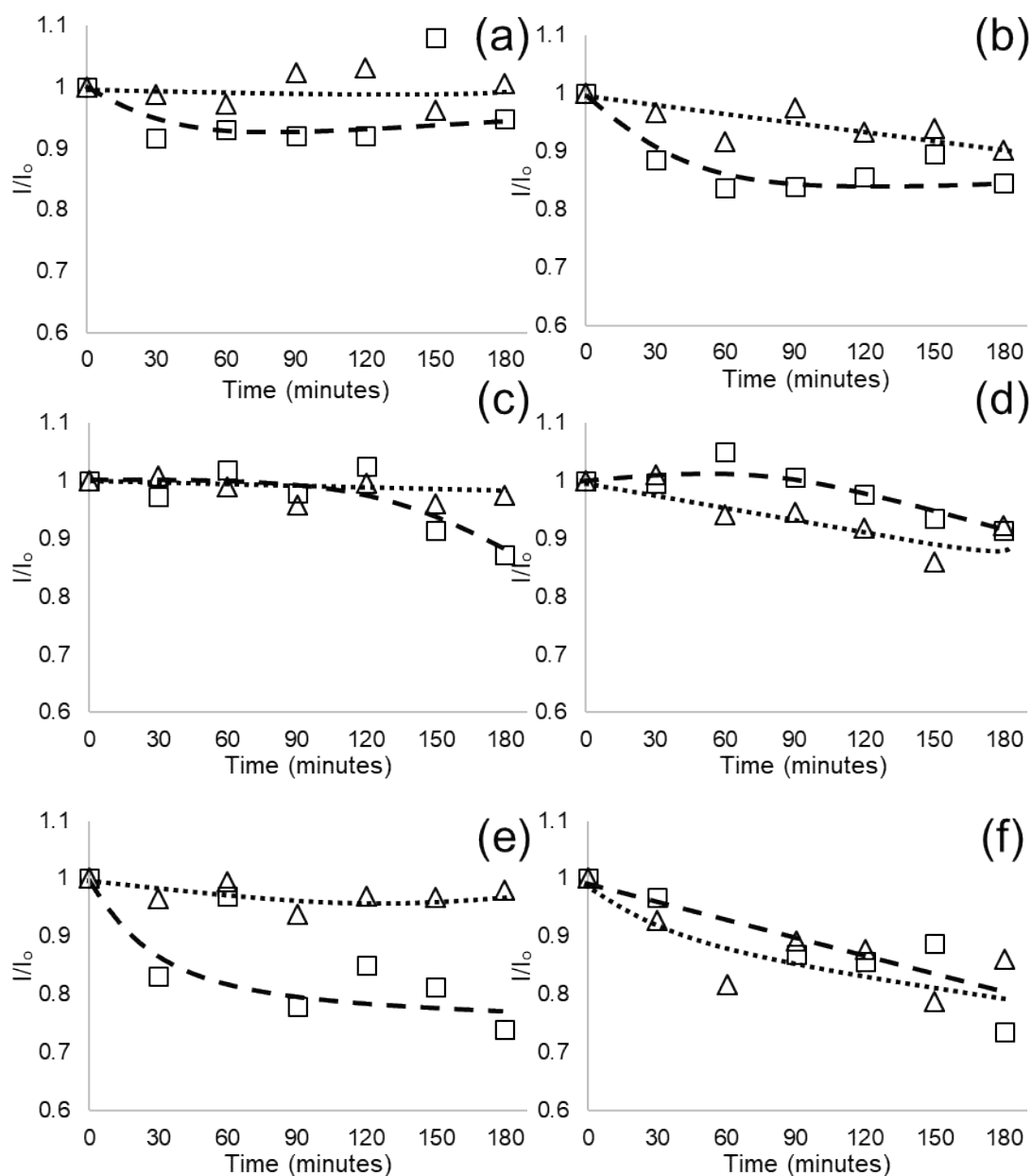


Figure 4.3.6: Plots showing the change in intensity of the C-H band (squares) and the carbonyl band (triangles) in the degradation of stearic acid by: (a) 4hr Au1, (b) 4hr Au3, (c) 4hr Au30, (d) 4hr Au60, (e) 8hr Au1, (f) 8hr Au3
As above in **Figure 4.3.3**, the dashed line shows the trend for C-H band, the dotted line shows the trend for the carbonyl band

species. [70] Whilst the 8 hour samples were characterised and tested with in a better time scale, as is evident by the presence of active gold species, that appears to have provided a more optimal mixture of gold oxidation states which is less disruptive on the photocatalytic activity. Of all the gold decorated arrays the 4hr Au3 and 8hr Au3 both performed the best

out of each set. FESEM analysis indicated that 3 minutes of photodeposition, for 8hr Au₃, resulted in a gold particle diameter of 30.7nm, a smaller size than after 1 minute. Studies have shown that gold particle size is strongly correlated to photodegradation efficiency, where results generally often show a particle size $\leq 15\text{nm}$ to be optimal. [71][72] It is therefore likely that the smaller particle size, resultant from 3 minutes of photodeposition, is closer to the optimal size required for photodegradation. Additionally, gold has been found to beneficially aid oxidative processes when the nanoparticles occupy sites on phase boundaries, [74] which is not possible here due to the monophasic characteristics of these nanotubes.

Deposition of palladium appeared to have a similar lack of success to gold. Although, the influence of palladium was notably less negative when compared to the liquid phase. This is potentially due to the reduced impact of chloride surface site poisoning when changing reaction media from the liquid phase to surface based degradation. None of the samples showed any improvement over the bare substrate, however the palladium did have varying effects on the changes to both metrics over time, as shown in **Figure 4.3.7** and **Table 4.3.2**. The most notable impact was to the change of the carbonyl stretch intensity of metric 2. The change in carbonyl intensity saw very little reduction, even when C-H area showed a significant decrease as seen in **Figure 4.3.7 (e) and (f)**. Using both 8 hour anodised photocatalysts, the removal of stearic acid C-H signal falls similarly to the undoped equivalent, a decrease of 35.7 and 24.3 %, the former showing a small improvement to the bare substrate, for 8hr Pd1 and 8hr Pd3 respectively. However, the samples only resulted in a decrease of 10.1 and 6.7% respectively. The other four samples, as seen in **Figure 4.3.7 (a) – (d)**, all show reduced activity in degrading the C-H and carbonyl regions. After 3 hours of reaction effectively no change in concentration or intensity is observed **(c)**, whilst the arrays in **(a), (b) and (d)** display a moderate amount change. It is evident that while the addition of palladium does not promote degradation, under these conditions, it is less inhibiting than gold. An explanation for this can be deduced from the XP spectra. Whereas gold was found to have deactivated to metallic gold, PdO was present in the palladium doped samples. As mentioned previously, the Pd²⁺ ion is a contender for better reactivity, rather than PdO, and so in future ensuring the formation of Pd²⁺ would be of foremost importance. XP spectra did suggest that 4hr Pd1 and 4hr Pd3 were lacking an active palladium species, however considering the reactivity results explored here this factor was not important. An influential aspect of palladium doped titania is the formation of Schottky barriers, an interface between

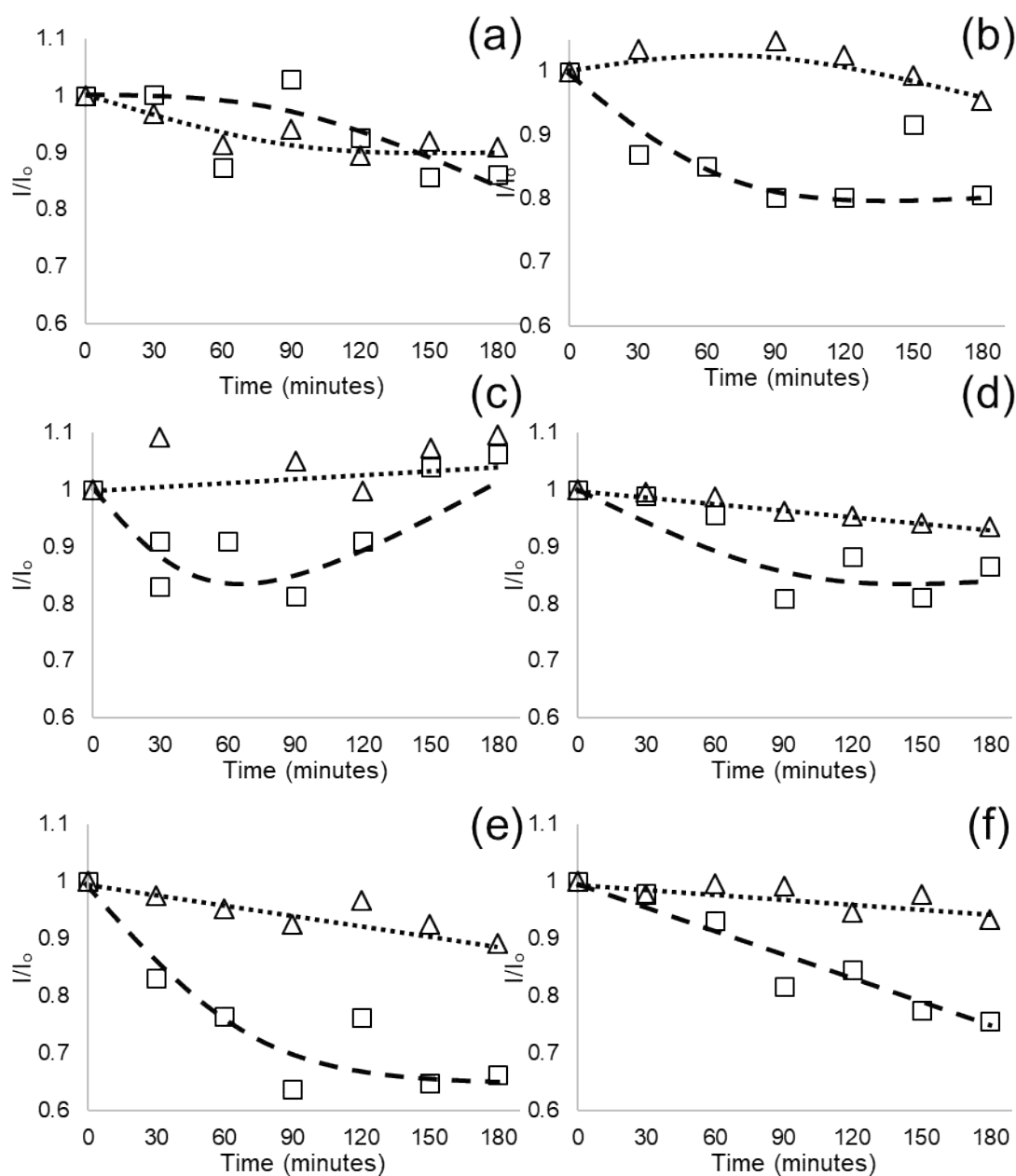


Figure 4.3.7: Plots showing the change in intensity of the C-H band (squares) and the carbonyl band (triangles) in the degradation of stearic acid by: (a) 4hr Pd1, (b) 4hr Pd3, (c) 4hr Pd30, (d) 4hr Pd60, (e) 8hr Pd1, (f) 8hr Pd3
As above in **Figure 4.3.3** and **4.3.5**, the dashed line shows the trend for C-H band, the dotted line shows the trend for the carbonyl band

the palladium and titania support useful for trapping electrons and reducing electron-hole recombination. In general, the greater the number of interfaces between metal and support, the more Schottky barriers form and the more beneficial to photocatalysis the palladium becomes. Whereas large particles are known to be recombination centres and result in a

negative impact. FESEM imaging showed the tendency for palladium particles to agglomerate into large masses spanning up to 1000 nm in width, whilst also indicating the notable lack of small particles despite XP spectra suggesting substantial amounts of palladium were present. As such it is suspected that palladium may be largely depositing as particles ≤ 10 nm; which are difficult to image, even when using backscattered electron detection. Further work is required to accurately establish the average size of the nanoparticles, as well as determine to what depth the nanoparticles penetrate during deposition.

4.4 Conclusions

Nanotube arrays were successfully formed for 4 different time scales and tested for their photocatalytic proficiency. Increasing anodisation time resulted in the increasing length and pore width of the nanotubes that correlated to a progressive increase in the tube aspect ratio. Heat treatment, of all length of tubes, produced purely anatase crystallinity with an increasing crystallite size that peaked with 8 hour anodised arrays, details summarised in **Table 4.2.1**. Tungsten was incorporated into the anodisation process with a small degree of success to form Ti/W mixed metal oxide nanotube arrays. XPS and EDX showed that the tungsten content increased with reuse of electrolyte to 0.46 atomic% after 3 uses. The development of a new chemical state, in the O1s region, was associated with the rising concentration of tungsten, the placement of this peak at 530.5 eV suggests the formation of tungsten trioxide in the samples. Microscopy indicated the tube width remained unchanged by the presence of tungsten, although an increase in malformed tubes was observed. The tungsten also did not affect the crystallinity or crystallite size, but a shift to a smaller bandgap was detected. Under all testing a clear trend for activity was found to be 8hr NT > 4hr NT > 1hr NT > 24hr NT \geq Ti/W NT. The testing of the arrays in both liquid and surface deposition reactions showed conclusively that nanotubes anodised for 8 hours were the most efficient and degrading both target molecules, with 4 hour anodised tubes following closely in all metrics. In the liquid phase degradation of cinnamic acid, **Table 4.3.1** shows 8 and 4 hour anodised arrays removed cinnamic acid at first order rates of 0.0054 and 0.0049 min⁻¹. 8 hour tubes were then the only arrays that displayed any activity above the control samples in the surface based degradation of cinnamic acid. Then in the surface based degradation of stearic acid, the 8 hour tubes were by far the most active in reducing the intensities of both the C-H and carbonyl bands by over 30% in 180 minutes. The data indicates that the factors

controlling the photocatalytic proficiency for liquid phase degradation are the same that govern the surface based degradation. Tubes anodised for 8 hours have the most optimal tube surface topography, owing to the reasonably large tubes with thin walls, that do not suffer from structural weaknesses from fluoride induced wall thinning. The tubes surface topography probably facilitates deeper UV light penetration and improved pollutant diffusion, factors that are hindered in the tubes anodised for shorter time lengths. Whereas the valley-like features observed on tubes anodised for 24 hours are preventing light penetration that have a severe impact on the nanotube arrays' photocatalytic efficiency. The inclusion of tungsten did not give any increase in activity, and resulted in the inhibition of degradation in comparison to the plain 4 hour anodised arrays.

Gold and palladium were both photodeposited onto 4 and 8 hour anodised arrays. Gold deposited as relatively large particles of 40.1 and 30.7 nm after 1 and 3 minutes of deposition, indicating the slightly longer deposition time formed smaller particles that had a greater preference of penetrating into the 8 hour tubes than the palladium equivalents, according to XPS and EDX data. Deposition of both metals resulted in the deposition of both Fresh gold deposited as both Au^0 and Au^{1+} , however XPS showed reduction to Au^0 occurred over time. Preparation methods could be altered to further oxidise gold to Au^{3+} to improve reactivity, although other studies do indicate photocatalysis promotes the in-situ oxidation of gold. [70] In general, the presence of gold was not beneficial to the photocatalytic degradation of either cinnamic acid or stearic acid. Testing in the liquid phase found, in the 8 hour samples, that nanoparticles deposited after 1 minute showed the lesser impact in retarding the degradation rate; whilst deposition after 3 minutes, on both 4 and 8 hour tubes, was shown to be the most effective in degrading stearic acid deposits. The biggest impact, in the degradation of stearic acid, was the notable departure from targeting the carbonyl functionality simultaneously to the C-H bands. It is believed that the smaller nanoparticles deposited after 3 minutes of photodeposition were a more optimal size, compared to the larger nanoparticles deposited after 1 minute. The smaller particles enabled deeper deposition within the tubes which better maximised the photoactivity. Palladium deposited as significantly smaller nanoparticles, compared to gold, although with a higher preference to agglomerate as seen in **Figure 4.2.5**. FESEM images found measurable nanoparticles of 15.3 nm after 1 minute of deposition, however no smaller particulate matter could be seen on the surface after 3 minutes of deposition despite XPS indicating a palladium content of 9.9% on

the surface. It is therefore possible that the small increase in photodeposition time results in smaller nanoparticles, as seen with gold, that are more difficult to image in FESEM. EDX found a distinct drop in palladium, in comparison to the XPS data, suggesting the deposition of palladium was largely surface based; however, an evaluation of the concentrations calculated from the Pd 3d region implied the region was not reliable for a quantitative assessment. Palladium doped arrays generally performed better than those decorated with gold, except for reaction in the liquid phase. **Table 4.3.3** showed palladium killed off the reactivity of 8 hour nanotubes when mineralising cinnamic acid, whereas **Table 4.3.2** indicated that the palladium nanoparticles were better suited to degrade stearic acid under the same conditions. It is asserted that the capacity for palladium to induce attract chloride ions is major factor in the liquid phase degradation of cinnamic acid due to the occupation of important surface sites. Whereas the occupation of surface sites is not as influential during the surface degradation of contaminants. Overall it was found that the photodeposition of gold and palladium onto titania nanotube arrays, under these circumstances, was not beneficial for the degradation of cinnamic acid or stearic acid.

4.5 References

1. H. Zhang and J. F. Banfield, *Chem. Mater.*, 2005, **17**, 3421–3425.
2. H. Zhang and J. F. Banfield, *J. Mater. Chem.*, 1998, **8**, 2073–2076.
3. Y. Lin, G. S. Wu, X. Y. Yuan, T. Xie and L. D. Zhang, *J. Phys.: Condens. Matter*, 2003, **15**, 2917.
4. M. Andersson, L. Österlund, S. Ljungström and A. Palmqvist, *J. Phys. Chem. B*, 2002, **106**, 10674–10679.
5. J. Yang, S. Mei and J. M. F. Ferreira, *Materials Science and Engineering: C*, 2001, **15**, 183–185.
6. J.-N. Nian and H. Teng, *J. Phys. Chem. B*, 2006, **110**, 4193–4198.
7. R. Armstrong, G. Armstrong, J. Canales, R. García and P. G. Bruce, *Adv. Mater.*, 2005, **17**, 862–865.
8. R. Govindaraj, N. Santhosh, P. M. Senthil and P. Ramasamy, *J. Cryst. Growth*, 2017, **468**, 125–128.
9. S.-T. Myung, N. Takahashi, S. Komaba, C. S. Yoon, Y.-K. Sun, K. Amine and H. Yashiro, *Adv. Funct. Mater.*, 2011, **21**, 3231–3241.
10. M. A. Khan, H. T. Jung and O. B. Yang, *J. Phys. Chem. B*, 2006, **110**, 6626–6630.
11. D. V. Bavykin, J. M. Friedrich and F. C. Walsh, *Adv. Mater.*, 2006, **18**, 2807–2824.
12. N. Viriya-empikul, T. Charinpanitkul, N. Sano, A. Soottitantawat, T. Kikuchi, K. Faungnawakij and W. Tanthapanichakoon, *Materials Chemistry and Physics*, 2009, **118**, 254–258.
13. Z.-Y. Yuan and B.-L. Su, *Colloids and Surfaces A: Physicochemical and Engineering Aspects*, 2004, **241**, 173–183.

14. V. Zwillig, M. Aucouturier and E. Darque-Ceretti, *Electrochimica Acta*, 1999, **45**, 921–929.
15. J. Choi, R. B. Wehrspohn, J. Lee and U. Gösele, *Electrochimica Acta*, 2004, **49**, 2645–2652.
16. Q. Cai, M. Paulose, O. K. Varghese and C. A. Grimes, *Journal of Materials Research*, 2005, **20**, 230–236.
17. J. M. Macak, K. Sirotna and P. Schmuki, *Electrochimica Acta*, 2005, **50**, 3679–3684.
18. J. M. Macak, H. Tsuchiya, L. Taveira, S. Aldabergerova and P. Schmuki, *Angewandte Chemie International Edition*, 2005, **44**, 7463–7465.
19. S. P. Albu, A. Ghicov, J. M. Macak and P. Schmuki, *physica status solidi (RRL) – Rapid Research Letters*, 2007, **1**, R65–R67.
20. C.A. Grimes, H. E. Prakasam, K. Shankar, M. Paulose and O. K. Varghese, *Journal of Physical Chemistry C*, 2007, **111**, 7235–7241.
21. M. Paulose, O. K. Varghese, L. Peng, K. C. Popat, H. E. Prakasam, G. K. Mor, T. A. Desai and C. A. Grimes, *Journal of Physical Chemistry C*, 2007, **111**, 14992–14997.
22. S. Yoriya, G. K. Mor, S. Sharma, and C. A. Grimes, *Journal of Materials Chemistry*, 2008, **18**, 3332.
23. S. Yoriya and C. A. Grimes, *Langmuir*, 2010, **26**, 417–420.
24. H. Yin, H. Liu, and W. Z. Shen, *Nanotechnology*, 2010, **21**, 035601.
25. J. Yu and B. Wang, *Applied Catalysis B: Environmental*, 2010, **94**, 295–302.
26. S. T. Nishanthi, D. Henry Raja, E. Subramanian and D. Pathinettam Padiyan, *Electrochimica Acta*, 2013, **89**, 239–245.
27. S. T. Nishanthi, S. Iyyapushpam, B. Sundarakannan, E. Subramanian and D. Pathinettam Padiyan, *Applied Surface Science*, 2014, **313**, 449–454.
28. V. Likodimos, T. Stergiopoulos, P. Falaras, J. Kunze and P. Schmuki, *J. Phys. Chem. C*, 2008, **112**, 12687–12696.
29. M. Grätzel, *Inorg. Chem.*, 2005, **44**, 6841–6851.
30. B. O'Regan and M. Grätzel, *Nature*, 1991, **353**, 737–740.
31. J. R. Jennings, A. Ghicov, L. M. Peter, P. Schmuki and A. B. Walker, *J. Am. Chem. Soc.*, 2008, **130**, 13364–13372.
32. F. Mohammadpour, M. Altomare, S. So, K. Lee, M. Mokhtar, A. Alshehri, S. A. Al-Thabaiti and P. Schmuki, *Semiconductor Science and Technology*, , DOI:10.1088/0268-1242/31/1/014010.
33. F. Mohammadpour, M. Moradi, K. Lee, G. Cha, S. So, A. Kahnt, D. M. Guldi, M. Altomare and P. Schmuki, *Chemical Communications*, 2015, **51**, 1631–1634.
34. M. Paulose, O. K. Varghese, G. K. Mor, C. A. Grimes and K. G. Ong, *Nanotechnology*, 2006, **17**, 398.
35. Y. Zhang, W. Fu, H. Yang, Q. Qi, Y. Zeng, T. Zhang, R. Ge and G. Zou, *Applied Surface Science*, 2008, **254**, 5545–5547.
36. O. K. Varghese, D. Gong, M. Paulose, K. G. Ong and C. A. Grimes, *Sensors and Actuators B: Chemical*, 2003, **93**, 338–344. 1
37. M. Altomare, M. Pozzi, M. Allieta, L. G. Bettini and E. Selli, *Applied Catalysis B: Environmental*, 2013, **136–137**, 81–88.
38. M. Kulkarni, K. Mrak-Poljšak, A. Flašker, A. Mazare, P. Schmuki, A. Kos, S. Čučnik, S. Sodin-Šemrl and A. Iglič, *Materiali in Tehnologije*, 2015, **49**, 635–637.
39. I. Kontos, V. Likodimos, T. Stergiopoulos, D. S. Tsoukleris, P. Falaras, I. Rabias, G. Papavassiliou, D. Kim, J. Kunze and P. Schmuki, *Chem. Mater.*, 2009, **21**, 662–672.
40. G. Kontos, A. I. Kontos, D. S. Tsoukleris, V. Likodimos, J. Kunze, P. Schmuki and P. Falaras, *Nanotechnology*, 2009, **20**, 045603.

41. Z. Zhang, Yuan, G. Shi, Y. Fang, L. Liang, H. Ding and L. Jin, *Environ. Sci. Technol.*, 2007, **41**, 6259–6263.
42. Z. Liu, X. Zhang, S. Nishimoto, M. Jin, D. A. Tryk, T. Murakami and A. Fujishima, *J. Phys. Chem. C*, 2008, **112**, 253–259.
43. M. Tian, G. Wu, B. Adams, J. Wen and A. Chen, *J. Phys. Chem. C*, 2008, **112**, 825–831.
44. B. D. Marien, T. Cottineau, D. Robert and P. Drogui, *Applied Catalysis B: Environmental*, 2016, **194**, 1–6.
45. X. Quan, X. Ruan, H. Zhao, S. Chen and Y. Zhao, *Environmental Pollution*, 2007, **147**, 409–414.
46. X. Quan, S. Yang, X. Ruan and H. Zhao, *Environ. Sci. Technol.*, 2005, **39**, 3770–3775.
47. H. Liang, X. Li, Y. Yang and K. Sze, *Chemosphere*, 2008, **73**, 805–812.
48. Mazzarolo, K. Lee, A. Vincenzo and P. Schmuki, *Electrochemistry Communications*, 2012, **22**, 162–165.
49. X. Zhang, K. Huo, L. Hu, Z. Wu and P. K. Chu, *Journal of the American Ceramic Society*, 2010, **93**, 2771–2778.
50. K. Gulati, A. Santos, D. Findlay and D. Losic, *J. Phys. Chem. C*, 2015, **119**, 16033–16045.
51. Regonini, A. Jaroenworuluck, R. Stevens and C. R. Bowen, *Surface and Interface Analysis*, 2010, **42**, 139–144.
52. D. Regonini, PhD Thesis, “Anodised TiO₂ Nanotubes: Synthesis, Growth Mechanism and Thermal Stability”, University of Bath, 2008.
53. S. F. Ho, S. Contarini and J. W. Rabalais, *J. Phys. Chem.*, 1987, **91**, 4779–4788.
54. J. Radnik, C. Mohr and P. Claus, *Physical Chemistry Chemical Physics*, 2003, **5**, 172–177.
55. M. Sankar, Q. He, M. Morad, J. Pritchard, S. J. Freakley, J. K. Edwards, S. H. Taylor, D. J. Morgan, A. F. Carley, D. W. Knight, C. J. Kiely and G. J. Hutchings, *ACS Nano*, 2012, **6**, 6600–6613.
56. M. G. Alemseghed, T. P. A. Ruberu and J. Vela, *Chem. Mater.*, 2011, **23**, 3571–3579.
57. C. B. Almquist and P. Biswas, *Journal of Catalysis*, 2002, **212**, 145–156.
58. X. Wang, L. Sør, R. Su, S. Wendt, P. Hald, A. Mamakhel, C. Yang, Y. Huang, B. B. Iversen and F. Besenbacher, *Journal of Catalysis*, 2014, **310**, 100–108.
59. R. Tahmasebpour, A. A. Babaluo, J. R. Shahrouzi, M. Tahmasebpour and M. Shahrezaei, *Journal of Environmental Chemical Engineering*, 2017, **5**, 1227–1237.
60. J. Liu, F. Chen, Y. Chen and D. Zhang, *Journal of Power Sources*, 2009, **187**, 500–504.
61. B. Gupta, A. A. Melvin, T. Matthews, S. Dash and A. K. Tyagi, *Renewable and Sustainable Energy Reviews*, 2016, **58**, 1366–1375.
62. Y. Paz, Z. Luo, L. Rabenberg and A. Heller, *Journal of Materials Research*, 1995, **10**, 2842–2848.
63. Mills and J. Wang, *Journal of Photochemistry and Photobiology A: Chemistry*, 2006, **182**, 181–186.
64. Mills, N. Wells and C. O’Rourke, *Catalysis Today*, 2014, **230**, 245–249.
65. T. Minabe, D. A. Tryk, P. Sawunyama, Y. Kikuchi, K. Hashimoto and A. Fujishima, *Journal of Photochemistry and Photobiology A: Chemistry*, 2000, **137**, 53–62.
66. V. Rome’as, P. Pichat, C. Guillard, T. Chopin and C. Lehaut, *New J. Chem.*, 1999, **23**, 365–374.
67. Z. Wu, Z. Sheng, H. Wang and Y. Liu, *Chemosphere*, 2009, **77**, 264–268.

68. H.-H. Ou and S.-L. Lo, *Journal of Molecular Catalysis A: Chemical*, 2007, **275**, 200–205.
69. T. Sano, S. Kutsuna, N. Negishi and K. Takeuchi, *Journal of Molecular Catalysis A: Chemical*, 2002, **189**, 263–270.
70. V. Subramanian, E. E. Wolf and P. V. Kamat, *Langmuir*, 2003, **19**, 469–474.
71. Cojocaru, Ș. Neațu, E. Sacaliuc-Pârvulescu, F. Lévy, V. I. Pârvulescu and H. Garcia, *Applied Catalysis B: Environmental*, 2011, **107**, 140–149.
72. S. Oros-Ruiz, J. A. Pedraza-Avella, C. Guzmán, M. Quintana, E. Moctezuma, G. del Angel, R. Gómez and E. Pérez, *Top Catal*, 2011, **54**, 519–526.
73. B. Koslowski, H.-G. Boyen, C. Wilderotter, G. Kästle, P. Ziemann, R. Wahrenberg and P. Oelhafen, *Surface Science*, 2001, **475**, 1–10.
74. D. Tsukamoto, Y. Shiraishi, Y. Sugano, S. Ichikawa, S. Tanaka and T. Hirai, *J. Am. Chem. Soc.*, 2012, **134**, 6309–6315.

Chapter 5 – Metal Loaded Nanoparticles for Photocatalytic Waste Water Treatment

| | |
|---|-----|
| 5.1 Introduction | 174 |
| 5.2 Photocatalyst Characterisation | 175 |
| 5.2.1 X-Ray Diffraction | 175 |
| 5.2.2 UV/Vis | 176 |
| 5.2.3 X-ray Photoelectron Spectroscopy Analysis | 177 |
| 5.2.4 DRIFTS-FTIR | 184 |
| 5.2.5 Transmission Electron Microscopy Particle Size Study..... | 186 |
| 5.3 Results | 187 |
| 5.3.1 The Photoactivity of Palladium Catalysts..... | 187 |
| 5.3.1.1 Kinetic Impact..... | 187 |
| 5.3.1.2 Mechanistic Impact..... | 188 |
| 5.3.2 The Photoactivity of Gold Catalysts | 192 |
| 5.3.2.1 Kinetic Impact..... | 192 |
| 5.3.2.2 Mechanistic Impact..... | 193 |
| 5.3.3 Carbon Dioxide Capture Experiments | 193 |
| 5.4 Discussion | 195 |
| 5.4.1 Pd/TiO ₂ Catalysts | 195 |
| 5.4.2 Au/TiO ₂ Catalysts | 199 |
| 5.5 Conclusions | 203 |
| 5.6 References | 204 |

5.1 Introduction

The use of supported metal nanoparticles has a well-established history in photocatalysis. Beneficial effects include; improved photoactivity due to superior charge species separation, [1][2] the extension of absorption characteristics into the visible range, [3][4][5][6] allowing metal based thermal catalysis to synergistically aid photocatalytic mechanisms, and providing new adsorption sites for species to interact with the photocatalytic material. [7] Nobel metals, like palladium and gold, are widely explored for these reasons and have been discussed in much greater depth in section 1.4 of the introduction chapter.

In this chapter we explore the effect of different weight loadings of palladium and gold on the degradation of cinnamic acid by powdered TiO₂ photocatalysts. The kinetic impact on cinnamic acid removal is assessed in oxygenated and deoxygenated conditions to evaluate how beneficial each metal is for pollutant mineralisation. Changes in intermediate selectivity are examined and explained in the context of co-metal participation, utilising the characterisation data at hand to interpret the observed trends. Finally, the photocatalysts are appraised for their effectiveness in improving mineralisation rates and selectively during the photocatalytic process.

| Wt Loading | E _g (eV) [Pd] | L _A (nm) [Pd] | L _R (nm) [Pd] | Av _{NP} Pd (nm) | E _g (eV) [Au] | L _A (nm) [Au] | L _R (nm) [Au] |
|------------|--------------------------|--------------------------|--------------------------|--------------------------|--------------------------|--------------------------|--------------------------|
| 0 % (mP25) | 3.10 | 25.7 ± 1.3 | 33.2 ± 1.7 | | | | |
| 0.1 wt% | 3.02 | 16.3 ± 0.8 | 19.5 ± 1.0 | 1.6 ± 0.12 | 3.14 | 22.8 ± 1.1 | 32.3 ± 1.6 |
| 0.25 wt% | 3.00 | 21.8 ± 1.1 | 29.9 ± 1.5 | 1.3 ± 0.04 | 3.17 | 21.1 ± 1.1 | 25.0 ± 1.3 |
| 0.5 wt% | 3.00 | 23.5 ± 1.2 | 35.7 ± 1.8 | 1.7 ± 0.06 | 3.14 | 21.8 ± 1.1 | 31.6 ± 1.6 |
| 1 wt% | 2.99 | 22.5 ± 1.1 | 35.7 ± 1.8 | 2.8 ± 0.12 | 2.92 | 20.4 ± 1.0 | 31.0 ± 1.6 |
| 2 wt% | 2.92 | 25.1 ± 1.3 | 33.2 ± 1.7 | 3.0 ± 0.14 | 3.11 | 20.0 ± 1.0 | 32.9 ± 1.7 |

Table 5.3.1:- Characterisation data for the palladium [Pd] and gold [Au] on TiO₂ catalysts

5.2 Photocatalyst Characterisation

5.2.1 X-Ray Diffraction

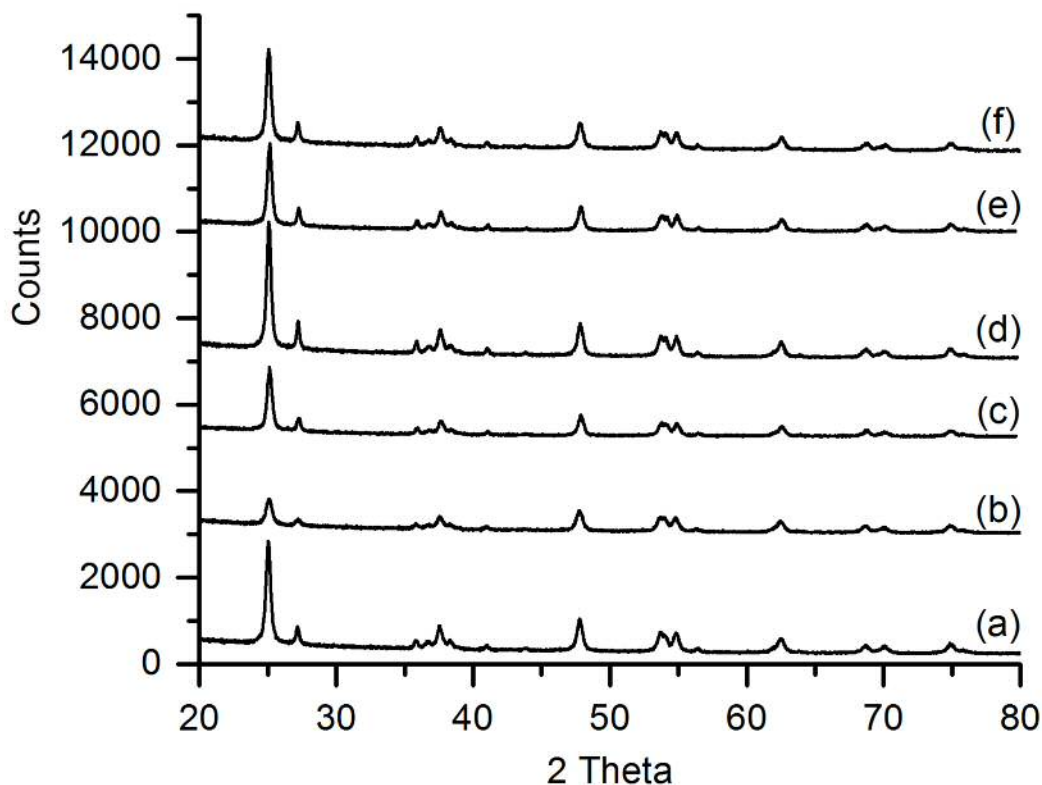


Figure 5.2.1:- X-ray diffraction patterns for: (a) mP25, (b) 0.1 wt% Pd/TiO₂, (c) 0.25 wt% Pd/TiO₂, (d) 0.5 wt% Pd/TiO₂, (e) 1 wt% Pd/TiO₂, (f) 2 wt% Pd/TiO₂

Figure 5.2.1 and **Figure 5.2.2** show the x-ray diffraction patterns for the fresh palladium and gold doped titania photocatalysts, respectively. The plain TiO₂ material used in this work is the same that was used in **Chapter 3**. It is P25 that has been treated via incipient wetness to agglomerate the powder and reduce dispersion for less problematic reaction analysis. Each diffraction pattern contains the same set of peaks as the clean modified P25 (mP25) titania powder, indicating they were all polymorphic materials that contained the anatase and rutile phases. **Figure 5.2.1** shows no evidence of palladium diffraction patterns, even at the highest concentration of 2 wt%, suggesting that palladium deposition did not occur in such a manner as to form palladium clusters large enough to produce detectable peaks. The same situation is found for the gold doped TiO₂ materials. Application of the Scherrer equation gave the crystallite sizes seen in **Table 5.2.1**. Anatase crystallite size (L_A)

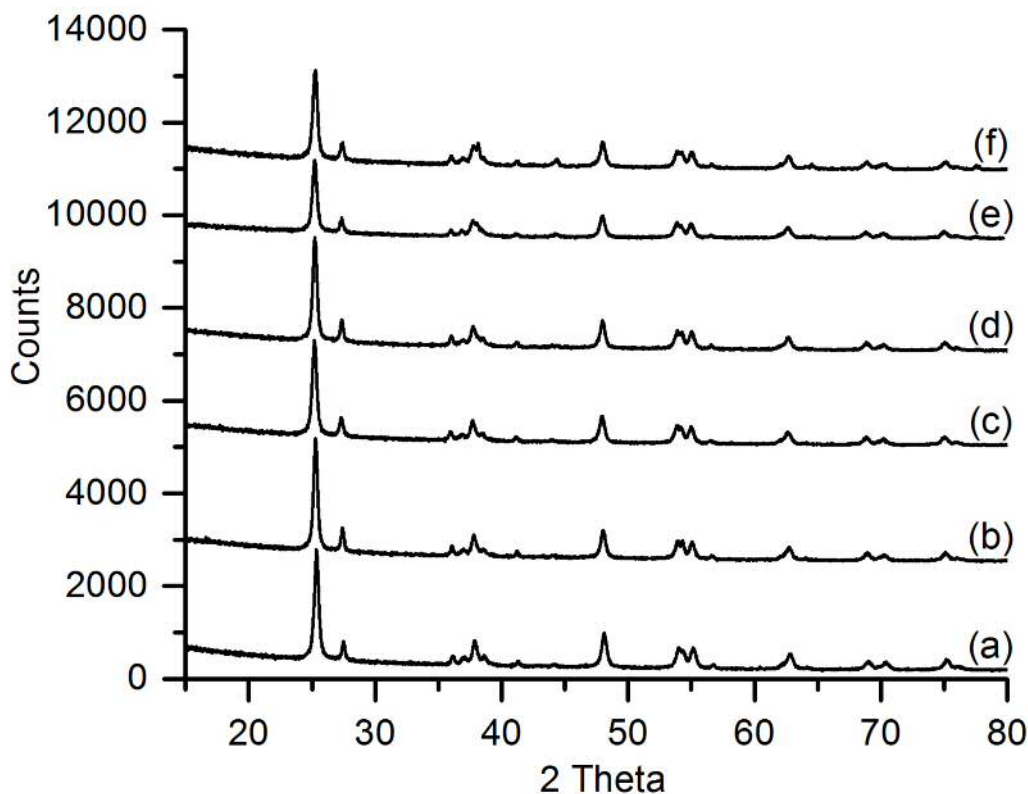


Figure 5.2.2:- X-ray diffraction patterns for: (a) mP25, (b) 0.1 wt% Au/TiO₂, (c) 0.25 wt% Au/TiO₂, (d) 0.5 wt% Au/TiO₂, (e) 1 wt% Au/TiO₂, (f) 2 wt% Au/TiO₂ is generally found to be above 20 nm. The palladium catalysts display a weak trend of increasing anatase crystal size as palladium concentration increases, whereas the L_A decreases slightly as gold loading increases. Applying a 5% error margin finds that this trend, of decreasing crystallite size, is statistically significant. The rutile crystallite size (L_R) shows no trends; for palladium the calculated sizes lie across the 33.2 nm value found for the plain titania sample (mP25), whilst for gold the sizes are all below the value.

5.2.2 UV/Vis

UV adsorption data for all samples was treated with the method described by Jan Tauc [8][9] and plotted to ascertain the bandgap of the materials, which can be found in **Table 5.2.1**. mP25 was found to have a bandgap of 3.11 eV, typical of mixed phase materials. Doping with palladium induced a drop in the bandgap size to 3.02 eV for 0.1 wt% Pd/TiO₂, and further increases in palladium loading resulted in a steady decrease in the bandgap size to the 2.92 eV for 2 wt% Pd/TiO₂. Changes in the metal loading of gold caused small increases in bandgap size, except for 1 wt% Au/TiO₂ which showed a decrease to 2.92 eV.

| | % Concentration | | | | | |
|-----------------------------|-----------------|--------|--------|---------|---------|---------|
| | Ti (2p) | O (1s) | C (1s) | Pd (3d) | Au (4f) | Cl (2p) |
| mP25 | 27.0 | 60.2 | 12 | 0 | 0 | 0 |
| 0.1wt% Pd/TiO ₂ | 29.3 | 65.7 | 3.7 | 0.2 | / | 0 |
| 0.25wt% Pd/TiO ₂ | 29.5 | 64.9 | 3.8 | 0.6 | / | 1.2 |
| 0.5wt% Pd/TiO ₂ | 26.2 | 58.4 | 13.4 | 1.0 | / | 1.0 |
| 1wt% Pd/TiO ₂ | 28.3 | 61.7 | 5.2 | 2.4 | / | 2.4 |
| 2wt% Pd/TiO ₂ | 27.2 | 59.3 | 9.8 | 3.2 | / | 3.7 |
| 0.1wt% Au/TiO ₂ | 27.9 | 62.7 | 7.7 | / | 0.1 | 1.5 |
| 0.25wt% Au/TiO ₂ | 22.9 | 53.0 | 23.0 | / | 0.1 | 1.0 |
| 0.5wt% Au/TiO ₂ | 28.8 | 64.3 | 4.5 | / | 0.1 | 2.1 |
| 1wt% Au/TiO ₂ | 29.3 | 65.1 | 4.4 | / | 0.1 | 1 |
| 2wt% Au/TiO ₂ | 27.9 | 61.8 | 7.2 | / | 0.2 | 2.6 |

Table 5.2.2:- XPS atomic percentage concentration data for the fresh catalysts

5.2.3 X-ray Photoelectron Spectroscopy Analysis

Palladium

All of the palladium photocatalysts were characterised by XPS before and after reaction, whilst all the fresh gold catalysts were characterised as well as some select spent catalysts. **Table 5.2.2** summarises the surface elemental composition of the fresh catalysts, whilst **Table 5.2.3** contains the data for those spent catalysts that were analysed. The incipient wetness preparation technique gave surface palladium concentrations that were roughly twice that of the intended loading, indicating that the palladium is well dispersed on the surface that results in an overrepresentation in surface concentrations. **Figure 5.2.3 (a)** shows the Pd(3d) region for the fresh 1 wt% Pd/TiO₂ catalyst. The spectrum was fitted with a Shirley background and a Gaussian-Lorentzian peak shape and shows there were two palladium environments present. The first Pd 5/2 peak had a chemical shift of 336 eV and a spin orbit coupling of 5.3 eV, typical of suggests PdO. The other set of peaks has a binding energy of 337.5 eV and has been assigned the Pd²⁺ state of PdCl₂. Peak fitting gave the percentage composition of the palladium as 73 % and 27 % for the PdO and PdCl₂ environments. Quantification of the XP spectra also found that chlorine deposited at near 1:1 levels to palladium. Spent catalyst analysis, the percentage concentrations of which are in **Table 5.2.3**, found the palladium concentration generally decreased after reactions with the greater amount of surface palladium disappearing after the oxygenated reactions in most cases. **Figure 5.2.3 (b)** and **(c)** show the palladium region for the 1 wt% Pd/TiO₂ spent catalysts from the oxygenated and deoxygenated reactions respectively. Oxygenated

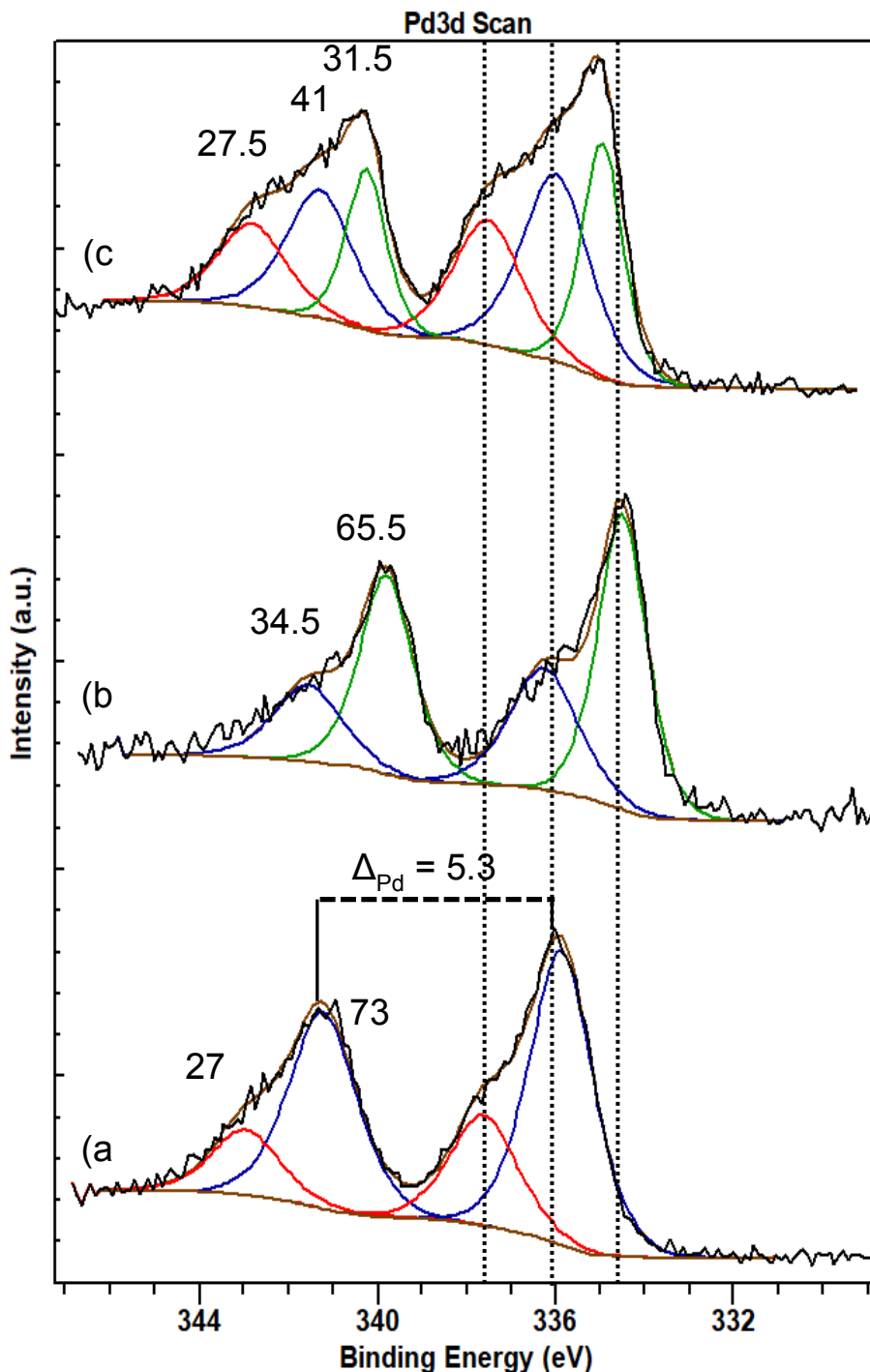


Figure 5.2.3:- XP spectra of the Pd 3d region for: **(a)** fresh 1 wt% Pd/TiO₂, **(b)** spent 1 wt% Pd/TiO₂, **(c)** spent 1 wt% Pd/TiO₂ (deoxy)

conditions resulted in a large degree of reduction to Pd metal. The Pd metal peak has a chemical shift at 334.5 eV, constituting 65.5% of the total palladium region where the other 35.5 % is the remaining PdO. Analysis of the palladium region after reaction under deoxygenated conditions found three chemical environments at 335, 336 and 337.5 eV which

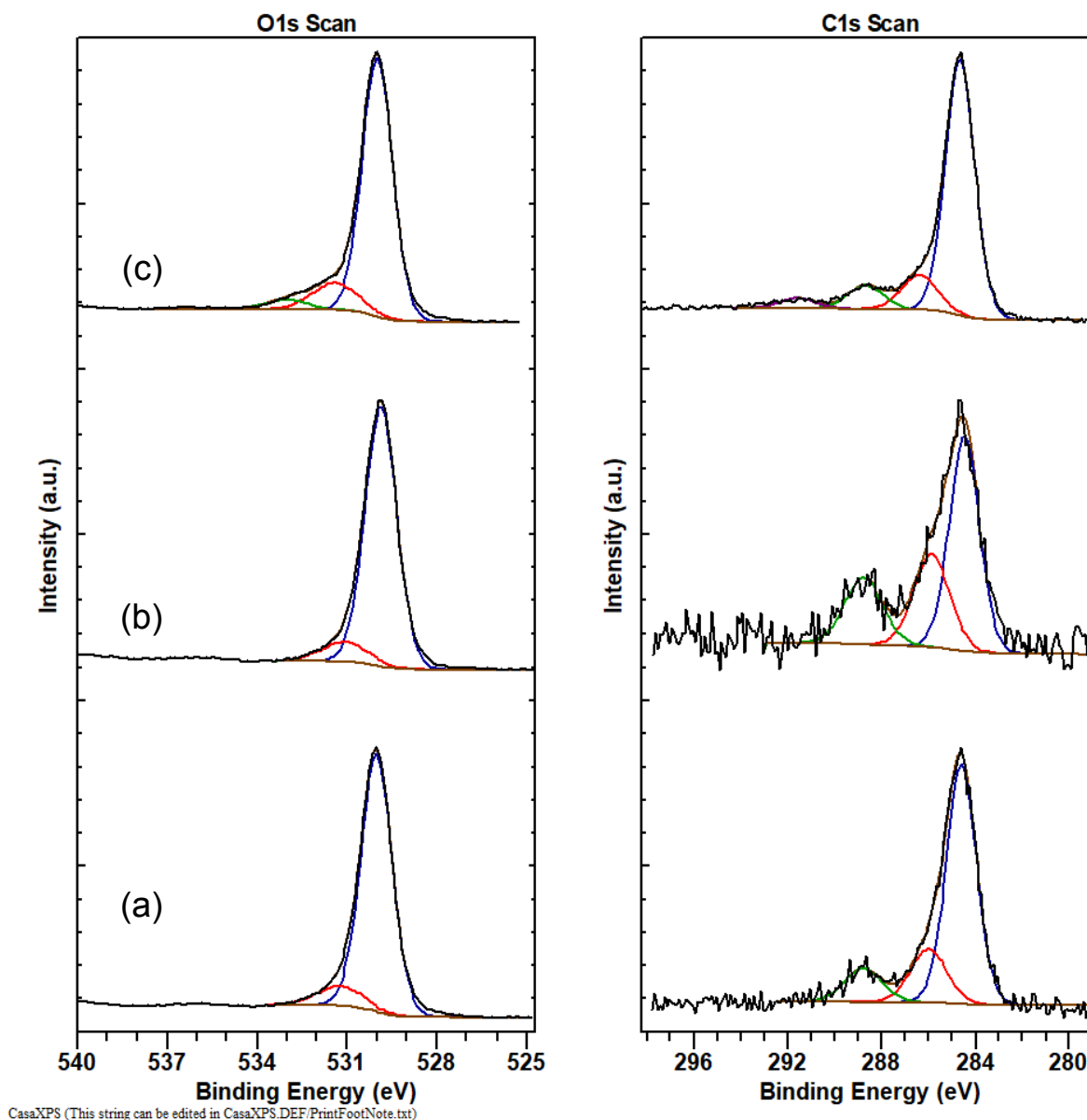


Figure 5.2.4:- Xp spectra of the O 1s and C 1s regions for: **(a)** fresh 1 wt% Pd/TiO₂, **(b)** spent 1 wt% Pd/TiO₂, **(c)** spent 1 wt% Pd/TiO₂ (deoxy) have been assigned to Pd metal, PdO and PdCl₂ respectively. The three chemical states constituted 31.5, 41 and 27.5 % of the total palladium. Quantification of the XP spectra also found that chlorine deposited at near 1:1 levels to palladium after catalyst preparation, which then mostly dropped to <0.5% after reaction both in the presence and in the absence of oxygen.

Examples of the oxygen and carbon regions for the fresh and spent 1 wt% catalyst are shown in **Figure 5.2.4**. The oxygen regions all contain the main lattice oxygen peak (530 eV) and the hydroxide oxygen peak (531.4 eV), whilst the spent catalyst from the deoxygenated reaction also has a third peak at 533 eV. The third peak could imply the formation of a carboxylate due to it also being observed in spectra of cinnamic acid on TiO₂ (**Appendix**

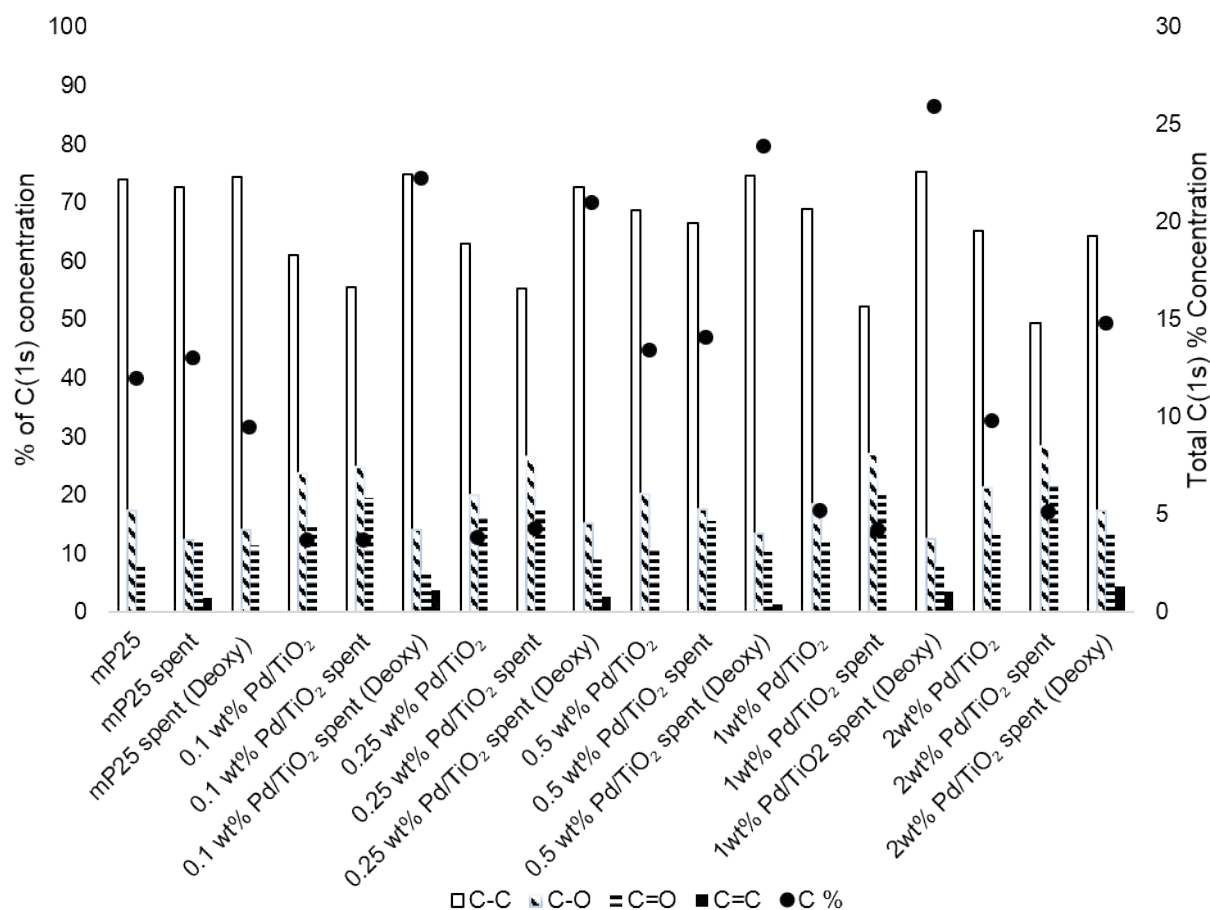
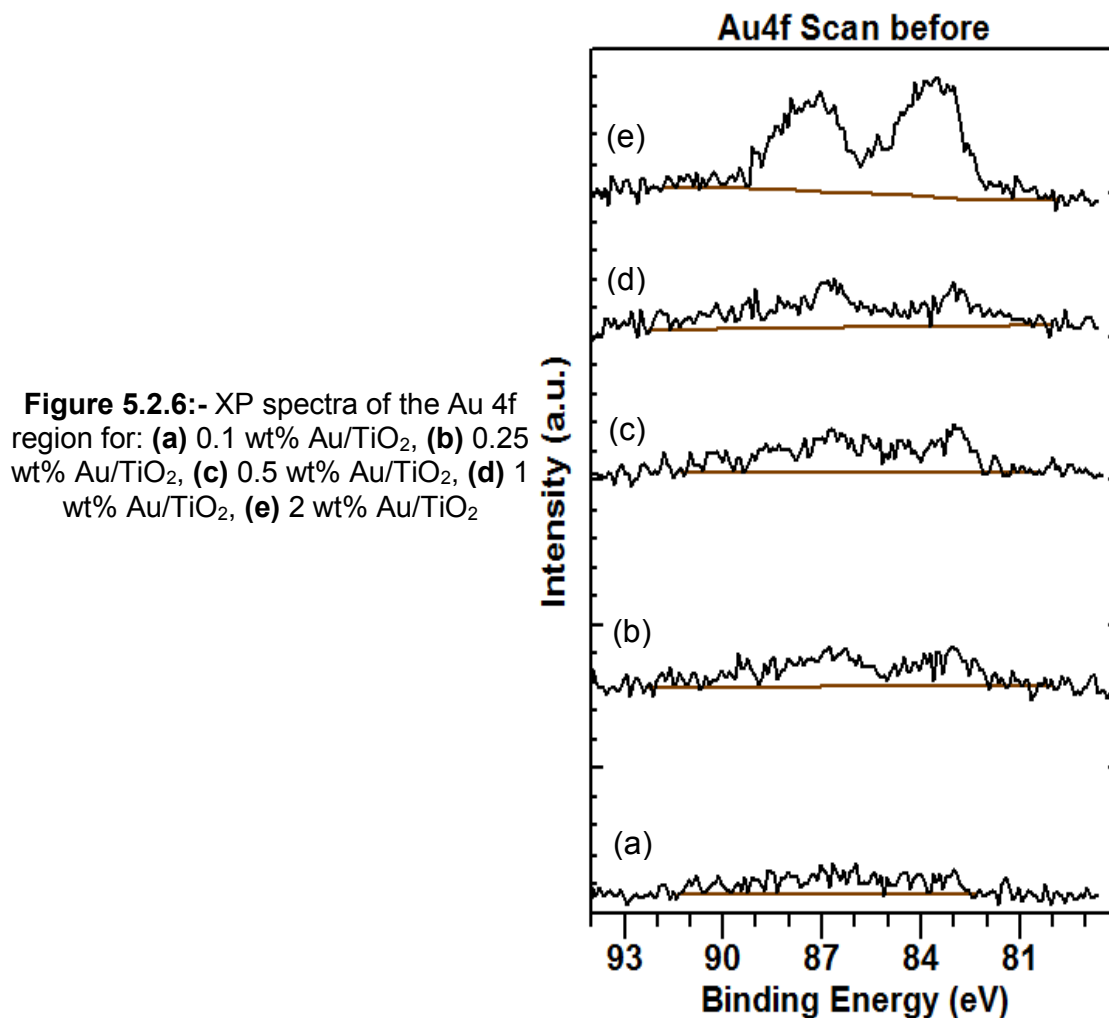


Figure 5.2.5:- The % concentration of the carbon environments (left axis) and the total amount of carbon detected in the sample (black dot, right axis) for the fresh and spent palladium catalysts

3.1), or alternatively it may indicate carbonate on the surface. This trend was common across all palladium containing catalysts. The carbon regions all contain three core peaks; the C-C peak (284.6 eV), the C-O peak (286.0 eV) and the C=O peak (288.8 eV). However, the spent catalyst from deoxygenated conditions also has a fourth peak at 291.6 eV that is probably a π - π^* transition indicating some level of delocalisation is occurring across the carbon. The trends in the carbon spectra are shown in **Figure 5.2.5**. In the absence of palladium, oxygenated reaction conditions cause a slight increase in the total carbon present and the appearance of a small π - π^* transition, whereas in deoxygenated conditions there is a small drop in total surface carbon present and the π - π^* transition is absent. Opposing trends are observed when palladium is present however. In oxygenated conditions, the total carbon stays at relatively similar values, or drops somewhat, while the percentage of C-C species present drops in favour of the oxygen-containing C-O and C=O functionalities suggesting that the carbon is being oxidised to give carbon species with a greater degree of oxygen. After

| | % Concentration | | | | | |
|---|-----------------|--------|--------|---------|---------|---------|
| | Ti (2p) | O (1s) | C (1s) | Pd (3d) | Au (4f) | Cl (2p) |
| mP25 Spent | 26.6 | 60.5 | 13.0 | | 0 | 0 |
| mP25 Spent (Deoxy) | 27.8 | 62.8 | 9.44 | | 0 | 0 |
| 0.1wt% Pd/TiO ₂ , spent | 29.5 | 66.6 | 3.7 | 0.2 | / | 0 |
| 0.1wt% Pd/TiO ₂ , spend (Deoxy) | 23.3 | 54.3 | 22.2 | 0.2 | / | 0 |
| 0.25wt% Pd/TiO ₂ , spent | 29.4 | 65.6 | 4.3 | 0.3 | / | 0 |
| 0.25wt% Pd/TiO ₂ , spend (Deoxy) | 23.5 | 55.2 | 21.0 | 0.4 | / | 0 |
| 0.5wt% Pd/TiO ₂ , spent | 25.8 | 59.0 | 14.1 | 0.6 | / | 0.2 |
| 0.5wt% Pd/TiO ₂ , spend (Deoxy) | 22.4 | 52.7 | 23.9 | 0.7 | / | 0 |
| 1wt% Pd/TiO ₂ , spent | 29.0 | 65.3 | 4.2 | 1.3 | / | 0.2 |
| 1wt% Pd/TiO ₂ , spend (Deoxy) | 20.9 | 50.7 | 25.9 | 1.9 | / | 0.3 |
| 2wt% Pd/TiO ₂ , spent | 28.0 | 64.0 | 5.1 | 2 | / | 0.5 |
| 2wt% Pd/TiO ₂ , spend (Deoxy) | 19.2 | 57.5 | 14.8 | 3.5 | / | 0.3 |
| 0.25wt% Au/TiO ₂ , spent | 27.6 | 62.9 | 8.9 | / | 0.1 | 0.2 |
| 0.25wt% Au/TiO ₂ , spend (Deoxy) | 24.2 | 55.5 | 20.0 | / | 0.1 | 0.1 |
| 1wt% Au/TiO ₂ , spent | 29.3 | 65.4 | 4.2 | / | 0.1 | 0.8 |
| 1wt% Au/TiO ₂ , spend (Deoxy) | 23.3 | 53.1 | 23.1 | / | 0.1 | 0.5 |

Table 5.2.3:- XPS atomic % concentrations for the spent catalysts



reaction in deoxygenated conditions several changes occur; a significant rise is observed in the total carbon percentage, the amount of carbon in the C-C environment rises at the expense of the C-O/C=O species, and a π - π^* transition develops. This suggests that photocatalytic reactions in the absence of oxygen are depositing aliphatic or aromatic carbon species on the catalyst surface, which may be occurring because the absence of oxygen is inhibiting oxidation of aromatic structures. The π - π^* transition is also observed in XP spectra of cinnamic acid (**Appendix 3.1**), potentially indicating the signal measured here is the result of aromatic ring structures.

Gold

All fresh gold catalysts were analysed using XPS, as well as select spent catalysts. Quantification only found small quantities of gold during analysis; where the surface concentration did not exceed 0.2 %, for any loading, despite increasing amounts of chlorine

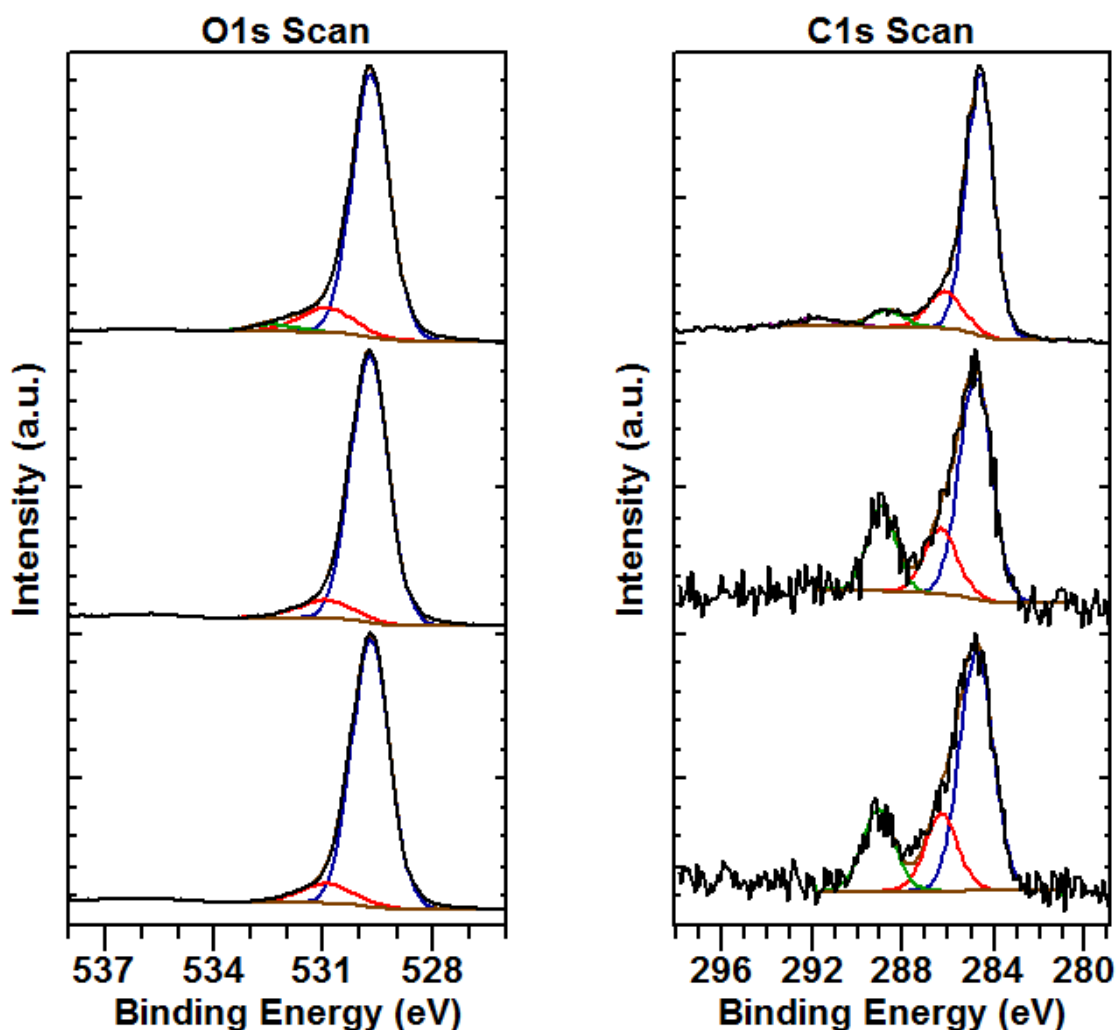


Figure 5.2.7:- XPS spectra of the O 1s and C 1s regions for: (a) fresh 1 wt% Au/TiO₂, (b) spent 1 wt% Au/TiO₂, (c) spent 1 wt% Au/TiO₂ (Deoxy)

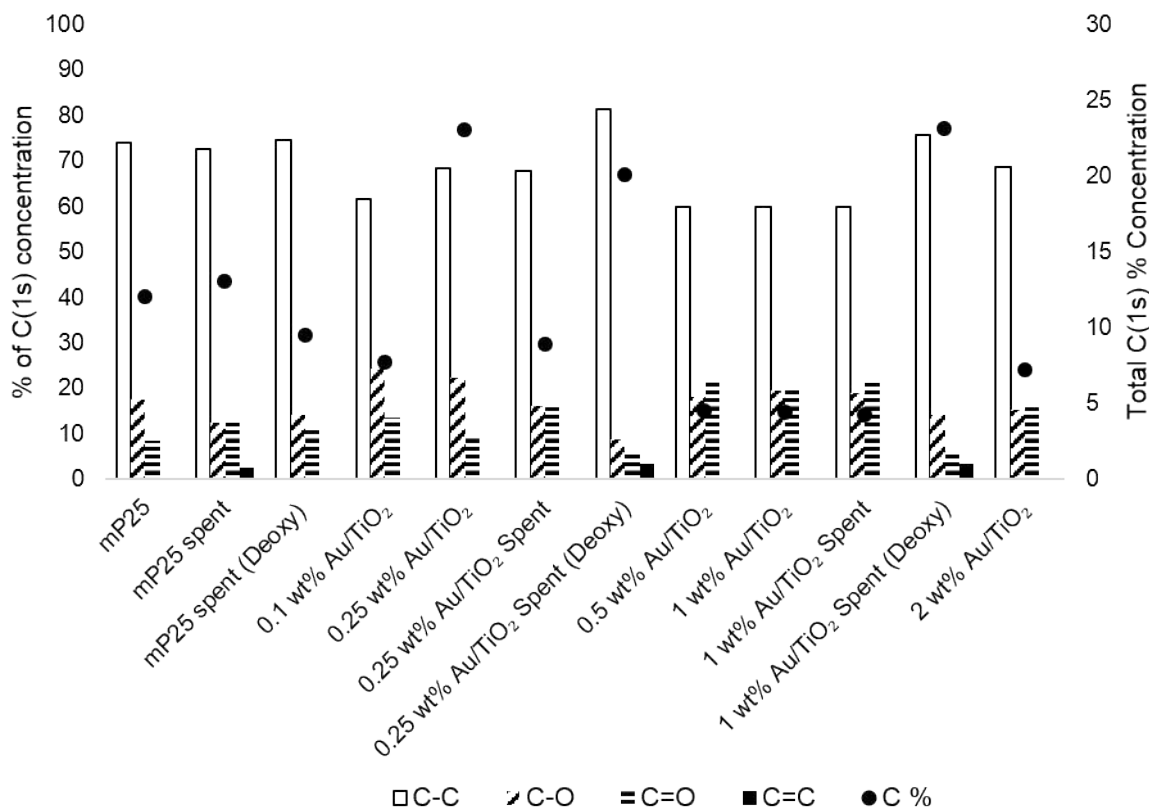


Figure 5.2.8:- The % concentration of the carbon environments (left axis) and the total amount of carbon detected in the sample (black dot, right axis) for the fresh and spent gold catalysts being detected. The Au 4f narrow scans, in **Figure 5.2.6**, show that only 2 wt% Au/TiO₂ (**Figure 5.2.6 (e)**) produced a spectrum with any semblance of a peak. Curiously, the freshly made powders becoming increasingly purple/blue as the intended loading increases, suggesting that the gold is present but XPS is unable to detect it. A possible explanation is that the gold deposits as large particles that results in the gold mostly existing in the bulk. This could also explain why the UV/vis analysis found no visible light sensitization, because the gold plasmon bandgap increases with increasing particle diameter. [10] Further, the chloride concentration increases in the same way as is observed with palladium, again suggesting the metal deposition should be increasing.

Examination of the oxygen 1s and carbon 1s regions offers the same trends and features as those observed with palladium. The oxygen 1s regions of fresh and spent catalysts all share the oxygen lattice (529.7 eV) and hydroxide oxygen (530.9 eV) peaks but the spent catalyst, from the deoxygenated reactions, also have a third peak (532.4 eV) that may be caused by carbonates (**Figure 5.2.7**) The carbon region also shows the same peaks for the fresh and spent catalysts; with **Figure 5.2.8** containing the percentage of each component and the total carbon present on the sample. The fresh Au/TiO₂ catalysts had carbon signals that

were composed of 60-70 % C-C, ~ 20% C-O and 20-10 % C=O character. Spent catalysts from the oxygenated conditions show little change from the fresh catalysts, either retaining or reducing the overall carbon content which is of similar composition. Although, the 0.25 wt% Au/TiO₂ fresh catalyst had a high overall carbon content, probably due to contamination or extended exposure to air. The spent 0.25 wt% catalyst from oxygen containing conditions showed a large reduction in overall carbon which is almost certainly due to the photocatalytic process oxidising much of the adventitious carbon layer off.

5.2.4 DRIFTS-FTIR

FTIR spectroscopy of the fresh and spent palladium catalysts did not reveal many vibrations. **Figure 5.2.9** shows representative examples of infrared spectra obtained for fresh and spent palladium catalysts. **Figure 5.2.9 (a)** shows that the fresh catalyst only had two identifiable peaks at 3700 and 1636 cm⁻¹. 3700 cm⁻¹ could be assigned to a surface bound hydroxyl species, [11] whilst 1636 cm⁻¹ is the water bending mode. Spent catalysts from deoxygenated conditions, **Figure 5.2.9 (c)**, had a vibration at 1406 cm⁻¹ that may indicate the presence of carbonates on the surface.

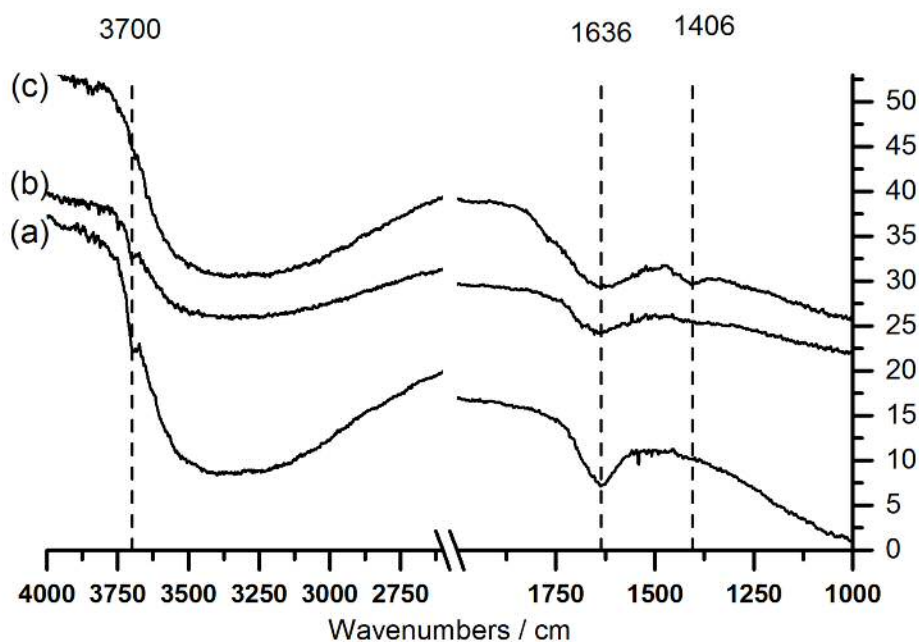


Figure 5.2.9:- FTIR DRIFTS for: (a) fresh 1 wt% Pd/TiO₂, (b) spent 1 wt% Pd/TiO₂, (c) spent 1 wt% Pd/TiO₂ (deoxy)

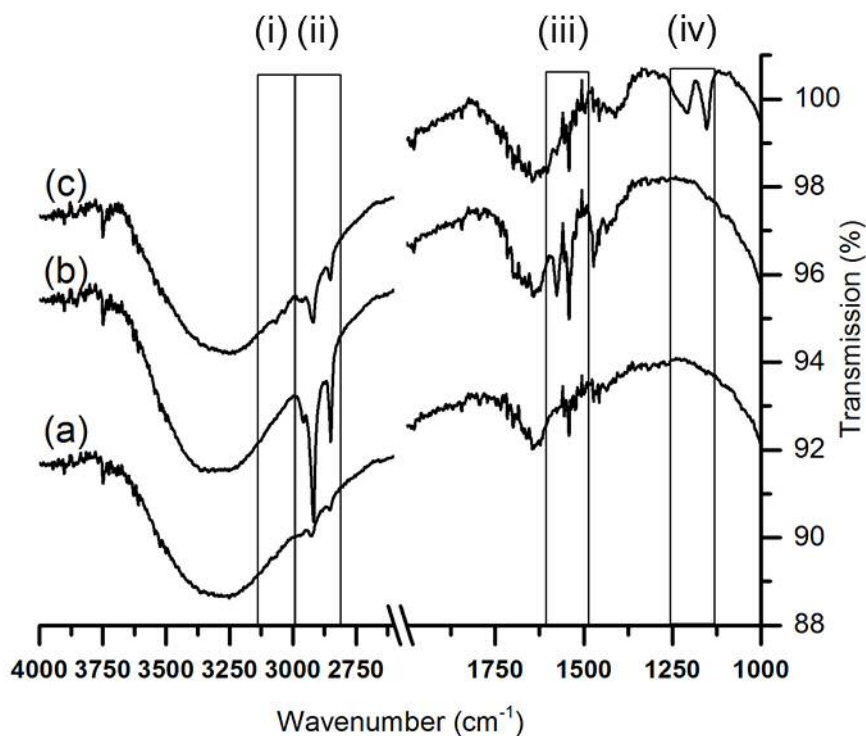


Figure 5.2.10:- FTIR DRIFTs for: **(a)** fresh 1 wt% Au/TiO₂, **(b)** spent 1 wt% Au/TiO₂, **(c)** spent 1 wt% Au/TiO₂ (deoxy)

Spectra of the fresh and spent gold catalysts were more informative about the species present on the catalyst surface. **Figure 5.2.10** shows the fresh **(a)**, and spent catalysts from the oxygenated **(b)** and deoxygenated **(c)** reactions. Four areas of interest have been identified, marked (i) – (iv), due to the notable differences between the spectra. Area (i) contains the vibrations for aromatic C-H stretches. **(c)** is the only spectra to have peaks populating this area, at 3067 and 3035 cm⁻¹, indicating the presence of aromatic ring structures. Area (ii) contains the aliphatic C-H stretches which are present in all three samples. The peaks resonate at 2957, 2919 and 2851 cm⁻¹ and can be assigned to antisymmetric CH₃, antisymmetric CH₂ and symmetric CH₃ stretching, respectively. All of which are usually observed after organic degradation has occurred on the catalyst surface as noted in **Chapter 3**. The weak signals in the fresh catalyst **(a)** are present due to the adventitious carbon layer that develops on powders exposed to air. However the significant increase in intensity of the stretches in this region, for the oxygenated spent catalyst **(b)**, signify that a large proportion of the carbon identified on the surface from XPS is derived from the advanced oxidation procedure that has resulted in the formation of short chained aliphatic species. Despite the large increase in carbon content on the surface, the spent catalyst from the deoxygenated conditions does not exhibit the same intensity for the

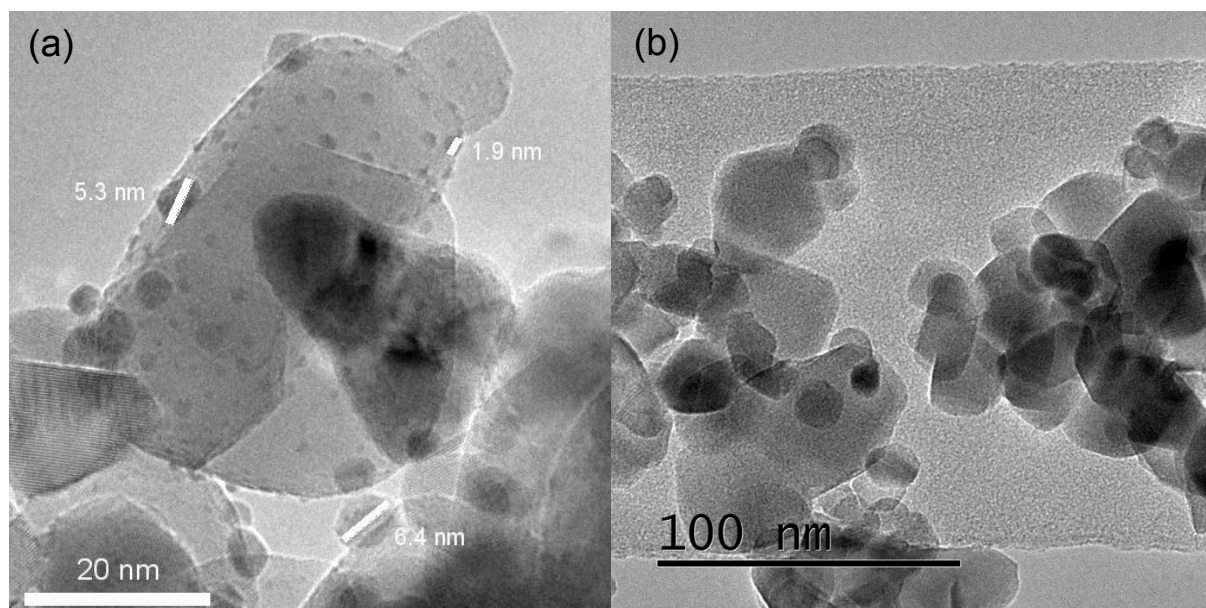


Figure 5.2.11:- TEM images for **(a)** fresh 1 wt% Pd/TiO₂ and **(b)** fresh 1 wt% Au/TiO₂ aliphatic C-H stretching frequencies much of the carbon still exists in the aromatic form. The carbonyl region contains a number of weak peaks that are difficult to discern. It is notable that the oxygenated spent catalyst bears the peaks of greater intensity, than the deoxygenated spent catalyst, indicating the presence of more carbonyl functionalities. Region (iii). 1500 – 1600 cm⁻¹, is a region that is often associated with aromatic C=C skeletal vibrations. However, here the most intense bands are observed at 1575 and 1543 cm⁻¹ for the oxygenated spent catalyst **(b)**, a sample that aromaticity is not expected to be present. The intensity of the two bands in this region contrasts with the absence of aromatic C-H stretches indicating that may be a symptom of other vibrations, perhaps related to interactions with the gold nanoparticles. The only sample to exhibit vibrational modes in region (iv) is the deoxygenated spent catalyst. The vibrations are at a frequencies of 1213 and 1158 cm⁻¹, vibrational modes we previously ascribed to C-O and C-C stretching modes that were indicative of the presence of alcohol functionalities.

5.2.5 Transmission Electron Microscopy Particle Size Study

Fresh catalyst samples were analysed using transmission electron microscopy to ascertain the nanoparticles' average diameter. **Table 5.2.1** shows the average palladium nanoparticle size for all loadings. Increasing weight loading, from 0.25 to 2 wt%, was found to correlate to an increase in average nanoparticle size. Although 0.1 wt% Pd/TiO₂ had an $A_{VNP} = 1.6 \pm 0.12$ nm, larger than 0.25 wt%, due to the small sample size (21 particles) which is evident from the size of the standard error associated with it. A_{VNP} for the other weight loadings were based on a minimum of 100 particle measurements. 0.25 and 0.5 wt%

had average nanoparticle sizes of 1.3 ± 0.04 and 1.7 ± 0.06 nm, the small size of the error owing to the larger sample size and high uniformity of the nanoparticles. 1 wt % showed a large increase, on 0.5 wt%, to 2.8 ± 0.12 and 2 wt% had an average size of 3 ± 0.14 nm. The large standard error for the two higher loading catalysts was due to the higher variation in particle size on both catalysts, 6.8 and 7.6 nm respectively. **Figure 5.2.11 (a)** shows a representative TEM image of a Pd/TiO₂ catalyst, a range of palladium nanoparticle sizes are observed, from 1.9 to 6.4 nm, and easily imaged. It was not possible to measure the average nanoparticle measurements for the gold catalysts. **Figure 5.2.11 (b)** shows a representative example of a Au/TiO₂ catalyst produced by incipient wetness. There is no sign of the titania support being doped with small gold nanoparticles, from any weight loading, leading to the conclusion that the particles are either very large and hard to locate or not present.

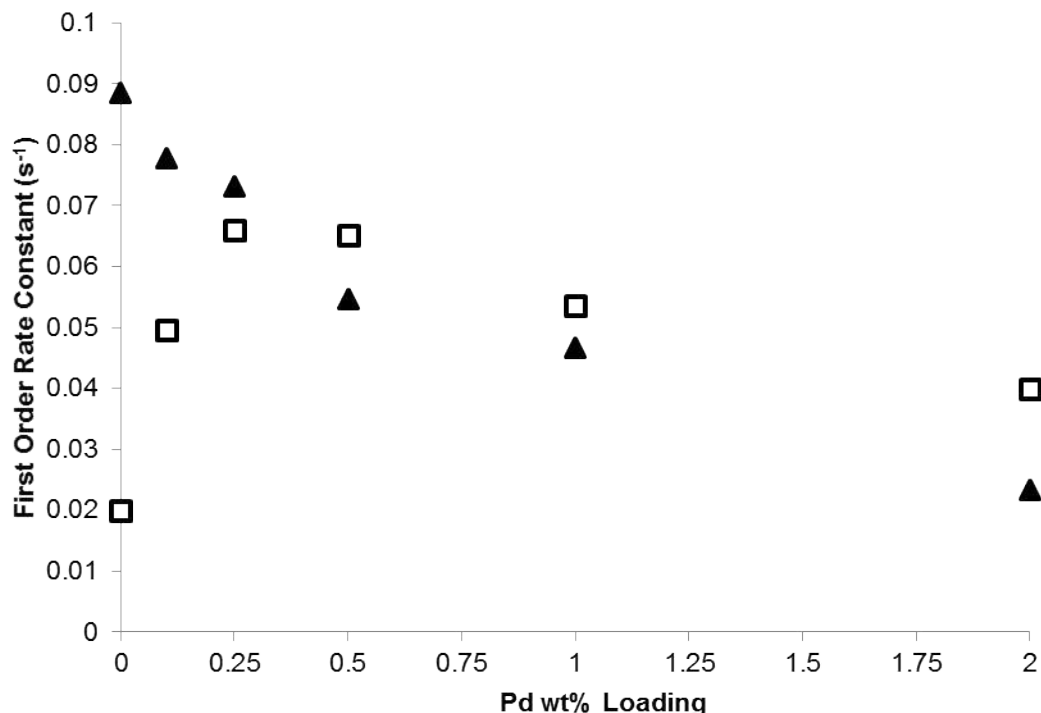
5.3 Results

All of the catalysts were tested on the photocatalytic degradation of cinnamic acid to ascertain what impact the changes of metal loading had in oxygenated and deoxygenated conditions. “Deoxygenated conditions” denote reactions where N₂ gas was flowed through the reaction mixture throughout the reaction to purge the molecular oxygen present, whereas “oxygenated conditions” denotes reactions where the N₂ gas flow was absent.

5.3.1 The Photoactivity of Palladium Catalysts

5.3.1.1 Kinetic Impact

Figure 5.3.1 shows the effect of palladium loading on the first order rate constants under oxygenated (triangles) and deoxygenated (hollow squares) conditions, the exact values of the first order rate constants are shown in **Table 5.3.1**. The non-metal doped mP25 removed cinnamic acid at a rate of 0.089 s^{-1} , whilst flowing N₂ resulted in the significant drop in degradation to 0.02 s^{-1} . In the presence of oxygen palladium acts as an inhibitor to the rate of degradation, an effect that is detectable even at the lowest weight loading of 0.1 wt% that yields a degradation rate of 0.078 s^{-1} . Further increases in weight loading result in further inhibition where the highest weight loading, 2 wt%, decreases the rate to 0.023 s^{-1} . In deoxygenated conditions, however, adding palladium causes an increase in the rate constant. 0.1 wt% Pd/TiO₂, under N₂ flow, exhibited a rate constant of 0.05 s^{-1} ; 2.5 times faster than the plain mP25 photocatalyst. 0.25 wt% gave the fastest rate, under deoxygenated conditions, of 0.066 s^{-1} followed closely by 0.5 wt% that had a rate of 0.065 s^{-1} . Higher weight loadings, than 0.5 wt%, causes an inhibiting impact that decreases the rate to 0.04 s^{-1} for 2 wt%



5.3.1:- First order rate constants for the palladium catalysts, in oxygenated (hollow squares) and deoxygenated (triangles) conditions plotted against the weight loadings

Pd/TiO₂. As shown in **Figure 5.3.1**, the 0.5 – 2 wt% catalysts have faster rates in deoxygenated conditions than in oxygenated conditions, indicating that the presence of palladium is catalysing the degradation of cinnamic acid in the absence of oxygen. It should also be noted that dark tests showed no degradation of cinnamic acid via UV sampling, as well as the lack of intermediates in the gas chromatograms.

5.3.1.2 Mechanistic Impact

Investigation into the mechanistic impact of the changes in palladium weight loading found some interesting changes. **Table 5.3.1** contains the selectivity for the intermediates benzaldehyde (**2**), phenylacetaldehyde (**3**) and acetophenone (**4**) at the 30 and 180 minute mark, whilst **Figures 5.3.2** and **5.3.3** show the concentration profiles for **2** and **3** under oxygenated and deoxygenated conditions, respectively. The concentration of **2** is impacted by the increasing palladium weight loading in oxygenated conditions, shown in **Figure 5.3.2 (a)**, where the concentration maximum decreases from 3.6 mg/L with mP25 to <0.5 mg/L with 0.5 wt% or greater. The selectivity for **2** in the absence of palladium is 5.6% after 30 minutes, and continuously falls as palladium loading increases until the selectivity is <0.5%. The rate at which **2** is formed and removed does appear to be linked to palladium concentration.

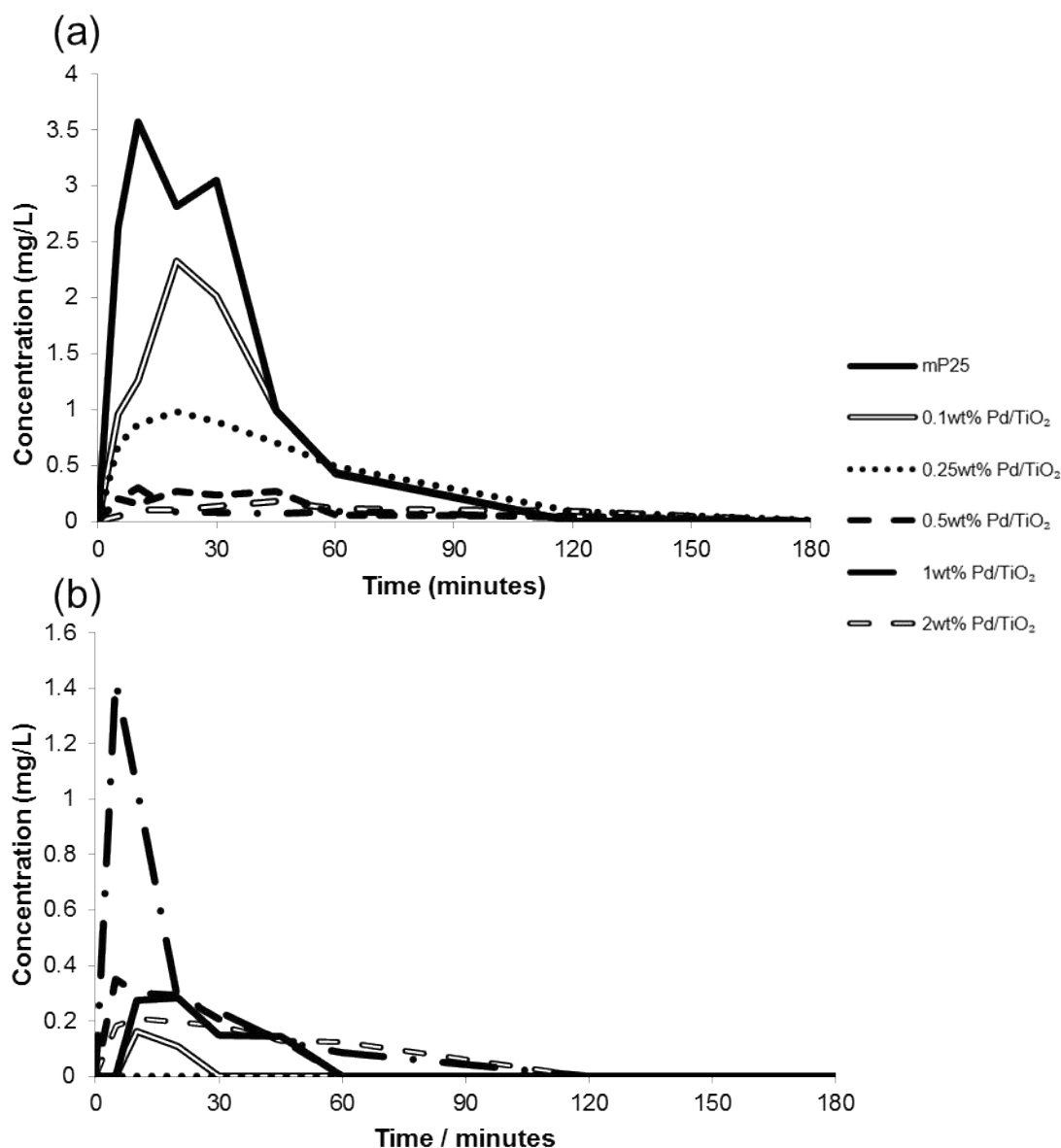


Figure 5.3.2:- Concentration profiles from Pd/TiO₂ oxygenated reactions showing the change in concentration of **(a)** benzaldehyde and **(b)** phenylacetaldehyde

Visible inspection of the concentration profiles suggests palladium causes a small reduction in the rate of formation, however the majority of **2** is destroyed after 120 minutes irrespective of palladium loading. Whilst the concentration of **3** is generally unaffected by the presence of palladium. Lower loadings of palladium, ≤ 0.5 wt%, tended to reduce the already low selectivity to **3** compared to mP25; although higher loadings had no effect. After 180 minutes all detectable intermediates were degraded in the presence of oxygen.

In the absence of oxygen, **2** is not produced in anything but trace amounts illustrating requirement for oxygen in the formation that was discussed in **Chapter 3**. This indicates that

palladium cannot introduce alternative pathways for form **2**. Selectivity to **3**, however, is promoted by the absence of oxygen and the presence of palladium. **Table 5.3.1** shows that selectivity for **3**, by mP25, is 1.5% after 30 minutes which rises to 3.4 % after 180 minutes. Introducing palladium in lower loadings, < 0.5 wt%, enhances the selectivity for **3** which results in small improvements in selectivity to 3.9 % after 180 minutes. Higher loadings, ≥ 0.5 wt%, progressively decrease the selectivity to below 1%.

Acetophenone (**4**) is also detected occasionally during the reaction. Its formation in the reaction is clearly linked to the presence of chloride on the reaction surface, although the detection limits of **4** resulted in infrequent and the almost random appearance of it in the GC

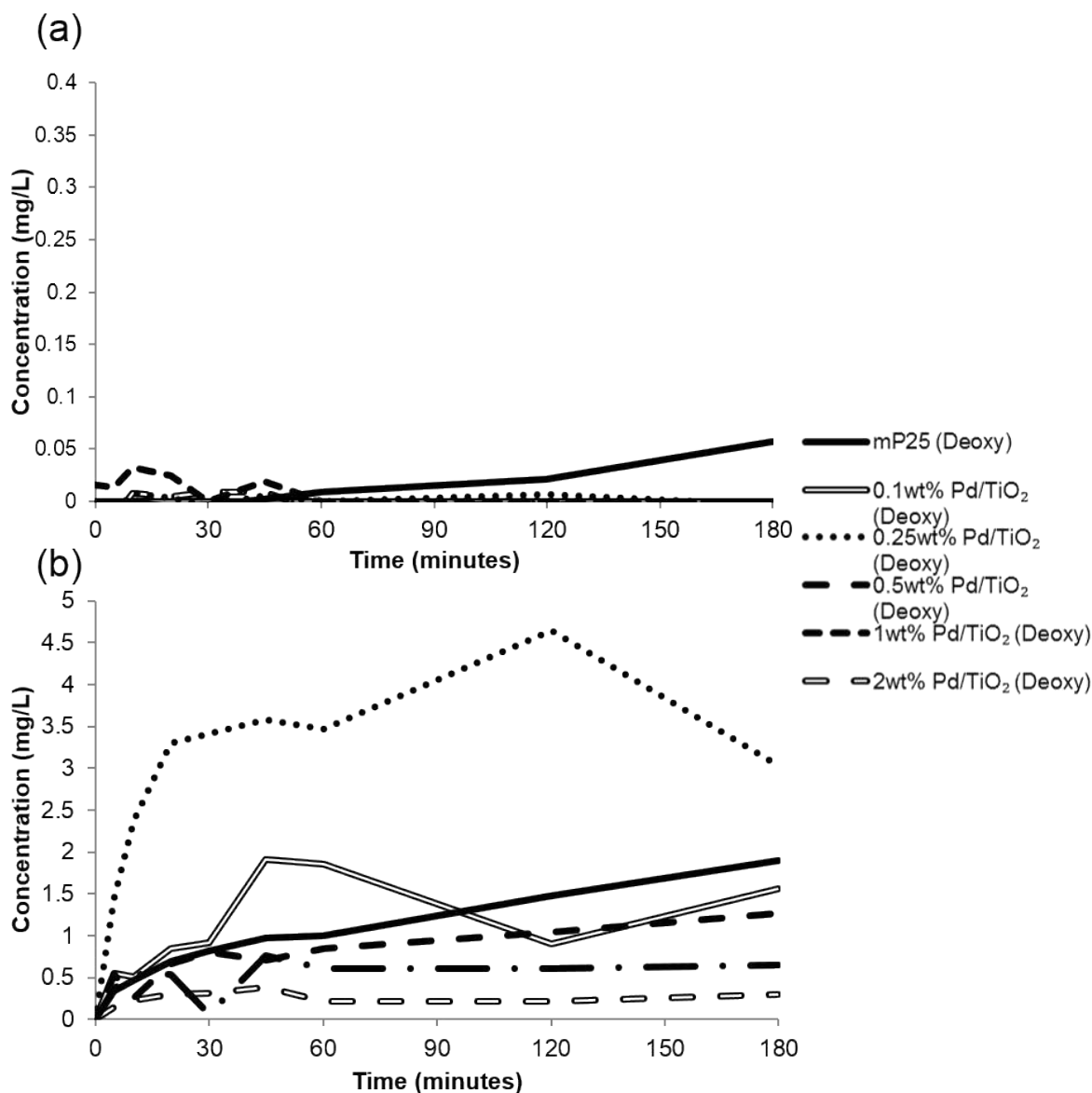


Figure 5.3.3:- Concentration profiles from Pd/TiO₂ deoxygenated reactions showing the change in concentration of (a) benzaldehyde and (b) phenylacetaldehyde

| | N ₂ Flow | 1 st Order Rate constant k (s ⁻¹) | S2 (%) | | S3 (%) | | S4 (%) | |
|------------------------------|---------------------|--|--------|-------|--------|-------|--------|-------|
| | | | t=30 | t=180 | t=30 | t=180 | t=30 | t=180 |
| mP25 | N | 0.089 | 5.6 | 0 | 0.3 | 0 | / | / |
| | Y | 0.02 | 0 | 0.1 | 1.5 | 3.4 | / | / |
| 0.1 wt% Pd/TiO ₂ | N | 0.078 | 3.5 | 0 | 0 | 0 | 0 | 0 |
| | Y | 0.05 | 0 | 0 | 1.8 | 3.0 | 0 | 2.22 |
| 0.25 wt% Pd/TiO ₂ | N | 0.073 | 1.6 | 0.02 | 0 | 0 | 2.08 | 0 |
| | Y | 0.066 | 0 | 0 | 2.6 * | 3.9 | 0 | 0 |
| 0.5 wt% Pd/TiO ₂ | N | 0.055 | 0.4 | 0 | 0.4 | 0 | 0 | 0 |
| | Y | 0.065 | 0 | 0 | 1.5 | 2.4 | 2.03 | 2.39 |
| 1 wt% Pd/TiO ₂ | N | 0.047 | 0.2 | 0 | 0.5 | 0 | 2.13 | 0 |
| | Y | 0.054 | 0 | 0 | 0.7 | 0.7 | 0 | 0 |
| 2 wt% Pd/TiO ₂ | N | 0.023 | 0.3 | 0 | 0.4 | 0 | 2.41 | 0 |
| | Y | 0.04 | 0.02 | 0 | 0.6 | 0.6 | 2.86 | 2.74 |
| 0.1 wt% Au/TiO ₂ | N | 0.055 | | | | | | |
| | Y | 0.015 | | | | | | |
| 0.25 wt% Au/TiO ₂ | N | 0.052 | 2.0 | 0 | 0 | 0 | 0 | 0 |
| | Y | 0.019 | 0 | 0 | 8.3 | 20.2 | 0 | 0 |
| 0.5 wt% Au/TiO ₂ | N | 0.06 | | | | | | |
| | Y | 0.019 | | | | | | |
| 1 wt% Au/TiO ₂ | N | 0.045 | 1.0 | 0.01 | 0 | 0 | 0 | 0 |
| | Y | 0.034 | 0 | 0.07 | 3.3 | 5.0 | 0 | 0 |
| 2 wt% Au/TiO ₂ | N | 0.062 | | | | | | |
| | Y | 0.036 | | | | | | |

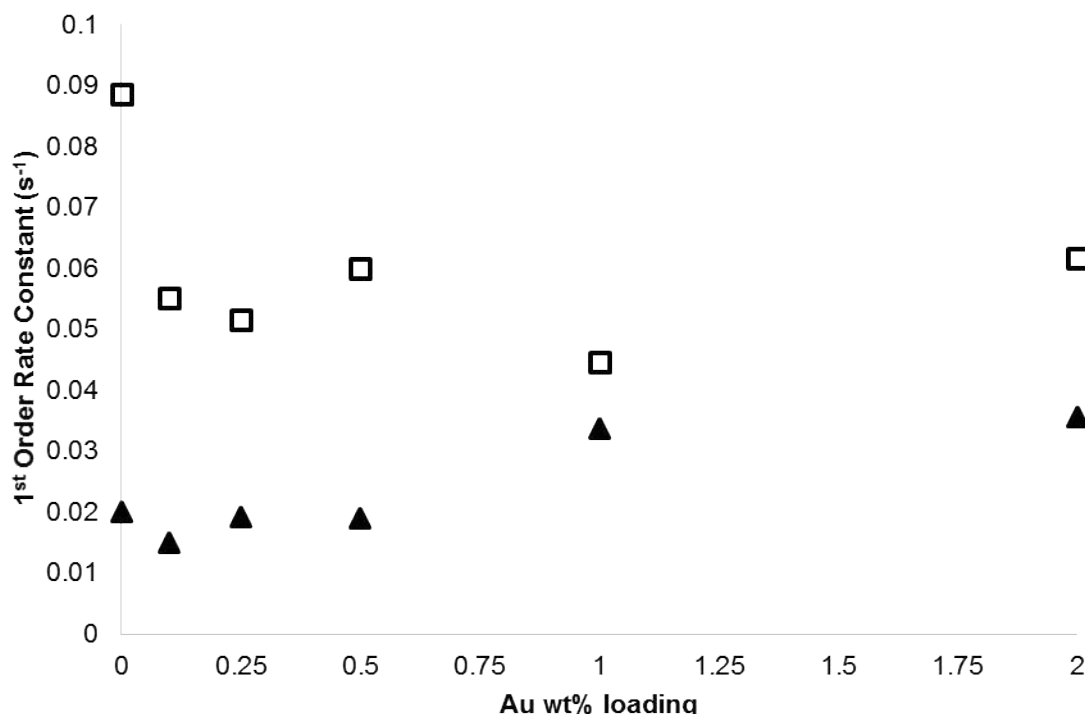
Table 5.3.1:- First order rate constants and the percentage selectivity for the intermediates: benzaldehyde (**2**), phenylacetaldehyde (**3**) and acetophenone (**4**)

traces. The detection limit results in its detection only at concentrations about 1.5 mg/L which equates to 2% or greater selectivity. 4 is more commonly detected at higher palladium loadings, as shown in **Table 5.3.1**, and also more frequently present in deoxygenated conditions.

5.3.2 The Photoactivity of Gold Catalysts

5.3.2.1 Kinetic Impact

The effect of gold metal loading is shown in **Figure 5.3.4**, with the measured first order rate constant values being found in **Table 5.3.1**. In oxygenated conditions, all gold loadings produced a similar inhibitory effect on the removal rate of cinnamic acid, an effect that did not increase with increasing loading. The rate constant decreases to 0.055 s^{-1} for 0.1 wt% Au/TiO₂, and all subsequent tests on the different catalyst loadings produced rates between 0.05 and 0.065 s^{-1} . In deoxygenated conditions increasing gold loading induced some promotion in cinnamic acid degradation, but only in the higher loading catalysts. 0.1 to 0.5 wt% Au/TiO₂ gave rates that fluctuate around the 0.02 s^{-1} value found for mP25 in deoxygenated conditions.



5.3.4:- First order rate constants for the gold catalysts, in oxygenated (hollow squares) and deoxygenated (triangles) conditions, plotted against the weight loadings

1 and 2 wt% Au/TiO₂ showed an increase in activity, having rate constants of 0.034 and 0.036 s⁻¹.

5.3.2.2 Mechanistic Impact

Figure 5.3.5 (a) and **(b)** show the effect of gold on the production of **2** and **3** respectively. Due to the kinetics indicating the only change in activity, as the amount of gold increased, in oxygenated and deoxygenated conditions occurred from 0.5 to 1 wt%, it was decided that only two loadings would be tested for mechanistic effects because of time constraints. As such, 0.25 and 1 wt% were chosen to examine to examine the full mechanistic impact. **2** appeared to be progressively inhibited as gold concentration increased. **Figure 5.3.5 (a)** shows the concentration maximum is lower, 1.8 and 1 mg/L for 0.25 and 1 wt%, and is reached later in the reaction in comparison to mP25. Additionally, the apparent rate of removal of **2** is also impacted by the gold. **2** is only completely removed by 180 minutes, whereas mP25 and Pd/TiO₂ removes **2** completely by 120 minutes. Formation of **3** is not promoted by gold in oxygenated conditions, an intermediate that is rarely observed during degradation with Au/TiO₂ catalysts. **Table 5.3.1** shows that the selectivity to **3** is 0% after 30 and 180 minutes with both catalysts. During deoxygenated conditions, production of **2** is significantly inhibited. Neither catalyst tested formed **2** in anything but trace amounts. **3**, however, was detected in much greater amounts. Despite the slow degradation rate of cinnamic acid, **3** was formed with a selectivity of 8.3 and 20.2%, after 30 and 180 minutes respectively, when 0.25 wt% Au/TiO₂ was used. The faster degradation rate of cinnamic acid found with 1 wt% Au/TiO₂ was coupled with the lower selectivity of 3.3 and 5% after 30 and 180 minutes respectively. The concentration is not observed to drop during deoxygenated reactions with gold, indicating the rate of destruction of **3** never exceeds the rate of formation. Unlike palladium containing catalysts, **4** was not detected during the reactions with gold despite the presence of chloride on the surface.

5.3.3 Carbon Dioxide Capture Experiments

A set of reactions were performed to track CO₂ evolution to establish how the co-metals might affect total oxidation and steps involving CO₂ formation. **Figure 5.3.6** shows the data obtained for these reactions. As discussed in **Chapter 3**, reactions involving mP25 result in the formation and release of CO₂ at a rate of 1.6 μmol/min, which begins after 30 minutes of reaction, and results in the 100% of the carbon being released as CO₂ after 3 hours. Whereas, under deoxygenated conditions CO₂ was released at a rate of 0.13 μmol/min where just 8.6% of the carbon is released after 3 hours. In reactions with 0.5 wt% Pd/TiO₂,

CO₂ is detected in considerable amounts after 30 minutes, being evolved at a rate of 1.7 μmol/min. The amount of CO₂ detected was also observed to increase over 100% of what is expected from cinnamic acid degradation, reaching 113% after 150 minutes. In the absence of oxygen the CO₂ evolution is slowed similarly to reactions with mP25, although after 180 minutes 30% of the carbon is detected in the gas phase. 0.5 wt% Au/TiO₂ exhibits similar behaviour to the palladium analogue; detection of 30% of CO₂ after 30 minutes as well as more CO₂ than expected being detected. After 180 minutes the percentage of CO₂ in the gas phase is >140%. In deoxygenated conditions the Au/TiO₂ catalyst, again like the palladium analogue, exhibits significantly reduced CO₂ evolution where just 13.9% is detected after 180 minutes.

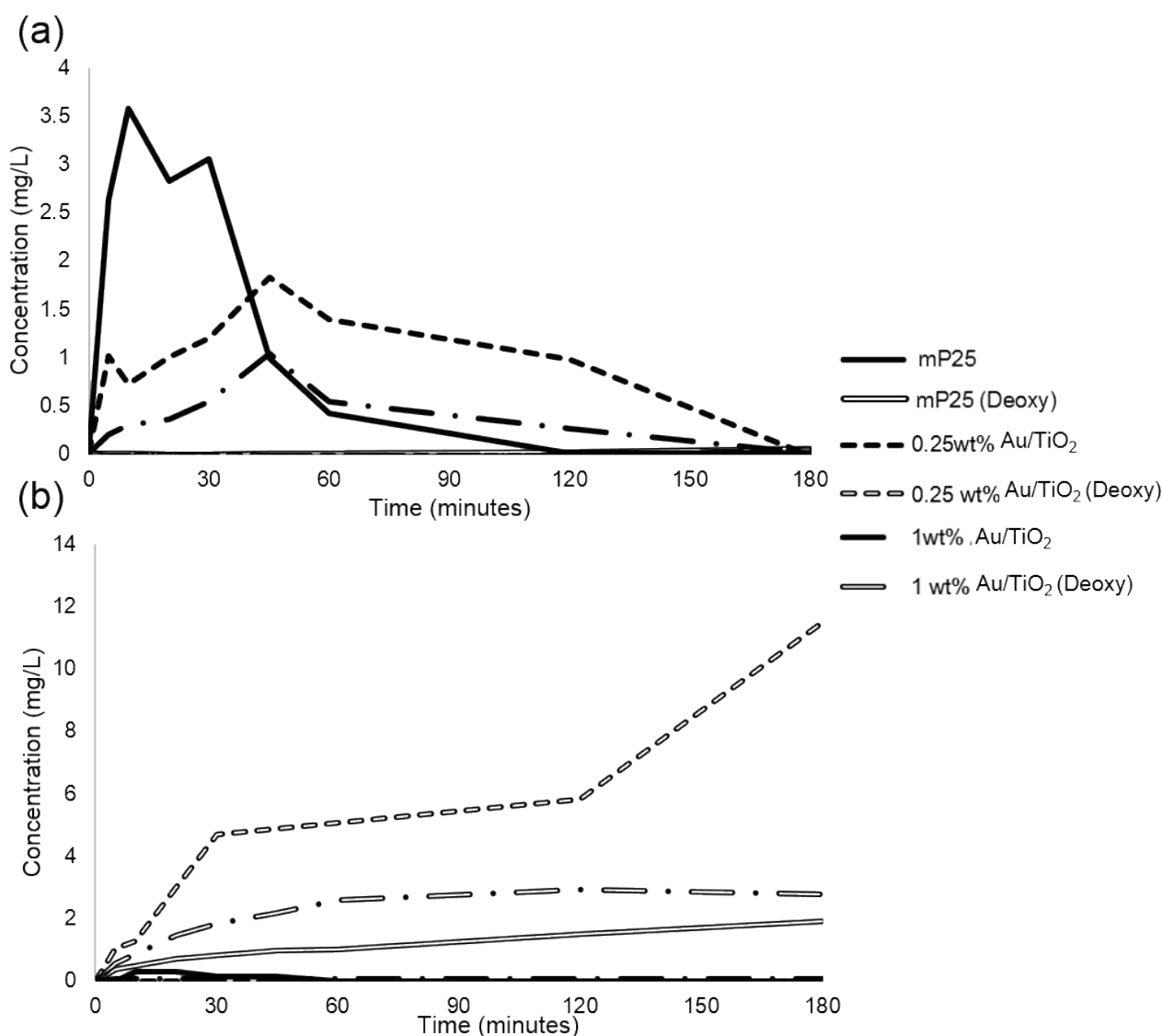


Figure 5.3.5:- Concentration profiles for (a) benzaldehyde and (b) phenylacetaldehyde in oxygenated and deoxygenated conditions

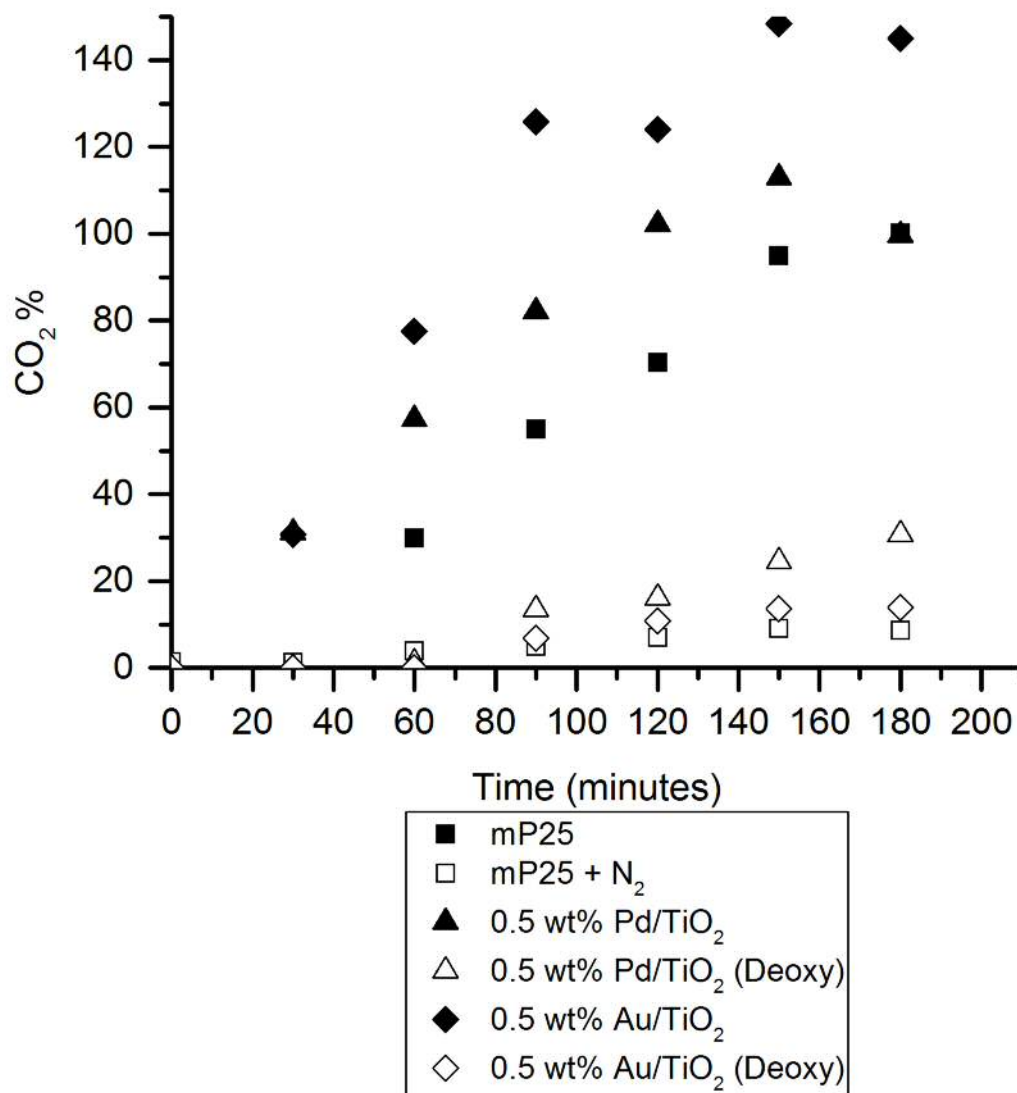


Figure 5.3.6:- Percentage CO₂ evolution during the degradation of cinnamic acid by various photocatalysts.

The percentage is based on the expected amount of CO₂ if 100% of the cinnamic acid present is mineralised.

5.4 Discussion

5.4.1 Pd/TiO₂ Catalysts

Characterisation of the palladium catalysts has shown that incipient wetness is an effective technique in forming relatively small nanoparticles supported on the titania support. Firstly, UV/Vis spectroscopic analysis indicated that increasing the loading of palladium resulted in the concurrent shortening of the bandgap. Some reports have suggested palladium

is not capable of improving visible light activity, [12] however other reports have also stated palladium can introduce accessible states within the titania bandgap that results in a smaller bandgap. [13] It is evident here that we are observing a small and steady red shift induced by palladium doping, although the impact of this shift towards visible light absorption has not been tested in these studies. It is not known if this shift is related to nanoparticle size, however it is more probable that the amount of palladium present is responsible for the change in absorption. X-ray diffraction patterns indicated that palladium initially decreases the calculated crystallite size. Increasing the palladium loading was coupled with an increase in crystallite size, for both the anatase and rutile phases present. Based on the trends observed here this changing crystallite size is probably not linked to the bandgap shortening.

The reactivity data clearly indicates that palladium is a negative influence on the degradation pathways in the presence of oxygen. However, in the absence of oxygen, palladium promotes the degradation of cinnamic acid. We know from the literature [14] and our work in **Chapter 3** that, in the presence of oxygen, cinnamic acid degrades via the benzaldehyde mechanism using molecular oxygen. **Figure 5.3.2** and **Table 5.3.1** show the clear correlation between the degradation rate constant and the formation of **2**; that increasing the loading of palladium decreases the maximum amount of **2** detected, although the rate of formation and destruction of **2** appears relatively unaffected. It is understood that the benzaldehyde mechanism proceeds via a surface oriented mechanism. As such, one could make the assertion that the presence of palladium on the catalyst surface is blocking surface sites that are important to the primary degradation mechanism. The blocking of surface sites causes a greater negative impact than the improved electron-hole separation induced by the introduction of Schottky junctions. Although palladium is inhibiting the initial degradation of cinnamic acid, it does not slow the rate of total oxidation of organic carbon. CO₂ evolution

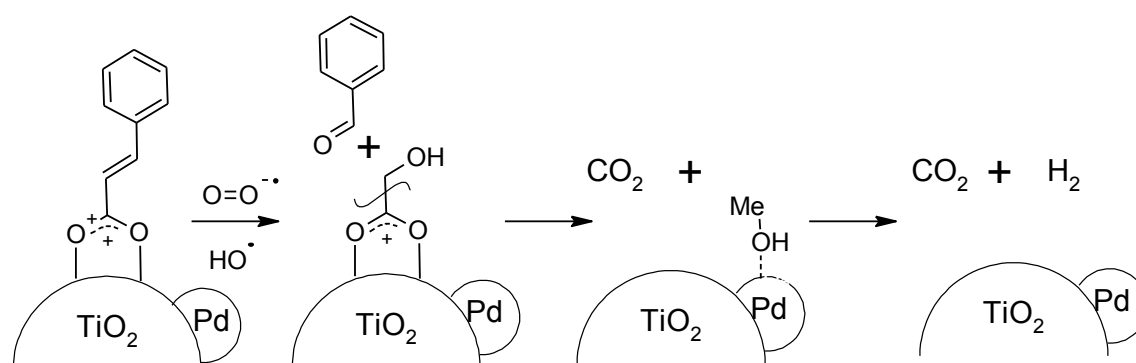


Figure 5.3.7:- Proposed mechanism showing the superoxide driven cleavage of the C=C bond of cinnamic acid, followed by the palladium driven oxidation of the cleaved carbon

occurs immediately upon irradiation, suggesting the co-metal is enhancing oxidation of the carbon deposited after the cleavage of the C=C bond. Palladium has previously been identified as an effective oxidiser of alcohol fragments during water splitting. [15] Therefore a possible mechanism to explain the increased CO₂ evolution despite slower degradation rates is shown in **Figure 5.3.7**. After the cleavage of the C=C, the remaining C₂O₃ species decarboxylates and forms a methanol fragment that adsorbs to a palladium nanoparticle and is oxidised to CO₂ and H₂. XPS has found that, in the absence of palladium, a small build-up of carbon is observed after the reaction; a phenomenon that does not occur during oxygenated conditions when Pd/TiO₂ catalysts are used. Carbon levels either remain at the levels they were before reaction or display a drop in surface concentration. This suggests that palladium facilitates mechanistic steps not possible with mP25, such as the “cleaning” of the carbon off of the surface that **Figure 5.3.7** is proposed to explain. It is also possible that metals, like palladium, behaving as “electron sinks” could inhibit the formation of radical oxygen species like the superoxide radical anion. Superoxide is largely believed to be formed from the reduction of molecular oxygen by shallow trapped electrons in TiO₂. [16][17] Trapping electrons at palladium centres, instead, may result in the reduced formation of the superoxide radical if molecular oxygen is less likely to be reduced by electrons located on the palladium. However XP spectral analysis, **Figure 5.2.3**, shows that reactions in oxygenated conditions caused a greater degree of deactivation to palladium metal than deoxygenated conditions. This suggests electrons are being retained in the palladium particles and not being transferred to other species, like O₂, which contrasts with the hypothesis that electrons could be transferring from the palladium centres. Future work would be required to provide a full explanation for this behaviour.

In the absence of oxygen palladium behaves as a promoter in the degradation of cinnamic acid. All loadings of palladium were more effective in degrading the molecule; with 0.25 wt% and 0.5 wt% being the most proficient, giving rates of 0.066 s⁻¹ and 0.065 s⁻¹ respectively. GCMS data indicated the improved degradation generally occurred in conjunction with greater amounts of **3** being detected and the near complete inhibition of **2** formation. The formation of **3** was previously asserted to occur through a hydroxyl radical mechanism that may occur in solution. The most obvious source of enhancement to degradation can be attributed to the improved electron-hole pair separation due to the presence of Schottky junctions between the titania support and palladium co-catalyst. More effective charge separation would then translate to a greater amount of hydroxyl radicals

forming that can degrade cinnamic acid to **3**. XP spectra indicate that reactions in deoxygenated conditions results in a large increase in carbon present on the catalyst surface, and that the carbon has a notable change in character compared to spent catalysts from oxygenated conditions. **Figure 5.2.5** shows that the carbon present after deoxygenated reactions has less oxygen functionality, which is replaced by a greater degree of C-C character and the presence of a $\pi - \pi^*$ transition. The carbon deposition implies that the lack of molecular oxygen reduces the catalyst capability to remove the carbon via oxidation, and additionally that the reaction to **3** could be occurring on the surface of the catalyst. Identification of surface compounds, via FTIR analysis, did not provide much information. The peak at 1406 cm^{-1} , in **Figure 5.2.9**, could indicate a small amount of carbonate on the surface; however the infrared spectra obtained for all spent palladium catalysts were inconclusive for identifying any surface functionalities.

It is also observed that only in reactions with 0.25 wt% Pd/TiO₂ was the formation of **3** seen to increase above that of mP25. 0.5 wt% exhibits a similar degradation rate to 0.25 wt% but lower concentrations of **3** are detected in solution. Similarly, both 1 and 2 wt% degrade cinnamic acid at twice the rate of mP25, but only half the concentration of **3** is detected during the reaction. How can this occur? In photocatalytic degradation reactions of this nature, the indiscriminate nature if the photocatalyst means the newly formed intermediates are often subject to degradation after formation. As such, it indicates that palladium is also catalysing the degradation of **3**. CO₂ capture experiments indicated that 30% of the expected carbon is released after 180 minutes, over three times the amount observed in the absence of palladium. This higher rate of CO₂ evolution indicates the degradation of **3** is occurring, a reaction that was not observed to occur in the absence of oxygen with mP25, suggesting palladium facilitates aldehyde degradation. However, no intermediates are detected via GCMS and so the route that the degradation follows is unknown. Additionally, most proposed routes for aldehyde degradation involve molecular oxygen or the superoxide radical anion aiding the oxidation to the carboxylic form, which are not present in deoxygenated conditions. [18][19] A possibility for degradation could revolve around alcohol degradation pathways as illustrated in **Figure 5.3.8**. [15] Aldehydes, like ketones, can tautomerise to its enol form; a process that is encouraged by the presence of features, such as aromatic groups and extended conjugation systems, which stabilise the tautomeric form. So there is potential for the tautomeric form of **3**, 2-phenylethanol, to interact with the palladium nanoparticles and decarboxylate to a toluene radical species

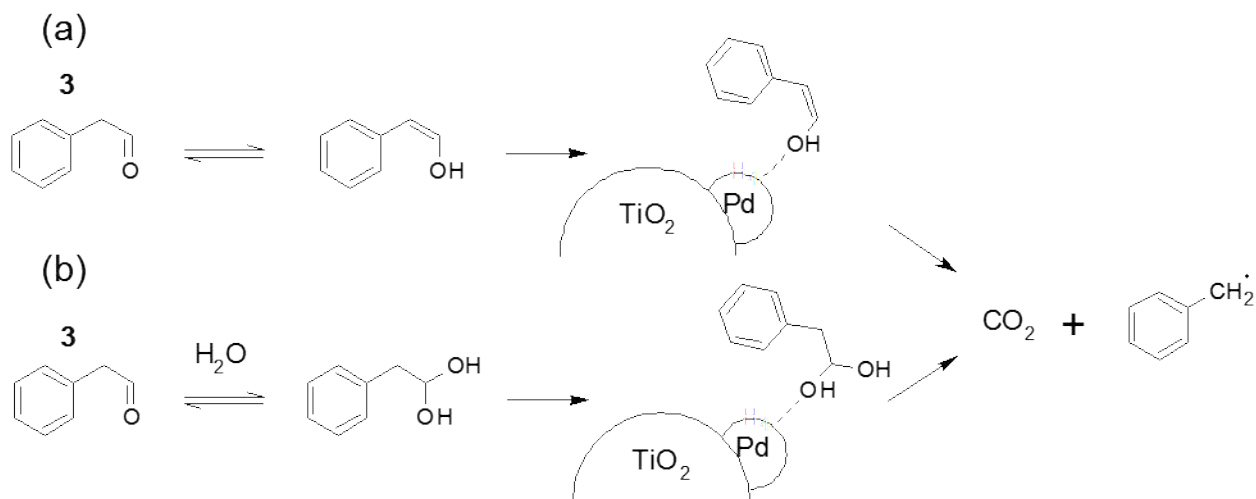


Figure 5.3.8:- Proposed mechanisms for the oxidation of phenylacetaldehyde (**3**) by Pd/TiO₂ photocatalysts.

(**Figure 5.3.8 (a)**). Alternatively, some aldehydes oxidise through a diol intermediate which could be the species that interacts with palladium (**Figure 5.3.8 (b)**). Unfortunately, the column used in the GC-MS was not suited to detecting toluene and other methods of intermediate analysis were not utilised to ascertain whether toluene formed. It should also be noted that palladium has been found to increase removal rates of toluene in the gas phase. [23] However one of the intermediates from toluene was found to be benzaldehyde; although an increase in 2 wasn't observed here it would arguably be formed in such low quantities that it would be difficult to discern if it was forming via this pathway.

5.4.2 Au/TiO₂ Catalysts

Characterisation of gold showed that it did not deposit as small nanoparticles, as was observed with palladium. During TEM analysis no gold particles were found, and XPS indicated very low surface concentrations of gold regardless of the intended weight loading. The chloride concentration is measured at concentrations greater than 1% for all fresh catalysts, which would indicate the gold should be depositing with it. The colour of the catalyst themselves, **Figure 5.3.9**, suggests gold is being deposited in amounts greater than the XPS is detecting. This leads us to the assumption that the gold is either depositing in large nanoparticles, >50 nm, or sintering during the calcination step. This would explain the low gold concentrations found by XPS, because the large gold particles are preventing the majority of the gold from being detected due to the small penetration depth of the technique.

Au/TiO₂ catalysts also didn't promote cinnamic acid degradation in oxygenated conditions. 0.1 wt% caused a drop in the rate constant to 0.055 s⁻¹ and the higher loading materials all fluctuated around this value. Evidently, increasing amounts of gold did not offer

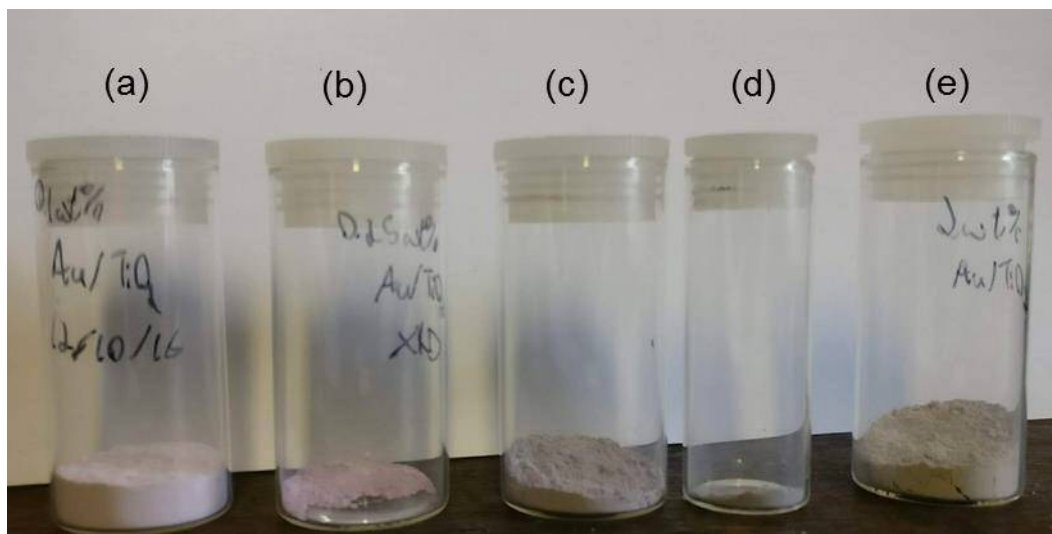


Figure 5.3.9:- The colour of the gold containing catalysts: **(a)** 0.1 wt% Au/TiO₂, **(b)** 0.25 wt% Au/TiO₂, **(c)** 0.5 wt% Au/TiO₂, **(d)** 1 wt% Au/TiO₂, **(e)** 2 wt% Au/TiO₂

positive or negative effects to the degradation mechanisms. Since it was concluded that gold was depositing as very large particles, increasing amounts of gold would probably just form even larger particles. It is commonly reported that the most effective nanoparticle size for selective oxidation and photocatalytic mineralisation is between 3 and 6 nm. [4][20][21][24] The size of the nanoparticles, we suspect are forming here, far exceed the optimal sizes reported by others. This would explain why increasing gold loading does not result in progressive changes as observed for the palladium analogues, as the particle size is already far beyond the optimal size. Importantly, the nature and frequency of the Schottky junctions present are key to improving the photocatalytic efficiency. Due to gold forming very large nanoparticles here the frequency of Schottky junctions is significantly reduced compared to equivalent loadings with small, <10 nm, nanoparticles. Besides this reducing the benefits associated with incorporating Schottky junctions into a material, the Schottky barrier for gold has experimentally been shown to be size dependent. [2]

Mechanistically it is difficult to draw many concrete conclusions from the data without using assumptions based on the palladium work. Increasing gold loading from 0 to 1 wt% caused a drop in detected amounts of **2**, similarly to with palladium catalysts. The drop in observed formation of **2** cannot be explained in the same way as it was for Pd catalysts, because the gold is not occupying significant amounts of surface sites that will block cinnamic acid adsorption. Surface chloride concentrations are also reasonably similar so this is unlikely to be an inhibiting factor, **4** was also not detected during reactions and so would not be in competition with the benzaldehyde pathway. By a process of elimination it therefore

reasonable to assume the inhibition could be related to a reduced photocatalytic activity from the oversized gold nanoparticles. Although, further work is required to support this explanation. **3** is sometimes observed, in small amounts, in oxygenated conditions. A reduction in the formation of **3** could be a symptom of the decreased charge separation assumed to be occurring due to the presence of large gold nanoparticles. The supporting characterisation data suggests similar mechanistic behaviour to palladium. XP spectra showed that oxygenated conditions always produced catalysts with around 5% overall carbon content, of which the carbon character was around 70% C-C with the remaining 30% being split between C-O and C=O. If the carbon content was initially high, as it was for 0.25 wt% Au/TiO₂, then the carbon was essentially “cleaned” off of the surface leaving a carbon layer that was lower in surface coverage but bared a resemblance in character. IR spectra displayed strong vibrations in the aliphatic C-H region, a weak population of peaks in the carbonyl region and two peaks at 1575 and 1543 cm⁻¹ that are usually indicative of aromatic skeletal stretches. Assigning the latter two peaks as skeletal stretches would contrast with the absence of aromatic C-H vibrations, especially considering the intensity of the peaks, although it is possible that the aromatic stretches are covered by the broad O-H stretch. The data does indicate that the 50 ppm of cinnamic acid is not completely oxidised after 3 hours of reaction, so there is potential for these aromatic frequencies to be related to cinnamic acid or perhaps benzaldehyde. However, **Appendix 2.1** shows that the carbonyl vibration modes of cinnamic acid and benzaldehyde are both stronger than the aromatic C=C skeletal vibrations. More work will need to be performed to adequately explain the significance of this IR data.

Further unexplainable data appears in the CO₂ capture experiments. Repeat experiments found <100% of the expected carbon was evolved during the course of the oxygenated reaction, despite no significant carbon deposits being identified on the 0.5 wt% catalyst before the reaction. The data shows large amounts of CO₂ being evolved after 30 minutes of reaction, similar to the palladium analogue reactions, but the CO₂ continues to evolve at a high rate which results in around 140% of the expected CO₂ to be detected in the gas phase. The anomalous results could be due to difficulties in the gas calibration, however this issue will need to be addressed in future work.

Lower catalyst loadings, 0.1 to 0.5 wt%, and deoxygenated conditions reduced the rate of cinnamic removal to the same rate observed for mP25 in the absence of oxygen. This suggest that the large gold nanoparticles were not offering any benefits to the titania support. Increasing the loading to 1 and 2 wt% did display some improved degradation rates, with

rates increasing to 0.034 and 0.036 s⁻¹ respectively. Some reports have indicated 2 wt% to be an optimal loading for gold related photocatalysis, but the nanoparticles in these studies have been considerably smaller than ours so it is difficult to compare them. The introduction of deoxygenated conditions was coupled with a stark increase in the detection of **3**, as shown in **Figure 5.3.5 (b)**. 0.25 wt% showed the greatest selectivity for **3**, 20.2% after three hours of reaction, whilst the slightly increased rate of 1 wt% Au/TiO₂ brought on a lower selectivity of 5 % after three hours. The improved selectivity occurring alongside reduced activity suggests that the lack of oxygen is inhibiting the benzaldehyde mechanism, whereas the gold is inhibiting the mechanism by which **3** degrades. Additionally, just 14% of the expected carbon is released after 3 hours, indicating just over one carbon of cinnamic acid is transformed into CO₂ per molecule. Gold has been found to enhance selectivity during photocatalysis by influencing the absorption kinetics of the catalyst; in the case of phenol degradation, it favourably desorbed hydroquinone once hydroxylation had occurred and resulted in an improved selectivity for hydroquinone. [7] It is therefore possible that gold is slowing the degradation of **3** by discouraging the adsorption of **3** once it has formed. An alternative explanation could lie in the difference surface chemistry of the catalyst system. It is unclear whether gold is capable of the same oxidative pathways associated with palladium and alcohols. If gold is not capable of them, then this could be an important factor as to why the catalysts are less effective than palladium in removing **3**, therefore improving the selectivity for it. Even if gold is capable of such reactions, the large particles believed to be present here would have a notably lower surface area than the smaller palladium nanoparticles. This would in turn reduce the number of surface sites capable of engaging in this reaction pathway. XP spectra indicate similar behaviour is occurring between the gold and palladium catalysts. For the spent gold catalysts from deoxygenated conditions, we observed the same rise in carbon with largely C-C character that also had a small π - π^* transition; which suggests similar surface behaviour is occurring. FTIR data found evidence of aliphatic and aromatic C-H stretches, as well as some C-C or C-O bends. The latter could suggest some alcohol functionality, although it is also probable that one of the vibrations is present due to the C-C bonds in the aliphatic chain of **3** that is still present in solution after 180 minutes.

Overall more work is required to ascertain the exact effects of gold loading on the degradation of cinnamic acid. In particular, a more appropriate deposition method is needed to deposit smaller nanoparticles of comparable size to those formed in the Pd/TiO₂ photocatalysts. Gold is known to have some very size dependent attributes including the

wavelength that LSPR effects come into effect, [3][4] and the Schottky barrier height. [2][22] As such it would be very beneficial to future research to utilise gold nanoparticles that are smaller than 10 nm.

5.5 Conclusions

These studies have investigated some important facets involving the gold and palladium assisted degradation of cinnamic acid. Incipient wetness was shown to effectively disperse palladium nanoparticles on the P25 support; producing a series of different sized nanoparticles as the metal loading increased. Pd/TiO₂ catalysts were found to be ineffective photocatalysts for the degradation of cinnamic acid in oxygenated conditions, due to the palladium particles reducing the amount of available surface sites for cinnamic acid to bind to and inhibiting the benzaldehyde mechanism by which the majority of cinnamic acid degrades through. In deoxygenated conditions the palladium catalysts displayed degradation rates up to three times faster than the palladium free titania. Rate promotion was coupled with an increase in formation of phenylacetaldehyde which was attributed to the enhanced charge separation due to the introduction of Schottky barriers. The palladium also catalysed the degradation of phenylacetaldehyde, resulting in an increase in CO₂ evolution. Two different mechanisms for this degradation were proposed and depicted in **Figure 5.3.8 (a)** and **(b)**. The first, **(a)**, involves the tautomerisation of phenylacetaldehyde to 2-phenylethanol and the subsequent adsorption to palladium, where decarboxylation occurs. The second, **(b)**, is based on the equilibrium of the aldehyde with water. The diol then undergoes a similar decarboxylation, as **(a)**, to form toluene. This work ultimately illustrates the possibility to use palladium based photocatalysts in waste water treatment where the low oxygen content or high BOD/COD would significantly hinder photocatalytic degradative processes.

Whereas, incipient wetness was shown to be a very ineffective preparation technique for photocatalysts used in degradation experiments. The colour of the catalyst and levels of chlorine suggested gold had deposited, but XP spectra showed little surface gold and TEM found no particles. It was assumed the gold was depositing as large particles (>50 nm) or sintering during calcination. Testing found that gold deposition inhibited the degradation of cinnamic acid in oxygenated conditions, however increasing loading did not exacerbate this inhibition. Based on the assumption of large gold nanoparticles being present, we argued that the increasing gold loading resulted in larger nanoparticles or more large nanoparticles that were not chemically distinct. In deoxygenated conditions the gold did not enhance cinnamic

acid degradation until the gold loading reached 1 wt% or greater. Gold was found to cause a 6 fold increase in selectivity for phenylacetaldehyde, potentially by discouraging the surface based degradation by which it is oxidised. Au/TiO₂, synthesised by incipient wetness, was found to be an ineffective photocatalyst for the total mineralisation of cinnamic acid. Although it did show promise in improving the selectivity in low oxygen conditions.

5.6 References

1. R. T. (• • □ . Tung, *Applied Physics Reviews*, 2014, **1**, 011304.
2. Y. Maeda, M. Okumura, S. Tsubota, M. Kohyama and M. Haruta, *Applied Surface Science*, 2004, **222**, 409–414.
3. P. M. Kowalski, M. F. Camellone, N. N. Nair, B. Meyer and D. Marx, *Phys. Rev. Lett.*, 2010, **105**, 146405.
4. D. Tsukamoto, Y. Shiraishi, Y. Sugano, S. Ichikawa, S. Tanaka and T. Hirai, *J. Am. Chem. Soc.*, 2012, **134**, 6309–6315.
5. X. Zhang, Y. L. Chen, R.-S. Liu and D. P. Tsai, *Rep. Prog. Phys.*, 2013, **76**, 046401.
6. B. K. Min, J. E. Heo, N. K. Youn, O. S. Joo, H. Lee, J. H. Kim and H. S. Kim, *Catalysis Communications*, 2009, **10**, 712–715.
7. Y. Ide, R. Ogino, M. Sadakane and T. Sano, *ChemCatChem*, 2013, **5**, 766–773.
8. J. Tauc, R. Grigorovici and A. Vancu, *phys. stat. sol. (b)*, 1966, **15**, 627–637.
9. J. Tauc, *Materials Research Bulletin*, 1970, **5**, 721–729.
10. S. Link and M. A. El-Sayed, *J. Phys. Chem. B*, 1999, **103**, 4212–4217.
11. S. H. Szczepankiewicz, A. J. Colussi and M. R. Hoffmann, *J. Phys. Chem. B*, 2000, **104**, 9842–9850.
12. O. Tahiri Alaoui, A. Herissan, C. Le Quoc, M. el M. Zekri, S. Sorgues, H. Remita and C. Colbeau-Justin, *Journal of Photochemistry and Photobiology A: Chemistry*, 2012, **242**, 34–43.
13. E. A. Obuya, W. Harrigan, D. M. Andala, J. Lippens, T. C. Keane and W. E. Jones, *Journal of Molecular Catalysis A: Chemical*, 2011, **340**, 89–98.
14. H. Maeda, H. Nakagawa and K. Mizuno, *Journal of Photochemistry and Photobiology A: Chemistry*, 2007, **189**, 94–99.
15. H. Bahruji, M. Bowker, P. R. Davies and F. Pedrono, *Applied Catalysis B: Environmental*, 2011, **107**, 205–209.

16. T. Berger, M. Sterrer, O. Diwald, E. Knözinger, D. Panayotov, T. L. Thompson and J. T. Yates, *J. Phys. Chem. B*, 2005, **109**, 6061–6068.
17. I. Kuznetsov, O. Kameneva, A. Alexandrov, N. Bityurin, P. Marteau, K. Chhor, C. Sanchez and A. Kanaev, *Phys. Rev. E*, 2005, **71**, 021403.
18. W. J. McElroy and S. J. Waygood, *J. Chem. Soc., Faraday Trans.*, 1991, **87**, 1513–1521.
19. T. Shi, W. Chang, H. Zhang, H. Ji, W. Ma, C. Chen and J. Zhao, *Environ. Sci. Technol.*, 2015, **49**, 3024–3031.
20. S. Zhu, S. Liang, Q. Gu, L. Xie, J. Wang, Z. Ding and P. Liu, *Applied Catalysis B: Environmental*, 2012, **119**, 146–155.
21. Y. Ide, M. Matsuoka and M. Ogawa, *J. Am. Chem. Soc.*, 2010, **132**, 16762–16764.
22. V. Subramanian, E. E. Wolf and P. V. Kamat, *J. Am. Chem. Soc.*, 2004, **126**, 4943–4950.
23. J. Kim, P. Zhang, J. Li, J. Wang and P. Fu, *Chemical Engineering Journal*, 2014, **252**, 337–345.
24. I. Tanabe, T. Ryoki and Y. Ozaki, *RSC Adv.*, 2015, **5**, 13648–13652.

Chapter 6 – Conclusions and Future Work

| | |
|---|-----|
| 6.1 The Effect of Salts on the Photocatalytic Degradation of Cinnamic Acid | 207 |
| 6.1.1 The Cinnamic Acid Photocatalysed Degradation Mechanism | 207 |
| 6.1.2 The Impact of Salts on the Degradation of Cinnamic Acid..... | 207 |
| 6.1.3 Future Considerations for Work | 208 |
| 6.2 Metal Doped Titania Nanotubes for the Photocatalytic Degradation of Organic Contaminants | 209 |
| 6.2.1 Titania Nanotubes and Their Photocatalytic Efficiency | 209 |
| 6.2.2 Ti/W Mixed Metal Oxide Nanotubes | 209 |
| 6.2.3 Gold and Palladium Doped Nanotubes..... | 210 |
| 6.2.4 Future Considerations for Work | 211 |
| 6.3 Metal Loaded Nanoparticles for Waste Water Treatment | 211 |
| 6.3.1 Palladium Photocatalysts | 211 |
| 6.3.2 Gold Photocatalysis | 212 |
| 6.3.3 Future Considerations for Work | 212 |
| 6.4 References | 212 |

6.1 The Effect of Salts on the Photocatalytic Degradation of Cinnamic Acid

6.1.1 The Cinnamic Acid Photocatalysed Degradation Mechanism

Cinnamic acid was found to degrade through two separate mechanisms. The first mechanism formed benzaldehyde (**2**) and was determined to be the mechanism by which most of the cinnamic acid is photocatalytically degraded through. Oxygen was confirmed to be a vital part in the mechanism; forming a superoxide radical and that nucleophilically attacks the C=C, cleaving it to form benzaldehyde in the manner proposed by Maeda *et al.* [1] Benzaldehyde is then hydroxylated and oxidised to CO₂, presumably through the same muconaldehyde ring cleavage pathway asserted from investigations into naphthalene and benzene photocatalytic oxidation. [2][3] The second, slower, pathway forms phenylacetaldehyde (**3**) via a mechanism that does not include molecular oxygen and likely occurs away from the catalyst surface. Phenylacetaldehyde degrades through intermediates that are not observed in GCMS, although CO₂ capture experiments indicated that it does not fully mineralise in the absence of O₂. The confirmation of these pathways illustrates the importance of molecular oxygen in the complete oxidative degradation of aromatic species, as industrial waste water often only contains low levels of oxygen.

6.1.2 The Impact of Salts on the Degradation of Cinnamic Acid

Sulfate and chloride are both common inorganic contaminants in industrial wastewaters from the palm oil and fishing industries, so the effect on the degradation of cinnamic acid was investigated. Sulfate caused no mechanistic deviations, although 80% of the carbon was mineralised to CO₂ after 3 hour of reaction. Sulfate is presumed to fill oxygen vacancies in the lattice and inhibit degradation by blocking cinnamic acid adsorption and FTIR found signs of sulfate interaction with surface bound carbonyl species. Chloride initiated faster degradation of cinnamic acid and GCMS found that it caused the formation of the new intermediates; acetophenone (**4**), 2-chloroacetophenone (**5**), 2'-chloroacetophenone (**6**) and 1,2-dibenzoylthane (**7**). The new intermediates formed in competition with the benzaldehyde mechanism, and it was determined the mechanistic steps required both oxygen and a radical chlorine species. The most plausible mechanism involved the superoxide radical species attacking across the C=C followed by the nucleophilic attack by the chlorine radical to form a possible chloro-peroxy intermediate that decarboxylates in preference to the cleavage of the C=C bond. Firstly a clean decarboxylation that forms 2-chloroacetophenone, or a

decarboxylation coupled with the loss of chloride. The latter leaves an acetophenone radical that can abstract a hydrogen to form acetophenone or dimerise to form 1,2-dibenzoylthane. 2'-Chloroacetophenone was the product of the photolysis of 2-chloroacetophenone where chlorination at the ortho position was the most favourable. The mechanistic changes resulted in only 25% of carbon was fully mineralised after 3 hours of reaction, indicating that chloride presents a real issue in the effort to total mineralisation of recalcitrant organic matter. Not only does it slow down the rate of oxidation, chloride produces more toxic chlorinated intermediates that will ultimately be more environmentally damaging.

6.1.3 Future Considerations for Work

A more comprehensive examination of the degradation mechanisms occurring in the presence of chloride would be very interesting. Firstly, the mechanism by which the suspected chlorine radical forms here would be very interesting to investigate. Presently, a number of publications have explored the reactivity of the chlorine atom produced from laser flash photolysis experiments, [4][5] and some publications have hinted at chloride radical species forming during heterogeneous photocatalysis; however no information currently exists to demonstrate how electron or hole mediated pathways could oxidise a chloride anion. Our evaluation of the literature in **Chapter 3 section 3.1.3** suggests that the radical may form from a hydroxyl radical driven mechanism; exploring this hypothesis with ESR techniques would yield interesting insights into the formation of these chlorine radicals and reveal if the photogenerated hole plays a direct role or not.

Further investigation of chlorine radical mechanisms in degradative process would also be insightful. Our data shows the chlorine radical mechanisms outcompete the oxygen radical driven pathways, opting to decarboxylate the molecule instead of cleaving the C=C bond. ¹⁸O studies and radical scavenging experiments would be very useful in confirming if the oxygen added during the benzaldehyde mechanism and the acetophenone mechanism have the same origin, and further what the exact origin is. Understanding this mechanism could provide valuable insight into selectively cleaving C-C bonds during photocatalysis and the selective oxidation to useful platform chemicals like benzaldehyde and acetophenone.

6.2 Metal Doped Titania Nanotubes for the Photocatalytic Degradation of Organic Contaminants

6.2.1 *Titania Nanotubes and Their Photocatalytic Efficiency*

Nanotubes, anodised for four different timescales, were successfully formed in ethylene glycol electrolyte and characterised in various ways. The nanotubes, anodised at all timescales, were found to be relatively inhomogeneous on their surfaces, containing regions of completely open nanotubes and regions where the tubes were blocked with “grassy” detritus or a thin titania layer. Photocatalytic testing was found to follow the trend: 8hr NT > 4hr NT > 1hr NT > 24hr NT \geq Ti/W NT. The trend was consistent throughout the reactions indicating the factors responsible for degradation in the liquid phase are also applicable to surface based degradation. Surface topography was determined to be the key factor for aqueous degradation, because tube length becomes irrelevant after 3 μm due to the limits of light penetration. [4] The longer the anodisation time, the wider the tubes pores; which allows a greater penetration depth of light and easier diffusion of pollutant molecules. However, FE-SEM showed 24 hour anodised tubes were often over grown and structurally weaker which resulted in the formation of valley structures that probably reduced photoactivity by restricting light penetration. Additional correlations suggested the larger crystallite sizes of the 4 and 8 hour nanotubes may have improved electron/hole charge separation and increased photoactivity. The rates measured here, even for the more photoactive 8 hour nanotubes, cannot currently compete with powdered P25 of an equal weight, partially due to the inability to develop mixed polymorph nanotubes to benefit from anatase-rutile synergistic effects. It should also be noted that the first two batches of nanotubes grown in ethylene glycol are not appropriate for use in a reactor; the structural weakness that results in cracking and detachment is problematic and is also noted to occur in other organic electrolytes like glycerol. [7]

6.2.2 *Ti/W Mixed Metal Oxide Nanotubes*

Addition of a tungsten salt to the anodisation mixture resulted in tungsten being incorporated into the nanotube structure in small amounts, increasingly so as the electrolyte mixture was re-used. The nanotubes showed very similar chemical properties to the non-tungsten analogues; pore size, wall thickness and crystallite size were all of relatively comparable values. Band gap was the only major measurable difference, showing a decrease in size to 2.87 eV, although FESEM imaging did indicate a noticeable increase in malformed

tubes. However, the nanotubes showed no photocatalytic activity when tested for the surface degradation of cinnamic acid and stearic acid.

6.2.3 Gold and Palladium Doped Nanotubes

Gold and palladium were, separately, photodeposited onto 4 and 8 hour anodised nanotubes for 1, 3, 30 and 60 minutes. Testing showed that the presence of either metal negatively affected the photoactivity in the liquid phase and for surface degradation. Liquid phase experiments showed gold was less inhibitive than palladium. During the surface degradation of stearic acid, 8hr Au₃ and 8hr Pd₁ were found to be the most effective, of the metal doped samples, in decreasing the strength of the C-H and C=O bands. 8hr Pd₁ was able to decrease the strength of the C-H band more effectively than the plain 8 hour nanotube, but all metals suffered from a reduced ability to oxidise the carbonyl functionality. Overall, palladium was a better co-catalyst for stearic acid degradation. Several reasons have been presented to explain the reactivity trends:

- Elevated amounts of chloride on palladium doped samples, the adsorption of which is promoted by palladium, is proposed to occupy surface site and restrict cinnamic acid adsorption. This restriction majorly inhibits the key adsorption step in the benzaldehyde mechanism, described in **Chapter 3**, during liquid phase degradation.
- The smaller gold nanoparticles deposited after 3 minutes of deposition ($A_{v_{np}} = 30.1$ nm), rather than one minute ($A_{v_{np}}=40.7$ nm), more effectively penetrate the nanotubes during deposition and are closer to the size the literature suggests is more optimal. [8][9]
- Palladium photodeposited as smaller nanoparticles, $A_{v_{np}} \approx 15$ nm after 1 minute of deposition, with a large amount of it depositing on top of the nanotubes rather in in the tubes. The amount of particles observed during imaging did not explain the amount of palladium detected from XPS, suggesting that palladium must also be depositing as very small particles that were at or beyond the detection limit.
- Based on the above assumption, palladium photodeposition forms numerous small nanoparticles that increases the amount of Schottky interfaces, therefore showing improved photoactivity in comparison to gold deposited samples.

6.2.4 Future Considerations for Work

The nanotubes produced here lacked surface homogeneity, hindering the efficiency of the nanotubes. In the future it would be recommended to add a cleaning step involving HF to remove any surface detritus and open up the tubes completely. A lack of mixed phases is hindering the charge separation in the bare nanotubes, so future work could implement supporting rutile nanoparticles to improve photocatalytic activity. Including rutile particles will also provide appropriate phase boundaries for gold nanoparticles to accumulate at which has been found to improve the visible light induced plasmonic resonance. [10] The methodology used for the photodeposition of gold and palladium could be adjusted to try gain greater control of particle sizes. Gold deposited as particles larger than the often cited optimal size from between 4 to 15 nm. Whereas, while palladium deposited in smaller particles, it suffered from agglomeration and high chloride contamination. The use of an alternative palladium precursor would be wise to eliminate the issue of chloride contamination.

6.3 Metal Loaded Nanoparticles for Waste Water Treatment

6.3.1 Palladium Photocatalysts

Palladium was found to have an increasing negative effect on the degradation rate of cinnamic acid as the weight loading increased. It was determined that the occupation of surface sites instilled a greater negative impact on the surface oriented oxidation, of cinnamic acid to benzaldehyde, than the benefits associated with the introduction of Schottky Junctions. Palladium was also observed to improve the oxidation of carbon deposited on the catalyst surface to CO₂ through an alcohol based decarboxylation step. [11] Degrading cinnamic acid in deoxygenated conditions found that palladium promoted the hydroxyl radical driven oxidation to phenylacetaldehyde. 0.25 and 0.5 wt% were shown to be the most active of the catalysts, providing degradation rates three times faster than in the absence of palladium. In addition to rate improvements, palladium catalysts were also observed to catalyse the photo-oxidation of phenylacetaldehyde. Two possible mechanisms have been proposed that involve the formation of an alcohol, by tautomerisation or solvent oxidation, which may decarboxylate to a toluene intermediate. This work indicates that these palladium doped titania photocatalysts are not an improvement for photocatalytic degradation in oxygenated conditions, compared to mixed phase materials like P25. However, a remarkable increase in degradation was found in low oxygen environments that has potential to be implemented into the treatment of waste water with a low oxygen content.

6.3.2 Gold Photocatalysis

The gold catalysts used in these experiments exhibited poor reactivity for the total oxidation of cinnamic acid. Characterisation showed that the synthesis technique was not appropriate for producing well dispersed gold nanoparticles on the TiO₂ support. Increasing gold loading did not change the magnitude of the impact on the initial degradation of cinnamic, which was attributed to the minimal size effects changing the catalysts surface chemistry. Examination of the fresh and spent XP spectra found the same changes to the carbon character that was observed with palladium, which inferred similar surface reactivity may be occurring. As such it was determined that the poor degradation efficiency was due to the large gold particles acting as recombination centres instead of improving charge separation. 20% selectivity was achieved for phenylacetaldehyde in the absence of oxygen, illustrating the potential for gold catalysts to selectively cleave a C=C bond in aqueous media.

6.3.3 Future Considerations for Work

Just as for future work for **Chapter 3**, ¹⁸O studies would be very illuminating in examining the mechanistic details of the experiments detailed here. Determining exactly how palladium and gold nanoparticles interject in the degradative mechanisms here, by investigating where the oxygen source for the CO₂ originates, would provide some crucial data in understanding the role of metal co-catalysts in photocatalytic mechanisms. Additionally it would be pertinent to fully examine the effects of gold, in particular it would be advantageous to produce gold nanoparticles of similar diameters the palladium particles synthesised for these studies.

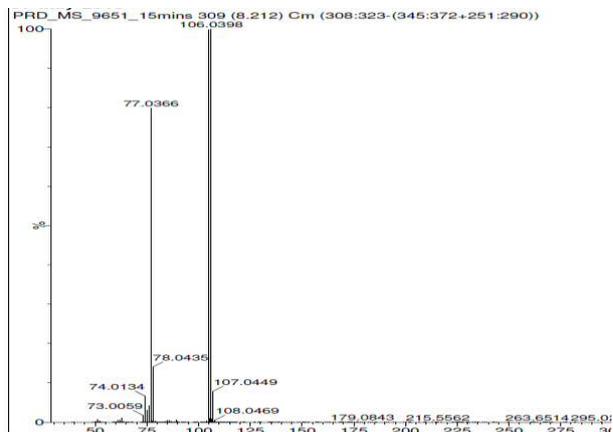
6.4 References

1. H. Maeda, H. Nakagawa and K. Mizuno, *Journal of Photochemistry and Photobiology A: Chemistry*, 2007, **189**, 94–99.
2. X. Pang, C. Chen, H. Ji, Y. Che, W. Ma and J. Zhao, *Molecules*, 2014, **19**, 16291–16311.
3. M. Muneer, M. Qamar and D. Bahnemann, *Journal of Molecular Catalysis A: Chemical*, 2005, **234**, 151–157.
4. Mazzarolo, K. Lee, A. Vincenzo and P. Schmuki, *Electrochemistry Communications*, 2012, **22**, 162–165.

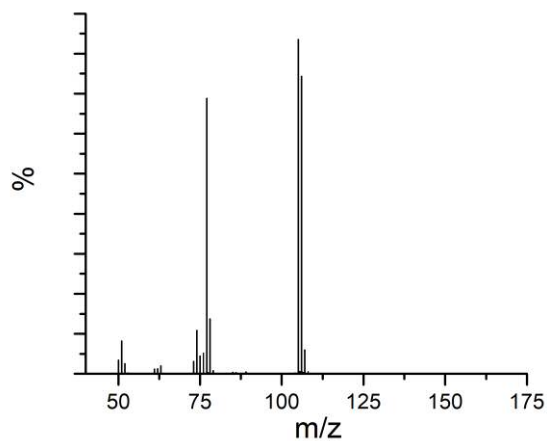
5. G. V. Buxton, M. Bydder, G. A. Salmon and J. E. Williams, *Phys. Chem. Chem. Phys.*, 2000, **2**, 237–245.
6. E. W. Kaiser and T. J. Wallington, *J. Phys. Chem.*, 1996, **100**, 9788–9793.
7. D. Regonini, PhD Thesis, “Anodised TiO₂ Nanotubes: Synthesis, Growth Mechanism and Thermal Stability”, University of Bath, 2008.
8. S. Oros-Ruiz, J. A. Pedraza-Avella, C. Guzmán, M. Quintana, E. Moctezuma, G. del Angel, R. Gómez and E. Pérez, *Top Catal*, 2011, **54**, 519–526.
9. Tanabe, T. Ryoki and Y. Ozaki, *RSC Adv.*, 2015, **5**, 13648–13652.
10. D. Tsukamoto, Y. Shiraishi, Y. Sugano, S. Ichikawa, S. Tanaka and T. Hirai, *J. Am. Chem. Soc.*, 2012, **134**, 6309–6315.
11. H. Bahruji, M. Bowker, P. R. Davies and F. Pedrono, *Applied Catalysis B: Environmental*, 2011, **107**, 205–209.

Appendix 1 – Mass Spectra

1.1 Mass Spectra for Cinnamic Acid Degradation



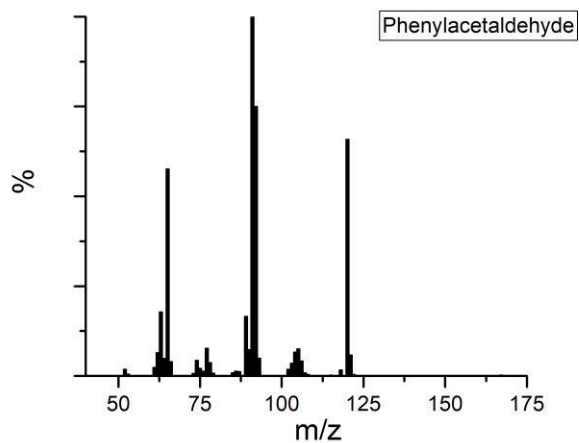
1.1.1 A mass spectrum at taken from the photocatalytic degradation of cinnamic acid 15 minutes after irradiation has begun. (Retention time = 11.1 minutes)



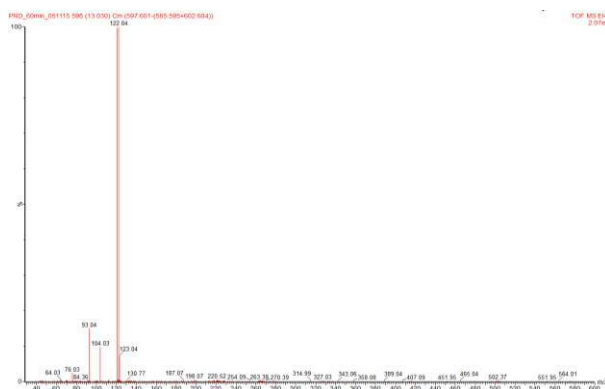
1.1.2 Mass spectrum from a benzaldehyde calibration sample (retention time = 11.1 minutes)



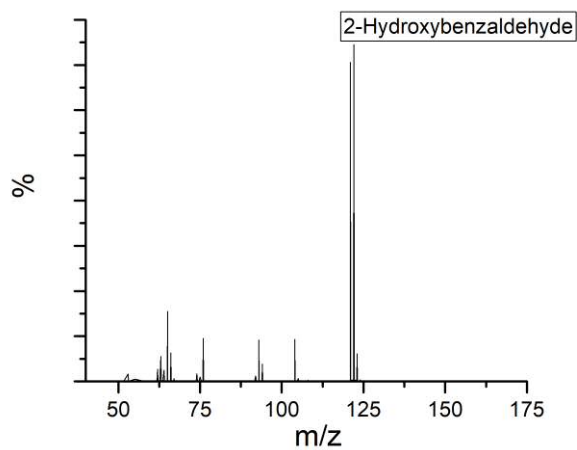
1.1.3 A mass spectrum at taken from the photocatalytic degradation of cinnamic acid 20 minutes after irradiation has begun. (Retention time = 13.2 minutes)



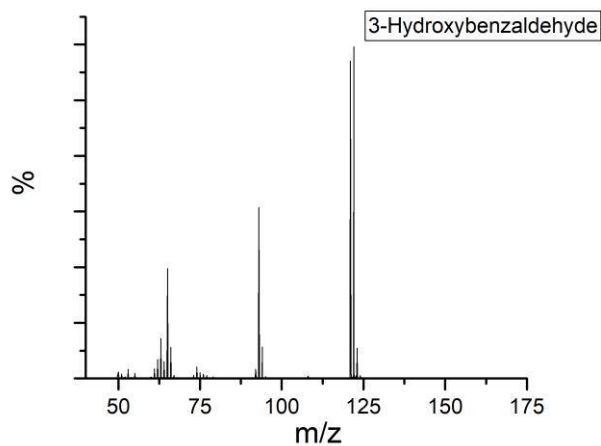
1.1.4 Mass spectrum from a phenylacetaldehyde calibration sample (retention time = 13.1 minutes)



1.1.5 A mass spectrum at taken from the photocatalytic degradation of cinnamic acid 60 minutes after irradiation has begun. (Retention time = 13.0 minutes)



1.1.6 Mass spectrum from a 2-hydroxybenzaldehyde calibration sample (retention time = 12.9 minutes)

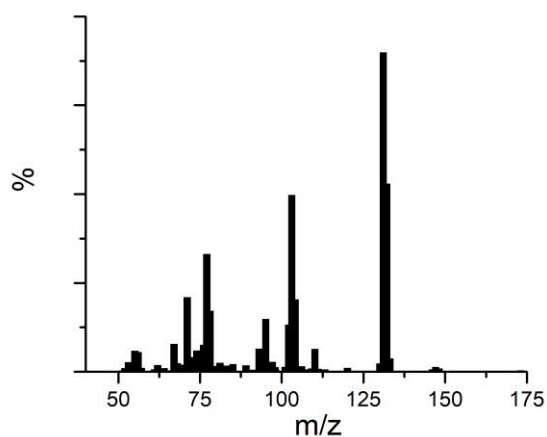


1.1.7 A mass spectrum at taken from the photocatalytic degradation of benzaldehyde 20 minutes after irradiation has begun. (Retention time = 18.4 minutes)

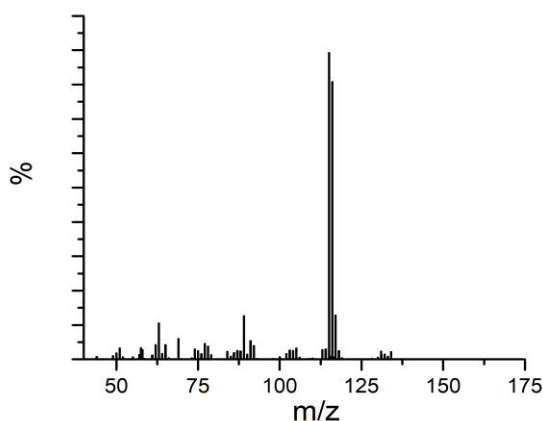


1.1.8 Mass spectrum from a 3-hydroxybenzaldehyde calibration sample (retention time = 18.4 minutes)

1.2 Mass Spectra for Cinnamyl Alcohol Degradation

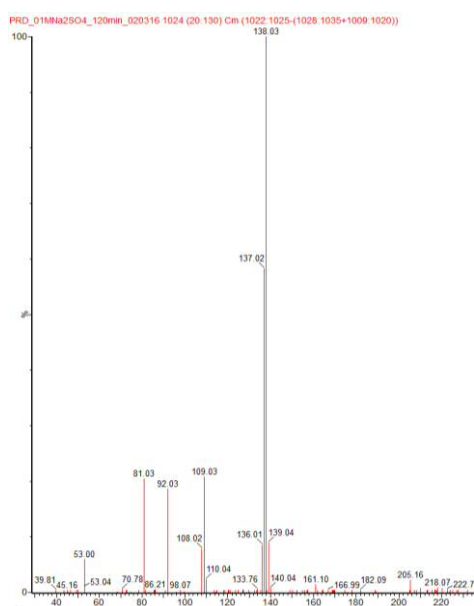


1.2.1 A mass spectrum at taken from the photocatalytic degradation of cinnamyl alcohol 30 minutes before (-30 minutes) irradiation has begun. (Retention time = 18.1 minutes)



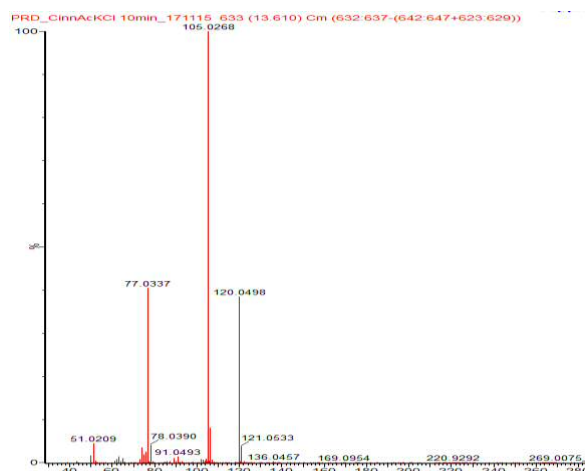
1.2.2 A mass spectrum at taken from the photocatalytic degradation of cinnamyl alcohol after 30 minutes of stirring (0 minutes) with mP25 (Retention time = 18.1 minutes)

1.3 Mass Spectra for Cinnamic Acid Degradation in the Presence of Sulfate

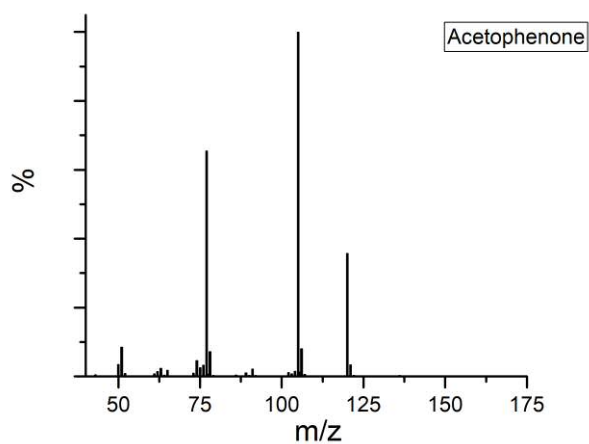


1.3.1 A mass spectrum at taken from the photocatalytic degradation of cinnamic acid, in the presence of Na₂SO₄, 120 minutes after irradiation has begun. (Retention time = 20.1

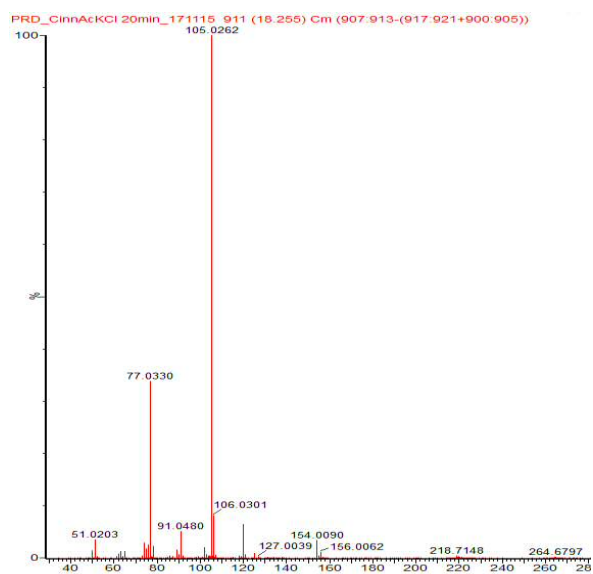
1.4 Mass Spectra for Cinnamic Acid Degradation in the Presence of Chloride



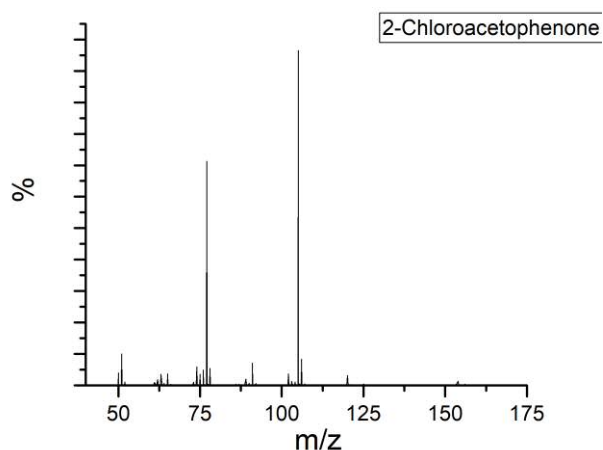
1.4.1 A mass spectrum at taken from the photocatalytic degradation of cinnamic acid, in the presence of KCl, 10 minutes after irradiation has begun. (Retention time = 13.6 minutes)



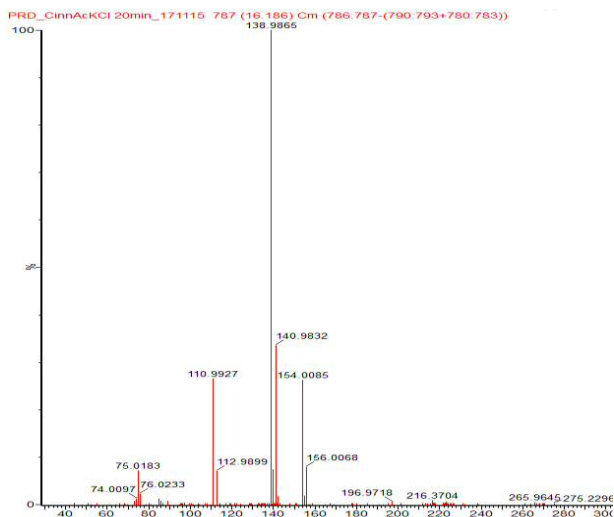
1.4.2 Mass spectrum from an acetophenone calibration standard (retention time = 13.6 minutes)



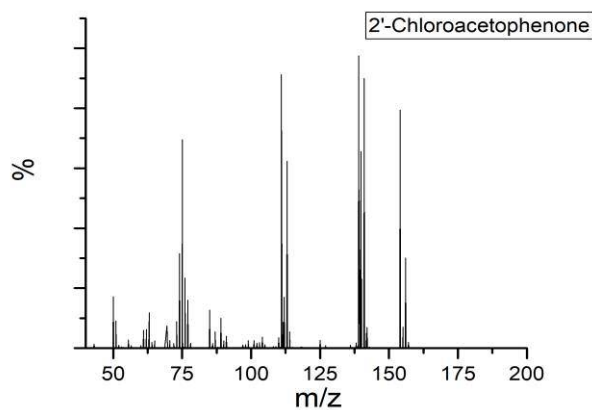
1.4.3 A mass spectrum taken from the photocatalytic degradation of cinnamic acid, in the presence of KCl, 10 minutes after irradiation has begun. (Retention time = 18.1 minutes)



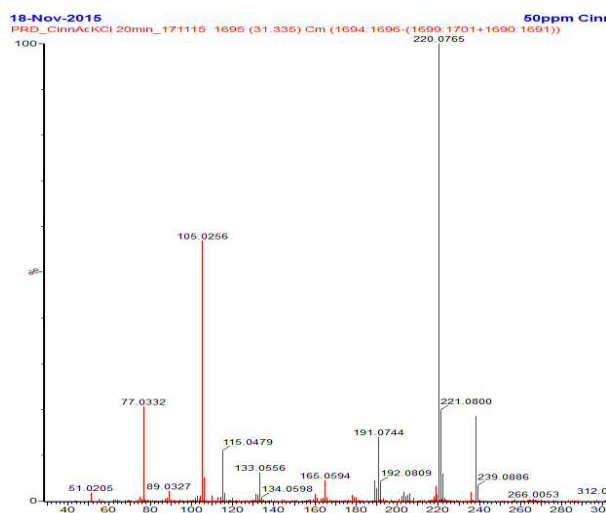
1.4.4 Mass spectrum from a 2-Chloroacetophenone calibration standard (retention time = 18.2 minutes)



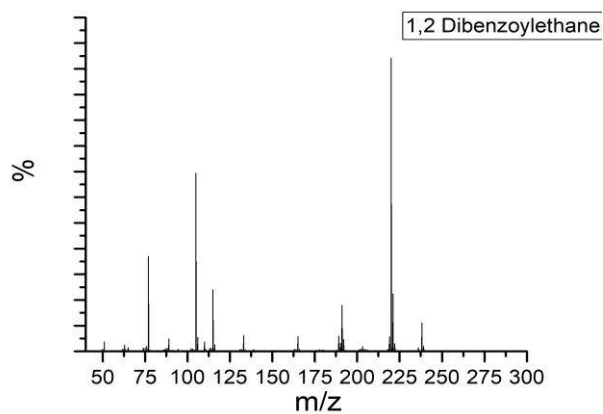
1.4.5 A mass spectrum at taken from the photocatalytic degradation of cinnamic acid, in the presence of KCl, 20 minutes after irradiation has begun. (Retention time = 16.2 minutes)



1.4.6 Mass spectrum from a 2'-Chloroacetophenone calibration standard (retention time = 16.1 minutes)

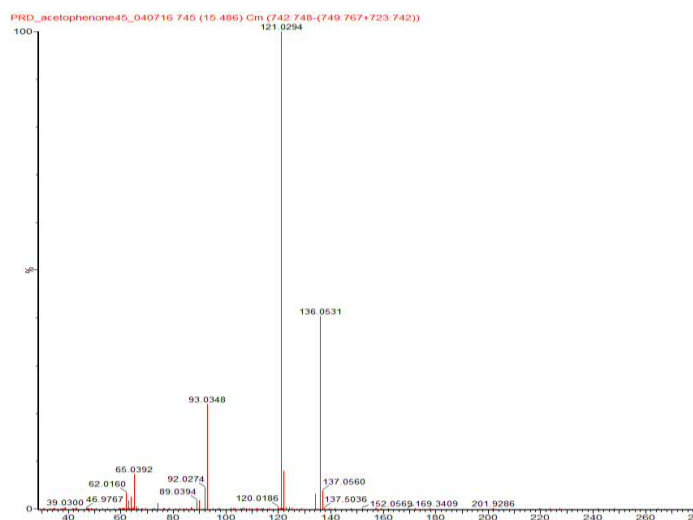


1.4.7 A mass spectrum at taken from the photocatalytic degradation of cinnamic acid, in the presence of KCl, 20 minutes after irradiation has begun. (Retention time = 31.3 minutes)

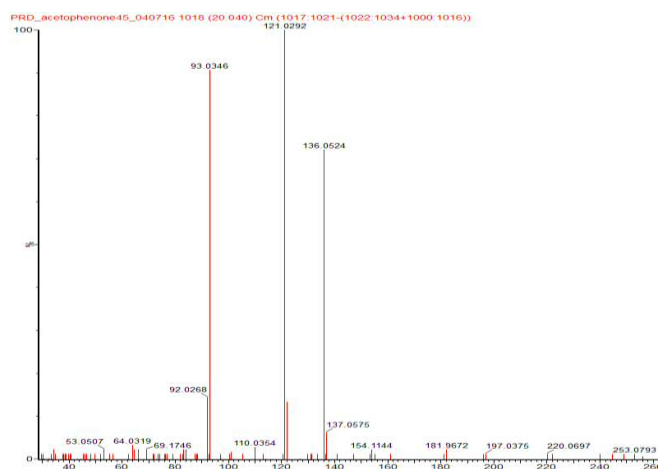


1.4.8 Mass spectrum from a 1,2-Dibenzoyl ethane calibration standard (Retention time = 31.3 minutes)

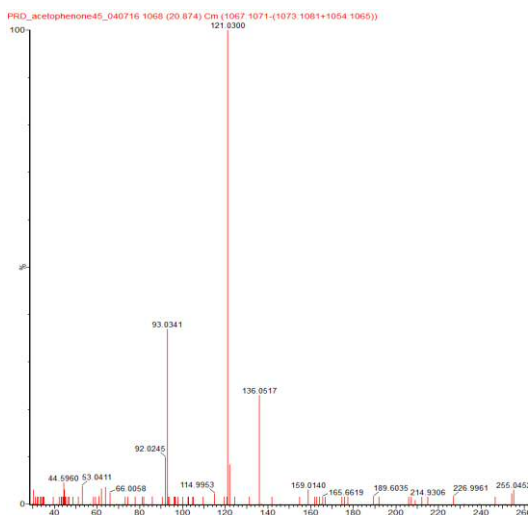
1.5 Mass Spectra for Acetophenone Degradation



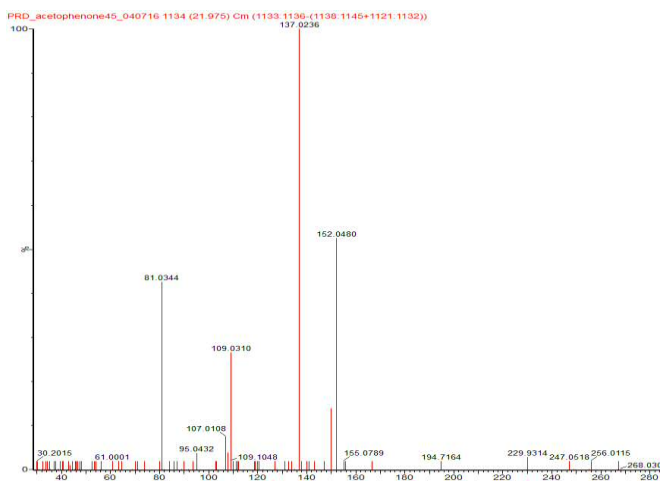
1.5.1 A mass spectrum at taken from the photocatalytic degradation of acetophenone 45 minutes after irradiation has begun. (Retention time = 15.5 minutes)



1.5.2 A mass spectrum at taken from the photocatalytic degradation of acetophenone 45 minutes after irradiation has begun. (Retention time = 20 minutes)

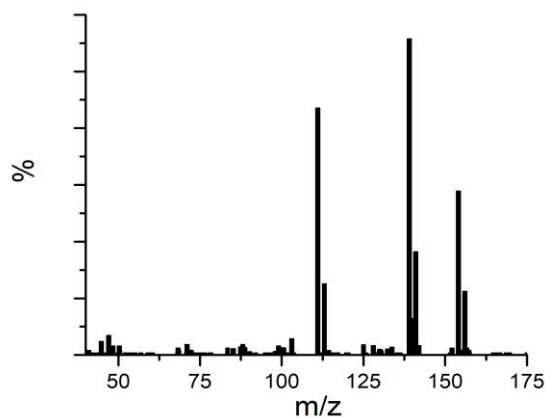


1.5.3 A mass spectrum at taken from the photocatalytic degradation of acetophenone 45 minutes after irradiation has begun. (Retention time = 20.9 minutes)



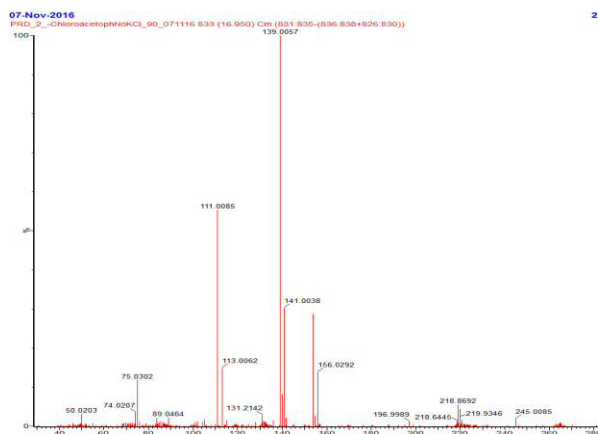
1.5.4 A mass spectrum at taken from the photocatalytic degradation of acetophenone 45 minutes after irradiation has begun. (Retention time = 22.0 minutes)

1.6 Mass Spectra for 2-Chloroacetophenone Degradation

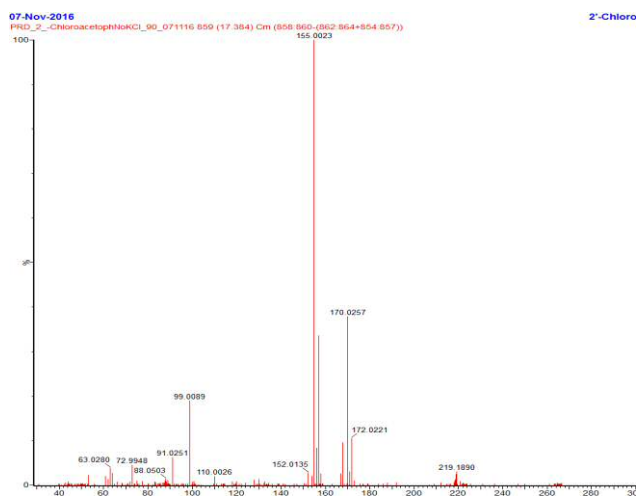


1.6.1 2-Chloroacetophenone (5) reaction 17.0 mins

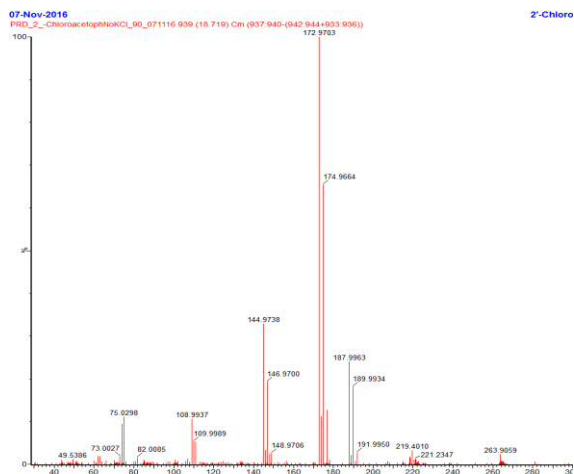
1.7 Mass Spectra for 2'-Chloroacetophenone Degradation



1.7.1 A mass spectrum at taken from the photocatalytic degradation of 2'-chloroacetophenone, in the absence of chloride, 90 minutes after irradiation has begun.



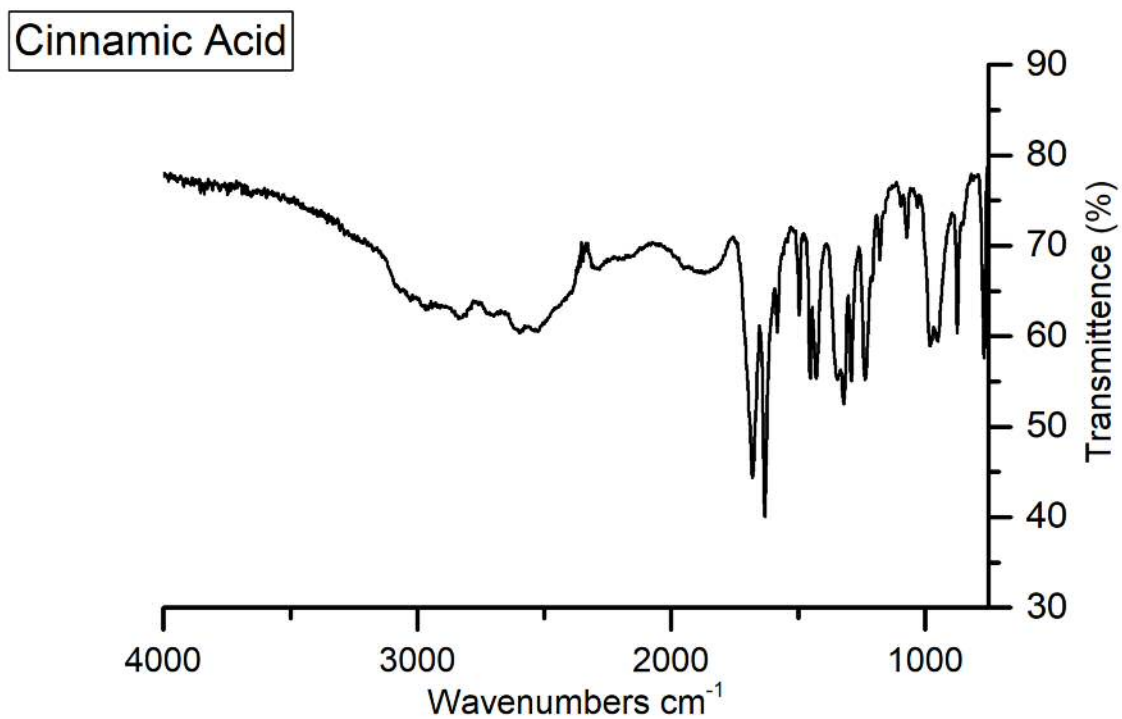
1.7.2 A mass spectrum at taken from the photocatalytic degradation of 2'-chloroacetophenone, in the absence of chloride, 90 minutes after irradiation has begun.



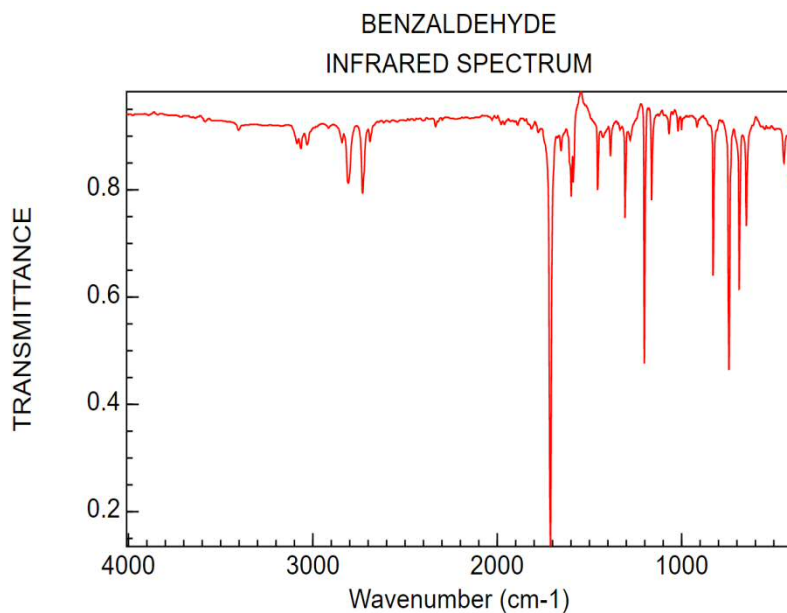
1.7.3 A mass spectrum at taken from the photocatalytic degradation of 2'-chloroacetophenone, in the absence of chloride, 90 minutes after irradiation has begun.

Appendix 2 – Infrared Spectra

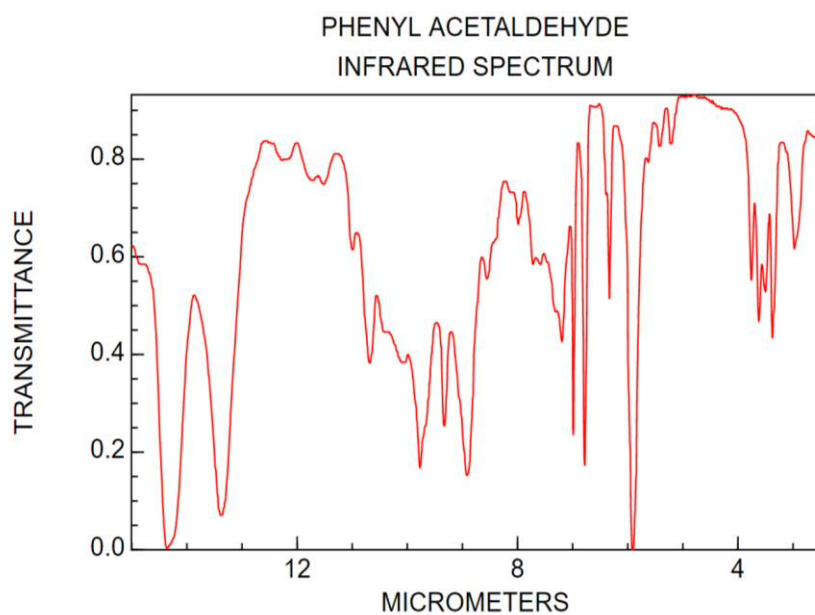
2.1 Infrared spectrum of Cinnamic Acid



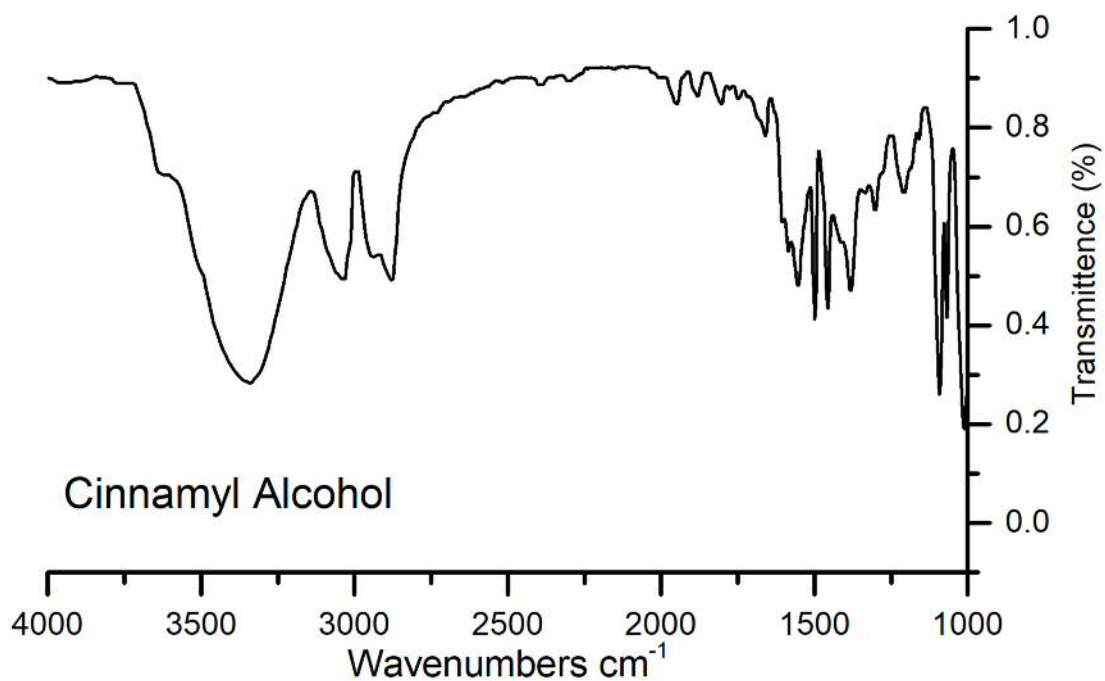
2.2 Infrared spectrum of benzaldehyde (2)



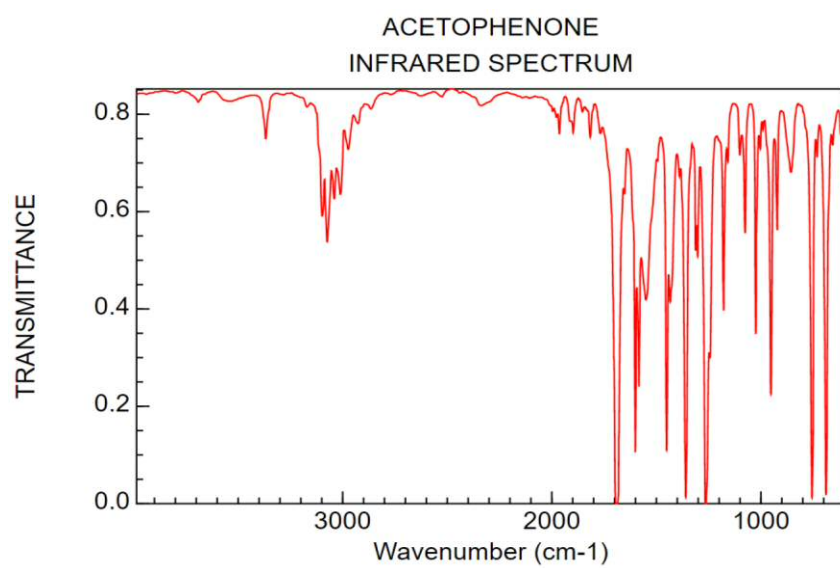
2.3 Infrared spectrum of phenylacetaldehyde (3)



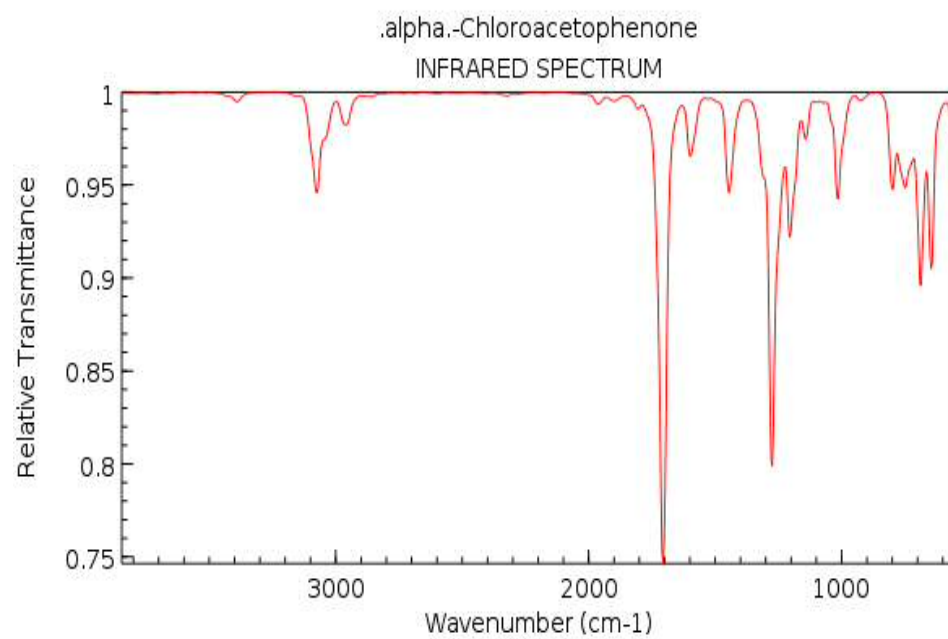
2.4 Infrared spectrum of cinnamyl alcohol



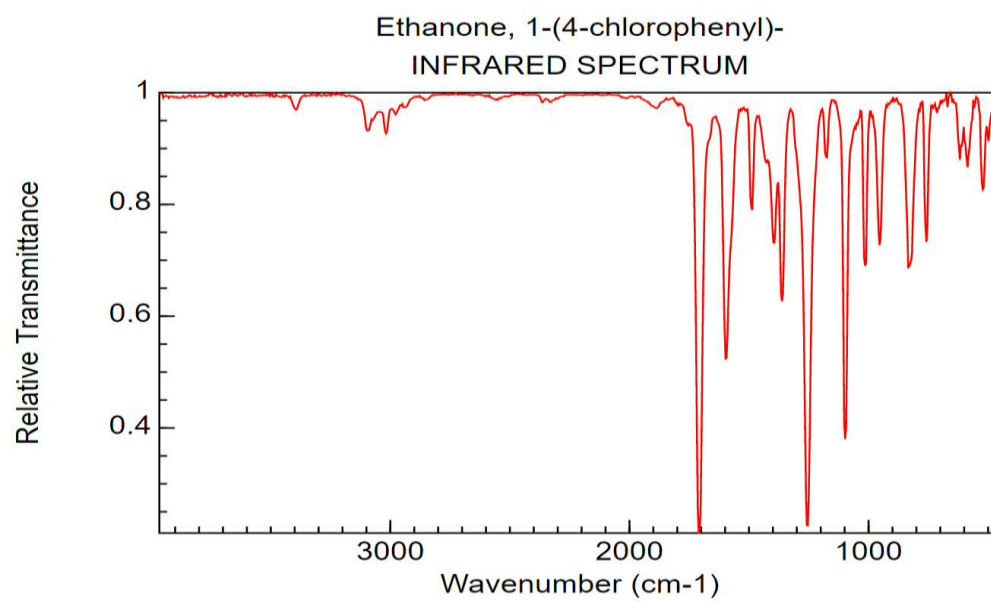
2.5 Infrared spectrum of acetophenone (4)



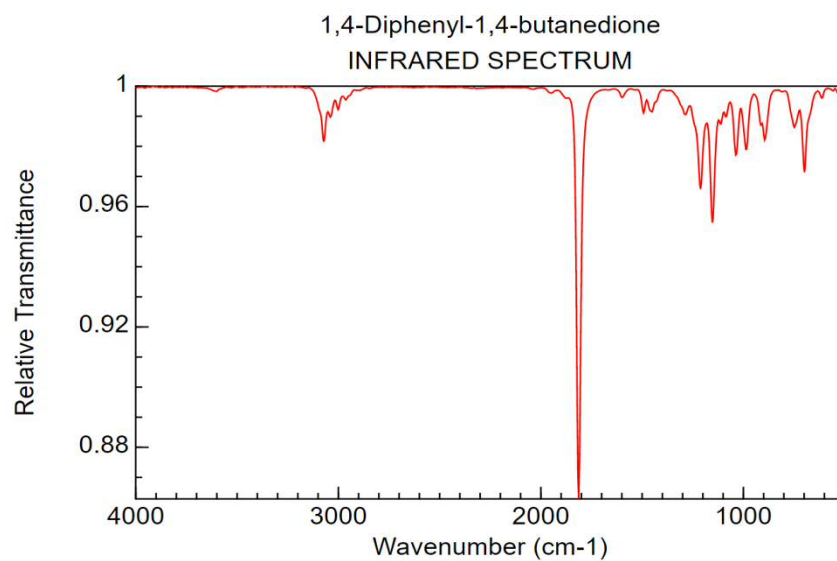
2.6 Infrared spectrum of 2-chloroacetophenone (5)



2.7 Infrared spectrum of 2'-chloroacetophenone (6)

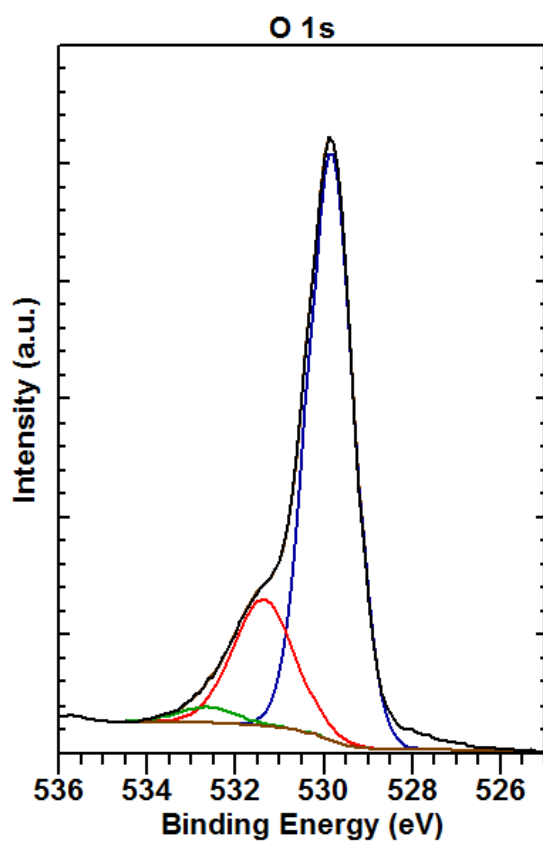


2.8 Infrared spectrum of 1,2-dibenzoylthane (7)



Appendix 3 – XP Spectra

3.1 Cinnamic Acid XP Spectra



CasaXPS (This string can be edited in CasaXPS.DEF/PrintFootNote.txt)

